GREEN SYNTHESIS OF GRAPHENE-METAL OXIDE COMPOSITES AS A PROMISING ELECTRODE FOR ENERGY STORAGE

EZEIGWE EJIKEME RAPHAEL

Thesis submitted to the University of Nottingham

for the Doctor of Philosophy degree

December 2017

Abstract

The key motivation of this study is to investigate the potential of graphene/metal oxides nanocomposites as electrodes for electrochemical capacitor applications. It is envisioned that the positive synergistic effect between graphene and metal oxides (where novel graphene material acts as a highly conductive platform for ease of ion transfer kinetics and metal oxide acts as spacers to avoid the restacking of graphene sheets to make available more active surface areas) results in excellent electrode material for high performance electrochemical capacitor.

In this thesis, a series of hybrid composites comprising of graphene and low cost transition metal oxides were synthesised and characterised for their potential as electrode for electrochemical capacitor applications. In order to achieve this, the graphene used in the preparation of the hybrid composites was successfully synthesised from highly pyrolytic graphene in a proper ratio of ethanol and water before the integration of the metal oxides via a solvothermal route. A parametric study was carried out in a step by step approach to validate the success of the composite synthesis before the electrochemical stage. X-ray Diffraction, Field emission and Transmission scanning electron microscopy, energy-dispersive X-ray and Raman spectroscopy, cyclic voltammetry and galvanostatic charge/discharge tests were used to verify the integrity of the as-produced graphene/metal oxide composites and their applicability to electrochemical capacitors.

Upon the completion of the experimental work, the electrochemical tests demonstrated that the introduction of graphene to the metal oxide improved the electrochemical performance in-terms of capacitance, energy density, power density, equivalent series resistance and cycling stability. The results also indicated that the ratio of graphene to metal-oxide plays a significant role in the electrochemical performance of the composite. In comparison with the different graphene/Zinc oxide (ZnO) nanocomposites studied, the electrode material with a weight ratio of 1:8 (graphene: ZnO) displayed a specific capacitance of 236 F/g at a scan rate of 10 mV/s with energy and power densities of 11.80 Wh/kg and 42.48 kW/kg respectively. The specific capacitance of the graphene-Manganese oxide (MnO_2) composite electrode material with a weight ratio of 1:16 (graphene: MnO_2) demonstrated the best performance of 380 F/g at a scan rate of 5 mV/s among the four ratios studied. The G1Co4 composite electrode with a weight ratio of 1:8 (graphene: Co_3O_4) demonstrated a superior specific capacitance of 384 F/g at a current density of 0.3 A/g coupled with retention of 80% of its capacitance after 1000 cycles among the graphene-cobalt composites. The Graphene-Nickel cobaltite composite electrode with weight ratio of 1:8 (graphene: $NiCo_2O_4$) labelled G-8NC_2 displayed a superior specific capacitance (698 F/g at a current density of 0.5 A/g) and good cycling stability (74% capacity retention after 5000 cycles at current density of 1 A/g). The 1:8 ratio exhibited well attached Nickel molybdate nanorods on the surface and edges of the graphene sheets with the highest specific capacitance of 670 F/g at 0.3 A/g, as compared to other tested composites.

The significance of these findings details a synthesis route that provides an effective, simple and practical method of preparing graphene-metal oxide composite materials for electrochemical capacitor applications.

Acknowledgement

I want to express my heartfelt gratitude to amiable supervisors, Dr Michelle Tan and Professor Khiew Poi Sim, for their encouragement, support, guidance and willingness to talk with about the possibilities and problems of my research work. Thank you both for constantly being available throughout this research journey. I also thank Dr Chiu Wee Siong for his guidance with the Raman and Transmission Electron Microscopy at the University of Malaya. Special thanks to professor Dino Isa and Mr Anandan Shanmugam for their advices and the generous access to the equipment in the Supercapacitor Lab.

It’s my pleasure to have worked with a group of brilliant, warmhearted and lovely people, Dr Joanna Chia, Dr Ho Mui Yen and Dr Low Sze Shin. My sincerest appreciation goes to the wonderful technicians at our campus, Mr Fareez, Mr Andrew, Ms Filzah, Ms Farah and Ms Fatihah for their help in material characterisation and laboratory equipment arrangement.

I thank God for His Graces and Blessings, the entire Ezeigwe family for their continuous encouragement, boundless love, prayers and support in making me achieve this feat. Last but not least, to all my good friends, Obiga, Bruno, Ola, Feven, Nemat, Agnes, Lillian, Jing Yang, Chioma, Kenneth, Haruna, who have been there for me throughout this journey, reminding me to eat, dragging me out when they realize that I need some relaxation. It has been wonderful moments and this thesis exists because of you.

Table of Contents

Chapter 1

Chapter 2

Chapter 3

Chapter 5

Chapter 6

Chapter 7

Chapter 8

Chapter 9

List of Abbreviations

BTMO	Binary transition metal oxide
CCD	Charge coupled device
CNT	Carbon nanotube
$Co(NO_3)_2.6H_2O$	Cobalt (ii) nitrate hexahydrate
Co_2	Carbon dioxide
Co_3O_4	Cobalt oxide
$CoCl_2$	Cobalt (ii) chloride hexahydrate
$CoMoO_4$	Cobalt molybdate
CV	Cyclic voltammetry
CV	Cyclic voltammogram
DI	Deionised
DWCNT	Double-walled carbon nanotube
EDLC	Electrochemical double layer capacitance
EDS	Energy dispersive x-ray spectroscopy
EIS	Electrochemical impedance spectroscopy
ESR	Equivalent series resistance
FESEM	Field emission scanning electron microscopy
FWHM	Full width of at half maximum
GCD	Galvanostatic charge/discharge
HOPG	Highly pyrolytic graphite
HRTEM	High resolution transmission electron microscopy
ICDD	International centre for diffraction data
JCPDS	Joint committee on powder diffraction standards
$KMnO_4$	Potassium permanganate
KOH	Potassium hydroxide
MnO_2	Manganese oxide
$MnSO_4.H_2O$	Manganese sulphate
MTMO	Mixed transitional metal oxide
MWCNT	Multi-walled carbon nanotube

$NaMoO_4.2H_2O$	Sodium molybdate dehydrate
NaOH	Sodium hydroxide
$Ni(NO_3)_2.6H_2O$	Nickel (ii) nitrate hexahydrate
$NiCo_2O_4$	Nickel cobaltite
$NiMoO_4$	Nickel molybdate
NMP	N-methyl-2-pyrrolidinone
PVDF	Polyvinylidene fluoride
R_{ct}	Charge-transfer resistance
rGO	Reduced graphene oxide
SnO_2	Tin dioxide
SWCNT	Single-walled carbon nanotube
TEM	Transmission electron microscopy
$TiCl_3$	Titanium(iii) chloride
TMO	Transition metal oxide
XRD	X-ray power diffraction
XRD	X-ray diffraction
$Zn(NO_3)_2.6H_20$	Zinc nitrate hexahydrate
Zn_2SnO_4	Zinc stannate
$ZnCo_2O_4$	Zinc cobaltite
ZnO	Zinc oxide

List of Figures

List of Tables

Chapter 1

Introduction

1.1 Background

The use of energy is pivotal to the growth of human civilization and the improvement of modern technology [1]. The increase in global population, robust economies, depletion of non-renewable resources and rapid advancement in technology has led to great demand of renewable energy to power homes, business endeavors, transportation and industries. The consumer need to use power is greater than the power generated by energy source at any time hence the necessity of energy storage devices to recompense for the insufficient amounts of power provided by renewable and non-renewable energy sources [1]–[3].

Energy storage devices are systems aimed to provide energy on demand; they store up electric charges into a form that can be converted back to electrical energy when the need arises. For example, to generate additional electricity during times of low demand and using it to augment capacity at times of high demand hence enabling effective utilisation of energy. Energy storage devices can improve the consistency of electric energy and play an integral role in integrating alternatives to fossil fuels to reduce emission of CO_2 gas to the environment. This important tool towards efficient and versatile energy applications has gained remarkable attention among the industry, society and academia. An improvement in energy storage technology could aid consumers in meeting their daily energy demands and may be able to bring electric supply to regions that are not currently possible [1], [4], [5].

Energy storage systems are generally termed to adopt the technology of either an external electrical or external thermal interface. A thermal energy storage system uses the latent heat capacity of materials to provide a cooling or heating resource that can be called upon when required while in contrast, an electrical energy storage system embraces all systems and processes with external electrical interfaces [6]. Energy storage system can be classified into groups by the amount of power and energy made accessible for the load which includes fuel cells, capacitors, batteries and supercapacitors [7]. The Ragone plot (Figure 1.1) depicts that the various energy storage devices are characteristically located in different regions. It also shows the available energy of an energy storage device for a fixed amount of power. The fuel cells having the highest energy density stores more energy compared to other various energy storage devices as shown in Figure 1.1, but it has the least amount of time for charging and discharging. Batteries store a large amount of energy due to its high energy density but are limited to their slow charging time. On the other hand, capacitors have the fastest time of charging and discharging electric current but have low energy storage. The supercapacitor also known as electrochemical capacitors stores more energy when compared to the capacitor and has a faster charging time when compared to batteries.

The ability of electrochemical capacitors to exploit higher surface area electrodes and thinner dielectric to achieve greater capacitance allows it to have more power densities than those of batteries and greater energy densities than those of capacitors [8]. Advances in research and application of electrochemical capacitors have increased ominously over the years due to the unique properties of their ability to operate at temperatures from -20 to 55 ^{o}C under various application conditions, environmental friendliness, long cycle life, high power density and it is an intermediary in the energy gap between batteries/fuel cells (high energy storage) and capacitors (high power density) [3], [9]

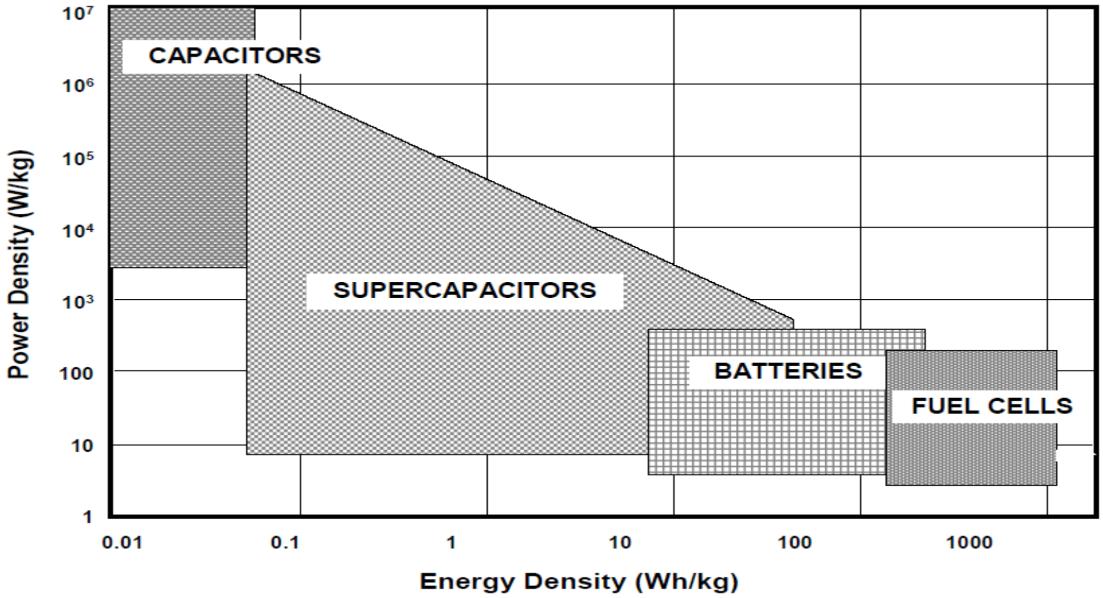

Figure 1.1: Ragone plot showing the available energy of various energy storage devices for constant power request [7].

1.2 Motivation of the Project

Electrochemical capacitors application areas includes portable energy sources where it may act as a rechargeable individual power source, power electronics due to their high capacitance values ranging from 1 to 2700 F, hybrid electric vehicles where it provides necessary power acceleration and recovery of break energy, it also acts as a standby power supply to prevent power fluctuations by complementing fuel cells or batteries in energy storage functions. Despite the availability of electrochemical capacitors in the market, some factors limit its attractiveness to consumers: long term durability issues, high cost and most importantly its low energy density [9], [10].

Scientific and technological advancement have indicated 10 - 20 % improvements of supercapacitor performance in terms of energy density, improved cycle life and a reduction of production cost with continual study and development on its current collectors, electrolytes, plates, seals and electrodes [6]. The electrode material which is an integral part of the supercapacitor plays a significant role in the electrochemical performance hence making it an essential component to overcome its challenges. The advancement and innovation of electrode materials with tailored structure and highly electrochemically active materials can improve the overall performance of electrochemical capacitors [1], [3]

Graphene, an allotrope of carbon consisting of a flat single layer of sp^2 boned carbon atoms into a two-dimensional honey comb lattice is highly anticipated to be an excellent electrode material owing to its distinguished properties such as high specific surface area, good electrochemical stability, good elasticity and an excellent electrical conductivity. Unfortunately, restacking and serious agglomeration of graphene sheets causes great loss of active surface area resulting in poorer electrochemical performance [11], [12].

Due to its limited capacity, efforts have been made to substitute graphene as electrode material with metal oxides which are known to have larger capacitance and higher energy density. However, the poor electrical conductivity, low rate capability and cycling stability of metal oxides call for better substitutes [3], [11], [13], [14].

Further research has demonstrated that exploiting the practical use of the collective merits of both graphene and metal oxides as electrode materials can improve the electrochemical performance of the supercapacitor. As composite material, the metal oxides are able to improve the overall capacitance of the electrode by providing high capacitance while graphene offers an improved chemical functionality and compatibility. The synergistic effects between graphene and metal oxides see the graphene reducing the resistance by providing a conductive platform for easy ion kinetics while the metal oxide acts as spacers to avoid the restacking of graphene sheets to make available more active surface areas [2], [11], [15]. The resulting composite is a new material with new properties and functionalities and not a mere sum of the individual components [11]. The advantages and disadvantages of graphene, metal oxides and the pros of graphene/metal oxides composites as electrode materials are summarised in Table 1.1.

Table 1.1: A summary on the pros and cons of graphene, metal oxide and pros of graphene/metal oxide as electrode material in electrochemical capacitors.

Electrode materials	Advantages	Disadvantages
Graphene	• High electrical conductivity [16]. • High surface/volume ratio [17]. • Chemical stability [18].	• Agglomeration [19]. • Restacking [20]. • Rapid capacity fading [11]. • Low energy density [11].
Metal Oxides	• Large capacitance [1]. • High packing density [11]. • High energy density [21]. • Abundant resources [22].	• Low electrical conductivity [17]. • Large volume changes during charge/discharge process [23]. • Low initial coulombic efficiency [24]. • Poor cycling stability [25].
Graphene/ metal Oxide composites	• Synergistic effects [26] • Suppress the volume change of metal oxide [11]. • Highly conducting network [27]. • Improved cycling stability [28]. • Improved energy and power densities [29]. • Prevents agglomeration of metal oxides and re-stacking of graphene [30].	

Several studies have reported different synthesis route to produce graphene-metal oxide composites for electrochemical capacitors such as hydrothermal synthesis [31]–[33] microwave synthesis [34]–[36], electro-deposition [37]–[39], sol gel [40] and chemical bath deposition [41]–[43]. It should be noted that most of the work reported on graphene-metal oxide composites had utilised graphene material synthesised via the modified Hummers method. This chemical route normally involves harsh acid treatment followed by chemical reduction to form reduced graphene oxide (rGO). The aim of the reduction process is to remove the oxygenated groups formed as a result of the oxidative treatment. Nevertheless, numerous literatures have reported that certain residual groups such as hydroxyls, epoxyls, carbonyls and carboxyls cannot be entirely removed even after reduction processes resulting in crystal defects that hinders the electrical conductivity of the reduced graphene oxide [44]–[46]. Additionally, harsh acid treatments not only hamper the quality of the graphene produced, it is also harmful to the researcher and the environment at large.

1.3 Rationale of current study

In this study, a green synthesis route to synthesise the graphene-metal nanocomposites material is presented. Compared to the modified Hummers method, the liquid phase exfoliation of graphite is a green strategy that avoids the use of harsh chemicals (strong acid and oxidizer) or high temperature for reducing graphene oxide. In this regard, this method basically involves the sonication of raw highly pyrolytic graphite flakes in an optimum ratio of ethanol and de-ionized water as reported in [45]. In principle, this technique makes use of a common reagent (ethanol) as its exfoliation medium which has a boiling point of 78.37 ^{o}C [47] thereby making this synthesis route relatively safe to the researcher and more importantly preserves the pristine structure of graphene. Different metal oxides under the classification of transition metal oxide (TMO) and binary transition metal oxide (BTMO) were synthesised with graphene using facile solvent exfoliation and low temperature solvothermal processing methods forming binary and ternary composites respectively. It is the aim of the study to develop various graphene/metal oxides composite materials with enhanced electrochemical performance as electrodes for supercapacitor application.

Overall, the scope of the research can be categorised into two main parts, as follows:

1. To develop a facile and environmental benign route for the synthesis of various graphene/metal oxide nanocomposites. To achieve this, various metal oxides within the classification of transition metal oxides (TMOs) and binary transition metal oxides (BTMOs) will be explored and incorporated with graphene. Additionally, different composites ratios of the metal oxides with graphene would be prepared. The crystallographic information of the as-prepared composites would be characterised by X-ray power diffraction (XRD) and Raman spectroscopy. The surface characteristics and elemental compositions of the composites analysed using a scanning electron microscope and transmission electron microscope.
2. To evaluate the electrochemical performances of the as produced graphene/metal oxides nanocomposites as electrode materials for electrochemical capacitors. The electrochemical performance comparison of the different weight ratios in terms of specific capacitance, cyclic voltammetry, cyclic measurement using charging/discharging, impedance spectroscopy and energy/power densities would be

studied. This is to determine the ratio with the best synergistic effect of the high electrical conductivity of graphene and the pseudocapacitance of metal oxide.

1.4 Report Organisation

In the next chapter of this report, a literature review carried out on electrochemical capacitors as an energy storage device will be presented.

Chapter 2, *Literature Review* covers the different categories of electrochemical capacitors as well as the synthesis and application of a hybrid composite material comprising of graphene and metal oxide as an electrode material. This chapter is followed by a technical run on the characterisation techniques used to characterise the as produced composites.

Chapter 3, *Experimental Characterisation Techniques,* will detail the chemical, reagents and the experimental methods used in this study. Furthermore, different basic working principles of the characterisation techniques required to analyse the resultant composite materials to determine its morphology, crystalline structure and chemical state. Methods required to evaluate the electrochemical performance of the electrode material were reviewed.

Chapter 4, *One-Step Green Synthesis of Graphene/ZnO Nanocomposites for Electrochemical Capacitors* reports a brief review on the interest of graphene/ZnO nanocomposites as an electrode material. The results obtained by varying the mass ratios of graphene to zinc precursor will be discussed and their electrochemical performance compared with the graphene electrode via cyclic voltammetry (CV), galvanostatic charge-discharge tests and electrochemical impedance spectroscopy (EIS) analysis.

Chapter 5, *Solvothermal Synthesis of Graphene/*MnO_2 *Nanocomposites and Their Electrochemical Behavior* presents an overview of the motivation behind graphene/MnO_2 nanocomposite as material for supercapacitor electrode. This is followed by the results of the characterization analyses carried out to determine the morphology, crystalline structure and chemical composition of the resultant composites. The electrochemical properties of the graphene-MnO_2 nanocomposites would be examined by cyclic voltammetry (CV), galvanostatic charge-discharge tests and electrochemical impedance spectroscopy (EIS).

Chapter 6, *Cobalt Oxide Nanoparticles Grown on Exfoliated Graphene for Enhanced Electrochemical Performance* documents a brief synopsis of graphene-cobalt oxide composites as an electrode material. It also contains the results of the characterization analyses carried out to determine the morphology, crystalline structure and chemical composition of the resultant composites. The electrochemical properties of the graphene-cobalt oxide nanocomposites are to be studied by cyclic voltammetry (CV), galvanostatic charge-discharge tests and electrochemical impedance spectroscopy (EIS).

Chapter 7*, Solvothermal Synthesis of Graphene/*$NiCo_2O_4$ *Nanocomposite as an Electrode Material for Electrochemical Capacitors* covers foremost the purpose on the significant attention drawn to graphene/$NiCo_2O_4$ as an electrode material, closely followed by the comparative results in terms of the surface characteristics, structural and electrochemical properties of the as-prepared graphene/$NiCo_2O_4$ nanocomposites.

Chapter 8, *Synthesis of* $NiMoO_4$ *Nanorods on Graphene and Superior Electrochemical Performance of the Resulting Ternary Based Composites*, details the motivation on the preferred ternary based nanocomposites as an electrode for electrochemical capacitors. The morphology, crystalline structure, chemical compositions and electrochemical properties of the resulting nanocomposites would be evaluated.

Chapter 9, *Conclusion and Future Direction* summarises the entire findings and work done with discussions and recommendations on the future work to be carried out for this research.

Chapter 2

Literature Review

2.1 Overview

Electric charge was first discovered when Thales of Miletus, a Greek Philosopher rubbed amber with a cloth and studied its magnetic particle attraction. This event resulted to the act of rubbing two non-conducting materials against one-another to produce a charge, hence termed the triboelectric effect [10]. Based on this phenomenon, Hermann von Helmholtz in 1858 proposed the electrochemical double layer theory for energy storage. The application of this principle in a cell or battery of cells was claimed by Becker in 1957 [9], the earliest supercapacitor with an unusually high capacitance comprising of carbon electrode material with an aqueous electrolyte projected to operate at low voltage [9], [10]. Further modifications by Boos as detailed in a 1970 patent brought about the first practical supercapacitor [10].

The global need for more energy which at the same time has to be cleaner has seen the increment of renewable energy sources in power generation for global energy consumption in 2015 rose to 2.8 % from 0.8 % compared to a decade ago [48] and a decrement on the value of fossil-fuel consumption to $325 billion from $500 billion compared to the previous year [49]. It has been predicted that as a result of the continuous worldwide development, the demand for energy by 2035 would be about 32000 TWh [50]. Thus, leading to extensive research and development on supercapacitors as alternative energy storage devices to store and provide high power when needed [51]–[53].

A supercapacitor is known by different colloquial names such as ‘electrochemical capacitor’, ‘ultracapacitor’ and ‘power capacitor’ [54]. It consists of two electrodes which are dipped in an electrolyte with a separator acting as a semi-permeable membrane that prevents electrical contact between the two electrodes and allows for ionic diffusion. Supercapacitors are grouped into three general classes based on how they store charges (Figure 2.1). The three general classes of supercapacitors are distinguished based on their charge storage mechanism, namely faradaic process (pseudocapacitors), non-faradaic process (electrochemical double layer capacitance (EDLC)) and the hybrid process which is a combination of the faradaic and non-faradaic process. The faradaic process involves the transfer of charges between electrolyte and electrode such as reduction-oxidation reactions while non-faradaic process involves charge distribution on the electrode surface without a chemical mechanism [8].

The following subsections will explore the fundamentals on the three different classes of the supercapacitor. This is followed by a comparison on the different synthesis methods for hybrid composites, in order to select a facile and scalable route.

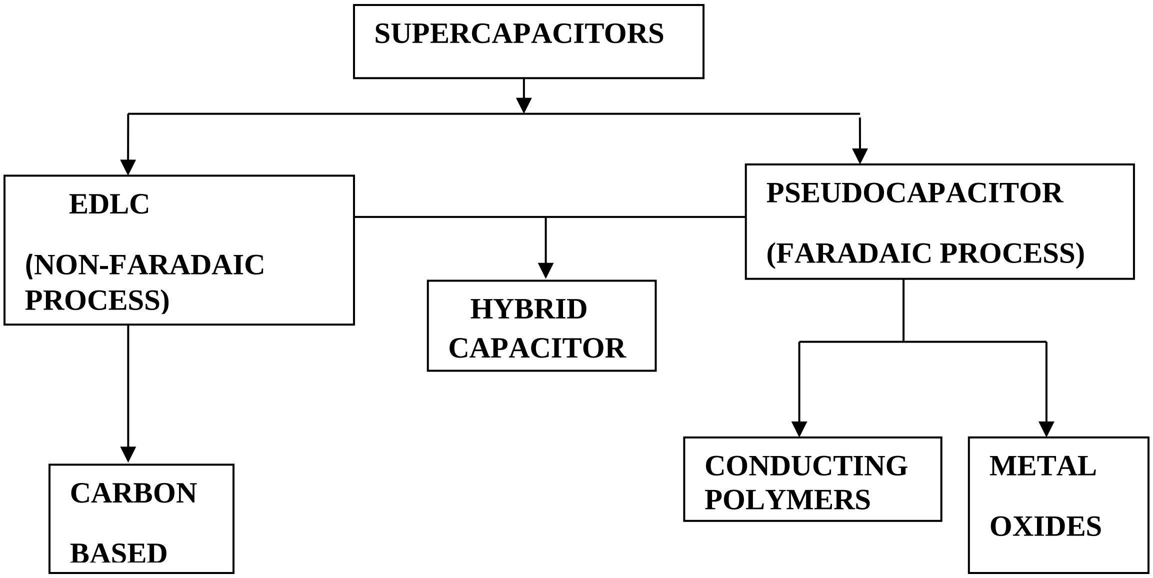

Figure 2.1: Block diagram showing the different classes of supercapacitors.

2.2 Electrochemical double-layer Capacitor (EDLC)

An EDLC is fabricated using two electrodes (carbon-based), a separator, and an electrolyte as illustrated in Figure 2.2 and stores charges using an electrochemical double layer.

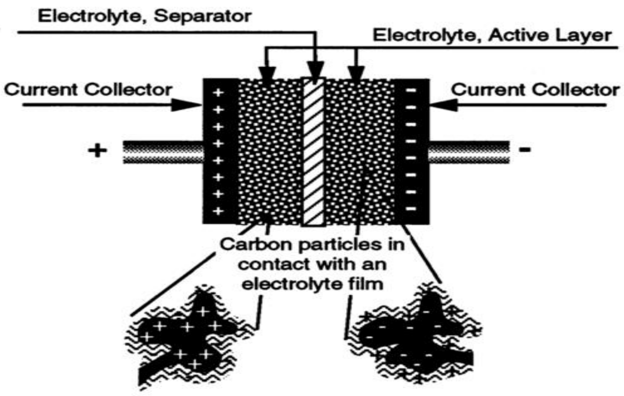

Figure 2.2: Schematic diagram of an electrochemical double-layer capacitor [54].

When voltage is applied across an EDLC, there is an accumulation of charges at the interface between the electrolyte and the surface of the electrodes. Due to Coulomb's force across the electrolyte, the positive charges accumulated on the positive electrode attract an equal amount of negative charges around the electrode, while the negative charges on the negative electrode also attract an equal number of positive charges onto it [10] (Figure 2.3).

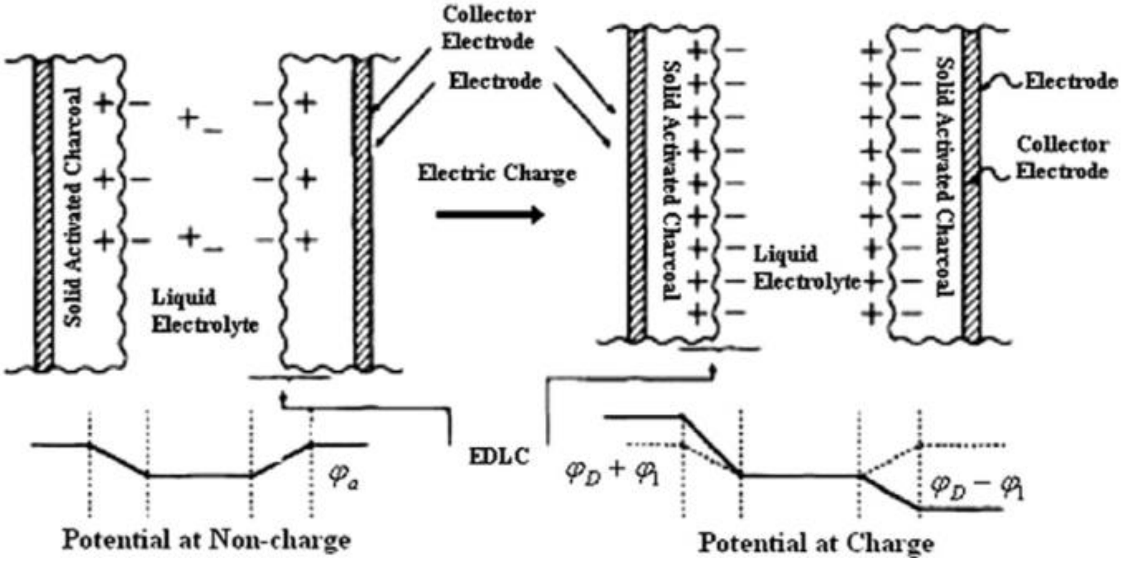

Figure 2.3: EDLC charge storage mechanism [55].

The ions from the electrolyte pass through the separator into the pores of the electrode. The separator which is ion-permeable is located between the electrodes to help isolate them electrically; hence there will be no charge transfer between the electrodes and the electrolyte resulting in no chemical changes in the EDLC [8], [9]. A complete double-layer capacitor has a double-layer of charge produced at each electrode; a negative electrode-electrolyte interface and a corresponding positive electrode-electrolyte interface. These two layers constitute the main frame of the capacitor in determining its performance [8], [10].

2.2.1 The Different EDLC Models

Chemical scientists over the years have developed several models to explain the concept of comprehending the electric charge process that occurs at the boundary between an electrolyte and a conducting electrode.

2.2.1.1 The Helmholtz's double layer model

The word "double layer" was first brainstormed by a scientist called Helmholtz in 1853 when he observed that at the interface of two completely different metals there is a presence of two layers of charge. He went ahead in 1879 to relate this metal-metal interface to an aqueous-metal interface and the results leading to the Helmholtz's double layer model. This model states that two layers of dissimilar charges are formed at the interface of an electrode-electrolyte and the charges are parted by an atomic distance [9], [56]. Figure 2.4 depicts the Helmholtz model; d represents the double layer distance while ψ_0 and ψ refers to the potentials at the surface of the electrode and the interface of the electrolyte-electrode respectively.

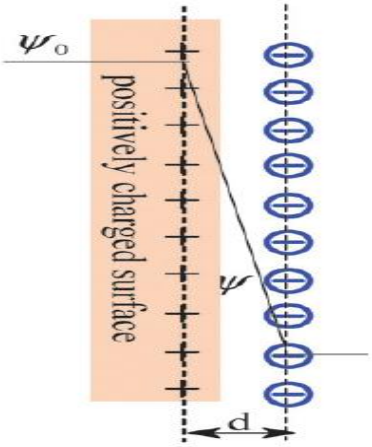

Figure 2.4: The Helmholtz's model [56].

2.2.1.2 The Gouy-Chapman model

Gouy and Chapman modified the Helmholtz model based on the fact that capacitance is not a constant but depends on the continuous dispersion of ions (anions and cations) in the solution compelled by thermal motion. The thermal motion keeps the ions from disseminating on the surface of the electrode thereby forming a diffuse layer hence the closer the charge ions to the surface of the electrode the greater the value of the capacitance of the capacitor [56]. As shown in Figure 2.5, ψ_0 and ψ represents the potentials at the surface of the electrode and the interface of the electrode-electrolyte of the Gouy-Chapman model.

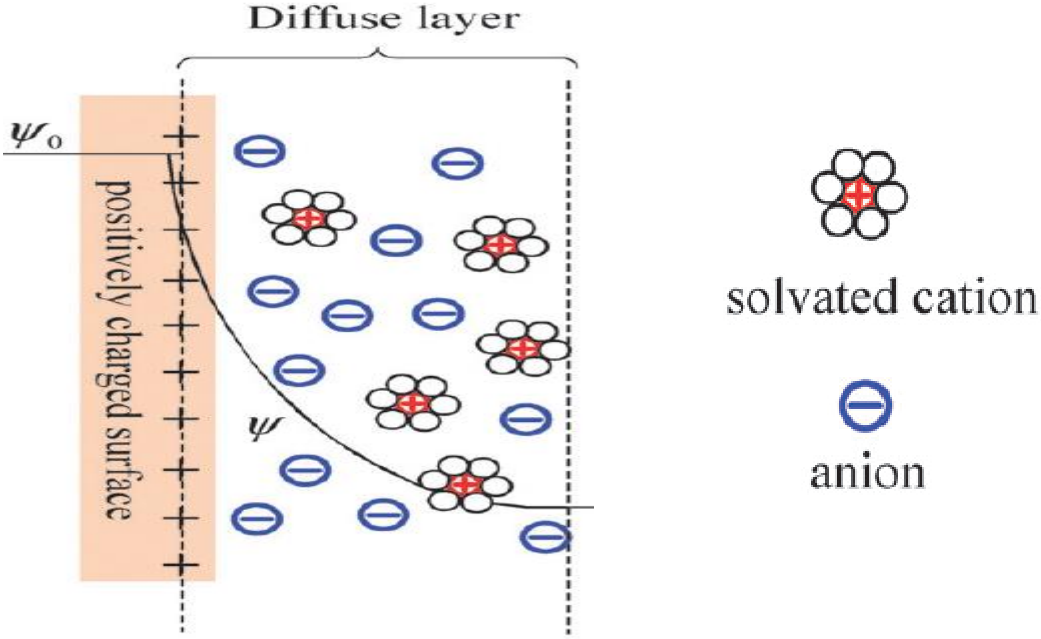

Figure 2.5: The Gouy-Chapman model [56].

2.2.1.3 The Stern model

A combination of Helmholtz's model and the Gouy- Chapman's was done by Stern in 1942. He observed two areas of ions allocation; the inner area called the Stern (compact) layer and the diffuse layer. In the Stern layer, ions are actively absorbed by the electrodes also it consists of two layers that differentiate the absorbed ions. The inner Helmholtz plane (IHP) which is a layer that consists of specifically absorbed ions at the surface of the electrode and an outer Helmholtz plane (OHP) which is a layer consisting of non-absorbed ions with closest access to the surface of the electrode [56]. In the Stern model,

ψ_0 and ψ represents the potentials at the surface of the electrode and the interface of the electrode-electrolyte (Figure 2.6).

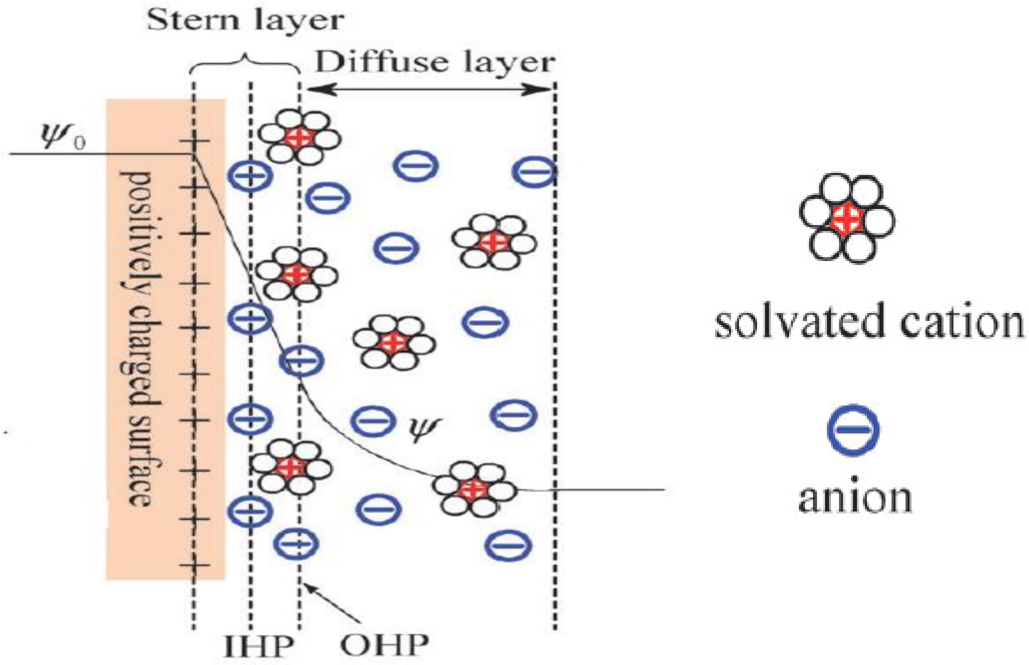

Figure 2.6: The Stern model [56].

The capacitance of the EDLC's (C_{EDLC}) can be expressed as a combination of the capacitance of the capacitance of the Stern Layer (C_{SL}) and the diffuse area (C_{DA}). Hence, C_{EDLC} is described by equation 2.1 [56].

$$\frac{1}{C_{EDLC}} = \frac{1}{C_{SL}} + \frac{1}{C_{DA}} \tag{2.1}$$

2.3 Carbon based Electrical Double Layer Capacitors (EDLC)

The first electrochemical capacitor fabricated by Becker at SOHIO in 1957 consisted of carbon electrodes [9], [10]; hence carbon has over the years become the widely used electrode material for electrochemical capacitor [9], [57]. Why carbon? It is the sixth most abundant element on earth making it readily available coupled with its high conductivity over a high surface area, ecofriendly and its ability to exist in different forms [9], [57]–[60]. Furthermore, its unique position on the periodic table is responsible for the electronic structure ($1s^2$, $2s^2$, $2p^2$) and semiconducting properties [9], carbon has low thermal expansion coefficient, low density, low cost and easy obtainable in high purity [54], [57].

The electrochemical performance of the carbon electrode is determined mainly by relationship between surface area accessible to the electrolyte, pore size distribution and the electrolyte properties. The charge storage capacity is a reflection of the electrode-electrolyte interactions due to the fact that the electrochemical double layer is built on the electrode-electrolyte interfacial region as stated in section 2.2; while the pore distribution determines the power density of the EDLC [57], [61] because carbon materials with higher pores deliver high energy at a high rate [62].

Theoretically, it is expected that carbon materials with higher surface area produces higher capacitances. Practically, some reported studies have indicated a linear relationship between the surface area and the capacitance [63], [64] while other studies have refuted this relationship [62], [65]. Table 2.1 shows a study on the comparison of the capacitance, surface area and pore distribution of different carbon derivatives.

Deyang et al reported that the reason for this derivation is that no matter how large the surface area of the carbon material is, the part of the area not accessible to ions of the electrolyte don't contribute to the double-layer capacitance of the electrode. They also proposed that the different process and treatments required to process this carbon materials from their precursors affects the double-layer capacitance [62]. This reasons were also reported in literatures [9], [60], [61]. Huang et al concluded their study by stating that majority of the capacitance is contributed by the pores inside the carbon particles and the specific surface area offers relatively small contribution [61],[62].

Table 2.1: Comparison of capacitances, surface area, and pore distribution of different carbon derivatives.

Carbon Derivatives	Specific capacity (F/g)	BET surface area (m^2/g)	Pore volume (cc/g)	Average pore size (Å)
M-10	55.95	1370	0.500	9.12
M-14	57.20	1223	0.561	9.60
M-15A	78.10	1800	0.629	9.17
SACF-25	27.9	2371	0.977	11.93
SACF-20	48.8	1839	0.699	9.74
A-10	35.3	1150	0.424	-
A-20	41.20	2012	0.902	14.23
M-20	100	2130	0.709	14.73
M-30	62.9	2571	1.230	14.95

Carbon exists in many forms and not all can be used as an electrode material. According to Conway [9], carbon material to be used for an EDLC must possess these essential properties: (1) have a specific surface area on the order of 1000 m^2/g (2) The intrapore surface area of the carbon material can be easily accessed by electrolyte and (3) excellent inter and intraparticle conductivity in porous matrices. According to these properties, a few examples which are representative are discussed below:

2.3.1 Activated carbon

Activated carbon is a commonly used material due to its easy process ability, good electrical properties, relatively cheap and a large surface area [9], [10], [56], [60], [62], [66]. It can be made from chemical and/or thermal (physical) activation of different types of carbon precursors (coconut shells, coal, wood etc.) at different temperature ranges as shown in Figure 2.7. In physical activation, these carbon precursors are treated in the presence of oxidising gases (carbon dioxide, oxygen) to a high temperature of around 700 to 1200 ^{o}C. Chemical activation involves the treatment of these carbon precursors with activating agents like potassium hydroxide, zinc chloride, sodium hydroxide and phosphoric acid to a temperature of around 400 to 700 ^{o}C [56], [67].

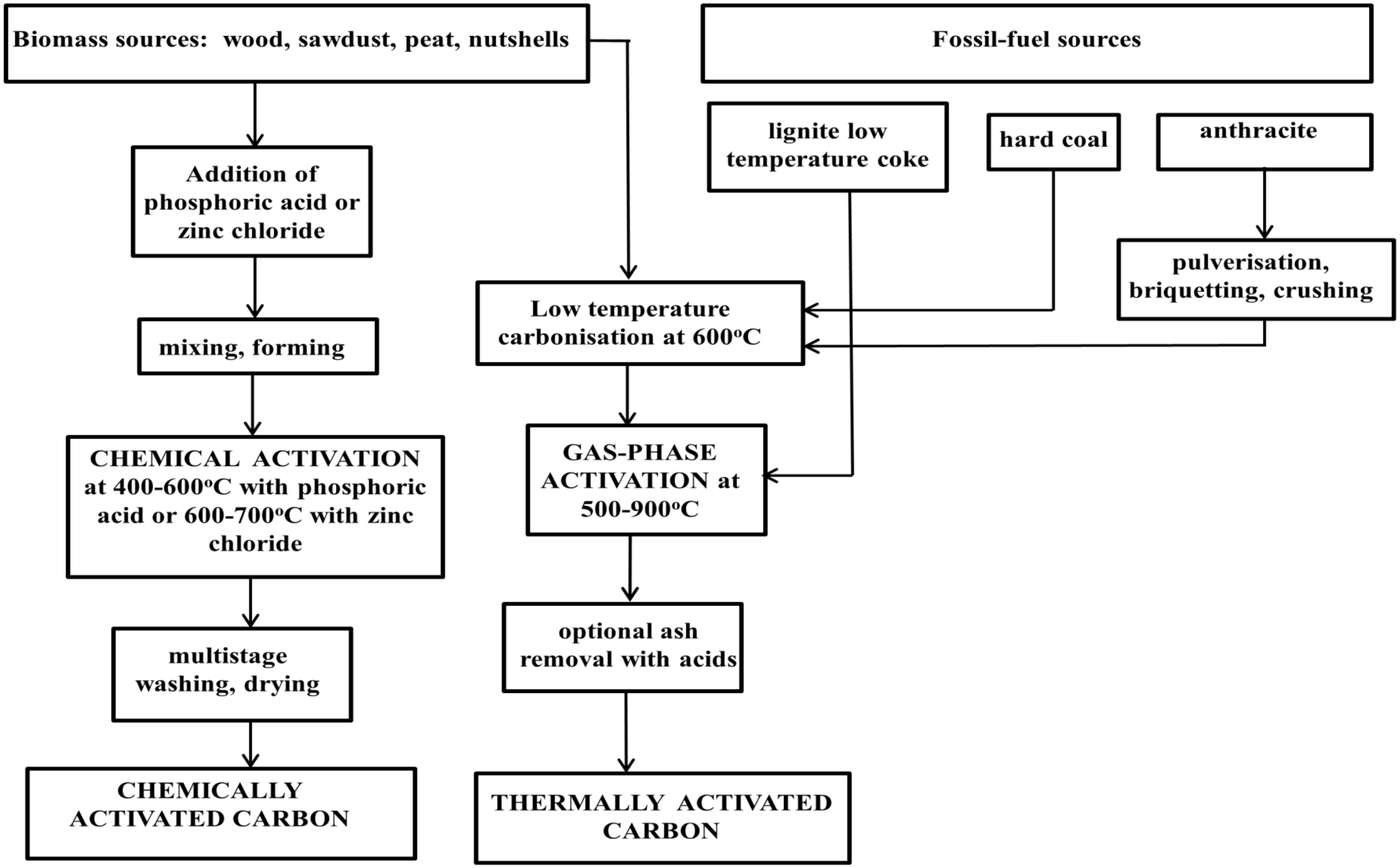

Figure 2.7: Production of activated carbon based on literature [67].

Several studies have been performed on these as-prepared activated carbon powders. Table 2.2 details a summary on some activated carbon materials prepared from different precursors using separated methodologies and their performances as an electrode in an electrolyte made with acetonitrile and 2 M $LiBF_4$. It was deduced that (1) the surface area of activated carbon does not correlate to better performance and (2) the precursor materials and activation process are paramount to their capacitive performance. There are other factors that also influence its performance, they include surface functionality, pore shapes and sizes, electrical conductivity, and pore size distribution [56], [68]. It can be noted that the activated carbon produced via KOH activation produced the best capacitance of 154 F/g; based on these results. Raymundo-Pinero et al discussed a series of activated carbon prepared by heat treatment of coal followed by KOH activation and the relationship between their capacitive properties in different electrolytes. They concluded the study by saying that an adequate pore size is more important than a higher surface area in achieving a better capacitance. The pore filling seems to be optimal at a pore size range of 0.7 nm to 0.8 nm in both organic and aqueous medium [69] Wang et al in a review stated that various studies had reported a pore size of 0.4 or 0.7 nm suitable for aqueous electrolyte and 0.8 nm better for organic electrolyte. Figure 2.8 depicts the pore size network of an activated carbon grain which consist of complex structures namely macropores with sizes greater than 50nm, mesopores having a size range of 2 to 50nm and finally micropores with sizes less than 50nm [66]. Zhang et al discussed that excessive activation during preparation of activation carbon results in large pore volume which in turn causes low material density and conductivity. These detriments led to drawbacks of low energy density and power capability when used as electrode materials [56]

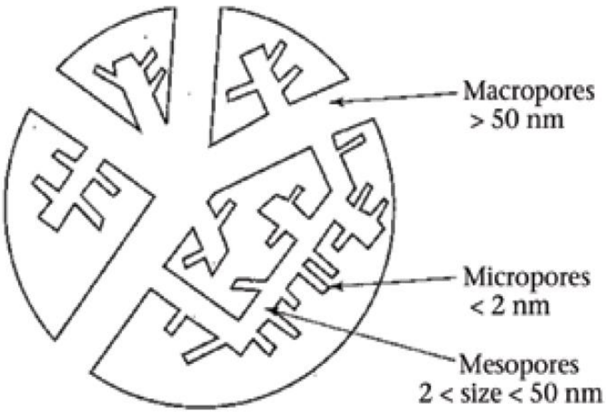

Figure 2.8: Schematic diagram of the pore size network of an activated carbon grain [66].

Table 2.2: Various activated carbon powders produced through different Methodologies and their capacitive performance in an Organic electrolyte [10].

Carbon	**Supplier**	**Precursor**	**Activation process**	**BET SA (m^2/g)**	**Average Pore size (nm)**	**Capacitance (F/g)**
Grade 1 Cloth	Marketech International	Resorcinol Formaldehyde	None	402	4.14	28
RP-15	Kurray	Phenolic resin	Steam	1318	1.94	90
NK-260	Kurray	Mesophase pitch	KOH	2040	1.92	154
Nuchar RGC	MeadWestvaco	Mixed hardwoods	Chemical	1622	2.99	82
Supra 50	Norit	Coconut shell	Steam	1989	2.05	81
TDA-1	TDA	Sucrose	Carbon dioxide	2053	2.04	86
Generation 1	University of Kentucky	Filtration carbon	Carbon dioxide	1907	2.46	88

2.3.2 Carbon Nanotubes (CNTs)

In 1991, Sumio Iijima discovered CNTs [70], [71], since then it has been extensively studied because of its highly accessible surface area, good electrical conductivity, shows good mechanical strength, good thermal and chemical stability and a unique pore structure [56], [72]–[74]. According to its physical structure, carbon nanotubes can be viewed as graphite carbon sheets grouped into single-walled (SWCNT) , double-walled (DWCNT) and multi-walled (MWCNT) carbon nanotubes respectively and the radii of their cylindrical shapes (Figure 2.9) are of the order of nanometers and length of several millimeters [10], [71] , of which all have been widely studied as an electrode material for electrochemical capacitors. Niu et al in 1997 became the first group to recommend its use as electrodes materials for EDLCs [73]. They demonstrated a gravimetric capacitance of 102 F/g with electrodes prepared by MWCNTs functionalised in nitric acid. Honda et al prepared MWCNT array electrodes to illustrate the prospective of CNTs as high power EDLCs. The fabricated MWCNT electrodes retained 2.2 kW/kg at a current density of 200 A/g corresponding to a power density of 125 kW/kg [75]. Frackowiak et al performed an intensive study on supercapacitors electrodes prepared from MWCNTs. MWCNTs prepared from the catalytic decomposition of acetylene at 700 ^{o}C using cobalt support on silica was tagged A700Co/Si, another sample prepared through the same process but at 900 ^{o}C was labelled A900Co/Si. A600Co/NaY was marked to the MWCNTs prepared from the decomposition of acetylene at 600 ^{o}C using NaY zeolite as a cobalt support and a P800AI to the MWCNTs synthesised by chemical vapor deposition of propylene on an alumina template. The electrochemical characteristics were analysed in correlation with their elemental composition and microtexture respectively as shown in Table 2.3. Results showed a linear relationship between the surface area and the specific capacitance. They also highlighted the importance of the mesopores forming an accessible interconnected network of nanotubes as beneficial to specific capacitance [76].

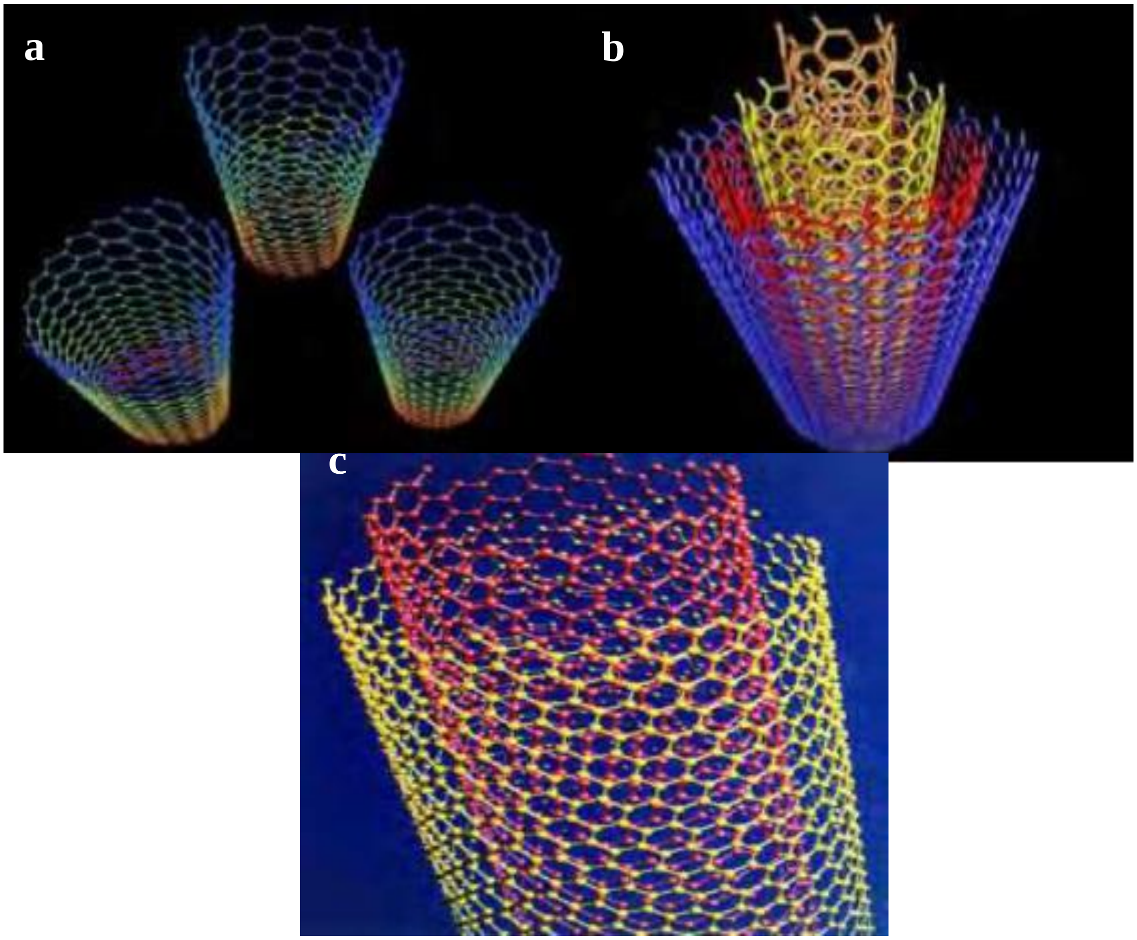

Figure 2.9: Schematic diagrams of (a) SWNTs with different helicities, (b) MWNT and (c) DWNT [77].

Table 2.3: BET specific surface area, mesopores volume, percentage of oxygen and capacitance of the analysed carbon nanotubes [76].

Types of nanotubes	**A700Co/Si**	**A900Co/Si**	**A600Co/NaY**	**P800/Al**
V_{meso} (cm^3 STP/g)	435	381	269	643
S_{BET} (m^2/g)	411	396	128	311
Oxygen (mass %)	10.8	4.6	0.8	<0.3
Capacitance (F/g)	80	62	4	36

Using organic electrolyte, Zhang et al fabricated EDLC using CNT as electrodes material, demonstrated an energy density of 20 Wh/kg at a 10mA discharge current [78]. An et al investigated the factors that influenced the performances of SWCNT based EDLC, concluded that the parameters of the binders, current collectors, calcination temperature, and charging-discharge current density can be optimised for enhanced energy and power density of the EDLCs [79]. Pan et al contributed to the study of CNT for EDLCs by listing factors such as pore size, conductivity, specific surface area and pore size distribution among others that may affect capacitive performances. Functionalisation doping and oxidation of the CNTs have been studied to enhance resultant capacitance via improvement in ion diffusivity, conductivity and addition of pseudocapacitance [73].

2.3.3 Carbon Aerogels

Carbon aerogels are also an interest in electrode making of EDLCs due to its monolithic three-dimensional structure which results to a very high surface area of about 400-1100 m^2g^{-1}, their ability to form a chemical attachment with the current collector, high electrical conductivity, and its interconnected and open pore structure with pore size of about (3-50 nm) [60], [66], [80]. They are prepared mainly by the pyrolysis of organic aerogels based on phenol-furfural (PF) or resorcinol-formaldehyde (RF) precursors through sol-gel method. The particle size and pore distribution of the final carbon aerogel is determinant of the pyrolysis temperature and gel composition (catalyst, precursors, solid ratio) [60], [80]. An electrochemical double-layer capacitor which has its two electrodes made from carbon aerogels is called an aerocapacitor [80], [81]. The aerocapacitor was first developed by researchers at the Lawrence Livermore National Laboratory (LLNL). Pekala et al reported capacitive performance of about 26 F/cm^3 and an equivalent energy and power densities of 19 J/cm^3 and 6 W/cm^3 respectively [81]. Fischer et al prepared carbon aerogels by the pyrolysis of resorcinol-formaldehyde (RF) via sol-gel method, they went further to optimise the pyrolysis temperature and starting solution and presented an improved capacitance of 46 F/cm^3 [82]. Lee et al [83] using the established theory of the addition of surface oxygen on carbon surface to improve rate capability [84], [85] prepared modified carbon aerogels using the process shown in Figure 2.10. In addition, they prepared different modified carbon aerogels using different conditions and compared their specific capacitances with activated carbon aerogel (Table 2.4).

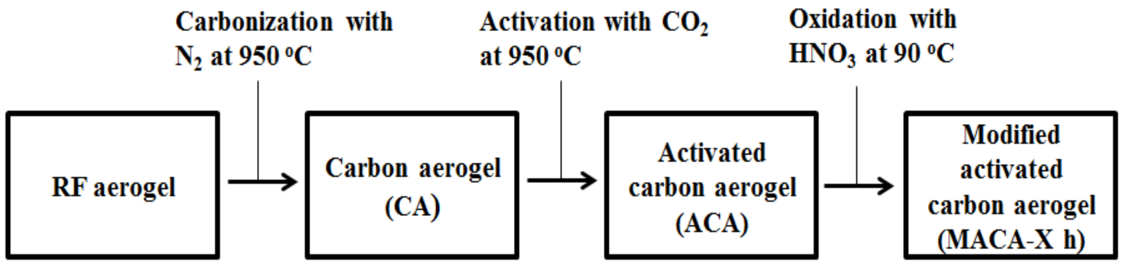

Figure 2.10: Preparation process for modified activated carbon aerogel [83].

Table 2.4 Specific capacitance of ACA and MACA -X (X=3, 6, 9 and 12 h) measured at a scan rate of 10 mV/s and 100 mV/s in an aqueous solution of 6M KOH [83].

Modified carbon aerogels electrode	**Calculated specific capacitance (F/g)**	
	10 mV/S	**100 mV/s**
ACA	84	46
MACA-3 h	102	73
MACA-6 h	120	94
MACA-9 h	95	57
MACA-12 h	75	27

They concluded that MACA-6 h demonstrated the best performance due to two factors: (i) electrolyte wettability and (ii) the presences of mesopores. Furthermore, they established that an optimal condition might exist in achieving a desirable performance judging from the opposite trend of performance displayed in Table 2.4. Frackowiak et al contributed to the study of carbon aerogels as electrode materials by detailing that its performance depends mainly on the starting reactant concentration and precursor to catalyst ratios [60].

2.3.4 Graphene

Graphene a member of the carbon family is known in the world as the thinnest and strongest material ever measured [70], [86]. It is a two dimensional material that can be made into a roll of a single dimensional (1D) carbon nanotube, stacked up into a three-dimensional (3D) graphite (Figure 2.11) or wrapped into fullerenes (0D); hence termed the ‘parent’ and mother of graphitic structures [87]. The uniqueness of graphene has generated a lot of research activities in studying its properties, production and application [11], [87].

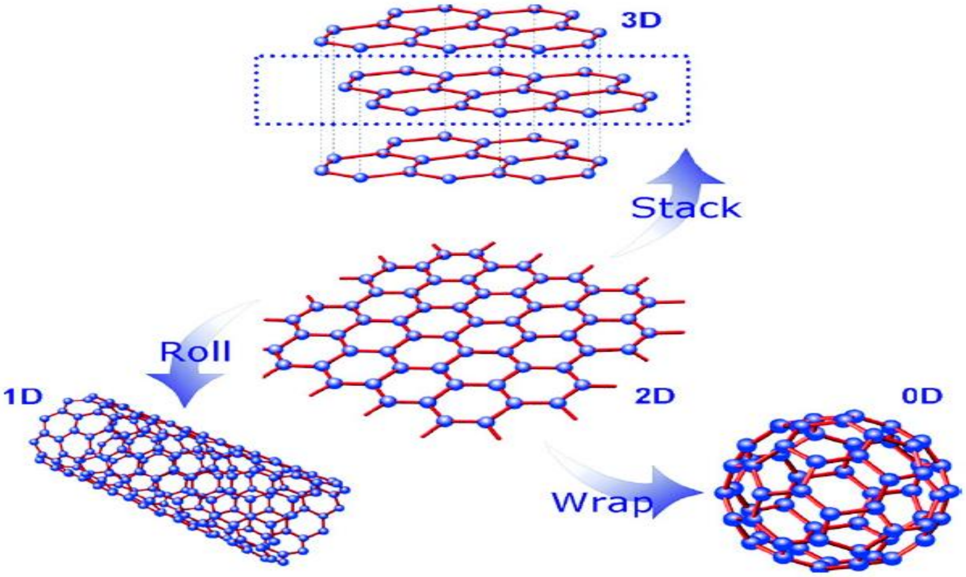

Figure 2.11: Graphene the mother structure of carbon-based materials; CNT (1D), fullerene (0D) and graphite (3D) [87].

2.2.4.1 Properties of graphene

Electronically, graphene is a gapless (zero-gap) semiconductor which is an important property associated with conductivity without charge carriers, ballistic movement, Dirac-like equation description of electron transport and a “Berry phase” based pseudospin chirality. The movement of charges in graphene was recorded as the fastest in the world (~15,000 $cm^2V^{-1}cm^{-1}$). Graphene has at room temperature, an effective Fermi velocity

(10^6 ms^{-1}) similar to that of the speed of light and a very high movement of temperature independent electrons, 200 times higher than silicon i.e. 200,000 $cm^2V^{-1}s^{-1}$.

The thermal conductivity of graphene was recorded at about 5000 W $m^{-1}k^{-1}$ with a single layer graphene having an optical transmittance of ~97.7 %, outstanding mechanical properties, very flexible and a high hypothetical specific surface area (2620 m^2/g) [11], [51], [86], [88]. Table 2.5 summarises the superiority of graphene's mechanical, thermal, optical and electrochemical properties when compared to properties of other carbon allotropes such as diamond, graphite, carbon nanotube and fullerene.

Research and advances on the approach of the synthesis of graphene sheets can be grouped into the following methods:

i) Chemical and vapor deposition (CVD) and epitaxial growth of graphene on substrates, such as Silicon carbide and matched metal surfaces [88].

ii) Mechanical cleavage of graphite; i.e. use of adhesive tape or scotch tape to obtain very thin platelets of graphite [89].

iii) Exfoliation of graphite in organic solvents such as N-methyl-pyrrolidone (NMP) to high intensity ultrasound [90].

iv) Production via arc-discharge method [91] .

v) Chemical reduction of graphene oxide obtained from the oxidation of graphite (Figure 2.12) [92].

Table 2.5: The properties of graphene and other graphite structures [11].

Properties	**Graphite**	**Graphene**	**Fullerene**	**CNT**	**Diamond**
Dimension	Three	Two	Zero	One	Three
Optical properties	Uniaxial	97.7 % of optical transmittance	Non-linear optical response	Structure-dependent properties	Isotropic
Electronic properties	Electrical conductor	Zero-gap semiconductor	Insulator	Metallic and semiconducting	Insulator, semi-conductor.
Electrical conductivity (Scm^{-1})	Anisotropic	2000	10^{-10}	Structure-dependent	Nil
Hybridized form	sp^2	sp^2	Mainly sp^2	Mainly sp^2	sp^3
Crystal structure	Hexagonal	Hexagonal	Tetragonal	Icosahedral	Octagonal
Thermal conductivity ($W\ m^{-1}k^{-1}$)	1500-2000	4840-5300	0.4	3500	900-2320
Tenacity	Flexible non-elastic	Flexible elastic	Elastic	Flexible elastic	Nil
Experimental specific surface(m^2/g)	~10-20	~1500	80-90	~1300	20-160
Density (gcm^{-3})	2.09-2.23	Greater than 1	1.72	Greater than 1	3.5-3.53

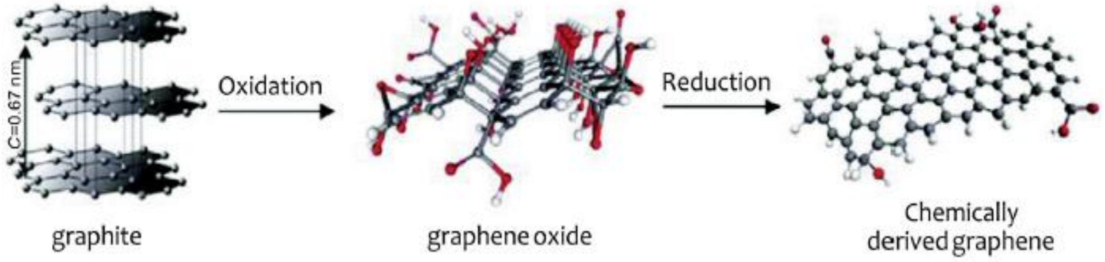

Figure 2.12: Illustration of the route to chemically derived graphene [93].

Ruoff et al using graphene electrodes reported a specific capacitance of 99 and 135 F/g using organic and inorganic electrolytes respectively [94]. Vivekchand et al produced a specific capacitance and energy density of 75 F/g and 31.9 Wh/kg with graphene electrodes using an ionic liquid and a specific capacitance of 117 F/g in aqueous H_2SO_4 [95]. In 2 M KCl electrolyte, Yu et al using graphene electrodes recorded a specific capacitance of 135 F/g and a power density of 7200 W/kg [96]. Contrarily to other mention carbon materials in subsections 2.3.1 - 2.3.3, Wang et al concluded their study by stating that the interfacial capacitance of graphene depends on its number of layers rather than pore distribution and sizes [97]. Also, that a single or few layered graphene with low agglomeration is expected to have a better supercapacitor performance. This is because graphene sheets have the tendency to restack themselves during the stages of synthesis and electrode production hereby forming intergraphene pore sizes that are not easily accessible to the electrolytes and formation of EDLC process [98]. In order to avoid aggregation of the graphene sheets, Wang et al reduced graphene oxide sheets with hydrazine gas at room temperature to produce graphene and achieved a specific capacitance of 205 F/g in an aqueous solution with an energy density of 28.5 Wh/kg [99]. Liu et al prepared curved graphene to prevent face to face restacking and accomplished a remarkable specific energy density of 85.6 Wh/kg and specific capacitance of 154.1 F/g at current density of 1 A/g [98]. Inspired by the biological process of the hydration of cells and tissues to prevent collapse; Yang et al prepared solvated graphene and kept it wet in water during the reactions and storage. Performance analysis detailed that the resultant solvated graphene (SSG) attained a specific capacitance of 156.5 F/g at a charge/discharge rate of 1080 A/g in 1 M H_2SO_4 electrolyte. At a discharge current density of 108 A/g, the SSG a demonstrated a power density of 414 kW/kg [100]. Studies have been reported on altering the structure of graphene to achieve enhanced electrochemical performance in supercapacitor applications. Zhu et al expending the successful reports of boosting the capacitance of activated carbon through KOH oxidation investigated the capacitive performance of thermally KOH activation of graphene. They reported that the addition of KOH generated addition nanoscale pores coupled with definite pore distribution (Figure 2.13) of mesopores (~4 nm) and micropores (~0.8 nm). As a result of which the supercapacitor obtained a specific capacitance of 166 F/g at a current density of 5.7 A/g in organic electrolyte [101]. Zheng et al using KOH to chemically activate graphene nanoribbons reported a specific capacitance of 130 F/g at a scan rate of 1 mV/s in an ionic electrolyte. They concluded that the chemical activation using KOH generated suitable porosity and created edge sites for the electrolytes [102].

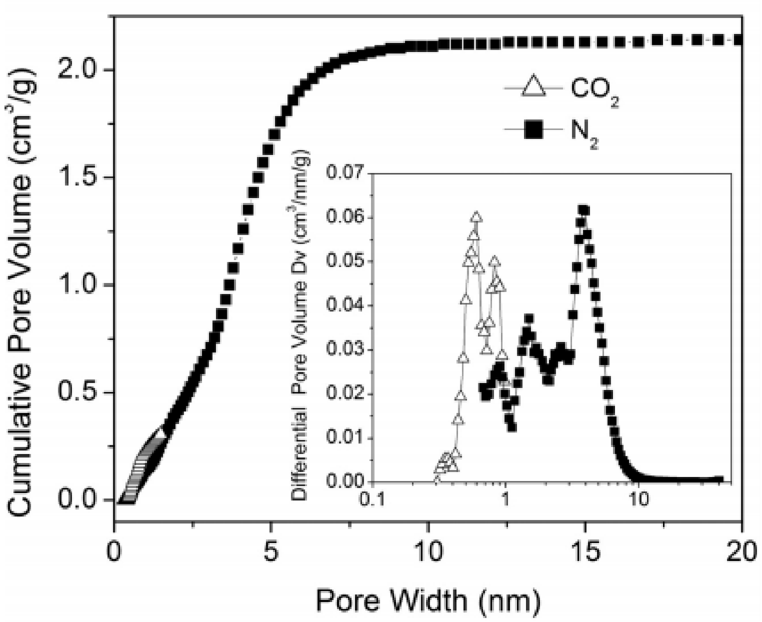

Figure 2.13: The differential pore size distribution achieved by the KOH activation of microwave exfoliated graphene oxide [101].

2.4 Pseudocapacitors

As discussed in section 2.2, the double layer capacitance of an electrochemical capacitor is due to the net electrostatic charge accumulation and separation at the electrode-electrolyte interface; the charges are accumulated at the electrode surface thereby making the electrodes forming the double layers largely responsible for capacitances. Carbon materials with large surface area are required to form a porous layer electrode to store charges; however, not all the active sites of the carbon are accessible by the electrolyte ions hence limiting the capacitance [10]. To increase the capacitance, different storage methods and electrochemical active materials were explored for electrode use to provide better capacitance compared to double-layer capacitance.

Pseudocapacitors store charges through the convection of charges among electrolyte and electrodes (Faradaic process). The faradaic process is fast and depends on the voltage in producing a capacitive occurrence [10]. The faradic processes are achieved through reduction-oxidation reactions (redox), adsorption of ions and intercalation process. This process accounts for large percentage of the overall capacitance. Conducting polymers and metal oxides are good examples of materials that store charges through faradaic process [3], [9], [10], [103].

In transition metals, the charges are stored through easily accessibly surface oxidation states. Some metals with multiple adsorption states within the supercapacitor range of operation further boost pseudocapacitance. Pseudocapacitance in conducting polymers is obtained from the ion intercalation occurring entirely at the electrode during doping, exposing the ions to more than the surface interface of the polymer. This results in Pseudocapacitors to achieving better energy and capacitance than the EDLCs. Its major setbacks are its lack of stability during charge and discharge and its poor electrical conductivity (low power density) [9], [10] .

2.4.1 Conducting polymer based Pseudocapacitors

Conducting polymer is a category of promising pseudocapacitive electrode material suitable for supercapacitor application due to its high conductivity, low cost and ease of synthesis [3], [9], [10]. The storage mechanism in conducting polymers can be summarised schematically in Figure 2.14. In the process of p-doping the conducting polymers (Figure 2.14(a)), the electrons are absorb from the polymer backbone through the external circuit and the integration of an anion from the solution into the polymer to balance the positive charge. An inverse of this mechanism is observed during the n-doping process (Figure 2.14(b)); herein, the electrons are moved through the polymer backbone by the external circuit and the charge neutrality is maintain by the cations from the solution [104].

The process of swelling and shrinking (mechanical stress) of the bulk volume of the polymer film during doping (intercalation) and de-doping (de-intercalation) causes poor cycling stability thereby hindering its application as electrode materials [9], [10], [72], [104], [105]. In order to achieve the best power densities and potential energy for an electrochemical capacitor based on conducting polymer electrodes, it should have one positively charged (p-doped) and one negatively charged (n-doped) conducting polymer electrode [9], [10], [72], [104], [105].

Conducting polymer based supercapacitors have three electrode configurations in a study done by Rudger et al [104]: (1) Type I (p-p) supercapacitor, both electrodes consists of the same p-doped conducting polymer; (2) Type II (p-p') supercapacitor, the electrodes are made up of individual p-doped conducting polymer with different range of electroactivity; Type III (n-p) supercapacitor, the electrodes use the same polymer which can be n- and p- doped in the same molecule.

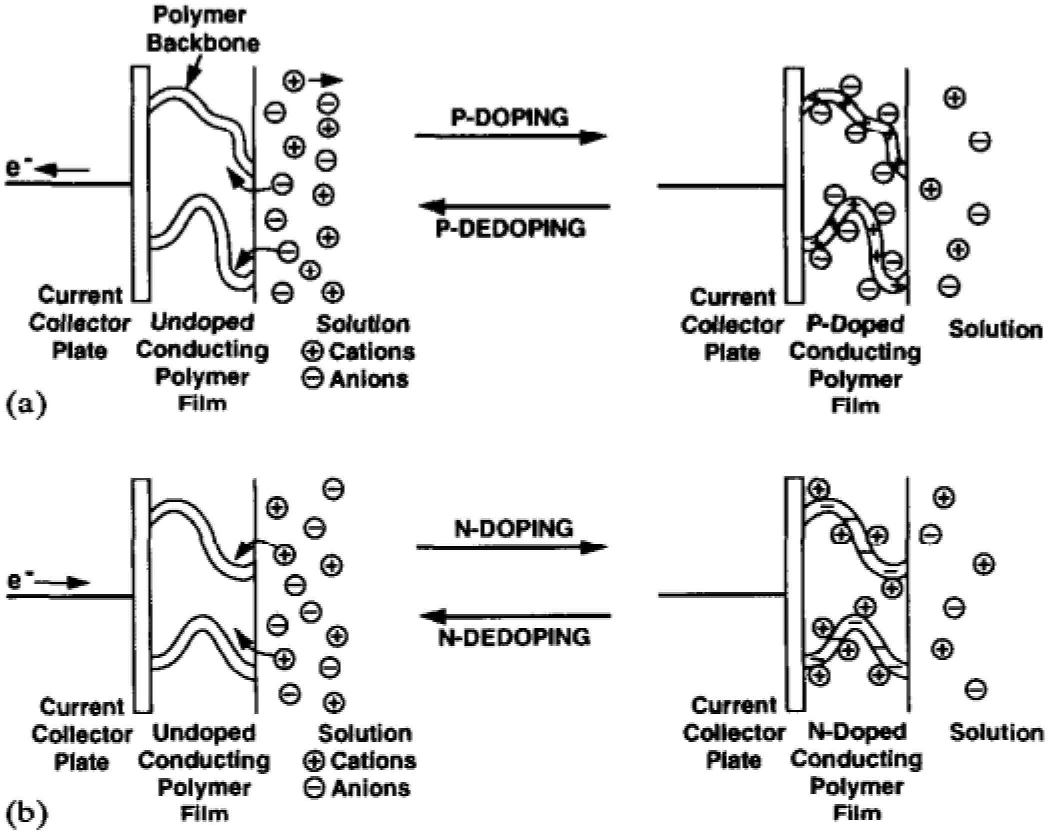

Figure 2.14: Schematic illustration of the charging and discharging process at conducting polymer electrodes associated with (a) p-doping and (b) n-doping [104].

Experimentally, they prepared the three types of conducting polymers and detailed their electrochemical performances in Table 2.6. Polyprrole was the polymer based electrode material used in the Type I supercapactior, polypyrrole and polythiophene used in Type II and poly-3-(4-fluorophenyl)-thiophene in Type III. They concluded by stating that Type III presented a significant advancement in conducting polymer based supercapacitors in terms of design and energy storage.

Table 2.6: Electrochemical performance obtained on the three types of conducting polymers as electrode materials [104].

Scheme type	Voltage (V)	Charge density		Energy density		
		(C/cm^2)^a	(C/g)^b	(J/cm^2)^a	(J/g)^b	(W h/kg)^b
I	1.0	1.2	86	0.56	41	11
II	1.5	2.2	120	1.9	100	27
III	3.1	1.3	52	3.5	140	39

[a] **Charge and energy densities calculated per geometric cm2 of the carbon paper electrodes**.

[b] **Charge and energy densities calculated per gram of active material on both electrodes in the capacitor configuration. This does not therefore include the mass of the carbon paper.**

Common examples include polyaniline (PANI), poly(3,4–ethylenedioxythiophene) (PEDOT), polypyrrole (PPy), polythiophene (PTh) and their corresponding derivatives [3], [9], [10], [52], [72], [106]. Table 2.7 shows the analysis done by Snook et al on the theoretical and experimental of some conducting polymers [106].

Table 2.7: A table showing a comparison between theoretical and experimental specific capacitance of conducing polymer [106].

Conducting polymer	Mw (g mol-1)	Potential range	Theoretical specific capacitance (F/g)	Measured specific capacitance (F/g)
PANI	93	0.7	750	240
PPy	67	0.8	620	530
PTh	84	0.8	485	-
PEDOT	142	1.2	210	92

Yuan et al [107] using PANI based electrodes in a thick polyvinyl alcohol (PVA)/H_3PO_4 electrolyte displayed a power density and energy density of 3 W/cm^3 and 0.01 Wh/cm^3 respectively. A major setback on the use of the PANI electrodes is that it requires an acidic or ionic solution to generate protons for an effective charge and discharge process [52], [104]. In another study, a specific capacitance value of 524 F/g was obtained from PANI nanofiber modified stainless–steel electrode in 1 M H_2SO_4 electrolyte prepared by Li et al [108]. Poly(3,4–ethylenedioxythiophene) (PEDOT) and its derivatives has been studied to provide high stability as an electrode material [109]–[114]. Polypyrrole Huang et al [115] demonstrated stretchable polypyrrole based supercapacitors with 98% and 87% capacitance retention at a current density of 10 A/g after 10,000 cycles under 0% and 20% strains respectively. The stretchable supercapacitors based on polypyrrole electrodes prepared by Zhao et al [116] retained 83% of its initial capacitance without strain and 74% at 30% strain.

2.4.2 Transition metal oxide based (TMO) Pseudocapacitors

Metal oxide is another electrochemical capacitor electrode material that uses the principle of faradaic process (redox) to store charges. They produce higher energy density compared to carbon materials and provide electrochemical stability better than conducting polymers [3]. The metal oxide material to be used in electrochemical capacitor applications depends on the following factors:

I. Its ability to be electronically conductive.
II. It should be able to exist in two or more oxidation states that exist together over an unending range with no changes in phase when it is associated with an irreversible modification of a 3-D structure.

III. Protons should be able to freely interpolate into and out of the oxide lattice during reduction and oxidation respectively allowing easy $O^{2-} \leftrightarrow O^{H-}$ conversion [3], [9], [10].

Transition metal oxides used for as electrode making material are classified into noble transition metal oxides and base transition metal oxides.

- **Noble Transition metal oxides**

They are kind of transition metal oxide with a rutile structure. Examples includes; Titanium dioxide (TiO_2), Ruthenium (IV) oxide (RuO_2) and Iridium (IV) oxide (IrO_2). They have been found to exhibit good capacitance as electrode materials however they are limited by their high cost of production [117].

- **Base Transition metal oxides**

They are a class of metal oxides discovered to address the high cost of producing noble transition metal oxides as electrode materials. They are environmentally friendly as well as exhibit excellent capacitive performance. Examples includes; Manganese dioxide (MnO_2), Nickel oxide and Iron (III) oxide (Fe_3O_4) [117].

2.3.2.1 Binary Transitional metal oxides (BTMOs)

Studies on the exploration of TMOs as electrode materials for electrochemical capacitors have detailed a lot of significant increase on capacitance; however, majority of TMOs have suffered from bad electrical conductivity, rate capability, cycling stability and low initial coulombic efficiency [9]–[11], [19]. This has raised concerns for scientists to design novel materials to further improve capacitance [117]. Advances have stated that the synergistic effect of pure metals can ameliorate the capacitive performance by improving conductivity, stability and providing more active sites [103]. BTMOs comprises of at least one transitional metal ion and one or more electrochemical active/inactive ions. They exist in a variety of crystal structures such as scheelite, spinel and $CaFe_2O_4$ – type. Examples of BTMOs investigated as electrode materials includes $NiCo_2O4$ [118]–[120], $NiMoO_4$ [121]–[123], Zn_2SnO_4 [124], $ZnCo_2O_4$ [125] and $CoMoO_4$ [21]. These results detailed different structures, morphology, particle size and an improved capacitance when compared to TMOs. For instance, the substitution of Ni for Co in the spinel Co_3O_4 lattice provided richer redox process resulted from the ionic contribution of both nickel and cobalt ions as against single nickel oxide or cobalt oxide [119]. The difficulty in fabrication to explore the optimal synthesis and material properties are challenges of BTMOs for electrochemical capacitor application. Also, long cycling stability stills remains a challenge for researchers [103].

2.3.2.2 Mixed Transitional metal oxides (MTMOs)

Mixed transition metal oxides (MTMOs) are prepared by the amalgamation of multiple transition metal cations with stoichiometric or even non-stoichiometric compositions in the form of spinel-like structures; denoted as ($A_xB_{3-x}O_4$; A,B = Co, Ni, Zn, Fe, Mn and so on) [5], [19], [126]. Manganese-Nickel-Cobalt [127]–[129], Zinc-Nickel-Cobalt [126], [130], [131], Zinc-Iron-Cobalt [132] and Zinc-Nickel-Aluminum-Cobalt [133] are examples of mixed metal oxides explored as electrodes material; the experimental results detailed that the mixed transition metal oxides (MTMOs) exhibited a better electrochemical performance when compared to the transitional-metal oxides (TMOs). This was as a result of relatively low activation energy for electron transfer between cations which improves electrical conductivity [5], [131]; the desirable mesoporosity which shortens the diffusion paths for ionic transportation [5], [126], [133]; complex chemical compositions and the synergy between them contributing to higher specific capacitance [5], [127], [131]. It was also revealed that the crystalline phase, structural and morphological features, composition and the surface interaction properties between the electrode and electrolyte greatly affect the electrochemical performance of these MTMOs [5].

Despite the remarkable capacitive performance of MTMOs, there have been failed mechanisms reported upon cycling establishing the urgent need to develop an electrode material with enhanced electrochemical performance.

2.5 Hybrid Electrochemical capacitors

The drawbacks associated with carbon materials and pseudocapacitors have been highlighted in the previous sections respectively. Advances and breakthroughs in energy storage techniques have exploited the merits and demerits of the double layer and pseudocapacitors to complement each other forming hybrid electrochemical capacitors to achieve enhanced capacitive performance [9], [10]. Studies on hybrid electrochemical capacitors have been centered on three different configurations of the electrode which are asymmetric, battery-type and composite.

The asymmetric hybrid electrochemical capacitor comprises of a pseudocapacitive material (metal oxide or conducting polymer) electrode and a corresponding double layer electrode (carbon material). Using this system, cycling life and power density are traded for an increase in energy density [8], [10]. Belanger et al assembled an asymmetrical hybrid electrochemical capacitor using a MnO_2 coated cathode with a carbon anode and operated it at a cell voltage of 2 V in a neutral aqueous electrolyte. The results obtained showed an energy density of 17.3 Wh/kg and a maximum power density of 19 kW/kg, which was the best result when compared to the symmetrical assembly of individual MnO_2 and activated carbon cells [10].

The battery-type hybrid electrochemical capacitor comprises of a rechargeable battery-type electrode and a double layer electrode in a lithium salt (Li^+BF_4 or Li^+PF_6) organic electrolyte to increase energy density [8], [10]. An example of a battery type hybrid is the lithium-ion capacitors. Amatucci et al were among the very first researchers to fabricate lithium-ion capacitors with LTO as an anode and activated carbon was used as a cathode, it was recorded that the energy density exhibited by the electrochemical capacitor were at least 4-5 times greater than EDLCs [134]. A major disadvantage is the poor diffusion coefficient and poor electronic conductivity if lithium compared to carbon materials and fast redox materials [10].

Composite electrode comprises of the integration of pseudocapacitive materials with a carbon material; this means incorporating the physical and electrochemical storage process together in a single electrode. The two charge storage systems complement each other to achieve excellent capacitance than either individual carbon or metal oxide electrodes [8]. Numerous studies have investigated the incorporation of metal oxides into CNTs forming composites for electrode materials. CNT provided a backbone structure coupled with an enhanced ionic movement and charge storage capabilities. The CNT arrangement also saw the improvement of the cyclability of the metal oxides by suppressing the volumetric changes that occur during cycling [14], [135]–[138]. Despite the inherent advantages of CNTs, they suffer a setback of a low specific surface area which can be addressed by graphene [10], [11], [139].

2.6 Graphene and metal oxides composites

This is aimed at maximising for practical use the combined advantages of both graphene and metal oxides as electrode materials for improving energy storage in electrochemical capacitors. It is believed that the anchoring of metal oxides on graphene yields the following advantages for electrochemical applications:

- Construction of a conductive 3D network: To improve the poor conductivity of metal oxides, graphene is added not only as a conductive carbon material but also as an electrochemical active material with a 3D conductive network ensuring good electrical contacts.
- An increase in specific capacitance of electrochemical capacitors: Metal oxides have good capacitive properties as electrode materials and a combination of the pseudocapacitance from metal oxides with the double layer capacitance from graphene can benefit the total capacitance.
- Larger power and energy density: Metal oxides have a large energy density because of its capacitance while graphene has a high power density because of its large surface area. Hence, a composite of graphene-metal oxide can be considered as a high power and density electrode material.
- Discouraged the re-stacking of graphene: The electrochemical performance of chemically reduced graphene is poor due to easy agglomeration and restacking caused by van der Waals interaction between the layers of graphene. The addition of

metal oxides helps by changing the polarity and surface morphology of the graphene sheet.

- Improved rate capacity: The rate capacity is an important factor in meeting the requirements of various supercapacitor applications such as electric vehicles and hybrid electric vehicles. It has been reported that graphene-metal composite electrodes exhibit a better rate capacity than metal oxide electrodes.
- Improved cyclic performance: Pseudocapacitors suffer from capacitive fading during charge and discharge; many studies have reported that the anchoring of metal oxide on graphene produces a better cyclic performance [2], [11], [51], [58], [72], [103].

The synergistic effect of graphene and metal oxide does not produce a composite with the sum of each other's characteristics; rather it produces a new material (Figure 2.15) amidst new operatives and properties.

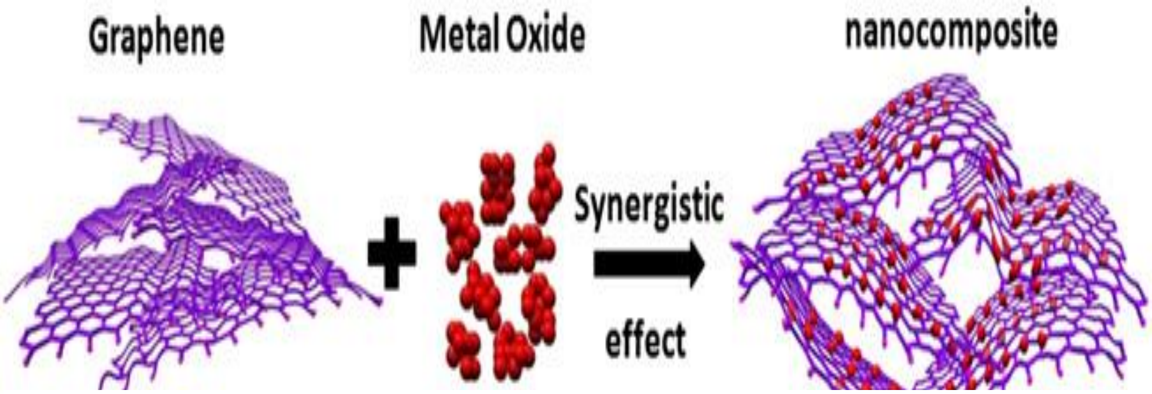

Figure 2.15: A diagram of the synergistic effect between graphene and metal [11].

2.7 Synthesis of graphene and metal oxide composites

The rapid advancement in research and development in the preparation of hybrid materials has led to different synthesizing methods that provide control over the size, structure and morphology of the hybrid materials. Several developments on the ease of producing hybrid materials, making it available for commercial purposes beyond laboratory scale have led to different methodologies over time. There are several methods setup to combine graphene and metal oxides for the application of electrochemical capacitors

2.7.1 Solvothermal /Hydrothermal Synthesis

This synthesis method is a solution based wet chemistry route for the synthesis of graphene/metal composites [5], [103]. The process involves the use of a solvent under pressure and temperature that assists the progress of interaction of precursors during synthesis [103]. The method is termed hydrothermal if water is used as the solvent and its synthesis under hydrothermal conditions is usually performed below the supercritical temperature of water (374^oC) [140]. A typical hydrothermal reaction process employs an aqueous solution (precursors) placed in a thermal reactor. A Teflon lined stainless steel autoclave (chamber) (Figure 2.16) also known as a hydrothermal “bomb” are mostly used as thermal reactors [141].

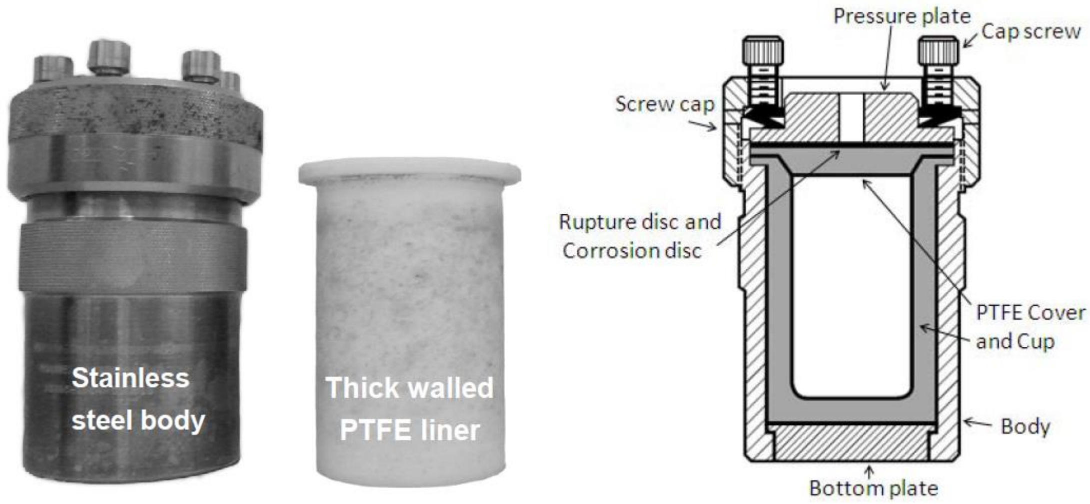

Figure 2.16: Schematic and photograph of a laboratory autoclave [142].

Some advantages of the use of solvothermal/hydrothermal synthesis method are listed below:

- The ability to control the stoichiometry of the resultant composites makes it an ideal metastable structure synthesis.
- There is no need for calcination after treatment in most cases.
- There is no need for milling after treatment in most cases.
- It has the ability to control particle size of the resultant composites.
- Composites are formed directly from the solution.
- Depending on the reaction temperature, resultant composites can be crystalline or anhydrous [1], [103], [142].

2.7.2 Microwave synthesis method

Microwave synthesis is a solution based synthesis method employed in the preparation of composites [1]. First reported in 1986 by the Gedye8 and Gigure Majetich9 group, it deploys the principle of microwave dielectric heating whereby some liquids and solids uses the electromagnetic radiation provided by the microwave oven (Figure 2.17) to generate heat to drive chemical reactions [143]. The ease of operating the microwave has grown over the years and this has led to microwave heating emerging as an essential process to synthesis composites. In many published works, microwave synthesis has reduced synthesis time from days to hours to minutes and seconds as well as produce better yields and cleaner chemistry [1], [103].

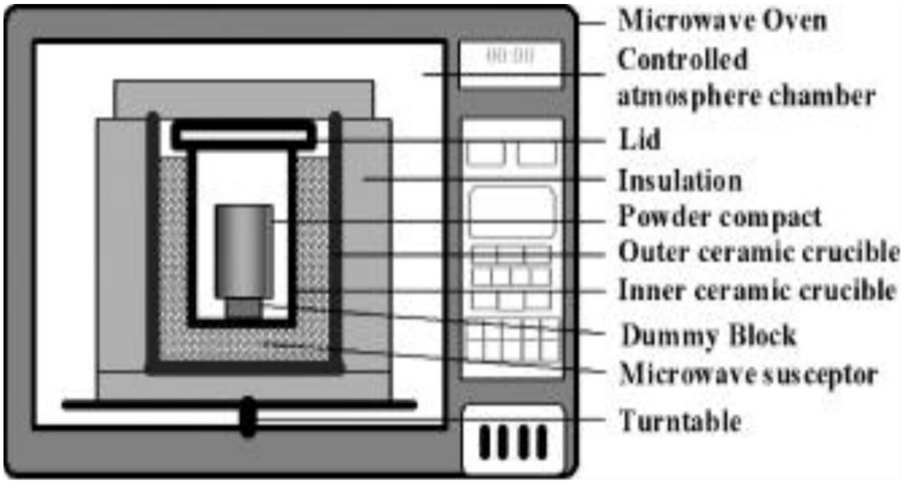

Figure 2.17: Schematic diagram showing an experimental microwave synthesis setup [142].

2.7.3 Electrochemical deposition method

Electrochemical deposition or electrodeposition for short, is a process of depositing a layer of metal or its oxides on the conducting electrode using an electrochemical cell [141] based on principle of electrochemical reduction-oxidation reactions [103]. The electrochemical cell as shown in Figure 2.18 constitutes of three electrodes; namely working, counter and reference electrode. The cell is connected to a potentiostat which controls the deposition process that occurs in electrode-electrolyte interface [144]. The electrodeposition method particularly is an attractive and simple route due to its cost effectiveness, good thickness controllability, good deposition rate and low temperature growth [1], [103]. In using this synthesis method, the electrical parameters of the cell as well as the composition of the electrolyte play a crucial role in the formation of the composites along with its morphology and composition [145].

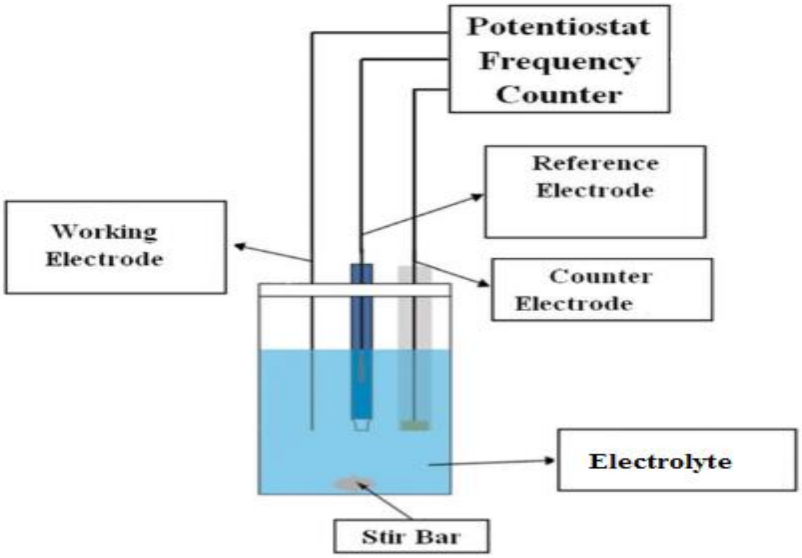

Figure 2.18: Schematic diagram of an electrodeposition cell [146].

2.7.4 Sol-gel method

The sol-gel route is a widely used synthesis method because of its generality. A large variety of host matrixes are formed under mild conditions with cost effective reagents using sol-gel chemistry. Sol is converted to gel under polycondensation and hydrolysis reactions with metal chloride or alkoxides acting as precursors under proper reaction conditions [147], [148]. For example in the preparation of graphene-titanium oxide, $TiCl_3$ and titanium isopropoxide has been used as precursors which has produced different morphologies (nanoparticles, nanorods) depending on the experimental conditions used. Titanium oxide was first coated with graphene oxide via hydrolysis and then crystalline by hydro thermal synthesis [147]. The advantage of using this synthesis route on graphene oxide or reduced graphene is that it provides an anchoring and reactive sites for growth and nucleation of nanoparticles which results in a better chemical bond between the two nanostructures [147] however the inability to control the particle size limits its application [148].

Table 2.8 summaries briefly the advantages and disadvantages of the mentioned synthesis methods used in preparing composites for electrochemical capacitors.

Table 2.8: Merits and demerits of different graphene/metal synthesis methods [1].

Methods	Merits	Demerits
Hydrothermal /Solvothermal	• Easy control in morphology • Large scale production	• Slow growth
Sol-gel	• Large scale production	• Difficult in controlling particle size
Electro-deposition	• Easy control in Morphology • Relatively fast	• Unsuitable for large-scale production
Microwave synthesis	• Relatively fast • Large scale production	• Difficult in morphology control

A tabled review (Table 2.9) presents research works that have been done on metal oxides and hybrid electrode materials, detailing the different combination of materials, various synthesis methods as well as electrolytes used and its specific capacitance at a particular current density or scan rate.

Table 2.9: Studies carried out on metal oxides and hybrid electrode materials with their corresponding capacitive values

Electrode material(s)	Configuration	Class of EC	Synthesis method	Electrolyte	Current density (A/g)	Scan rate (mV/s)	Specific capacitance (F/g)	Ref
Nickel oxide/graphene	Metal oxide /carbon	Hybrid	Hydrothermal	1 M NaOH	3	-	1829	[149]
Manganese oxide/graphene	Metal oxide/carbon	Hybrid	Hydrothermal	1 M Na_2SO_4	0.1	-	240*	[150]
$NiMoO_4$	Metal oxide	BTMO	Microwave	1 M KOH	1.25	-	1650	[151]
$NiCo_2O_4/CoMoO_4/Ni$	Metal oxide	MTMO	Hydrothermal	2 M KOH	10 #	-	1347	[152]
$NiMoO_4$	Metal oxide	BTMO	Hydrothermal	3 M KOH	1	-	974	[153]
$NiCo_2O_4$/graphene	Metal oxide/carbon	Hybrid	Solvothermal	6 M KOH	6	-	2173	[154]
Mn_3O_4/graphene	Metal oxide/carbon	Hybrid	Electrochemical deposition	1 M H_2SO_4	0.25	-	256*	[155]
$NiMoO_4/CoMoO_4$	Metal oxide	MTMO	Hydrothermal	1 M KOH	2	-	1602	[156]
manganese dioxide	Metal oxide	TMO	Hydrothermal	1 M Na_2SO_4	0.2	-	308	[157]
Zn-Ni-Al-Co	Metal oxide	MTMO	Chemical bath deposition	2 M KOH	1	-	839.2	[133]
ZnO/graphene	Metal oxide/carbon	Hybrid	Hydrothermal	6M KOH	2	-	110	[158]
Fe_3O_4/graphene	Metal oxide/carbon	Hybrid	Solvothermal	1 M $LiPF_6$	0.05	-	187*	[159]
Co_3O_4/graphene oxide	Metal oxide/carbon	Hybrid	Solvothermal	3M KOH	1	-	340	[160]
MnO_2 /graphene/Nickel	Metal oxide/carbon	Hybrid	Hydrothermal	0.5 M Na_2SO_4	-	1	234*	[161]
$NiMoO_4/CoMoO_4$	Metal oxides	MTMO	Hydrothermal	2 KOH	5	-	1079	[162]
Co_3O_4	Metal oxide	TMO	Solvothermal	6M KOH	10 #	-	1063	[163]
$MnNiCoO_4/MnO_2$/graphene	Metal oxide/carbon	Hybrid	Hydrothermal	6M KOH	0.8	-	1931	[164]

Electrode material(s)	Configuration	Class of EC	Synthesis method	Electrolyte	Current density (A/g)	Scan rate (mV/s)	Specific capacitance (F/g)	Ref
rGO/CNTs/MnO2	Metal oxide/carbon	Hybrid	Hydrothermal	1 M Na_2SO_4	0.5	-	319	[165]
$NaNiPO_4$	Metal oxide	MTMO	Solution combustion	1 M NaOH	2	-	368	[166]
MoO_3	Metal oxide	TMO	Solvothermal	Ethyl ammonium nitrate	-	5	288	[167]
$ZnCo_2O_4/MnO_2$/Nickel foam	Metal oxide	MTMO	Hydrothermal	1 M KOH	1	-	2339	[168]
Co_3O_4/Nickel foam	Metal oxide	BTMO	Solvothermal	6 M KOH	0.2	-	1936	[169]
FeOOH/carbon cloth	Metal oxide/carbon	Hybrid	Hydrothermal	2 M KOH	1	-	1066	[170]
$NiCo_2O_4$	Metal Oxide	TMO	Microwave	2 M KOH	20		400	[171]
SnO2/rGO	Metal oxide/carbon	Hybrid	Sol-gel/thermal reduction	PVA/KOH	-	2	229*	[40]
Zinc-Nickel-Cobalt	Metal oxide	MTMO	Hydrothermal	6 M KOH	1	-	2481	[130]
$ZnCo_2O_4$	Metal oxide	BTMO	Hydrothermal	2M KOH	1	-	689	[125]
Vanaduim pentoxide (V_2O_5)	Metal oxide	TMO	Precipitation	0.5 M K_2SO_4	1	-	316	[172]
V_2O_5/rGO	Metal oxide/carbon	Hybrid	Solvothermal	1 M Na_2SO_4	-	2	466	[173]
WO_3/carbon cloth	Metal oxide/carbon	Hybrid	Hydrothermal	1 M $LiPF_6$	1	-	521	[174]
$Co_3O_4/Ni(OH)_2$	Metal oxide	BTMO	Electrochemical deposition	1 M NaOH	-	5	1145	[175]
Ruthenium Oxide	Metal oxide	TMO	Microwave-Hydrothermal	1 M H_2SO_4	0.5	-	511	[176]
Iron oxide (Fe_2O_3)	Metal oxide	TMO	Sol-gel/hydrothermal	0.25 M $Na_2S_2O_3$	1	-	532	[177]

Current density in mA/cm^2 * Measurement using two-electrode cell configuration

2.8 Chapter summary

This chapter details the basis behind the motivation of this project that is harnessing the synergistic effect between graphene and metal oxides to produce composites material as an electrode for electrochemical capacitors. Having discussed past previous studies and researches as well as principles governing the electrochemical capacitor; it is paramount that an improvement in its electrochemical performance would be better for energy storage and consumption. In the following chapter, the various characterization techniques for determining the structural, morphological and elemental composition of the composites will be discussed as well as the methods for studying the electrochemical performance of the fabricated electrodes.

Chapter 3

Experimental Characterisation Techniques

3.1 Overview

This chapter describes the chemical and reagents as well as the basic working principles of relevant experimental techniques which are utilised in this research.

3.2 Reagents and apparatus

All the chemicals listed in Table 3.1 were received and used without further purification ` for the experiments reported in this thesis.

Table 3.1: Chemicals and reagents used for the synthesis of different graphene/metal oxide composites.

Chemical/Material	Grade	Supplier
Activated carbon (∝CH-0020)	BET surface ~1800 m^2/g	RHE resources
$Co(NO_3)_2.6H_2O$	98%	Sigma Aldrich
Cobalt (II) chloride hexahydrate	98%	Sigma Aldrich
Deionised water (DI)	-	Millipore system
Ethanol	>99.5%	Merck
Highly pyrolytic graphite (HOPG)	99% carbon purity	Bay Carbon
Manganese sulphate	A.C.S. Reagent	R&M chemicals
Nickel (II) nitrate hexahydrate	99%	Merck
N-methyl-2-pyrrolidinone	99%	Sigma Aldrich
polyvinylidene fluoride	Aqueous-based	Sigma Aldrich
Potassium Hydroxide	≥85%, pellets	Sigma Aldrich
Potassium permanganate	98%	R&M chemicals
Sodium hydroxide	≥97%, pellets	R&M Chemicals
Sodium molybdate dehydrate	98%	R&M chemicals
Urea	99.5%	R&M chemicals
Zinc nitrate hexahydrate	98%	Sigma Aldrich

3.3 Experimental Details

3.3.1 Synthesis of graphene

Highly pyrolytic graphite (HOPG) was used as the starting precursor for the synthesis of graphene, via a previously reported liquid phase exfoliation method [45]. Typically, HOPG (0.05 grams (g)) was dispersed in a 100 ml solution of ethanol and deionised water (2:3). Sonication treatment was performed on the resulting mixture in an ultrasonic bath with working frequency of 50/60 Hz at room temperature for 3 h to form a darkish black suspension. The solution was then centrifuged and dried at 80 ^{o}C for 10 h.

3.3.2 Preparation of graphene-ZnO composites

Graphene (0.2 g) nanosheets was then re-dispersed in 50 ml solution of ethanol and deionized water (2:3) under sonication for 30 minutes as illustrated in Figure 3.1. Zinc nitrate hexahydrate was added to the graphene solution and stirred for 15 minutes to produce a uniform dispersion. Diluted sodium hydroxide solution was then added to the mixture till a pH value of 12 is obtained and was stirred for 30 minutes. The mixture was transferred to a 50 ml Teflon stainless steel autoclave and put in an oven for 10 hours at 90 ^{o}C. The solid precipitation was isolated from the solution by centrifugation, washed repeatedly with excess water and ethanol, respectively and dried overnight at 70 ^{o}C in an oven.

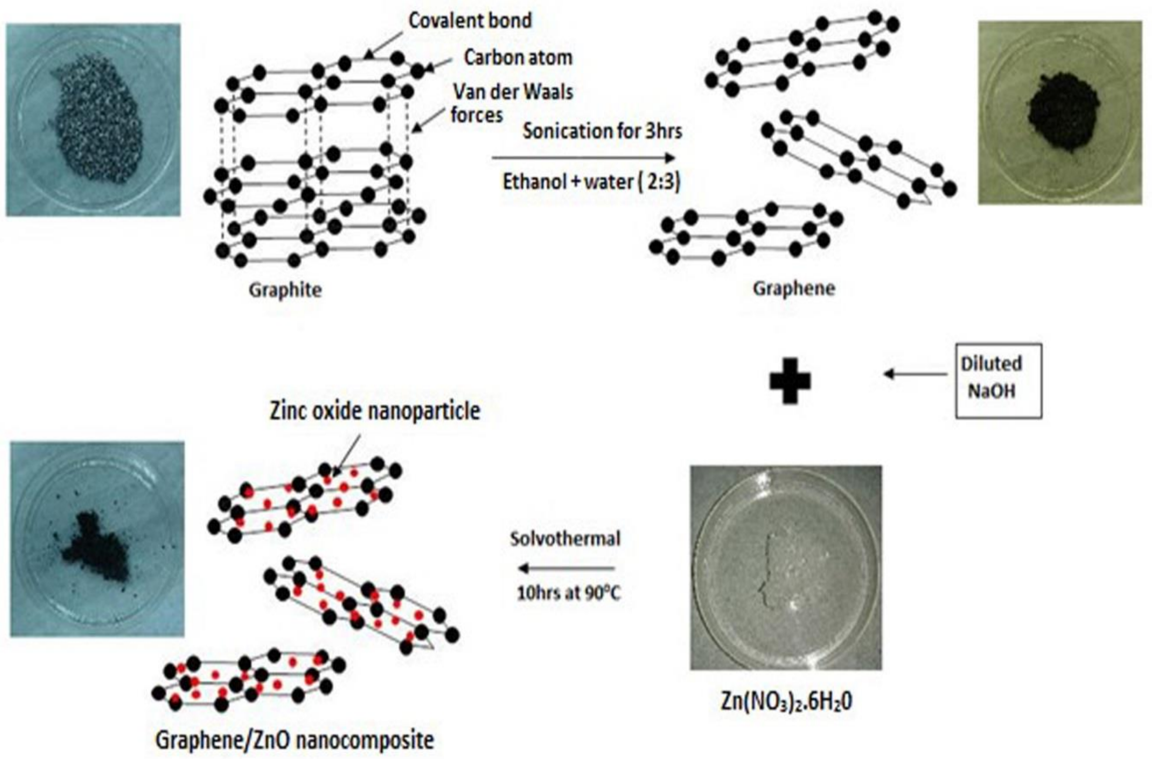

Figure 3.1: The schematic diagram of graphene-ZnO composites prepared via a facile green solvothermal synthesis.

The addition of NaOH solution in the mixture generates an intermediate hydroxide ($Zn(OH)_2$) colloids upon reaction with $Zn(NO_3)_2.6H_20$ as stated in equation 3.1, part of the $Zn(OH)_2$ colloids dissolves into Zn^{2+} and OH^- during the hydrothermal process according to equation 3.2. ZnO nuclei are formed when the concentration of Zn^{2+} and OH^- reaches the supersaturation degree of ZnO according to equation 3.3. The possible reactions process can be expressed in the equations as follows:

$$Zn(NO_3)_2.6H_20 + 2NaOH \leftrightarrow Zn(OH)_2\,(gel) + 2NaNO_3 + 6H_2O \tag{3.1}$$

$$Zn(OH)\,(gel) + 2H_2O = Zn^2 + 2OH^- + 2H_2O \leftrightarrow Zn(OH)_4^{2-} + 2H^+ \tag{3.2}$$

$$Zn(OH)_4^2 \leftrightarrow ZnO + H_2O + 2OH^- \tag{3.3}$$

Table 3.2 shows detailed information of the different ratios of graphene to zinc nitrate hexahydrate which were used to prepare the graphene-ZnO nanocomposites.

Table 3.2: Different mass ratios of graphene to zinc precursor used to form graphene-ZnO nanocomposites.

Name of sample	Mass of graphene (g)	Mass of zinc nitrate hexahydrate (g)	Weight ratio of graphene: zinc precursor
GZn1	0.2	0.2	1:1
GZn2	0.2	0.4	1:2
GZn3	0.2	1.6	1:8
GZn4	0.2	3.2	1:16

3.3.3 Preparation of graphene-MnO_2 composites

In a typical experiment, 0.2 g of the as-synthesized graphene is dispersed in 50 ml solution of ethanol and deionized water (2:3) under sonication for 30 minutes. Then, 0.2 g of $MnSO_4.H_2O$ and $KMnO_4$ were separately dissolved in 10 ml of deionized water and added sequentially to the graphene solution under vigorous stirring. The mixture was transferred to a 50 ml Teflon stainless steel autoclave and put in an oven at 90 ^oC for 15 hours. The precipitate was collected by centrifugation, washed repeatedly with excess ethanol and water, respectively and dried overnight at 70 ^oC in an oven. In this study the mass of graphene remained the same and the weight ratio of graphene to the manganese precursors were varied for the other samples at the same reaction conditions.

When $MnSO_4.H_2O$ was initially poured into the graphene solution, Mn^{2+} ions were evenly adsorbed on the surface and edges of the graphene sheets by electrostatic forces. The graphene sheets with a large area provided plenty of attachment sites for the formation of MnO_2 nuclei [178]. Then, upon addition of $KMnO_4$ into the mixture, many nucleuses were formed quickly as the appearance of a black-brown precipitate was clearly observed. A redox reaction between $MnSO_4.H_2O$ and $KMnO_4$ could occur as follows:

$$2KMnO_4 + 3MnSO_4 + 2H_2O \longrightarrow 5MnO_2 + 2H_2SO_4 + K_2SO_4 \tag{3.4}$$

Table 3.3 shows detailed information of the different ratios of graphene to manganese precursors used to prepare different graphene-MnO_2 composites.

Table 3.3: Different mass ratios of graphene to manganese precursor used to form graphene-manganese dioxide composites.

Name of sample	Mass of graphene (g)	Mass of $KMnO_4$ (g)	Mass of $MnSO_4.H_2O$ (g)	Weight ratio of graphene: MnO_2 precursor
GM1	0.2	0.2	0.2	1:1
GM2	0.2	0.4	0.4	1:2
GM3	0.2	1.6	1.6	1:8
GM4	0.2	3.2	3.2	1:16

3.3.4 Preparation of graphene-Co_3O_4 composites

0.2 grams of the as-prepared graphene was dispersed in a 50 ml solution containing ethanol and water (2:3) under sonication for 30 minutes. Then, 0.19 grams of cobalt (II) chloride and 0.01 grams of urea were separately dissolved in 5 ml of deionised water. The cobalt (II) chloride solution was added into the graphene solution under stirring followed by the dropwise addition of urea into the mixture and allowed to stir for 15 minutes. The addition of urea is favourable to the gradual release of hydroxyl ions that are needed for the formation of cobalt hydroxide intermediate species, which subsequently will be transformed to cobalt oxide nanoparticles after calcination [179]. The resultant mixture was transferred to a 50 ml Teflon stainless autoclave and put in a chamber furnace at 105 ^{o}C for 6 hours. The precipitate was collected by centrifugation, washed repeatedly with ethanol and water and dried overnight in an oven at 70 ^{o}C. The possible reactions involved in the formation of Co_3O_4 nanocomposites can be summarised as below:

$$CoCl_2 \rightarrow Co^{2+} + 2Cl^{-1} \tag{3.5}$$

$$CH_4N_2O + H_2O \rightarrow 2NH_3 + CO_2 \tag{3.6}$$

$$NH_3 + H_2O \rightarrow NH_4^{+} + OH^{-} \tag{3.7}$$

$$Co^{2+} + 2OH^{-} \rightarrow Co(OH)_2 \tag{3.8}$$

The cobalt hydroxide ($Co(OH)_2$) formed is thermodynamically unstable [180] and thus the as-prepared composites were calcined in a furnace at a temperature of 400 ^{o}C for 4 hours in air to induce the formation of Co_3O_4 nanoparticles. The as-prepared samples with different weight ratio of graphene to Co_3O_4 (1:1, 1:4, 1:8) were marked as G1Co1, G1Co4 and G1Co8, respectively. Pure Co_3O_4 was prepared following the same reaction conditions.

3.3.5 Preparation of graphene-$NiCo_2O_4$ composite

Figure 3.2 shows the synthesis route used in the preparation of the graphene-$NiCo_2O_4$ composite. 0.35 g of graphene was dispersed in 40 ml solution of ethanol and deionized water (2:3) by sonication for 20 minutes. The $NiCo_2O_4$ precursor solution was prepared by mixing 0.35 g of $Ni(NO_3)_2.6H_2O$ and 0.69 g of $Co(NO_3)_2.6H_2O$ in 40 ml of deionised water. After that, 0.48 g of urea was added to the solution and the mixture was mixed with the dispersed graphene solution under mild stirring for 30 minutes to achieve homogeneity. The entire solution was then transferred to a Teflon-lined stainless steel autoclave and heated to a temperature of 120 ^{o}C for 8 h in a furnace. The resulting precipitate was separated and washed with ethanol and deionised water repeatedly by centrifugation and dried in an oven at 70 ^{o}C overnight. During the solvothermal synthesis, metal cations Co^{2+} and Ni^{2+} released from $Ni(NO_3)_2.6H_2O$ and $Co(NO_3)_2.6H_2O$ react with Co_3^{2-} and OH^- anions which were released from the hydrolysis of urea. The co-precipitates consisting of nickel carbonate hydroxide hydrate and cobalt basic carbonate are thermodynamically unstable owing to their high surface energy [23]. The relevant reactions can be expressed as follows:

$$CO(NH_2)_2 + H_2O \rightarrow CO_2 + 2NH_3 \tag{3.9}$$

$$CO_2 + H_2O \rightarrow H_2CO_3 \rightarrow CO_3^{2-} + 2H^+ \tag{3.10}$$

$$NH_3 + H_2O \rightarrow NH_3.H_2O \rightarrow NH_4^+ + OH^- \tag{3.11}$$

$$(Co^{2+} + Ni^{2+}) + xOH^- + 0.5(2-x)CO_3^{2-} + nH_2O \rightarrow (Co,Ni)(OH)_x(CO)_{0.5(2-x).}nH_2O \tag{3.12}$$

The co-precipitates were then calcined in a furnace at a temperature of 400 ^{o}C for 2 h in air to induce the formation of $NiCo_2O_4$ composite.

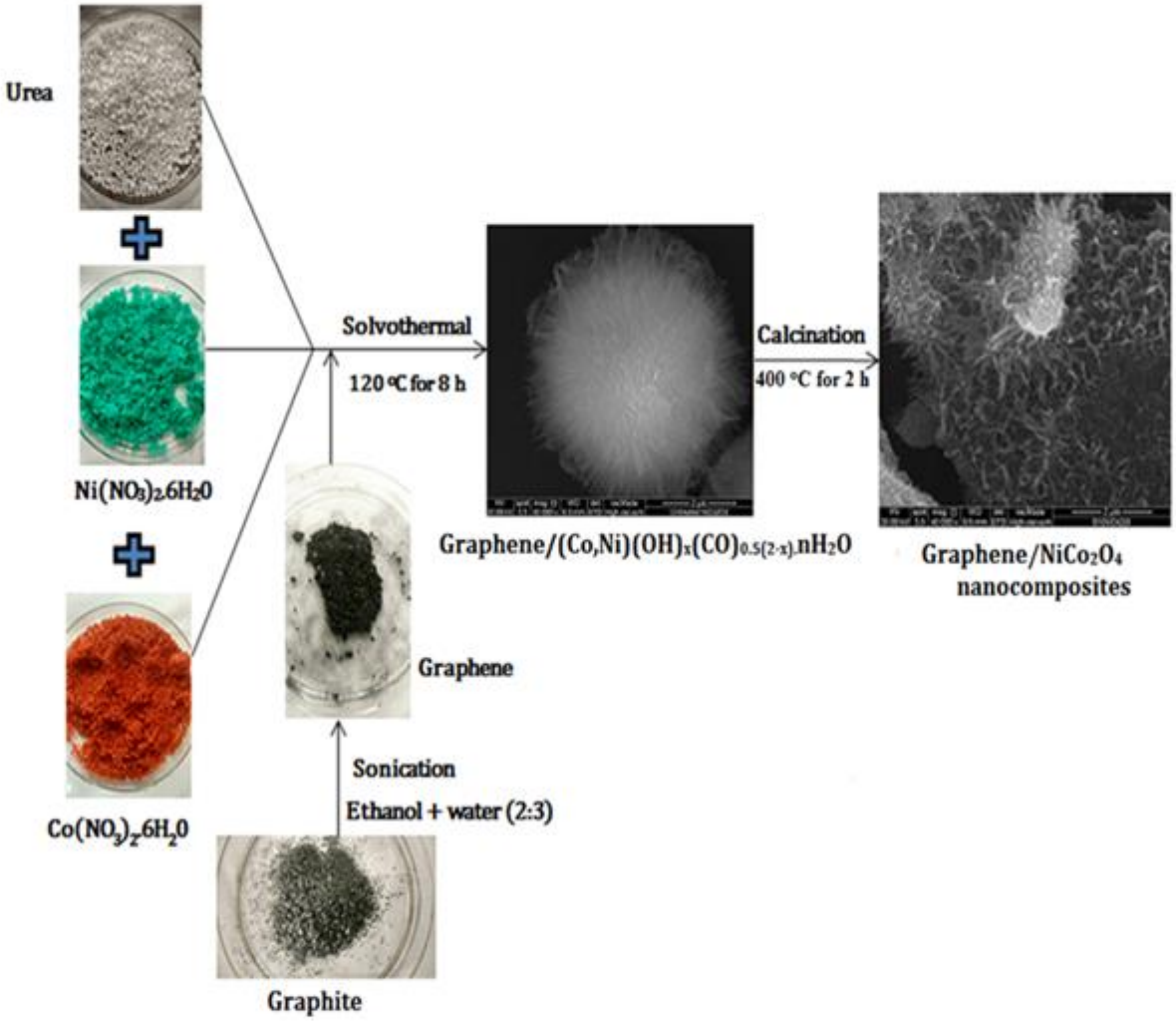

Figure 3.2: The schematic diagram of graphene-$NiCo_2O_4$ composites prepared via solvothermal synthesis.

For comparison analysis, the weight ratio of graphene to $NiCo_2O_4$ precursors was varied to form nanocomposites under the same reaction conditions. Detailed information of the precursors solutions of all composite samples are summarised in Table 3.4.

Table 3.4: Different mass ratio of graphene to $NiCo_2O_4$ precursors used to synthesize the nanocomposites.

Name of sample	Weight ratio of graphene: $NiCo_2O_4$	Mass of graphene (g)	Mass of $Ni(NO_3)_2.6H_2O$ (g)	Mass of $Co(NO_3)_2.6H_2O$ (g)	Mass of Urea (g)
G-NC_2	1:1	0.35	0.35	0.69	0.48
G-4NC_2	1:4	0.35	1.40	2.76	1.92
G-8NC_2	1:8	0.35	2.80	5.52	3.84
G-16NC_2	1:16	0.35	5.60	11.04	7.68

3.3.6 Preparation of graphene-$NiMoO_4$ nanocomposites

The as-synthesised graphene (0.2 g) was dispersed in a solution of ethanol and deionised water in optimum ratio (2:3) via sonication for 30 minutes to achieve even mixing. In a separate procedure, the $NiMoO_4$ solution was prepared by mixing 29 mg of nickel (II) nitrate hexahydrate ($Ni(NO_3)_2.6H_2O$) and 24 mg of sodium molybdate dehydrate ($NaMoO_4.2H_2O$) in 30 mL of deionized water and stirred for 20 minutes. The solution is added to the dispersed graphene solution under stirring for 10 minutes to achieve homogeneity. The solution was transferred into a 50 ml Teflon-lined stainless steel autoclave and heated to a temperature of 160 ^oC for 6 h. The precipitate was centrifuged and washed thoroughly with ethanol and deionised water and then dried at 80 ^oC overnight in an oven. During the solvothermal process, OH^- is one of the products of the reduction process of NO_3^- as suggested in equation 3.13. The metal cations Ni^{2+} and Mo^{6+} released from $Ni(NO_3)_2.6H_2O$ and $NaMoO_4.2H_2O$ respectively react with OH^- anions (as shown in equation 3.14) to form a Ni-Mo hydroxide precursor. The dried Ni-Mo hydroxide precursor was annealed at 400 ^oC for 4 h in air to induce the formation of graphene-

$NiMoO_4$ nanocomposites (equation 3.15). The fabrication process of the graphene-$NiMoO_4$ nanocomposites is illustrated in Figure 3.3.

$$NO_3^- + 7H_2O + 8e^- \rightarrow NH_4^+ + 10OH^- \qquad (3.13)$$

$$Ni^{2+} + Mo^{6+} + 8OH^- \rightarrow NiMo(OH)_8 \qquad (3.14)$$

$$NiMo(OH)_8 \rightarrow NiMoO_4 + 4H_2O \qquad (3.15)$$

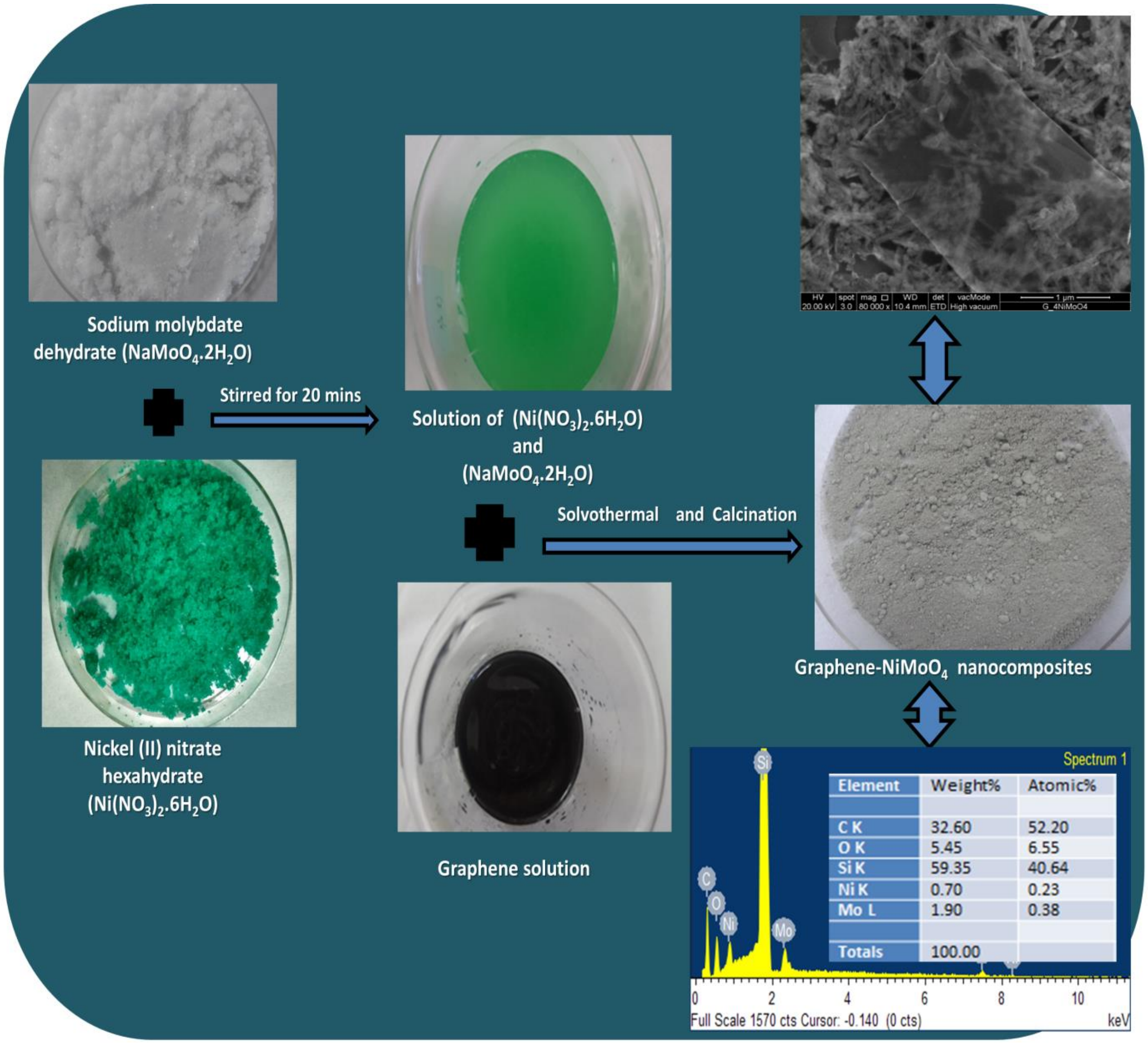

Element	Weight%	Atomic%
C K	32.60	52.20
O K	5.45	6.55
Si K	59.35	40.64
Ni K	0.70	0.23
Mo L	1.90	0.38
Totals	100.00	

Figure 3.3: The schematic diagram of graphene-$NiMoO_4$ nanocomposites prepared via solvothermal synthesis.

Table 3.5 presents comprehensive information of the precursor formulations. The various graphene-$NiMoO_4$ nanocomposites were synthesised by varying the weight ratio of graphene to $NiMoO_4$ precursors under the same reaction procedure.

Table 3.5: Different mass ratio of graphene to $NiMoO_4$ precursors used to synthesise the nanocomposites.

Name of nanocomposites	**Weight ratio of graphene: $NiMoO_4$ (g)**	**Mass of graphene (g)**	**Mass of $Ni(NO_3)_2.6H_2O$ (g)**	**Mass of $NaMoO_4.2H_2O$ (g)**
G-NM	1:1	0.2	0.29	0.24
G-4NM	1:4	0.2	1.16	0.96
G-8NM	1:8	0.2	2.32	1.92
G-16NM	1:16	0.2	4.64	3.84

3.3.7 Preparation of electrodes for electrochemical characterisation

The electrodes were prepared by mixing the active materials (composites), carbon black (conductivity agent) and polyvinylidene fluoride (PVDF) (binder) at a weight ratio of 7:2:1 and dispersed in N-methyl-2-pyrrolidinone (NMP). The resultant mixture was evenly coated on the aluminium coil and kept in the oven at a temperature of 70 ^oC overnight. The foil was taken out of the oven allowed to cool off and small coined electrodes are punched out. The electrochemical cell was assembled by sandwiching two symmetric electrodes separated by a separator as shown in Figure 3.4 forming a two-electrode test cell.

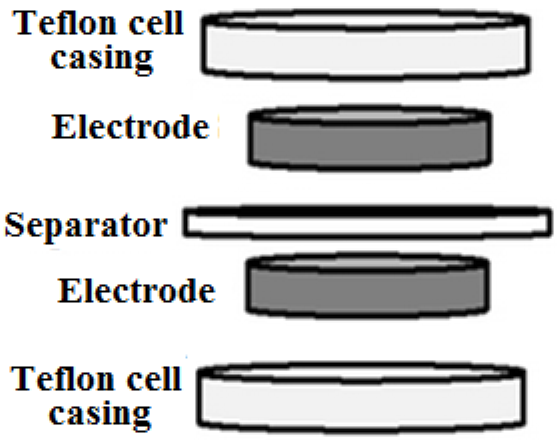

Figure 3.4: A schematic showing a two electrode cell assembly.

3.4 Characterisation techniques for composite materials

The basic requirements in preparation of composites for both laboratory and industrial purposes are its synthesis and characterisation. Characterisation is the study of the morphology, crystalline structure and chemical state of the composite material to determine its behavior. In order to ascertain the verity of the as-synthesised graphene/metal oxide composites, a range of analytical instruments were employed in order to determine their quantitative and qualitative quality. The analytical instruments used were field emission scanning electron microscopy (FESEM), energy dispersive x-ray spectroscopy (EDS), transmission electron microscopy (TEM), x-ray diffraction (XRD) and Raman spectroscopy. Elaborate details on the fundamentals and sample preparations of each approach are discussed in the following subsections.

3.4.1 X-ray Diffraction (XRD)

XRD is an essential and non-destructive analytical method used to analyse the crystalline structure of materials. This method aids with the quick analysis and characterisation of unknown materials among various fields such as mineralogy, archeology, forensic and biological sciences. XRD analysis can be said to be a fingerprint that lets you determine what is in your sample; i.e. every material has a unique identification and the XRD analysis makes it possible to identify that pattern [181]. It is the concept of the elastic scattering of x-ray photons by atoms in a periodic lattice; based on the principle that constructive interference results when monochromatic X-rays are in phase. This is comprehended using the Bragg's law (equation 3.16):

$$n\lambda = 2d\sin\theta \tag{3.16}$$

Where n = order of reflection; n = 1, 2, 3 …

λ = wavelength of x-rays

d = characteristic interplanar spacing

θ = angle between the incident beam and the normal to the reflecting lattice plane

The interplanar spacing (d) can be determined when the angles (θ) at which the constructively interfering x-rays leaving the material is measured. The schematic of Bragg's law (Figure 3.5) shows the relationship between the interplanar spacing, the angles involved in the interaction of the material and the x-rays [182], [183].

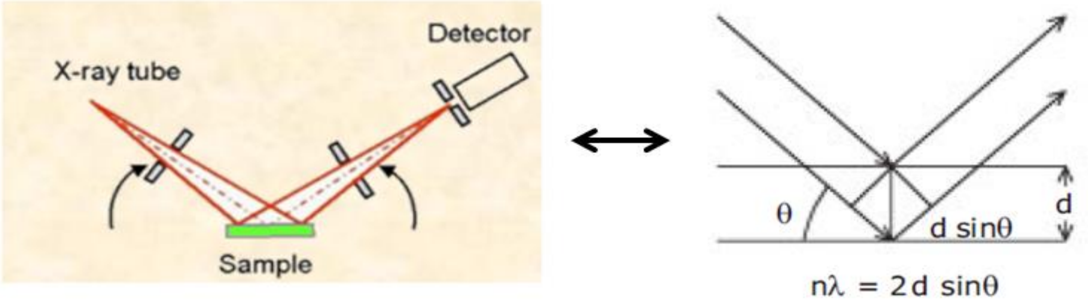

Figure 3.5: Schematic diagram of Bragg's law showing how the interplanar spacing (d) can be determined [183]**.**

To identify any unknown material, the diffraction pattern is recorded and a list of interplanar spacing (d) values of every phase is prepared along with the intensity of the diffraction lines. The diffraction pattern recorded is now matched with standard database housing over 60,000 patterns of different materials. This database is updated annually by the International centre for Diffraction Data (ICDD) [183].

Xiaomaio Feng et al investigated the structure of various graphene/MnO_2 compared with graphene oxide using XRD study. Figure 3.6 illustrates the graphene oxide samples having an intensive peak at $2\theta = 10.9^o$ which corresponds to the (002) graphene oxide reflection. This peaks disappeared in the graphene/MnO_2 composites reflecting the formation of graphene and the additional peaks detailed that the graphene surface was loaded with $MnO_{2.}$ The diffraction patterns of the graphene/MnO_2 composites (GM-1 and GM-2) matched the database (JCPDS no. 80-1098) for δ-MnO_2 and GM-4 and GM-8 corresponded to α- MnO_2 (JCPDS no. 44-0141).

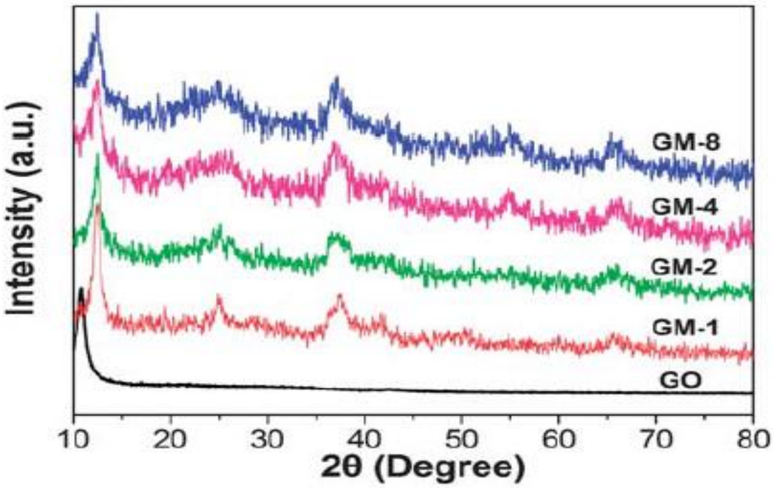

Figure 3.6: XRD patterns comparing GO and different graphene/MnO$_2$ composites [178]**.**

3.4.1.1 Sample preparation

All samples used for XRD analysis were all in powdered form. The XRD patterns of the powered samples obtained for this report was characterised by Philip PANanalytical X'pert X-ray diffractometer (Figure 3.7) operated at 33 mA and 45 kV. The patterns were recorded from a 2θ range of 10 to 70^{o} at a scan rate of 2.4 ^{o}/min using Cu-Kα radiation (λ = 1.54056 Å).

Figure 3.7: The Philip PANanalytical X'pert X-ray diffractometer used for the XRD study in this report.

3.4.2 Field emission scanning electron microscope (FESEM)

Field emission scanning microscopy is a straightforward non-destructive test used to study the structure, composition and sizes of materials [183], [184] over a wide variety of signals giving it the ability to provide a visual surface morphology and provide qualitative compositional information over relatively large areas [185]. This is governed by the principle of the bombardment of beams of primary electrons on the surface of the material and measuring the yield signals. When this beam of primary electrons strikes the material as shown in Figure 3.8 the electrons are either scattered or absorbed, producing various signals such as secondary electrons, auger electrons and backscattered electrons. The mode of the FESEM is designed to capture the secondary and backscattered electrons [182].

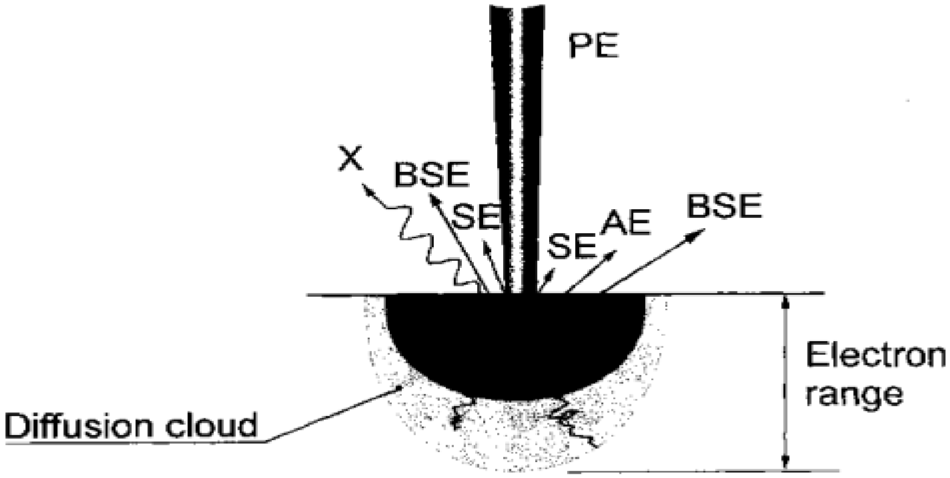

Figure 3.8: Different interactions of an electron beam (PE) with a target material BSE = backscattered electron, SE = secondary electron, X = x-ray, AE = auger electron [182].

The working principle of the FESEM is further explained with the aid of a schematic diagram detailing its principal parts as shown in Figure 3.9:

- Electron source: generates the primary electrons
- Lenses and aperture: they condense the electron beam produced by the electron source to a spot about 5 -100 nm in diameter at the specimen plane.
- Scan coils: coils for rastering scanning the beam.
- Scan generator: drives the scan coils presently in the microscope column and cathode ray tube simultaneously.

- Detector/photomultiplier: collects the secondary electrons (SEs) and backscattered electrons (BSEs) produced to form an image and provide chemical compositional data. i.e. converting light into an electric current.
- Amplifier: Improves the electric signal generated by the photomultiplier.
- Display: a monitor to show information gathered. [182], [186]

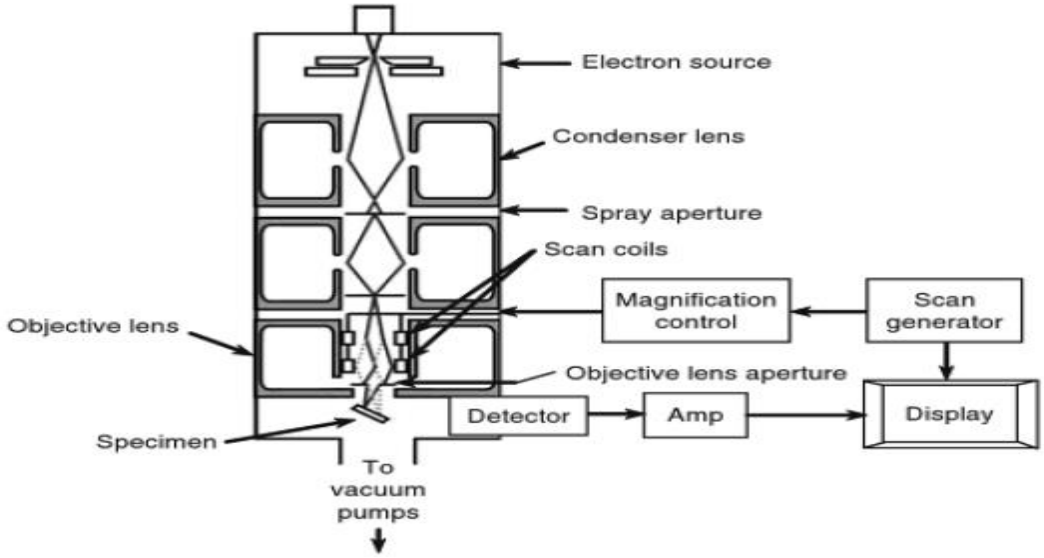

Figure 3.9: Schematic diagram of a FESEM detailing its principal parts [186]**.**

Figure 3.10 shows the FESEM image of graphene-SnO_2 composite films. It can be seen from the figure that the surface and edges of the graphene nanosheets are covered by irregular shaped and densely packed SnO_2.

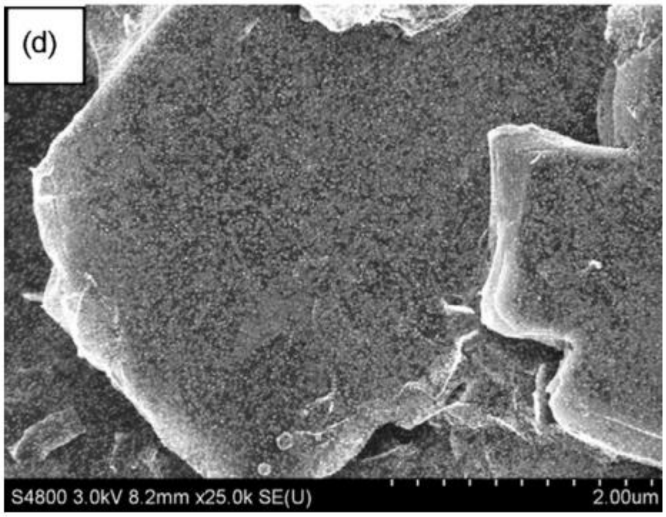

Figure 3.10: FESEM image of graphene-SnO$_2$ composite films [187].

3.4.2.1 Sample preparation

The FESEM system used throughout the course of this project was the FEI Quanta-400 FESEM (Figure 3.11). All samples were dispersed on a silicon wafer after dispersion with ethanol via sonication and bombarded at different magnifications as a measure of the qualitative morphology of the as-synthesised graphene/metal oxide composites.

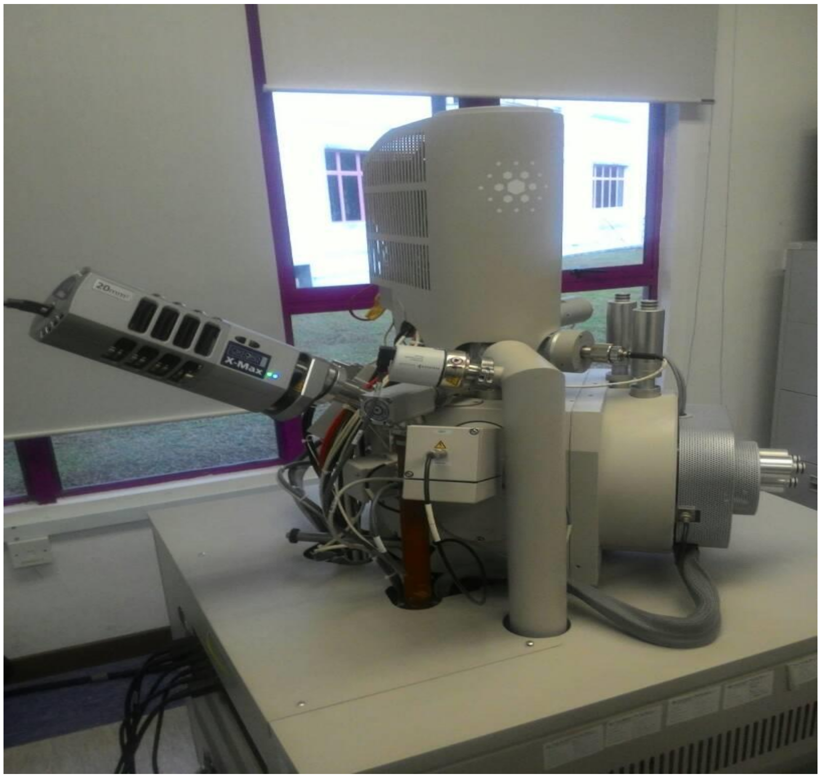

Figure 3.11: The FEI Quanta-400 FESEM used for scanning SEM samples used for this report.

3.4.3 Energy-dispersive X-ray spectroscopy (EDS)

The energy dispersive analyser is often used simultaneously with the SEM to study the morphology and analyse the elemental composition of materials. It is equipped with a detector and software [182]. The detector is used to differentiate the individual x-rays of different materials into an energy spectrum and the software is used to examine the energy spectrum to conclude on the elements present. The EDS analysis can be conducted in any of the four different modes:

- In the spot mode: using this mode, a small spot in the material is taken to analyse its elemental composition
- In the area mode: a large composition of the area is analysed for its elemental composition

- In dot mapping mode: A particular area of interest in the material is scanned for elemental mapping to study the distribution density of elements present in that region.
- In linear traverse mode: the mode is used to study the variation in concentration of one or more elements present along a line [182].

An energy dispersive analyser in a matter of seconds can acquire a full elemental spectrum and with the help of the supporting software makes readily the identified peaks hence making EDS a great quick surveying tool [182]. The result of EDS is displayed on a plot of x-ray counts against energy (keV) with the energy peaks proportional to the various elements present in the material as shown in Figure 3.12

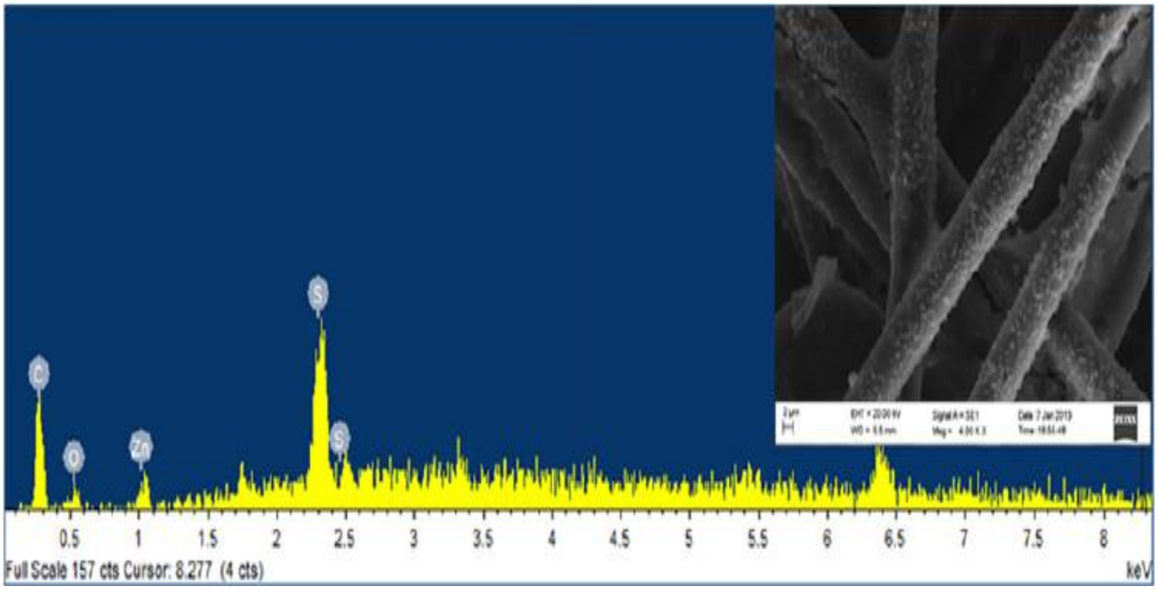

Figure 3.12: EDS and inset corresponding to the energy peaks of ZnO/carbon nanotube composite [198].

3.4.4 Raman Spectroscopy

Raman spectroscopy is a fast characterization tool that offers high resolution images, gives structural and electronic information on a material. It is non-destructive and can be employed in laboratories and industries [188]. Raman spectroscopy employs the principle of inelastic scattering of single-chromatic light. By this principle, samples absorb and re-emit the photons of the laser light causing a transition. The transition occurs when the original monochromatic frequency causes frequency shifting (up and down) of the reemitted photon; this is termed the Raman Effect. The information on the rotation, vibration and other low frequency modes of the samples can be acquired by this shift or transition [189]–[191].

The Raman spectrometer consists of four major components [190], [191]:

1. An Excitation source: continuous-wave (CW) lasers are common used as excitations for Raman spectroscopy due to their ability to provide the required intensity for scattering. Examples include argon ions, krypton ions, diodes and helium-neon ions.
2. Sample Illumination and collection system: this feature an interference filter that obtains the necessary bandwidth generated from the laser. The holographic notch filter allows Raman spectral measurements of ~100 $cm^{-1}$to pass through it.
3. Wavelength selectors: The detector/ selectors record the intensity of the Raman signal of each wavelength resulting from the propagation of the Raman scattered photons. Examples are multichannel detectors such as photodiode arrays (PDA), and charge coupled device (CCD) cameras.

4. Detection and computer/processing systems which allows the collection and processing of data.

A typical arrangement of these components is illustrated in the Figure 3.13

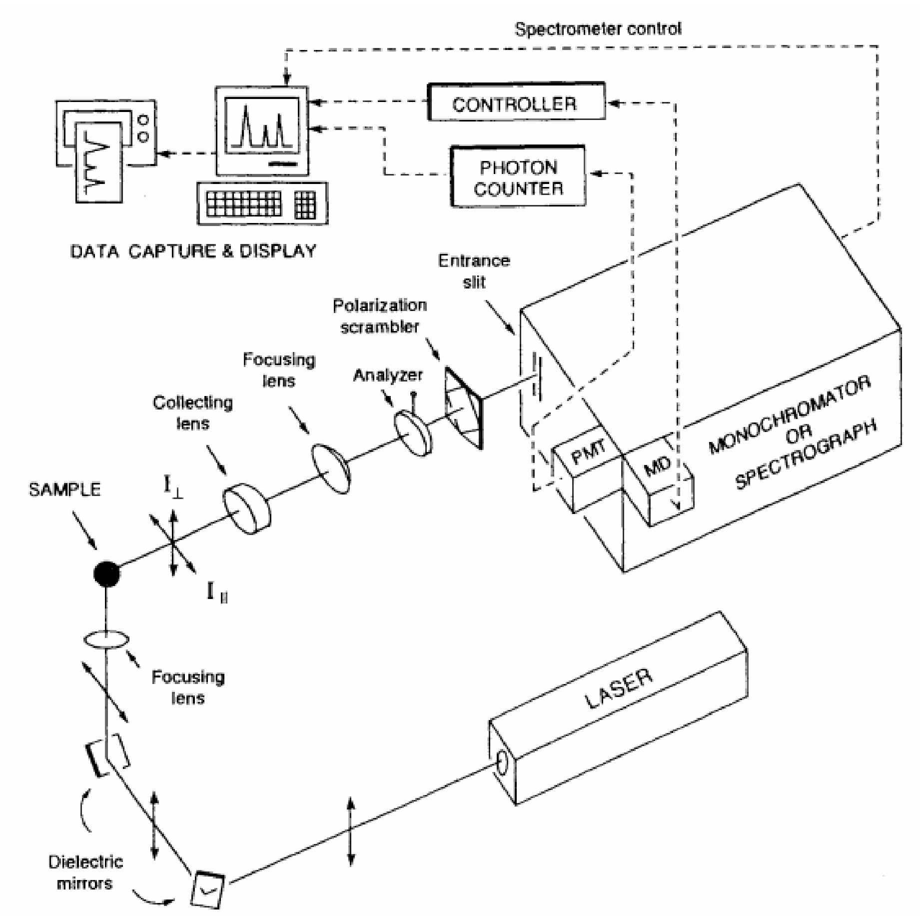

Figure 3.13: A Schematic diagram of the major components in a Raman Spectrometer [190]**.**

The result obtained from the Raman spectrometer is presented in a plot of the intensity of Raman scattered radiation as a function of shifted frequencies in wavenumber (cm^{-1}). The frequency difference of shift from the incident radiation is termed Raman shift. The peaks presented in the spectra are matched to characteristic peaks in databases to identify the chemical compound present in the sample [191] . From Figure 3.14, it can be seen that the peaks present in the spectra at 1347 cm^{-1}, 1580 cm^{-1} and 2877 cm^{-1}can be attributed to the D, G and 2D signature of graphitic sp^2-bonded carbon atoms.

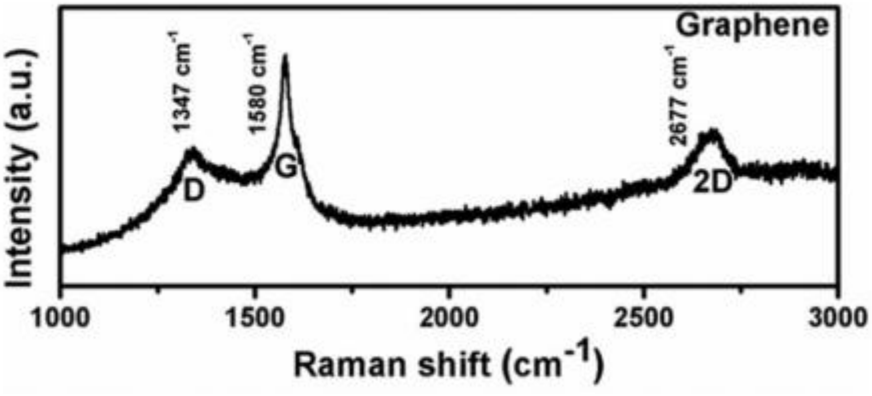

Figure 3.14: Raman spectra of graphene showing the D, G and 2D peaks [192]**.**

3.4.4.1 Sample preparation

The Raman spectra of the powered samples used throughout this project were recorded on a Renishaw inVia Raman microscope. The system was equipped with a CCD detector and a holographic notch filter using a 514 nm diode laser excitation source with power below 0.5 mW.

3.4.5 Transmission electron microscopy (TEM)

TEM is a microscopy technique that has been of great value in studying the shape and size of materials [183], [193]. The TEM follows the same working principle of focusing beams of electrons on a sample similar to the SEM, however in this case the electrons penetrate a thin specimen through a condenser to produce parallel rays that impinge on the sample. A sophisticated system of electromagnetic lenses focused the resultant scattered electrons into a diffraction pattern or an image. A bright field image is formed when the electron optics magnifies the two dimensional projection of the sample produced by the transmitted electrons while a dark field image is said to be produced from the diffracted electron beams which are in an angle slightly off the transmission beam [183].

The functionality of the different parts of a TEM instrument (Figure 3.15) can be categorised into three sections [193]:

- The Illumination system: This system comprises of the electron gun and the condenser lenses. Their design and operation determines the diameter of the electron beam at the sample and the intensity level in obtained TEM image.
- The specimen stage: At this stage, the sample aperture determines the mechanical stability of the samples which is an essential factor that determines the spatial resolution of the TEM image.
- The imagining system: The magnification of the TEM image is determined by the imaging system which consists of at least three lenses combined to produce an image or a diffraction pattern. The image/diffraction pattern produced by the lenses is displayed on a photographic film or fluorescent screen or on an electronic screen.

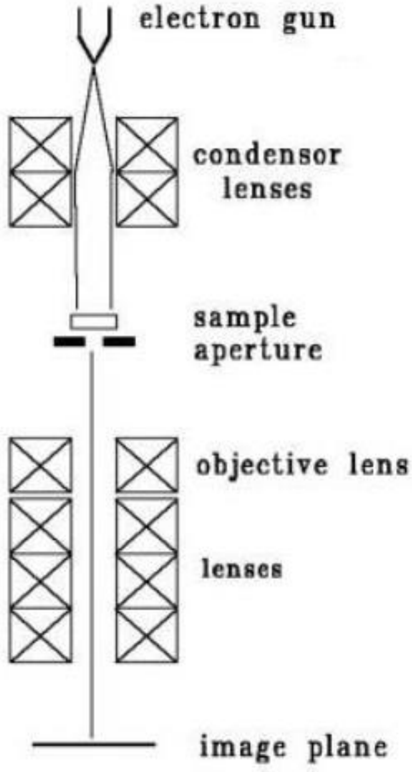

Figure 3.15: Schematic setup of a TEM system [183]**.**

TEM image (Figure 3.16) shows that surface of the graphene sheets were covered with a good distribution of MnO_2 particulars, with sizes ranging from 10-20 nm.

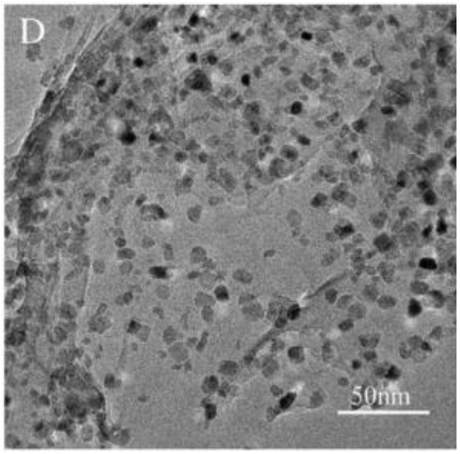

Figure 3.16: TEM image of MnO_2/graphene composites [194]**.**

3.4.5.1 Sample Preparation

The TEM samples used in this project were prepared in the same way as those used for SEM viewing detailed in section 3.4.2.1. The prepared samples were viewed by a transmission electron microscope JEOL JEM-2100F (Figure 3.17) at an operating voltage of 200 kV.

Figure 3.17: The JEOL JEM-2100F system used for TEM analysis throughout this project.

3.5 Electrochemical capacitor electrode material evaluation

The performance evaluation of an electrochemical capacitor is necessary to determine how it is suitable to its application and to compare it with different devices and technologies. It is not always practical to package a full sized cell when dealing with relatively small mass of the material and/or a larger number of different types of samples for testing. However, it is essential to evaluate an electrode material performance through experimental procedures that are flexible, repetitive and can be compared to studies/researches. These procedures can be grouped into (i) test fixture configuration; which details the mimicking of the unit cell configuration to matching the performance of a packaged cell and (ii) measurement procedures; this is the desired metrics obtained from computations of electrochemical measurements and parameters [195].

The two and three electrode cell configurations are the commonly used test fixture configurations of an electrochemical capacitor. The two electrode test cell which is similar to a commercial packed electrochemical capacitor is made up of two electrolyte-electrode assembly sandwiched by a separator while the three electrode test cell commonly used by electrochemical research consists of a working electrode, a counter electrode and a reference electrode. These two configurations differ from one another in some significant aspects such as: In using the three electrode cell configuration, only one electrode (working electrode) contains the active material being analysed while the active material is present in both electrode for the two electrode configuration [9], [10], [195]. In interpreting the representation of the voltage potential applied to the working electrode in a cyclic voltammogram (CV); for a three electrode cell, it is displayed on the X-axis of the CV diagram and the Y-axis displays the particular reference electrode. However in a symmetrical two electrode cell, the X-axis is a reflection of the potential difference in half the value of the two electrodes since the electrodes are equal to each other [195].

Electrochemical measurements and parameters used to evaluate comprehensively the characteristics and performance of electrochemical capacitors and also allow its comparison with other researches and accepted procedures includes:

3.5.1 Cyclic voltammetry (CV)

CV is a potential-controlled “reversal” electrochemical method widely used to determine the qualitative and quantitative information on the surface and solution electrochemical reactions and its effects of the electrode materials. This method of studying the electrochemical behaviour of electrode materials is convenient and sensitive. In general, CV is performed by applying a series of changing voltages to the electrochemical capacitor at a constant sweep rate (dV/dt) and measuring the response current (I) using a potentiostat [9], [10], [196].

The assembled cells are connected in a two or three electrode configuration to a potentiostat system. Figure 3.18(a) shows a three electrode system comprising of three electrodes: (1) the working electrode (WE), (2) the auxiliary or counter electrode (CE) and the reference electrode (RE). This system measures only half of the cell. The two electrode system as shown in Figure 3.18(b) has a working electrode connected alongside the sense electrode as a single mode (working) and the reference and counter electrode connected together forming the reference mode. This setup is termed a full cell configuration because it measures the entire cell [9], [10], [196].

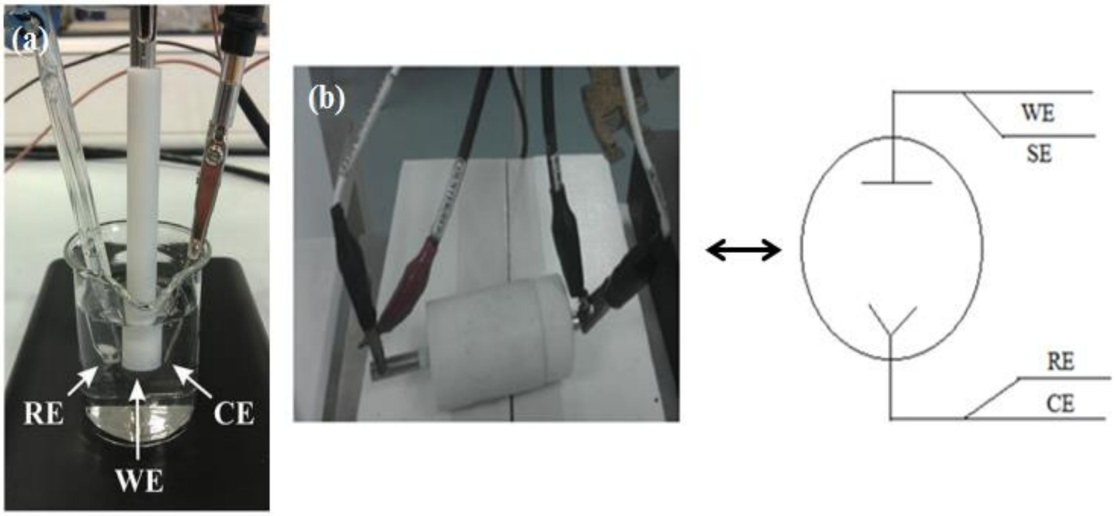

Figure 3.18: (a) three electrode and (b) two electrode configuration to a potentiostat system.

The potentiostat controls the parameters (initial (E_i), switching (E_s), final (E_f) potentials and scan (sweep) rate (v, in V/s)) of the experiment. It delivers cyclic linear potential sweep on the working electrode and records the resulting current-voltage curve of the experiment (Figure 3.19) [196]. During the CV test, the potential of the working electrode is measured against the reference electrode through linear back and forth scanning between the initial and final potential [10]. The electrochemical reaction occurs at the working electrode and the auxiliary or counter electrode driven by potentiostat circuit balances the reaction occurring at the working electrode. For instance, if an oxidation reaction is occurs at the working electrode, a reduction reaction happens at the auxiliary electrode. The process at the auxiliary electrode is negligible and hence has no influence at the process at the working electrode [196].

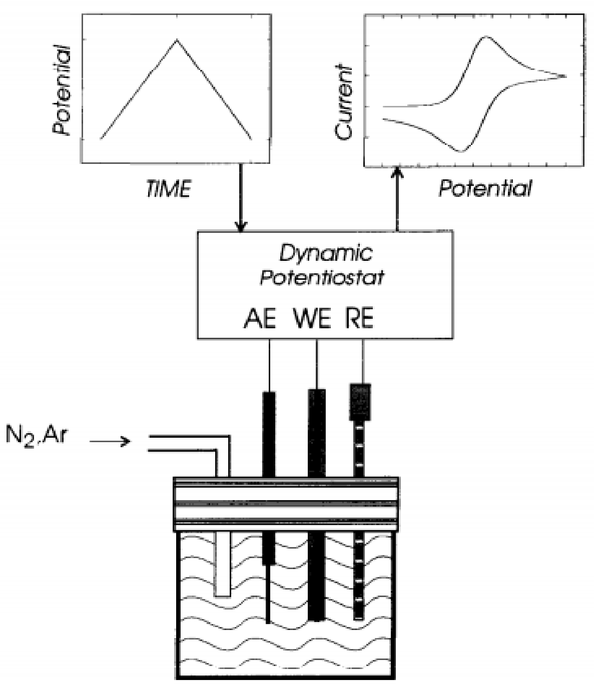

Figure 3.19: An overall view of the CV experiment [196].

A plot of the current sweep rate is plotted against the voltage to show its cyclic voltammetry [9], [10], [196]. For a two-electrode system, the CV curve obtained is the electrochemical information of the working electrode without any contribution form the reference electrode while the three electrode configuration is the overall electrochemical contribution of both electrodes.

An ideal capacitor would display a rectangular shape as represented in Figure 3.20 due to zero or no resistance, a carbon material electrode electrochemical capacitor forms the shape of a parallelogram with variable because of its non-faradaic process. The influence of redox reaction behavior results to prominent peaks appearing within narrow voltage windows [60].

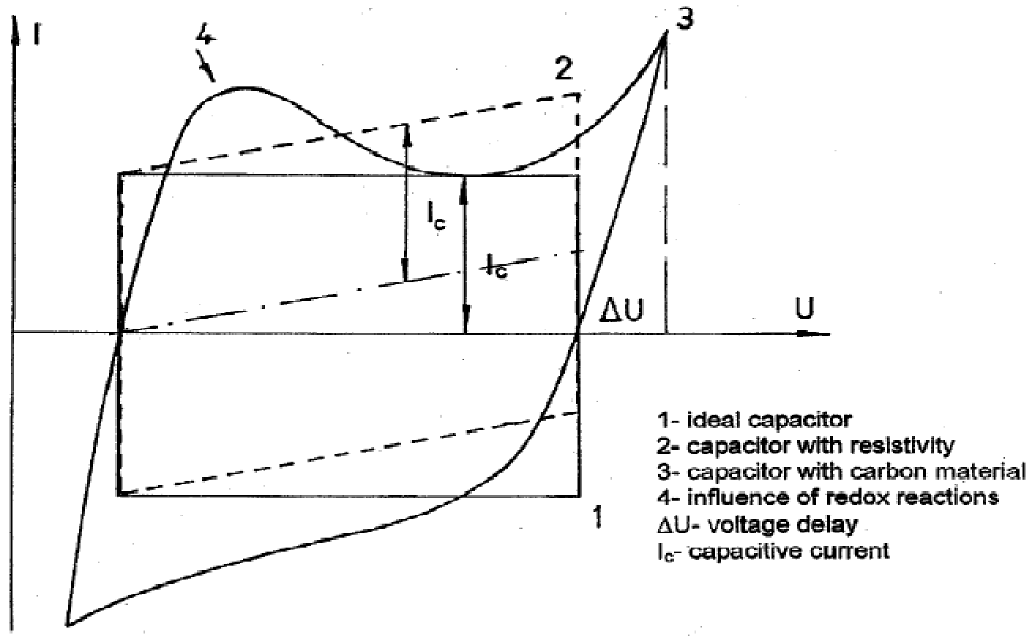

Figure 3.20: Conventional CV curves of various electrochemical capacitors [60].

The specific capacitance (C_s) which is the capacitance per unit mass for one electrode can be calculated from the data from the CV curve using equation 3.17.

$$C_s = C/m \tag{3.17}$$

where C = capacitance in Farad and m = mass of the electrode in grams. Furthermore, capacitance C can be express in relation to charge current (I) and constant sweep rate (dV/dt) stated in equation 3.18 as

$$C = I / (dV/dt) \tag{3.18}$$

For a symmetrical two-electrode cell, the capacitance measured is said to be expressed as two capacitance connected in series (equation 3.19) because $C_1 = C_2$.

$$1/C = 1/C_1 + 1/C_2 \tag{3.19}$$

Therefore equation 3.17 can then be equated to equation 3.20

$$C_s\ (\mathrm{F/g}) = 2 \times C/m \tag{3.20}$$

The factor of 2 converts the capacitance and combined mass of the two-electrode cell to the capacitance and mass of a single electrode [9], [10].

3.5.1.1 Sample measurement

All CV measurements of the electrodes weighing about 1mg were carried out in a typical two-electrode cell with two symmetrical electrodes on a Metrohm Autolab (PGSTAT302F) electrochemical workstation (Figure 3.21).

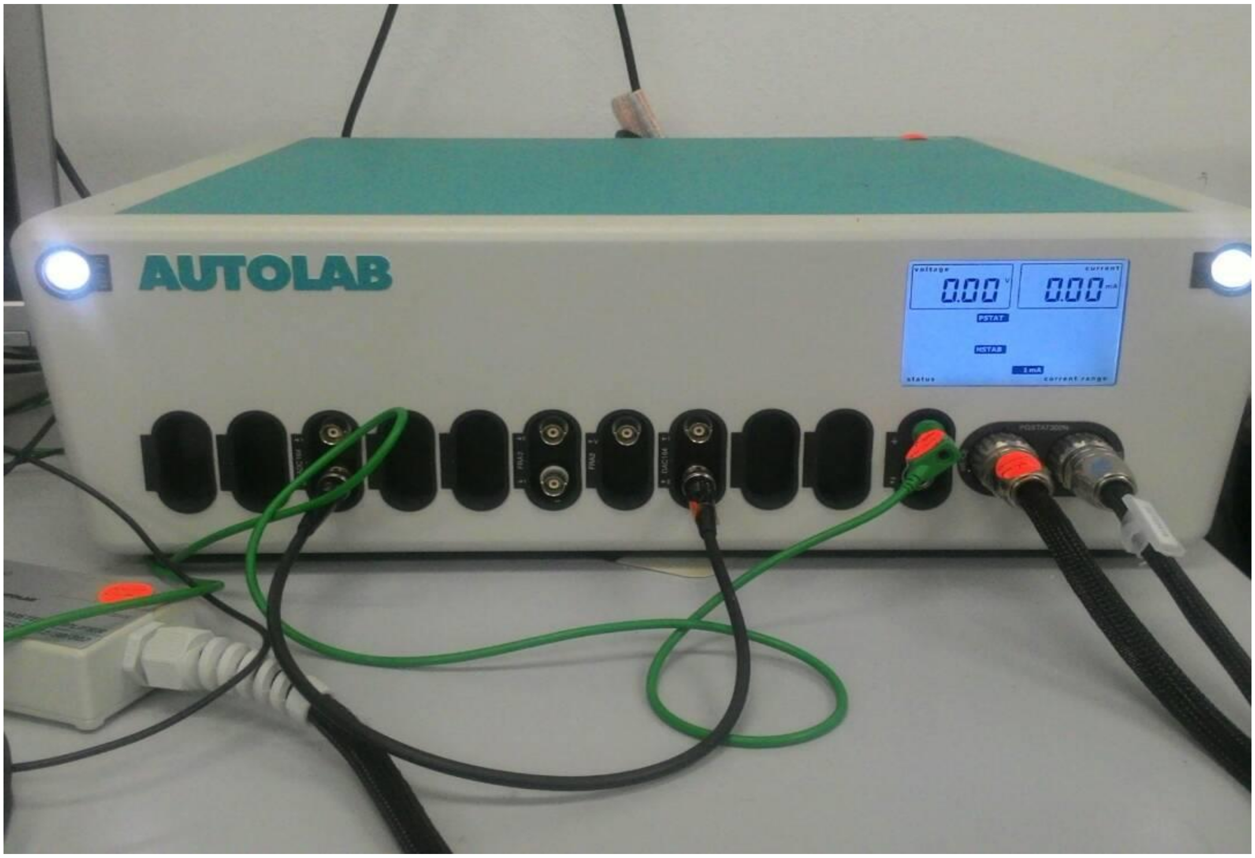

Figure 3.21: Metrohm Autolab (PGSTAT302F) electrochemical workstation used for the CV analysis in this project.

3.5.2 Galvanostatic charge/discharge analysis (GCD)

The charge/discharge analysis is a reliable approach in determining the electrochemical performance of an electrode under practical operating conditions. Properties of the electrochemical capacitor obtained through this evaluation method include its stability, equivalent series resistance, capacitance, energy and power densities. The two electrode or three cell configuration (Figure 3.18) can be used for charge/discharge characterisation [9], [10], [197].

In principle, GCD is performed by applying a series of charging and discharging currents into the electrochemical capacitor and measuring the voltage response between minimal and maximal values [9], [10]. The results of Galvanostatic charge-discharge analysis is displayed on a plot of voltage (V) against time (s). Figure 3.22 shows a typical curve of GCD process, the labeled part of the curve details:

(1) The cell behaviour during charging;

(2) The cell behaviour during discharging;

(3) The initial process;

(4) This section is responsible for the negative resistive ohmic lost associated with the resistance of the cell.

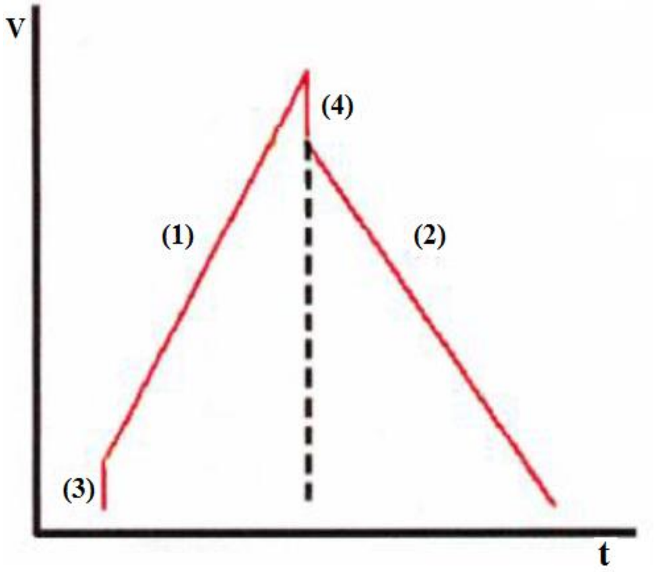

Figure 3.22: The typical curve of a galvanostatic charge/discharge process [10].

Using equation 3.17, specific capacitance (C_s) can also be calculated from the galvanostatic charge/discharge curve. However, C is calculated from the galvanostatic discharge curves using equation 3.21 with *I* the discharge current and (dV/dt) is obtained from the slope of the discharge curve.

$$C = I/(dV/dt) \tag{3.21}$$

For a two-electrode, the measured capacitance is multiplied by 4 to adjust the cell capacitance and the combined mass of two electrodes to the capacitance and mass of a single electrode leading to equation 3.22

$$C_s = 4 \times C/m \tag{3.22}$$

The charge/discharge analysis can be used to measure the degradation of electrochemical capacitor. This is achieved by subjecting the electrochemical capacitor to charge and discharge over many cycles (one cycle equals one charge and discharge) and then observe the changes in both specific capacitance and/or equivalent series resistance between the initial and the last cycle [9], [10], [195].

3.5.2.1 Sample measurement

Galvanostatic charge/discharge (GCD) was performed on an Arbin Instrument model BT-2000 (Figure 3.23) using the same assembled and configured cell as stated in section 3.3.7. Different current densities were applied to the EC and the response observed between the voltage range of 0 – 1 V over the course of the project.

Figure 3.23: Arbin Instrument model BT-2000 used for Galvanostatic charge-discharge analysis.

3.5.3 Electrochemical Impedance Spectroscopy (EIS)

Electrochemical impedance spectroscopy is a great technique for studying the electrode-electrolyte properties of conductive electrodes of materials over various fields [10], [182]. For electrochemical capacitors, its electrical and kinetic response is determined over a wide range of frequencies thereby providing information on its capacitance and equivalent series resistances [9], [10].

The theory of using EIS involves applying small of current signals or amplitude sinusoidal voltage to the electrodes and measuring the response in magnitude and phase over a range of frequencies, commonly 0.01 Hz to 100 kHz or more demandingly, 1 mHz to 1 MHz. This response is represented as impedance and defined as a vector of the ratio of the amplitude and phase between the voltage (V) and current (I) as detailed in (Eq 3.23):

$$Z\,(j\omega) = \frac{V(j\omega)}{I(j\omega)} \qquad \text{(Eq 3.23)}$$

where $\omega = 2\pi f$ and $j = \sqrt{-1}$.

The total impedance can be expressed as a function of its real (Z') and imaginary (Z") components (Eq 3.24 – 3.26):

$$Z\,(j\omega) = Z'(\omega) + jZ''(\omega) \qquad \text{(Eq 3.24)}$$

$$Z' = R_B \qquad \text{(Eq 3.25)}$$

$$Z'' = \frac{1}{\omega C_B} \qquad \text{(Eq 3.26)}$$

where R_B = series equivalent resistance of the cell and C_B = the series equivalent capacitance of the cell. The relationship between the real and imaginary components for different values of ω is presented on a complex plane plot knows as the Nyquist plot [3], [9], [10], [144], [182].

The Nyquist plot basically plots the imaginary part of the impedance against its real part. The EIS data is analysed using Nyquist plots and each data point is at a different frequency. The Nyquist plot consists of two frequency regions, a high frequency region denoted by a semicircle which represents the transfer of charges occurring at the electrode/electrolyte interface and the low frequency region signified by a straight line representing the diffusion of ions in the electrolyte [3], [9], [10], [144], [182], [198]. Figure 3.24 shows a typical Nyquist plot representation; the interception of the plot at the Zreal axis specifics the solution Rs or equivalent series resistance (R_B) of the electrochemical capacitor (EC) which defines the rate at which the EC is charged or discharged [98], [199]. The diameter of the semi circles denotes the charge transfer resistance R_{ct} of the EC and the slope of the low frequency region (45^o) of the plot is termed the Warburg resistance [9], [199].

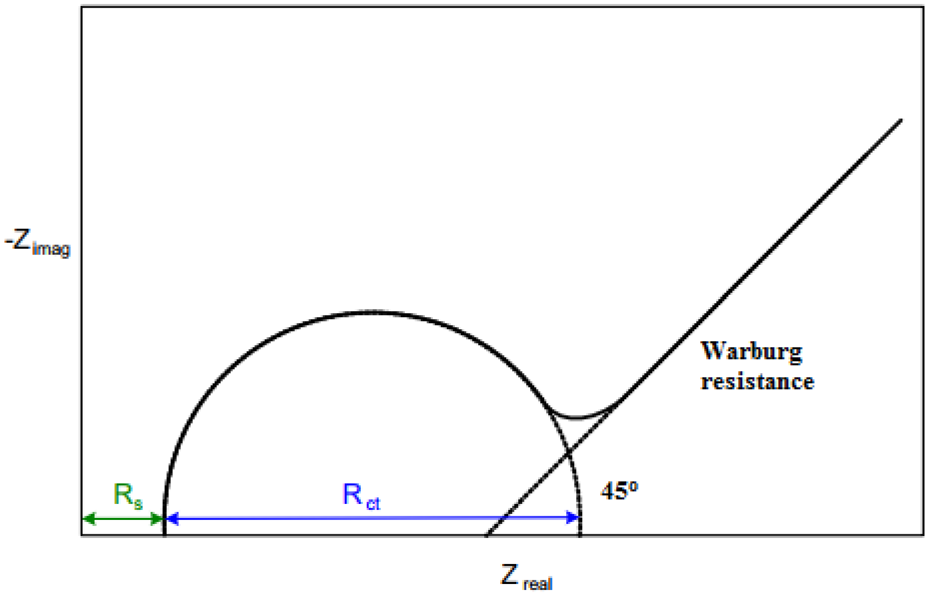

Figure 3.24: The respective resistances of an electrochemical electrode illustrated in a typical Nyquist plot.

3.5.3.1 Sample Preparation

Electrochemical impedance spectroscopy (EIS) was performed using Metrohm Autolab (PGSTAT302F) electrochemical workstation on the same assembled and configured cell as stated in section 3.3.7. The frequency response of the EC was carried out in a frequency range from 100 kHz to 0.01 Hz.

3.5.4 Specific energy and specific power

Specific energy and specific power are essential parameters in evaluating the performance of an electrochemical capacitor. Specific energy is defined as the capacity to perform work can be expressed in the relationship between specific capacitance C_s and cell voltage (V) in equation 3.27.

$$E_{max} = \frac{C_S V^2}{2} \tag{3.27}$$

Specific power is seen as the rate at which energy is delivered, it is based on the association between equivalent series resistance (R_B), and the cell voltage presented in equation 3.28

$$P_{max} = \frac{1}{4} \frac{V^2}{R_B} \tag{3.28}$$

Several fundamental studies on electrochemical capacitors have presented equation 3.29, equation 3.30 to calculating average energy density (E) in Wh/kg and power density (P) in W/kg with relationship based on the specific capacitance (C_s), Δt the discharge time in seconds and V is the potential window of discharge in volts.

$$E = \frac{1000\, Cs\, \nabla\, V^2}{2 \times 3600} \tag{3.29}$$

$$P = \frac{E}{\Delta t} \tag{3.30}$$

The results of the energy and power densities of an electrochemical capacitor can be presented in graphical relations called Ragone plot.

3.6 Chapter Summary

In this chapter, the elementary working principles and characterisation techniques used in studying the quality of as-synthesised graphene-metal oxide composites and its performance as an electrochemical capacitor were discussed in detail. The methods discussed are X-ray diffraction (XRD), field emission scanning electron microscopy (FESEM), energy-dispersive X-ray spectroscopy (EDS), transmission electron microscopy (TEM), Raman spectroscopy, cyclic voltammetry (CV) and galvanostatic charge/discharge. The sample preparation methods used in the different characterisation routes were also presented in the chapter for future reference. In the next chapter, graphene/zinc oxide nanocomposites will be prepared and the purity of the composites along with its application as an electrochemical capacitor would be discussed in aspect.

Chapter 4

One-Step Green Synthesis of Graphene-ZnO Nanocomposites for Electrochemical Capacitors

4.1 Overview

Much research and development have been carried out to improve the overall performance of electrochemical capacitors as energy storage materials. As discussed in Chapter 2, the introduction of graphene and metal oxide composites has demonstrated a better energy density, power density and capacitance for supercapacitors [11], [42], [200]. The synergetic effect between the metal oxide and graphene clearly indicates that metal oxides play the roles of spaces to expand the surface area of graphene and improves capacitance as a result of the redox reaction while graphene reduces the resistance by providing a conductive pathway for the easy diffusion of ions and movement of electrons [11]. Among the many metal oxides available, zinc oxide (ZnO) has attracted much attention as a promising electrode material for supercapacitors due to its low cost, abundant availability, environmental friendly nature and electrochemical activity [201]. ZnO is a battery active material which attains an energy density of 650 A/g. It has a large exciton binding energy (60 meV) and a wide band-gap (3.37 eV) [14–16]. In addition, it has strong emission of light at room temperature and it is transparent in nature [203].

In view of the outstanding individual properties of graphene and ZnO as electrode materials, the combination of graphene with ZnO nanocomposites as electrodes may result in improved supercapacitor performance. Several methods employed in preparing graphene-ZnO nanocomposites for supercapacitors have been reported. Lu et al [205] prepared graphene-ZnO nanocomposites via a microwave-assisted system, where the composite compound exhibited an improved electrochemical capacitance of 146 F/g at a scan rate of 2 mV/s. Li et al [206] reported a hydrothermal technique to grow ZnO nanorods that were distributed homogeneously on the graphene nanosheets. The nanocomposite materials were found to possess a specific capacitance of 156 F/g at a scan rate of 5 mV/s. Zhang et al [207] synthesised graphene-ZnO nanocomposites films for supercapacitors application by depositing ZnO on graphene by ultrasonic spray pyrolysis (USP). They reported that graphene/ZnO nanocomposites had demonstrated a better reversible capacitive process than graphene material alone. Wang et al [200] reported a successful synthesis of graphene nanosheets/ZnO nanocomposites prepared by an in situ crystallization method which displayed an improved capacitance of 62 F/g at a current density of 5 mA/cm^2. However, most of these studies had utilised graphene nanomaterials synthesised via the modified Hummers method, followed by chemical reduction producing the reduced graphene oxide (rGO).

This chapter reports the results of a composite synthesis method which incorporates a simple and green method of synthesising graphene-ZnO nanocomposite using facile solvent exfoliation and low temperature solvothermal processing approaches discussed in section 3.3.2.

4.1 Structural and morphological characterisation

The XRD patterns of the prepared graphene-ZnO nanocomposites, graphite and zinc oxide are shown in Figure 4.1. It can be seen that the ZnO XRD patterns of the nanocomposites with different mass ratios are similar to that of pure zinc oxide, indicating that no other impurity peaks were detected. It can be readily assigned to pure ZnO with hexagonal structure (ICSD No. 98-002-7781) with lattice constants a = b = 3.2540 Å, c = 5.2150 Å. The peaks at 2θ values of 32.0, 34.6, 36.5, 47.7, 56.8, 63.0, 66.6 and 68.1^o can be indexed to (102), (100), (012), (01-2), (014), (2-21), (201) and (2-23) crystal planes, respectively. This clearly indicated that ZnO nanoparticles were formed from the precursor. In addition, with the increase in mass loading of ZnO nanoparticles, the increase in intensities of the respective diffraction peaks of the composites were also observed. The two diffraction peaks of graphite at 2θ values of 26.8 and 54.9^o are attributed to the (002) and (1-20) reflections of graphite (ICSD No. 98-005-2916), and these diffraction maximums were clearly observed for the graphene-ZnO nanocomposites. These results indicate that the crystalline structure of the graphene material was intact and its pristine nature was preserved.

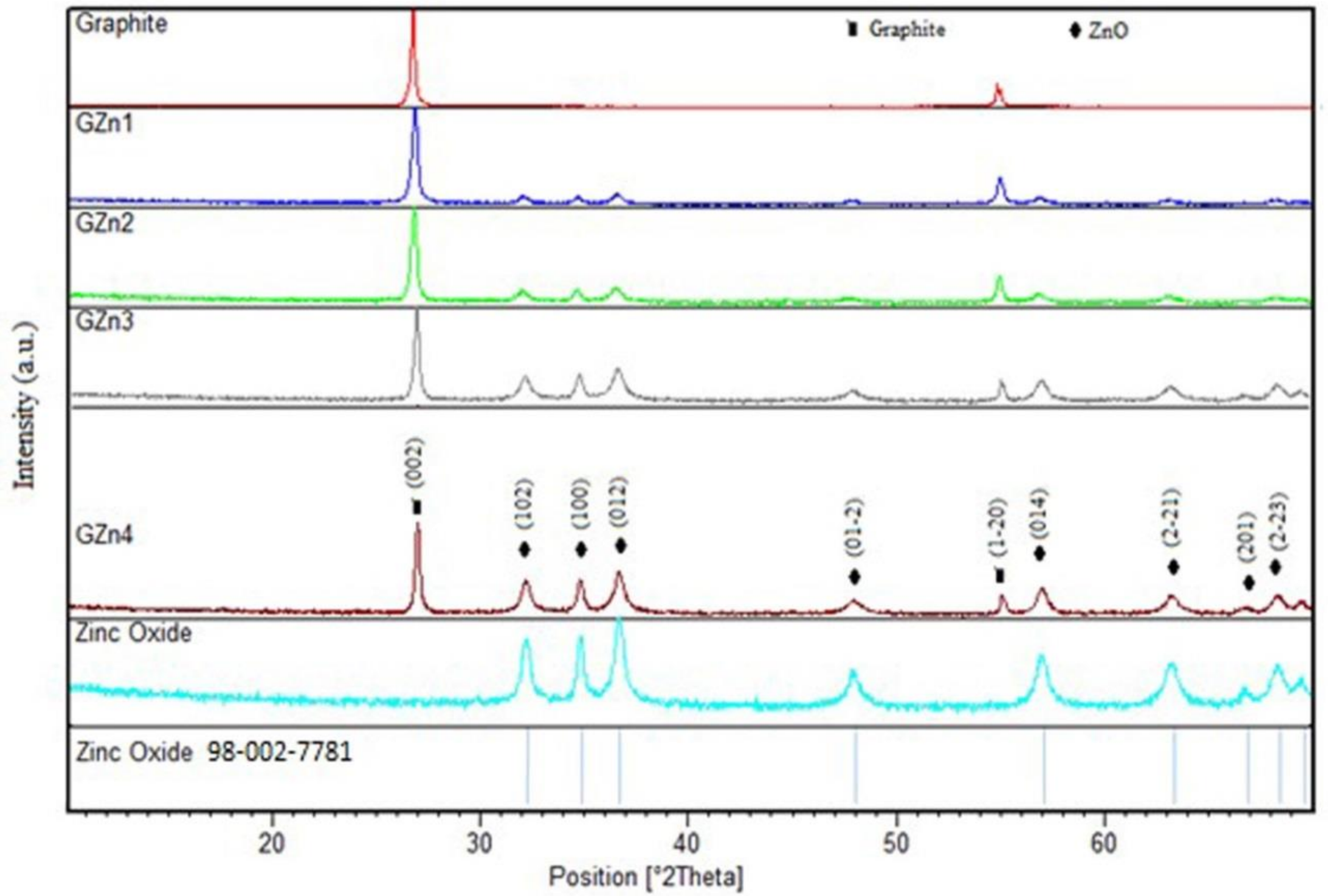

Figure 4.1: XRD patterns of graphite, zinc oxide and graphene-ZnO nanocomposite.

The Raman spectra of graphene and graphene/ZnO nanocomposites respectively are shown in Figure 4.2. Three distinct peaks are associated with the graphene Raman spectra; namely the G band at ~1580 cm^{-1} which corresponds to the in-plane vibration of sp^2 carbon atoms, the 2D band at ~2719 cm^{-1} and the D band at ~1351 cm^{-1} ascribed to the first-order zone boundary phonons, which is absent from defect-free graphene [208]. However, the formation of new edges which can be seen as defects from the exfoliated sheets due to the exfoliation process of graphene from graphite leads to the existences of a D peak [45], [188], [209]. After the hydrothermal treatment, four peaks indicated as 'X' in the graphene/ZnO spectrum belongs to ZnO. The peak at ~432 cm^{-1} agrees with the finger signal of the characteristic E_2 mode of ZnO wurtzite structure [210], while the peaks at ~327 cm^{-1} and ~568 cm^{-1} are well indexed to the transversal optical modes with A_1 symmetry and the longitudinal optical modes. The broad peak at ~1127 cm^{-1} corresponds to 2A1 (LO), 2E1(LO) and 2LO mode of ZnO [208], [210]. The D-band, G-band and 2D-band were located at ~1349 cm^{-1}, ~1574 cm^{-1} and ~2717 cm^{-1}; the shift of the bands are likely due to the doping effects of ZnO [16]. The Raman spectrum after the hydrothermal treatment confirms that the structure of graphene was not destroyed and the graphene/ZnO nanocomposites were formed, which is in good agreement with the XRD results (Figure 4.1).

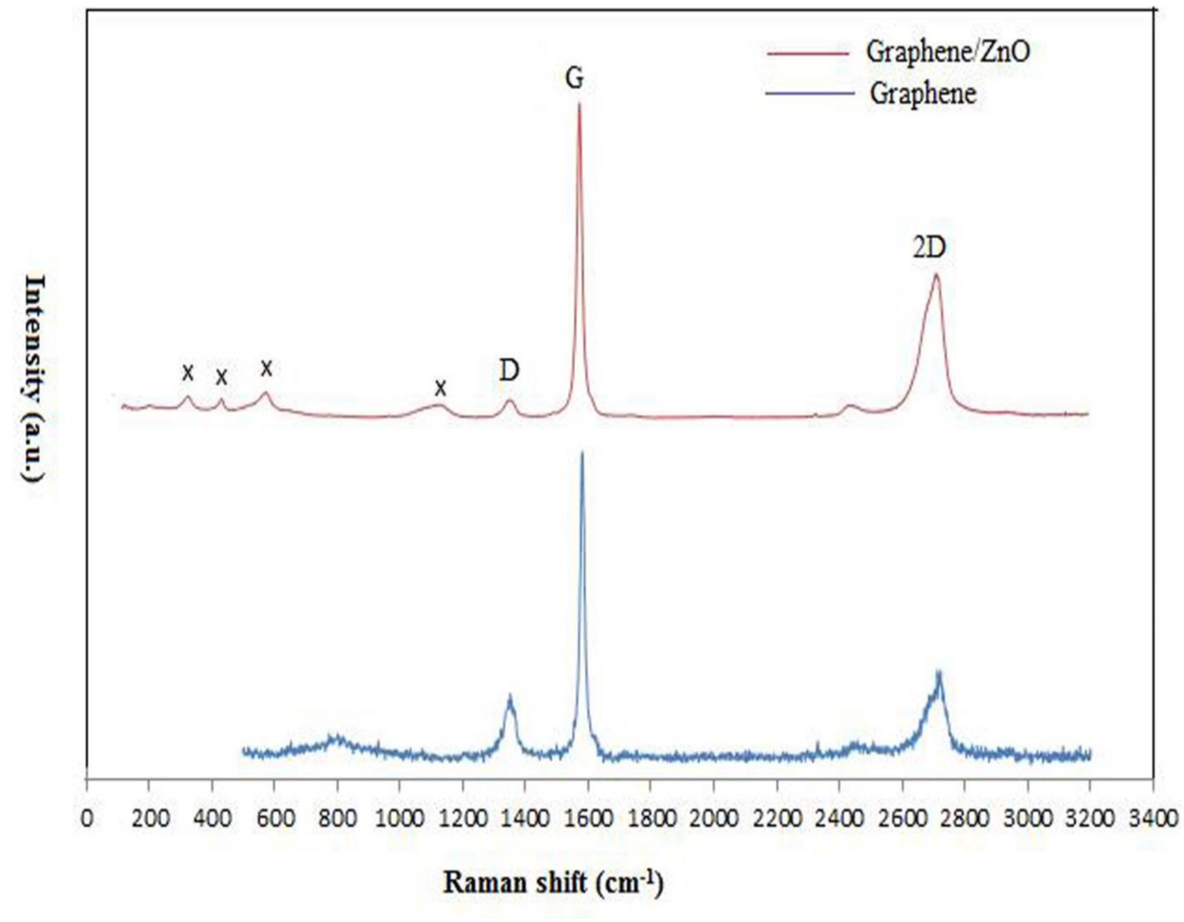

Figure 4.2: Raman spectra of graphene and graphene-ZnO nanocomposites.

Figure 4.3 (a-d) shows the FESEM images of graphene-ZnO nanocomposites synthesised from different precursor mass ratios. The ZnO nanoparticles formed on the graphene sheets were found to be of spherical to globular structures with diameter around 1500 nm for GZn1 and GZn2 (Figure 4.3(a-b)) and 200 nm for GZn3 and GZn4 (Figure 4.3(c-d)) respectively. The results illustrated that with an increase in the loading mass of Zn precursor, more ZnO nanoparticles will be formed on the surface and edges of the graphene sheets. It was also observed that in GZn1 and GZn2, the ZnO nanoparticles were not uniformly spread on the graphene surface. On the other hand, heavy clusters (agglomerated form) of ZnO nanoparticles were found on the graphene surface of GZn4, and these aggregates tend to form non-conducting layers that can affect its charge storage property [211]. Figure 4.3c shows that a uniform and homogenous spread of ZnO nanoparticles were anchored well on the edges and surface of the graphene sheet. The evidence of the formation of ZnO nanoparticles deposited on the surface of graphene is supplemented by images provided by TEM analysis (Figure 4.3(e-f)). The TEM results display the two dimensional structure of graphene and a well spread graphene sheet decorated with ZnO nanoparticles. Figure 4.3f illustrates that the ZnO nanoparticles were quasi-spherical in shape and are well deposited on the inside interlayer of the graphene sheet. No free ZnO nanoparticles were observed outside the graphene sheet.

The chemical composition of the composites were analysed by an energy dispersive spectroscopy (EDS). The peaks of C, O, Zn in the EDS spectrum depict the presence of carbon, oxygen and zinc compounds only, therefore confirming the purity of the composites material (Figure 4.3g). The peak corresponding to Si seen in the EDS spectrum is due to the silicon su0bstrate used for the characterization.

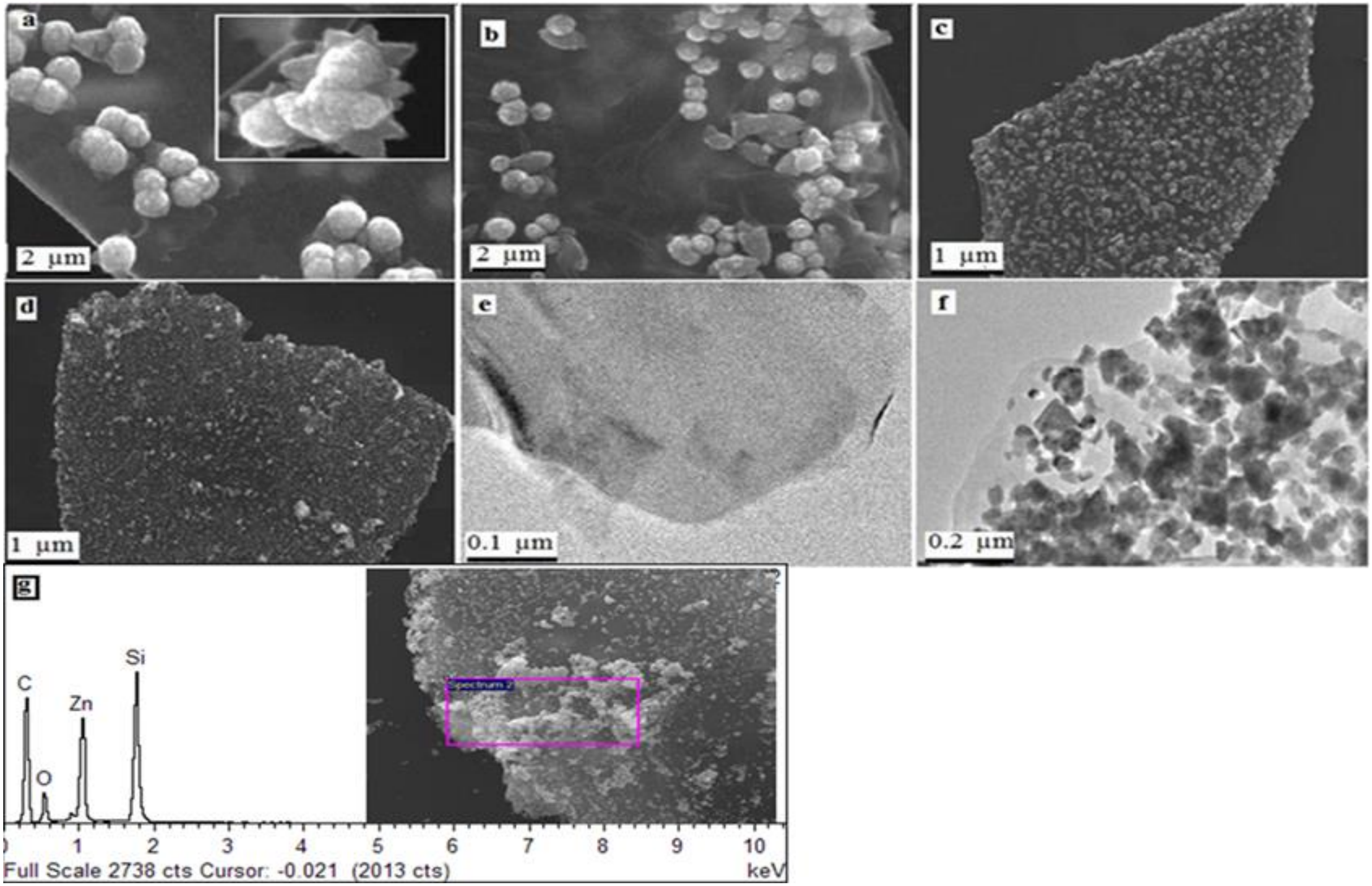

Figure 4.3: FESEM images at different magnifications of (a) GZn1, (b) GZn2, (c) GZn3, (d) GZn4, TEM images of (e) graphene (f) GZn3 (g) the EDS spectrum and its corresponding SEM image of GZn3.

4.2. Electrochemical performance

The cyclic voltammograms (CV) tests were studied in a two-electrode configuration in 1 M KOH using a VersaSTAT 3 (VE-400) electrochemical working station driven by the V3 studio version 1.0286 software within a potential range of -0.1 to 0.5 V at different scan rates varying from 5 to 100 mV/s. Figure 4.4a compares the CV curves of graphene, GZn1, GZn2, GZn3 and GZn4 at a scan rate of 10 mV/s. It can be seen that all the CV curves exhibited a nearly rectangular shape along the current – potential axis indicating good capacitive performance. In comparison to the graphene electrode, the graphene-ZnO composites electrode showed higher integrated area on the current- potential axis, disclosing better charge storage performance. This clearly indicates that the addition of ZnO increases the total capacitance of the electrode. The specific capacitances (Cs) were calculated from the CV curves using equation 3.20.

The calculated C_s values for these electrochemical capacitors were:- 236 F/g (GZn3) > 230 F/g (GZn2) > 188 (GZn4) > 185 (GZn1) > 100 F/g (graphene) at a scan rate of 10 mV/s. From the calculated results, it is noticed that the increase in mass loading of ZnO nanoparticles was not proportional to the improvement in C_s of the electrochemical capacitors. Sample GZn4 demonstrated lower specific capacitance as compared to GZn3 and GZn2, which can be attributed to excess agglomerations of ZnO nanoparticles on the graphene surface (Figure 4.3d). The particle aggregation tends to form non-conducting layers that can increase its intrinsic resistivity and deteriorate the charge storage capacity. In addition, these non-conducting layers on the graphene surface reduces the amount of surface area accessible to the electrolyte ions thereby limiting its capacitive performance [211]. The CV analyses on GZn3 at various scan rates were performed in order to obtain further information on its capacitive performance (Figure 4.4b). The CV curves for the composite material exhibited a nearly rectangular shape within a potential window of -0.1V to 0.5V signifying good capacitive performance. Generally, it was noticed that an increase scan rate produced an increase in integrated area on the current-potential axis, indicating good storage rate ability, which is similar to previous work reported [206], [212], [213]. Nevertheless, as clearly indicated in Figure 4.4c, a decrease in specific capacitance with increase in scan rate is observed instead. At a scan rate of 5 mV/s, a specific capacitance of 246 F/g was achieved while at higher scan rate of 100 mV/s the recorded specific capacitance was significantly reduced to 112 F/g. The results clearly implies that lower scan rates generally is more favorable, since it allows adequate time for ion adsorption and diffusion within the intrinsic pore structures of the active material, leading to a higher charge storage capacity [213].

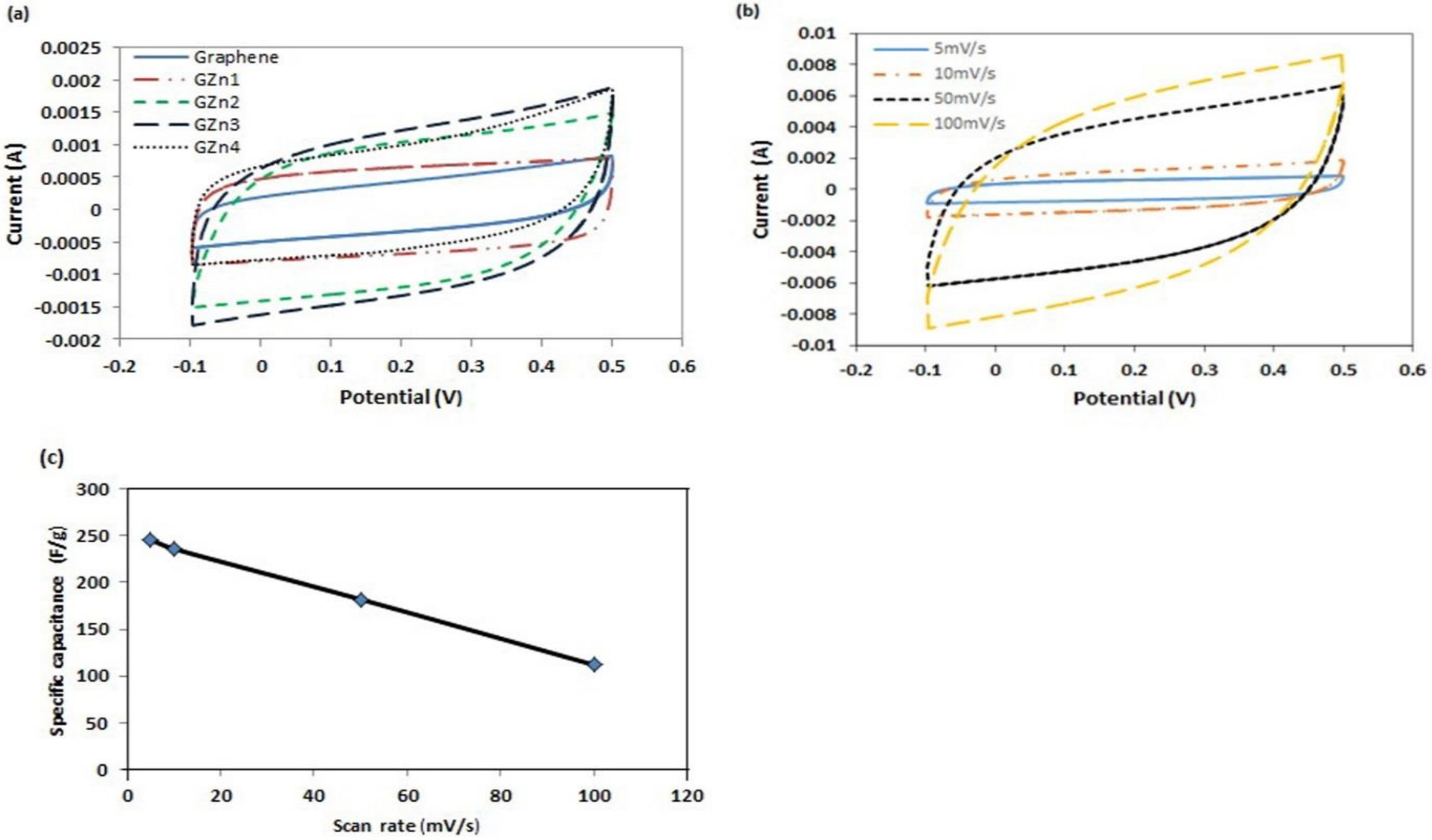

Figure 4.4: Cyclic voltammograms (CV) curves of (a) GZn1, GZn2, GZn3, GZn4 and graphene at a scan rate of 10mV/s (b) GZn3 at different scan rates in the range of 5-100 mV/s (c) variation of specific capacitance of GZn3 at different scan rates.

The long cycling life is an important requirement for practical applications of supercapacitors [206]. A cycling life test of graphene-ZnO composite electrode (GZn3) was carried out by repeating the CV measurements between -0.1 to 0.5 V at a scan rate of 50 mV/s for 200 cycles. As shown in Figure 4.5a, the respective CV curves retained their quasi-rectangular shapes throughout the whole cycling test. Furthermore, it was observed that more than 90% of its initial specific capacitance was retained after 200 cycles (Figure 4.4b), indicating good electrochemical stability during cycling and clearly implies its potential practical usage in various applications.

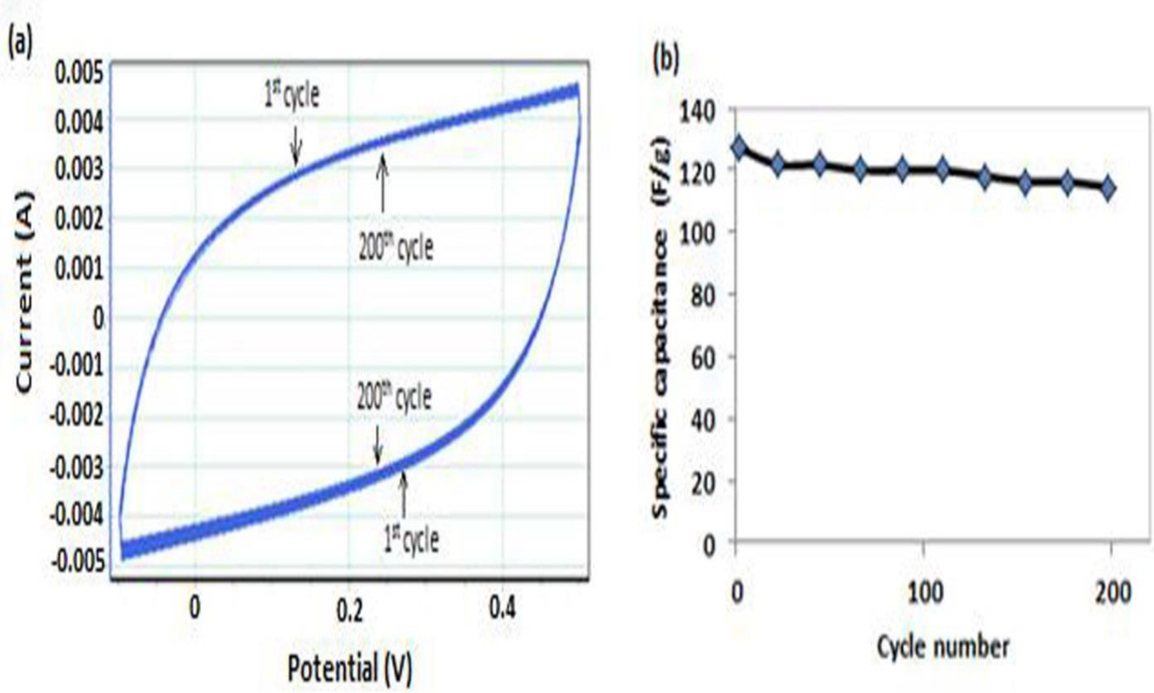

Figure 4.5: Cyclic Voltammograms (CV) curves of (a) GZn3 at a scan rate of 50 mV/s for 200 cycles (b) Cyclic performance of GZn3 electrode along the 200 cycles.

The galvanostatic charge-discharge tests were performed by applying a series of charging and discharge currents onto the electrochemical capacitors and measuring the voltage response. The voltage response of graphene, GZn1, GZn2, GZn3 and GZn4 electrodes were studied at a constant current density of 10 mA/g. The energy loss due to internal or equivalent series resistance is shown by the IR drop at the turning point of the charge and discharge curves, as seen in Figure 4.6a [198]. From these results, GZn3 sample has the least voltage drop of 0.2 V, thereby having the highest capacitance when evaluated with respect to their individual mass. These findings supports the results of the calculated specific capacitances obtained from the CV curves earlier (Figure 4.4). Figure 4.6b shows the representative galvanostatic charge-discharge measurements of the GZn3 electrode at different current densities of 1, 2, 3, 5 and 10 mA/g under an applied potential between 0 and 1 V. The charge-discharge curves of the GZn3 electrode exhibits near linear and symmetric triangles, indicating good capacitive performance and excellent reversibility [178], [214]. The IR drops on all the curves are negligible, implying low resistance and good contact between the collectors and the electrode material. The discharge curves were not straight lines suggesting that the capacitance includes the double-layer and redox capacitance [178]. The specific capacitance of graphene, GZn1, GZn2, GZn3 and GZn4 at different current densities were compared as shown in Figure 4.6c. It can be observed that with increase of current densities from 1 to 10 mA/g, there is a corresponding decrease in specific capacitance of the electrode materials. This could be explained by the discrepant insertion-desertion behaviour of ions from electrolyte to electrode material. The rending ions (OH^-) fail to fully occupy the sites at the electrolyte/electrode interface if compared to lower current density because of ions' limited migration velocity and fixed route in the interface thereby leading to an uncompleted insertion reaction [32]. GZn3 electrode exhibited a drop of 20.8% from its initial capacitance value as the current density increased from 1 to 10 mA/g compared to GZn2, GZn4, GZn1 and graphene which had a drop of 22.7%, 27%, 29% and 60% capacitance values respectively. In order to further evaluate the cycling stability of GZn3 electrode, galvanostatic charge-discharge analysis was performed at a constant current density of 10 mA/g between 0 to 1 V for consecutive 1000 cycles. As displayed in Figure 4.6d, the specific capacitance of GZn3 electrode retains 83% of its initial capacitance value, reflecting good electrochemical stability and reversibility upon repetitive charge-discharge process [214].

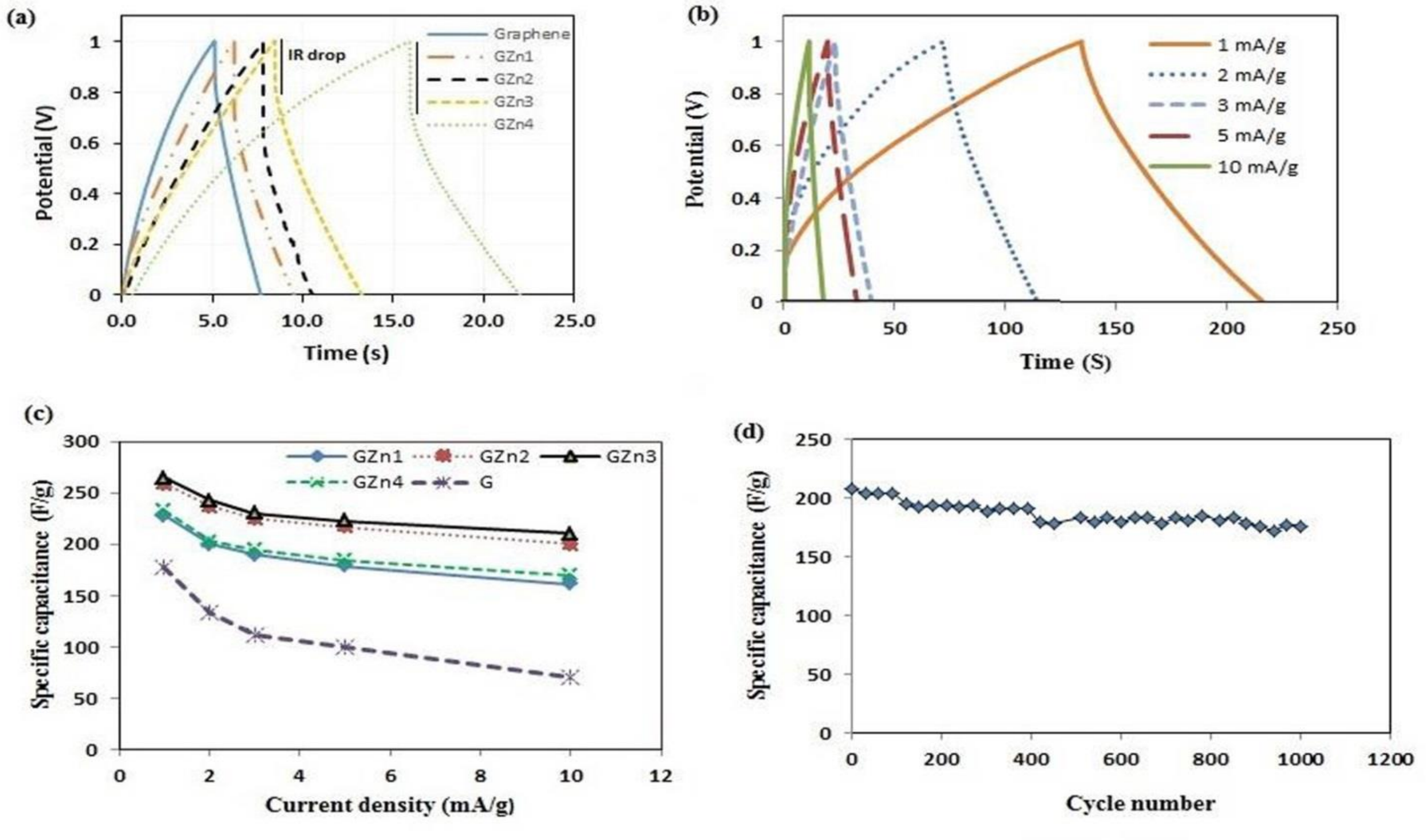

Figure 4.6: Charge-discharge curves of (a) graphene, GZn1, GZn2, GZn3 and GZn4 (b) for GZn3 at a current density of 10mA (b) charge-discharge curves of GZn3 at different current densities (1, 2, 3, 5 and 10 mA/g) (c) Plots of specific capacitance of graphene.

Electrochemical impedance spectroscopy (EIS) measurements are very essential in assessing the resistive characteristics of the electrode. It shows the response of components performance in the frequency domain [198]. EIS were carried out in a frequency range from 100 kHz to 0.01 Hz in order to evaluate the frequency response of both graphene and graphene/ZnO nanocomposites. The Nyquist plots for the electrodes are depicted in Figure 4.7. The EIS data was analysed using Nyquist plots and each data point is at a different frequency. The Nyquist plots consists of two frequency regions, a high frequency region denoted by a semicircle which represents the transfer of charges occurring at the electrode/electrolyte interface and the low frequency region signified by a straight line representing the diffusion of ions in the electrolyte. The equivalent series resistance (ESR) can be obtained from the x-intercept of the Nyquist plot and the charge transfer resistance R_{ct} can be directly measured as the diameter of the semicircle arc on the real axis [31], [198], [200]. The ESR and charge transfer resistance R_{ct} obtained from the Nyquist plot (Figure 4.7) are depicted in Table 4.1.

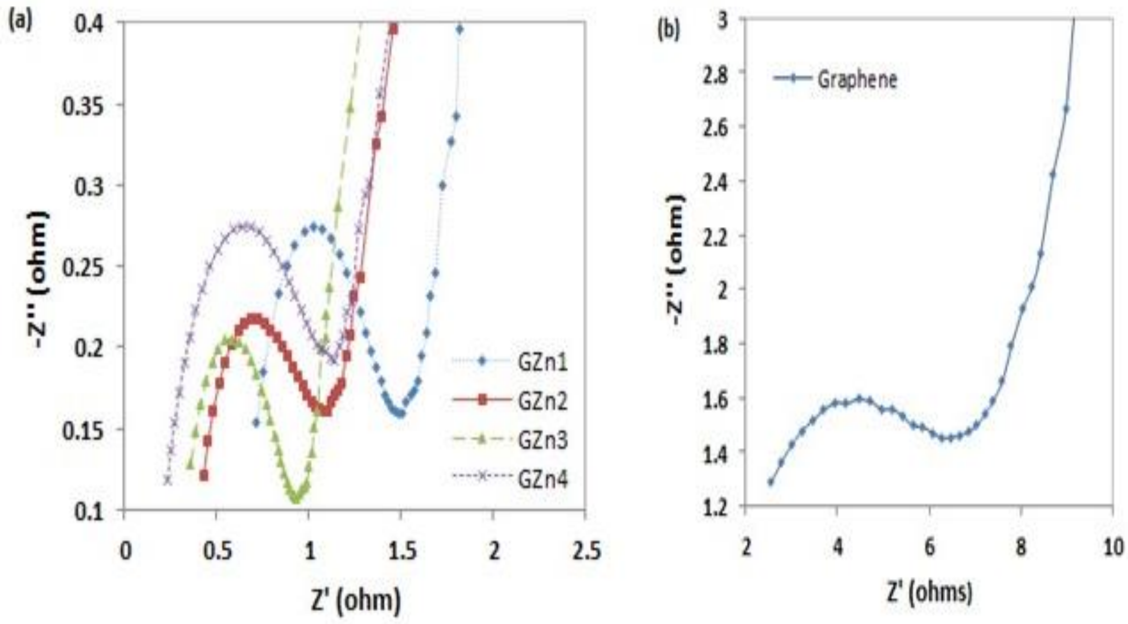

Figure 4.7: Nyquist plots for (a) GZn1, GZn2, GZn3, GZn4 (b) graphene over the frequency range of 100 kHz to 0.01 Hz in 1 M KOH.

The ESR and R_{ct} values of the electrochemical capacitors decreases in the order of graphene > GZn1 > GZn2 > GZn4 > GZn3 which is indirectly proportional to results of the specific capacitance, specifically, the higher the R_{ct} value, the lower the specific capacitance of the electrochemical capacitor [215]. Graphene having the highest ESR and R_{ct} values affirms that the addition of ZnO to graphene results in an improved charge transfer performance. From Table 4.1, GZn3 electrochemical capacitor has the smallest ESR and this could be due to the fact that the graphene/ZnO hybrid facilitates the highest accessibility of ions into the surface of graphene sheets made possible by the uniform dispersion of ZnO particles on the graphene surface, as evidenced in the SEM analysis (Figure 4.3c).

The average energy density (E) and power density (P) of the electrochemical capacitors were calculated using the following equations [206].

$$\mathrm{E} = \frac{1000\, Cs\, \nabla\, V^2}{2 \times 3600} \qquad (4.1)$$

$$\mathrm{P} = \frac{E \times 3600}{\Delta t} \qquad (4.2)$$

where E is the energy density of the electrode (Wh/kg), P is the power density (kW/kg), C_s is the specific capacitance of the electrochemical capacitor (F/g), Δt in seconds is the time for a sweep segment and ΔV is the voltage range for one sweep segment. The calculated average energy and power densities are tabulated in Table 4.1.

Table 4.1: Electrochemical performance of graphene and graphene/ZnO composite electrodes.

Samples	ESR (Ω)	R_{ct}(Ω)	Specific capacitance (F/g)	Energy density (Wh/kg)	Power density (kW/kg)
Graphene	4.34	2.31	100	5.00	18
GZn1	1.49	0.77	185	9.24	33.26
GZn2	1.04	0.61	230	11.52	41.47
GZn3	0.94	0.59	236	11.80	42.48
GZn4	1.14	0.91	188	9.40	33.84

On the basis of the results provided by Table 4.1, the graphene/ZnO nanocomposites electrodes showed a higher specific capacitance, improved charge transfer performance and a significantly enhanced energy and power densities when compared to the graphene electrode. The resulting specific capacitance of the graphene/ZnO nanocomposites is significantly higher than previous work reported on graphene/ZnO based supercapacitor

[200], [205], [206], [213]. The improved electrochemical performance of graphene/ZnO electrodes can be attributed to the following aspects: (i) the pristine nature of the synthesized graphene which improves the electrical conductivity of the hybrid structure. (ii) The electroactive property of ZnO nanoparticles anchored to the graphene sheets provides a three dimensional conductive system which provides more active sites for the formation of electric double layer. This distinctive system also aids the easy diffusion of ions into the inner channels hereby reducing diffusion resistance, similar to those reported in previous studies [211]. (iii) The pseudo-capacitance from the ZnO nanoparticles combined with the double-layer capacitance from graphene provides a higher specific capacitance [207], [216].

4.3 Chapter Summary

In summary, graphene/ZnO nanocomposites as an electrode for electrochemical capacitors was successfully synthesized from highly pyrolytic graphite via a green, facile, effective and scalable solvothermal technique. The structural analysis and electrochemical properties of graphene/ZnO nanoparticles have been studied comprehensively. In comparison with the pristine graphene electrode, the graphene/ZnO nanocomposite electrodes demonstrated an improved electrochemical performance. The graphene/ZnO nanocomposite electrode material with a weight ratio of 1:8 (graphene: ZnO) displayed the highest specific capacitance of 236 F/g at a scan rate of 10 mV/s with energy and power densities of 11.80 Wh/kg and 42.48 kW/kg respectively. This simple, facile and green synthesis method can be extended for other graphene/metal oxide nanocomposites based high performance electrochemical capacitor.

Chapter 5

Solvothermal Synthesis of Graphene-MnO_2 Nanocomposites and Their Electrochemical Behavior

5.1 Overview

The use of metal oxides for electrode materials of electrochemical capacitors owing to their very large capacitance, high packing density, fast redox process and high energy density have been extensively studied [1], [217]. MnO_2 among various transition metal oxides possess properties of being environmental friendly because of its low toxicity, high energy density, high theoretical surface capacitance (~1370) and low cost [218]. As a result of these distinctive properties, MnO_2 is a very popular electrode material and has great prospects to be widely used in electrochemical capacitor application.

Several studies have reported different synthesis route can be adopted to produce graphene-MnO_2 composites for electrochemical capacitors, including microwave [34], electro-deposition [21-22], hydrothermal [23–26] and simple solution process [223]. Kim et al. [224] reported the synthesis of graphene-MnO_2 composites prepared via reduction of GO-MnO_2 at various reduction times using fixed concentrations of hydrazine and found that 28 hour hydrazine-reduction protocol demonstrated the best electrochemical performance. Deng et al [33] prepared different composites ratio of MnO_2 nanorods-graphene composites via hydrothermal synthesis with the aim of studying their electrochemical properties and suggested that the composite of graphene and MnO_2 (1:5 ratio) was most favorable with a specific capacitance of 218 F/g at the scan rate of 5 mV/s.

In this chapter, the structural, morphological and electrochemical characterisation analyses of the graphene-MnO_2 nanocomposites synthesised via a green synthesis route (section 3.3.3) is explained. By varying their composites ratio, different graphene-MnO_2 composites were prepared by using facile solvent exfoliation and low temperature solvothermal processing methods. It is aimed at studying the electrochemical performance of the different composites ratio by harvesting the high electrical conductivity of graphene and the pseudocapacitance of MnO_2 nanomaterial.

5.2 Structural and morphological characterisation

The process for the formation of graphene-MnO_2 composites comprises the following two steps: (i) synthesis of graphene from graphite through liquid phase exfoliation route and (ii) the formation of MnO_2 nanorods on the graphene surfaces and edges via hydrothermal method. When $MnSO_4.H_2O$ was initially poured into the graphene solution, Mn^{2+} ions was evenly adsorbed on the surface and edges of the graphene sheets by electrostatic forces. The graphene sheets with a large area provided plenty of attachment sites for the formation of MnO_2 nuclei [178]. Then, upon addition of $KMnO_4$ into the mixture, many nucleuses were formed quickly as the appearance of a black-brown precipitate was clearly observed. A redox reaction between $MnSO_4.H_2O$ and $KMnO_4$ could occur as follows:

$$2KMnO_4 + 3MnSO_4 + 2H_2O \longrightarrow 5MnO_2 + 2H_2SO_4 + K_2SO_4 \qquad (5.1)$$

The structures of the various graphene/MnO_2 composites, graphite and MnO_2 were studied by the XRD patterns as shown in Figure 5.1. The two diffraction peaks of graphite at 2θ values of 26.8° and 54.9° corresponds to the (002) and (1-20) reflections of graphite, and these diffraction maximums can be clearly seen for the graphene/MnO_2 composites. In comparison with the graphene/MnO_2 composites, it can be observed that an increase in weight ratio of MnO_2 hinders the diffraction maximum of graphene at 26.8^o which is an evident of the growth of MnO_2 on the surface of graphene suggesting that the stacking of graphene sheets was prevented by MnO_2 in some extent due to van der Waals interactions [225]. The 54.9^o peak was superimposed by the MnO_2 peaks at 55.9^o as the weight ratio of MnO_2 increases signfying that the surface of the graphene sheet was fully decorated by MnO_2 (Figure 5.2) [178]. Furthermore, the diffraction peaks of the graphene/MnO_2 composites with different mass ratios are similar to that of MnO_2 and they can be readily assigned to pure tetragonal α-MnO_2 (JCPDS card 44-01410), space group I4/m with lattice constants of a = b = 0.9784 nm and c = 0.2863 nm which is in accordance with previous reports [33], [226], [227]. The peaks at 2θ values of 12.9, 18.4, 28.8, 37.8, 42.1, 50.0, 55.9, 60.2, 65.6 and 69.1^o can be indexed to (001), (011), (111), (1-2-1), (10-2), (213), (214), (2-31), (015) and (10-4) crystal planes respectively, clearly showing that MnO_2 was formed from the precursor. Taking the peak intensities and half-width of diffraction of the graphene/MnO_2 composites into consideration, the degree of the crystallinity follows the order: GM4 > GM3 > GM2 > GM1.

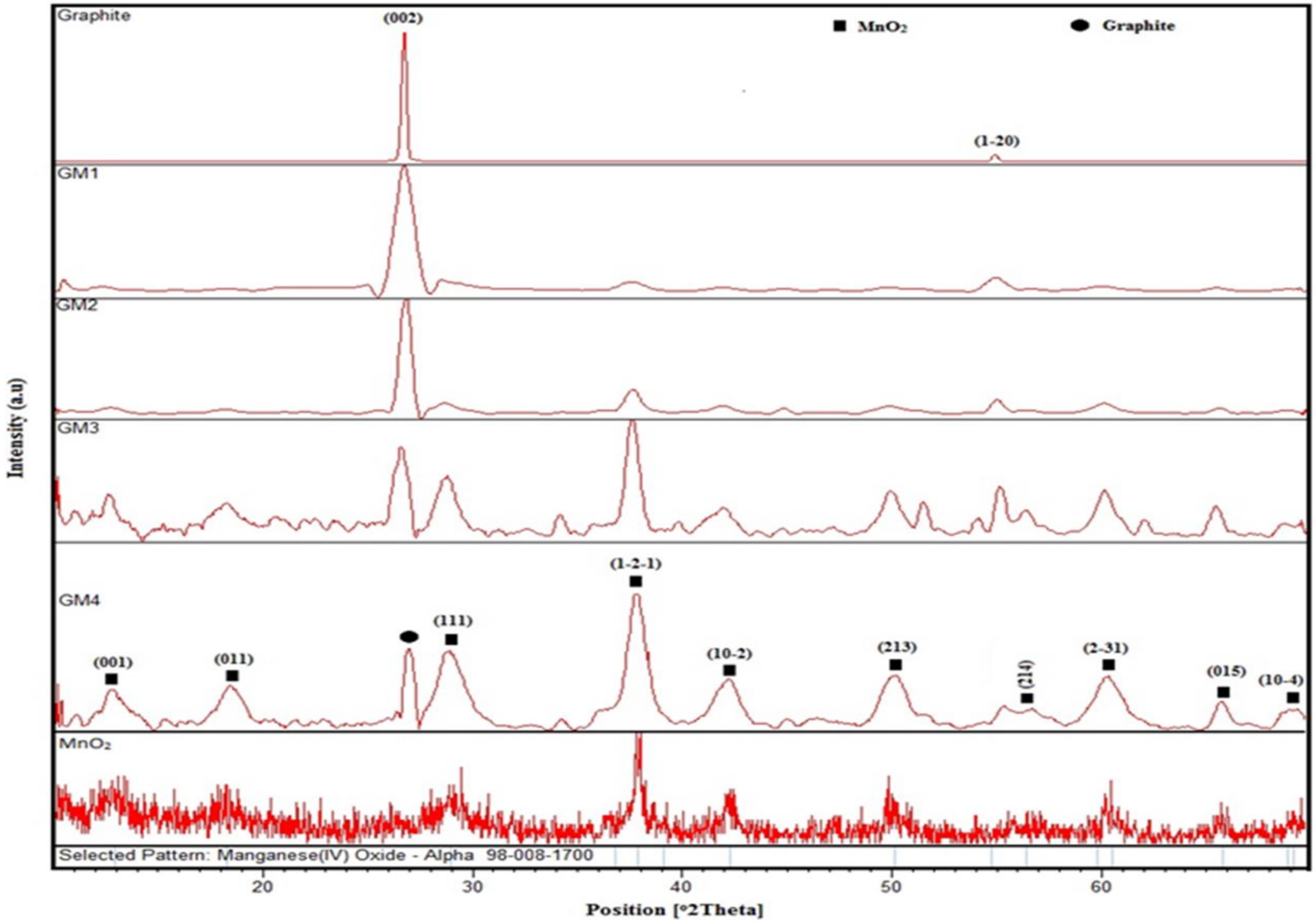

Figure 5.1: XRD pattern of graphite, MnO_2 and graphene-MnO_2 composites.

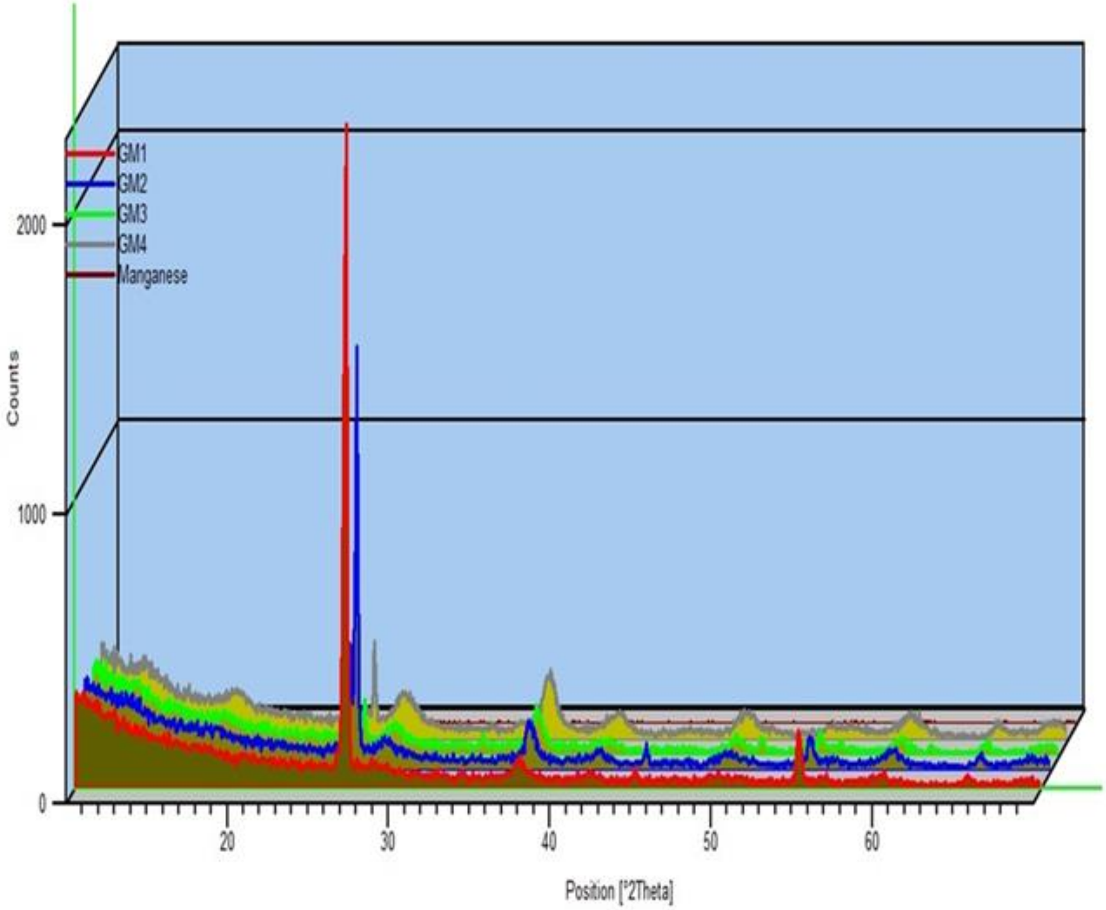

Figure 5.2: 3D view of the XRD pattern of graphite, MnO_2 and graphene-MnO_2 composites.

The Raman spectra of graphene and graphene/MnO_2 nanocomposites respectively are elucidated in Figure 5.3. The notable peaks in the Raman spectrum of graphene are indicated as “G”, “2D” and “D” in the graph. These marked peaks are in agreement with the G band at ~1580 cm^{-1} that is related to the C-C bond stretching and the main peak for all sp^2 carbons [228], the 2D band at ~2719 cm^{-1} and the D band (disordered carbon band) at ~1351 cm^{-1} associated to the first-order zone boundary phonons, which is not present in defect-free graphene [229]. However, new edges formed on the exfoliated graphene sheets as a result of the exfoliation of graphene from graphite can be seen as defects that leads to the existences of a D peak [45], [188], [209]. The Raman spectrum collected after the hydrothermal synthesis to form the graphene/MnO_2 nanocomposites displays the characteristic G, 2D and D peaks of graphene corresponding to their well-documented peaks respectively; specifying its presence in the obtained nanocomposites. Four strong peaks marked "O" at ~182, ~389, ~578 and ~633 cm^{-1} alongside three weak ones marked "X" at ~323, ~521 and ~747 cm^{-1} are also seen in the graphene/MnO_2 spectrum; these peaks are characteristics features assigned to α-phase of MnO_2 [230]. Structurally, the factor group analysis of α- MnO_2 type nanomaterials designates that 15 spectroscopic modes of 6Ag, 6Bg and 3Eg spectroscopic species are Raman-active. Nevertheless, it is naturally hard to observe all these predicted active modes in the polycrystalline sample [230], [231]. The peaks observed in our work are similar to other reports on α-phase of MnO_2 except for little deviation in wave numbers because of different structure modifications. The translational motion of the MnO_6 octahedra which causes an external vibration is assigned to the low frequency Raman peak at ~182 cm^{-1} while the Raman peak at ~389 cm^{-1} is due to Mn-O bending vibrations. The strong peaks at ~578 and ~633 cm^{-1} belonging to the A_g spectroscopic species is as a result of symmetrical Mn-O vibrations indicating well-formed tetragonal structure with an interstitial space consisting of (2 × 2) tunnels [230]–[232]. The Raman spectrum confirms that the formation of graphene/MnO_2 composites and the structure of graphene were not destroyed after the hydrothermal treatment, which is in good agreement with XRD results.

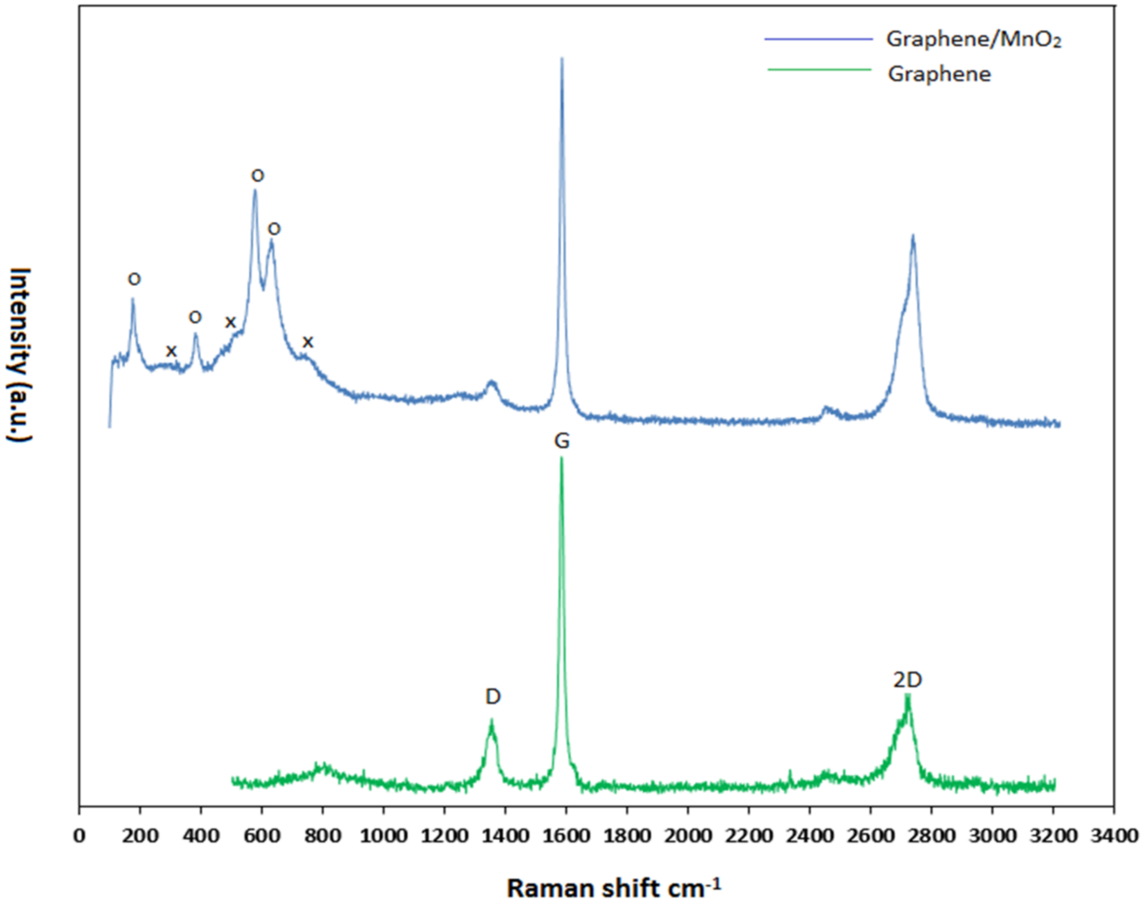

Figure 5.3: Raman spectra of graphene and graphene-MnO_2 composites.

Figure 5.4a depicts the surface morphology of MnO_2 prepared by hydrothermal synthesis, the low magnification FESEM image shows MnO_2 nanorods of length approximately 0.6 - 0.8 μm forming an interconnected structure. The nanorod-like morphology is the characteristics of the α- phase MnO_2 [33], [232] and no other morphology of MnO_2 was detected. In Figure 5.4b, the SEM image of the sandwiched morphology of intercalated MnO_2 nanorods on the graphene sheets with good and uniform distrubution can be observed. This indicates that the graphene/MnO_2 nanocomposites was successfully preparforminge hydrothermal synthesis. TEM observations were conducted for further study on the surface morphology and crystal struture of the graphene/MnO_2 composites. Figure 5.4c presents a transparent plate–like thin layer of the as-synthesized graphene which exhibited a very stable nature under the electron beam. The TEM image (Figure 5.4d) of the MnO_2 nanorods reveals that nanorods still had the interconnecting network on the surface of the graphene sheet after hydrothermal treatment and the length were approximately 0.2 - 0.3 μm. It is noted that the MnO_2 nanorods are well anchored and highly dispersed on the surface of the graphene sheet as seen in Figure 4e and the dark region on the image is due to the overlaps of thin graphene sheets which reflects that the prepared composites exist in the form of multi-layers. The high-resolution transmission micros4opy (HR-TEM) image of α-MnO_2 nanorod (Figure 5.4f) reveals a d-spacing of 0.29 nm which agrees with the (001) crystal plane of α-MnO_2 obtained in the XRD analysis (Figure 5.1). The chemical compositions of the composite were analyzed by an energy dispersive spectroscopy (EDS), where the presence of carbon, oxygen, manganese in the EDS spectrum (Figure 5.5) confirms the purity of the composites material. The Si peak is due to the silicon substrate used during characterization.

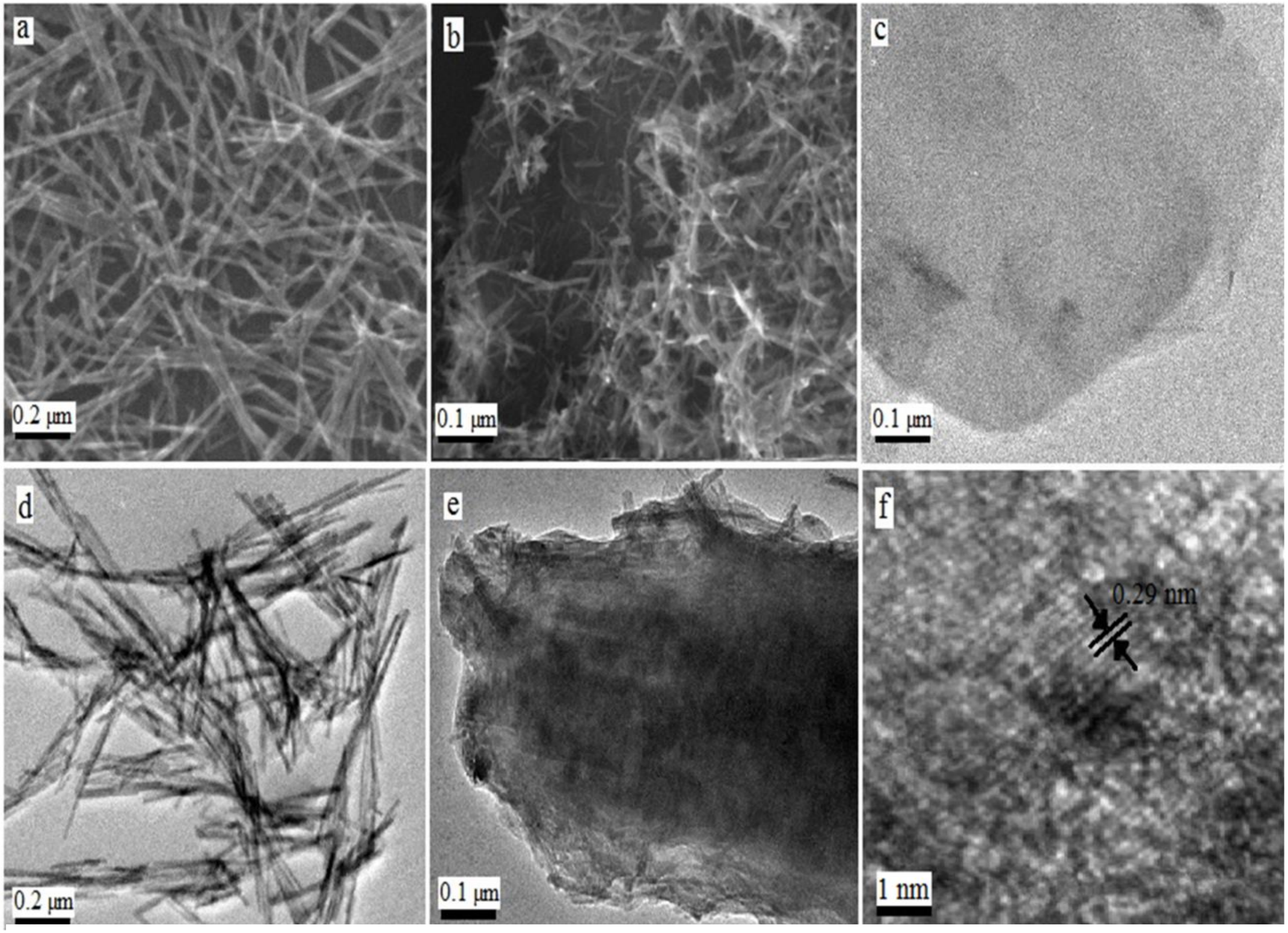

Figure 5.4: FESEM images at different magnifications of (a) MnO_2 (b) graphene-MnO_2 composite, TEM images of (c) graphene (d) MnO_2 (e) graphene-MnO_2 composite and HRTEM of (d) graphene-MnO_2 composite.

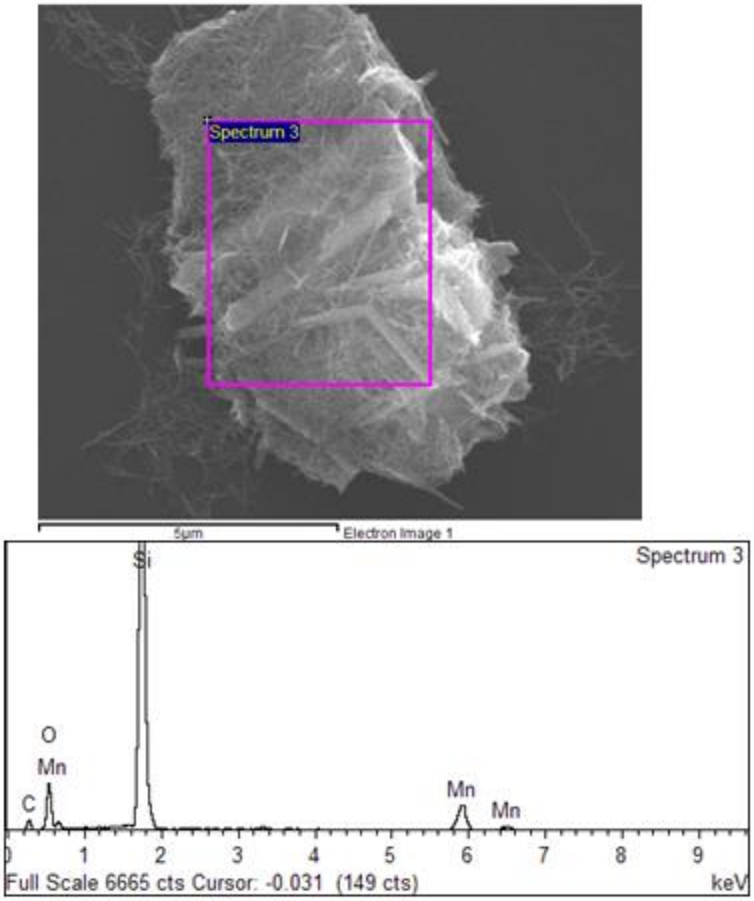

Figure 5.5: The EDS spectrum and its corresponding SEM image of graphene-MnO_2 composites.

5.3 Electrochemical performance

To explore the electrochemical properties of graphene/MnO_2 composites as electrochemical capacitors, the compoistes were fabricated into electrodes and characterized by cyclic voltammetery (CV) and galvanostatic charge-discharge analysis. The CV analysis were carried out at different scan rates varying from 5 to 100 mV/s using 1 M KOH aqueous solution with the potential window of -1 to 1 V. Figure 5.6a compares the CV curves of MnO_2, GM1, GM2, GM3 and GM4 at a scan rate of 50 mV/s.

The rectangular characteristics of all CV curves indicated the quick ion exchange in the charge-discharge process and good electrochemical properties of the electrode materials with no obvious redox peaks. By comparison, the CV curve area of GM4 along the current-potential axis is larger than that of MnO_2 and the other composite materials, disclosing better capacitance performance and synergistic effect of graphene and $MnO_{2.}$ Since the integrated area of the CV curve is proportional to the specific capacitance of the electrodes, this clearly shows that the specific capacitance of the electrodes increases with the ratio of MnO_2 in the composite materials. This evidently indicates that the combination of double layer and pseudo capacitance improved the total capacitance of the electrode. The rate-dependent CV curves of the as-prepared electrodes were studied over a wide range of scan rates from 5 to 100 mV/s. Figure 5.6(b-f) shows the CV curves of $MnO_{2,}$ GM1, GM2, GM3 and GM4 electrodes respectively over a potential range of -1 to 1 V which still exhibited a nearly rectangular shape signifying good capacitive performance. It was observed that an increase in scan rate lead to an increase in the CV area of the elctrode reflecting good storage rate ability as reported by previous reports [206], [233]. The specific capacitance (C_s) can be calculated from the CV curves by equation 3.20 [207]:

Based on equation 3.20, the C_s of the as-prepared elctrodes were calculated from the CV curves and plotted in Figure 5.7a which is mainly consistent with the order specified by the CV curves from Figure 5.6(a-f).

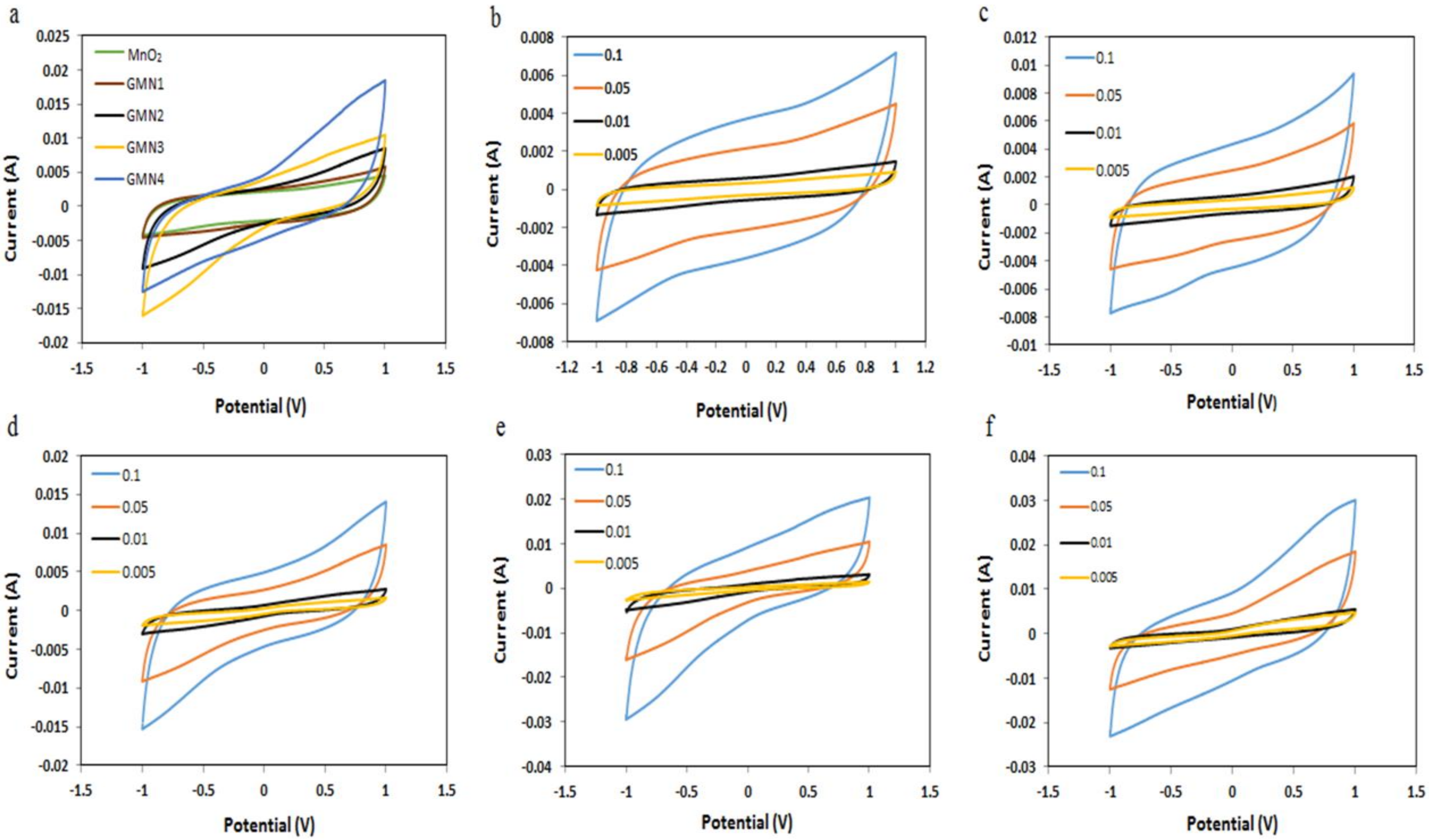

Figure 5.6: Cyclic voltammograms (CV) curves of (a) GM4, GM3, GM2, GM1 and graphene/MnO_2 composite at a scan rate of 100 mV/s, (b) MnO_2 at different scan rates in the range of 5-100 mV/s, (c) GM1 at different scan rates in the range of 5-100 mV/s, (d) GM2 at different scan rates in the range of 5-100 mV/s, (e) GM3 at different scan rates in the range of 5-100 mV/s and (f) GM4 at different scan rates in the range of 5-100 mV/s.

The decreasing trend of specific capacitance observed in Figure 5.7a suggests that parts of the surface area of the electrode material were not accessible at high charge-discharge rates implying that lower scan rates are more favorable because it allows time for ion diffusion and adsorption in the charge-discharge process. Galvanostatic charge-discharge analysis results of the as-prepared electrode materials performed at current density of 0.5 A/g are presented in Figure 5.7b. All the electrode materials exhibited near linear and symmetric triangles, indicating good capacitive performance [214], which is consistent with the results from the CV analysis. Comparing the discharging curves, GM4 electrode displayed the longest discharge time which is in agreement with the specific capacitance behavior since the discharging time of an electrode is directly proportional to its specific capacitance [234]. The internal resistance of an electrode material is indicated at the IR drop at the beginning of the discharging curve, the IR drops on all the curves are negligible implying low resistance of the electrodes. Comparing the IR drops of the materials (Figure 5.8), GM4 had the least IR drop suggesting that the introduction of graphene increased the electrical conductivity of the MnO_2. Figure 5.7c shows the respective galvanostatic charge-discharge analysis of the GM4 electrode at different current densities of 0.1, 0.2, 0.5, 0.6 and 1 A/g under an applied voltage from 0 to 1 V. The charge current curve is symmetrical to its corresponding discharge current curve throughout the different current densities denoting the high reversibility of the electrode [33]. It can be observed that the time of the charging–discharging process decreases gradually with increase in current, the slight curvature noticed in the charge and discharge curves indicates the contibution of double layer and faradaic capacitance. The cycle stability is an important requirement for practical application of electrochemical capacitors [235]. The cycle stablity of the GM4 electrode by consecutive galvonostatic charge-discharge experiments for 1000 cycles at a current density of 1 A/g (Figure 5.7d) were conducted in 1M KOH within a potential range of 0 – 1 V. The specfic capacitance of GM4 electrode retains 88.4% of its initial capacitance value which indicates its good long-term electrochemical cyclability upon repetitive charge-discharge process.

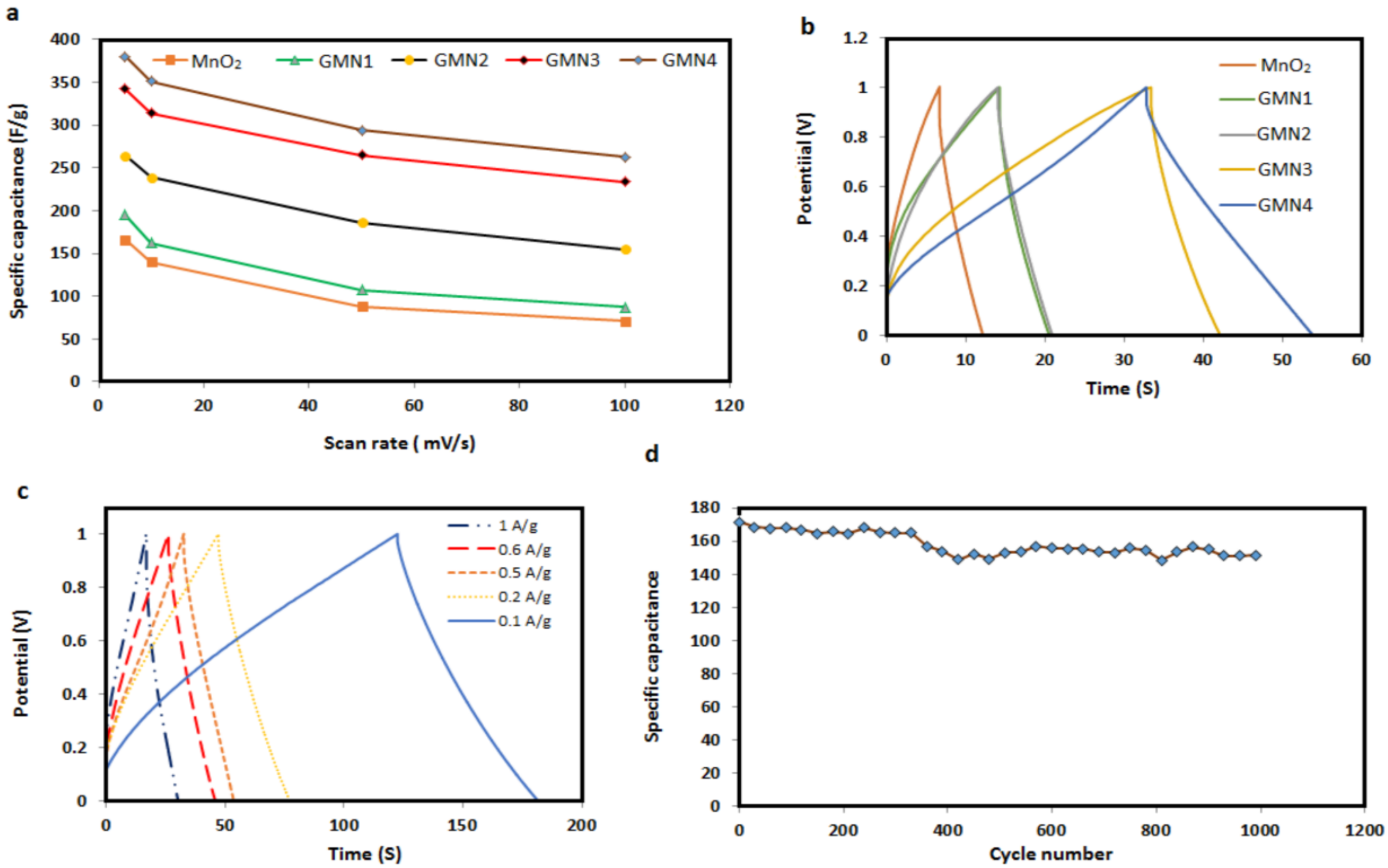

Figure 5.7: Plots of specific capacitance of (a) GM4, GM3, GM2, GM1 and graphene-MnO_2 composite at various scan rates (5, 10, 50, 100 mV/s), charge-discharge curves of (b) GM4, GM3, GM2, GM1 and graphene-MnO_2 composite at a current density of 1 A/g (c) charge-discharge curves of GM4 at different current densities (0.1, 0.2, 0.5, 0.6 and 1 A/g) (d) cycling test for GM4 at the current density of 1 A/g up to 1000 cycles.

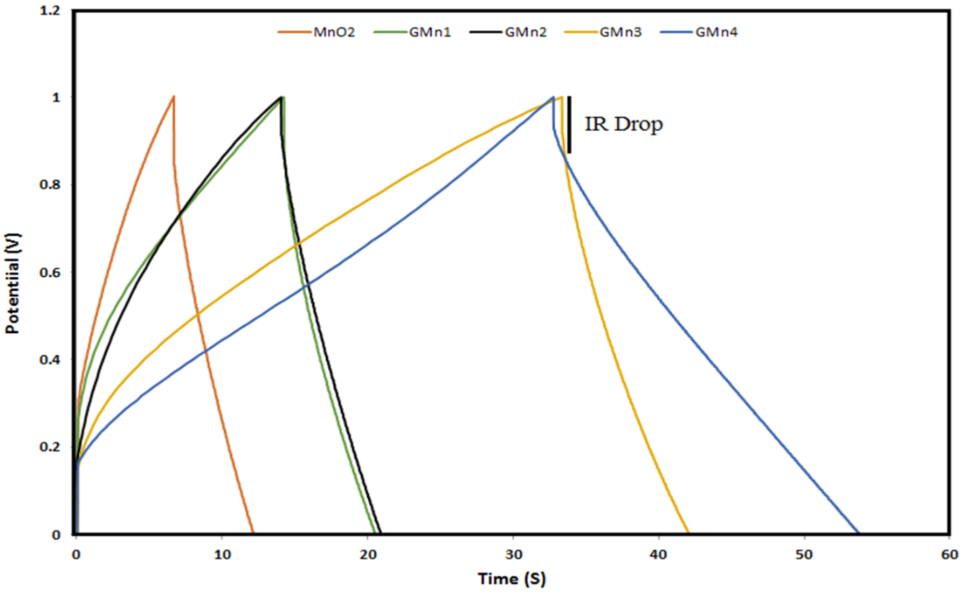

Figure 5.8: The charge-discharge curves of GM4, GM3, GM2, GM1 and graphene-MnO_2 composite at a current density of 10 mA/g.

All the Nyquist plots of MnO_2 and graphene/MnO_2 composites electrodes were semi-circular over the high frequency range and linear in the low frequency range as shown in Figure 5.9a. In comparison, the R_{ct} values of the electrochemical capacitors decreases in the order of MnO_2 > GM1 > GM2 > GM3 > GM4, inversely proportional to the results of the specific capacitance, which is in agreement as report in [215], the higher the R_{ct} value of the electrode the lower its specific capacitance.

The average energy density (E) and power density (P) of the electrochemical capacitors were calculated to further determine their electrochemical performance using the following equations 3.29 and 4.2 [206].

The calculated E and P of the electrode materials derived the charge-discharged were plotted in a Ragone plot (Figure 5.9b) at different scan rates. Compared with the different as-prepared electrode materials, GM4 electrode shows greatly superior energy density of 53 Wh/kg at a power density of 530 W/kg and a high power density of 2.2 kW/kg at an energy density of 37 Wh/kg. This is about twice the increase of energy density and 4 times increase of power density compared to the MnO_2 electrode. The resultant specific capacitance of graphene-MnO_2 composites is significantly higher than previous reported on graphene-MnO_2 [221], [225], [236].

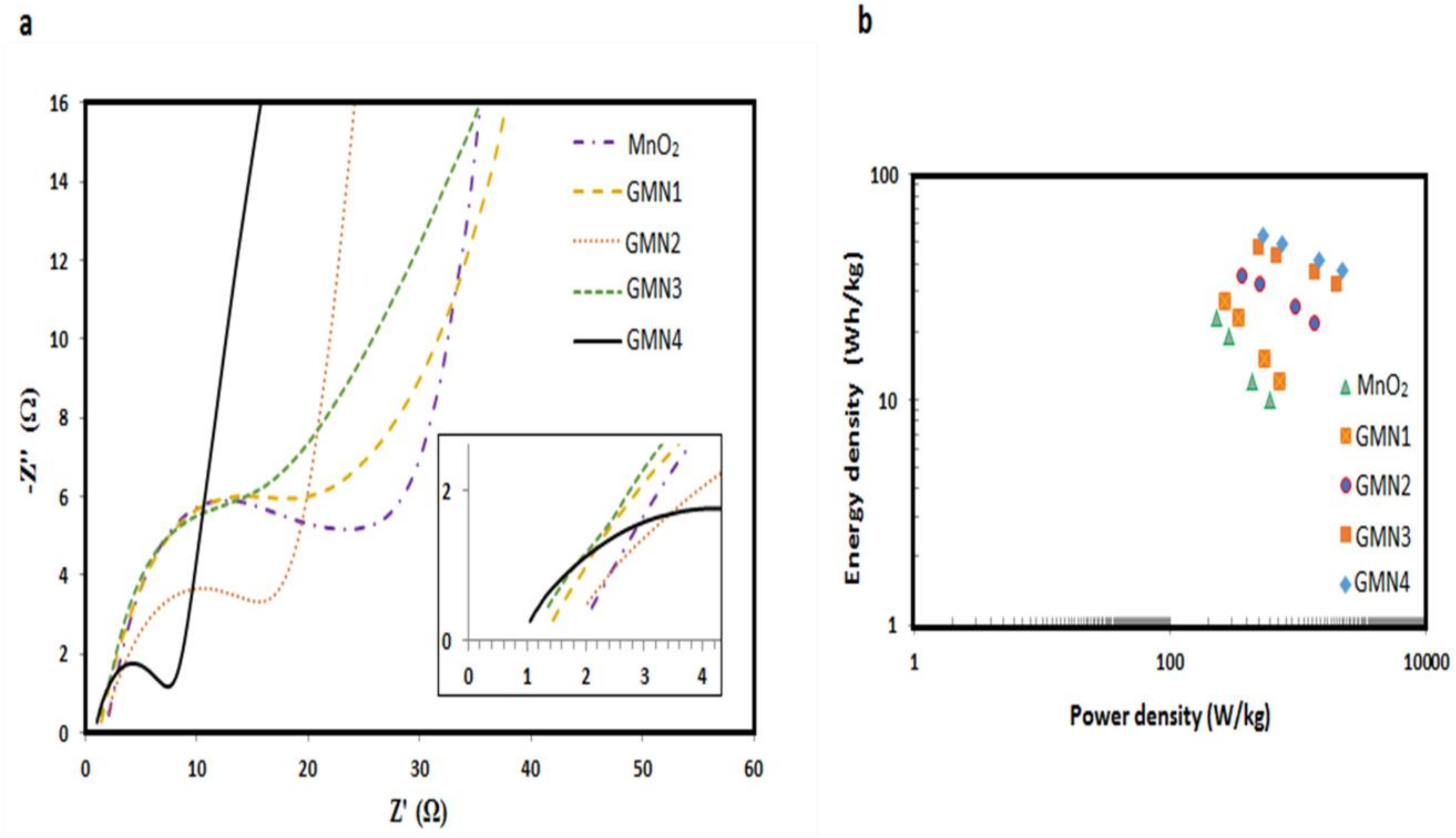

Figure 5.9: Nyquist plot for (a) GM4, GM3, GM2, GM1 and graphene- MnO2 composite (b) Ragone plot of GM4, GM3, GM2, GM1 and graphene- MnO_2 composite at various scan rates (5, 10, 50, 100 mV/s).

The enhanced electrochemical performance of graphene/MnO_2 can be as a result of the following aspects: (i) the pristine nature of the graphene which improves the electrical structure of the hybrid structure. (ii) The pseudo-capacitance of the MnO_2 coupled with the double-layer capacitance of graphene to achieve a higher capacitance. (iii) The 1D MnO_2 nanorods and graphene sheets forming a cross-link sandwiched structure as shown in the FESEM images (Figure 5.4) provides more micropores and prevent restacking of graphene thereby improving the adsorption/desorption of ions on the graphene sheet [220].

5.4 Chapter Summary

In summary, a simple, effective and practical technique to fabricate graphene-MnO_2 composites through combining a liquid phase exfoliation and solvothermal process was successfully carried out. The structural analysis and electrochemical properties of the graphene-MnO_2 composites have been studied thoroughly. The specific capacitance of the graphene-MnO_2 composite electrode material with a weight ratio of 1:16 (graphene: MnO_2) demonstrated the best performance of 380 F/g at a scan rate of 5 mV/s. For high power applications, it exhibited a specific energy and power densities of 53 Wh/kg and 2.2 kW/kg, respectively.

Chapter 6

Cobalt Oxide Nanoparticles Grown On Exfoliated Graphene for Enhanced Electrochemical Performance

6.1 Overview

Cobalt Oxide (Co_3O_4), a transition metal oxide is of special attention due to its high theoretical capacitance (3560 F/g) [237], low cost, environmental benign with well-defined redox characteristics [25], [237], [238]. Nevertheless, Co_3O_4 as most transition metal oxides is limited by its relatively poor electrical conductivity which causes poor cycling stability during charge/discharge process. To improve the electrical conductivity of Co_3O_4, studies have indicated that incorporating them into carbonaceous materials such as activated carbon, carbon nanotubes and graphene will achieve desirable results [28], [239]. Several carbon based materials have been used for various applications because of their desirable physical and chemical properties [136], [240]–[245]. Graphene, an extraordinary two-dimensional single sheet of sp2 hybridized carbon atoms arranged in a honeycomb lattice [246]–[248] is an elementary building block for all graphitic materials [2] and a palpable choice among other carbon based materials, owing to its unique properties such as large theoretical specific surface area (2630 m^2 g^{-1}) [2], [70], [249] and high electron mobility (15000 $cm^2V^{-1}s^{-1}$) [70], which are attractive to be exploited in electrochemical applications [250]. Most studies have reported the synthesis of graphene or reduced graphene oxide through modified Hummers and chemical reduction process, before they are incorporated with Co_3O_4 nanomaterials to form the graphene-Co_3O_4 composite electrode [239], [251], [252].

This chapter discusses the characterisation evaluations of the as-synthesised graphene-Co_3O_4 nanocomposites prepared via a solvothermal approach with subsequent calcination process detailed in section 3.3.4. Furthermore, the electrodes were fabricated using different composite ratios and their electrochemical performances were thoroughly investigated.

6.2 Structural and Morphological characterisation

Figure 6.1 shows the Raman spectra of the graphene and graphene-Co_3O_4 nanocomposite materials. The Raman spectrum of graphene exhibits a simple structure characterised by three distinguished vibrational bands designated as the G band ('C-C bond stretching') at ~ 1580 cm^{-1}, the D band ('disorder band') at ~ 1351 cm^{-1} and 2D band ('multipeak feature') at ~ 2719 cm^{-1}. These vibrational bands (G, D and 2D) details vital information about graphene and its layer thickness, acquired by studying the band's peak position, intensity and band shape [209], [253]–[255]. The formation of new edges on the graphene sheets which can be seen as defects due to the exfoliation process of graphene from graphite is responsible for the presence of the D band observed [45], [188], [209]. The band position and shape of the 2D band can be used to determine the graphene layer thickness [209], [253]–[255] . The 2D band exhibits a distinct shape of overlapping modes caused by symmetry lowering owing to a few layers up to 3-5 layers of graphene sheets [253]. After the solvothermal and calcination processes, it can be observed that there are additional Raman active modes such as two F_{2g} modes at ~ 524 and ~ 621 cm^{-1} and the A1g modes at ~ 693 cm^{-1} respectively, resulting from Co_3O_4. The photon modes of Co_3O_4 are in agreement with the standard Raman spectrum of Co_3O_4 material [256]. The slight right shift of the G band and 2D band respectively located at ~ 1583, and ~

2726 cm^{-1} are likely arising from the doping effects of Co_3O_4 on the graphene sheets [257].

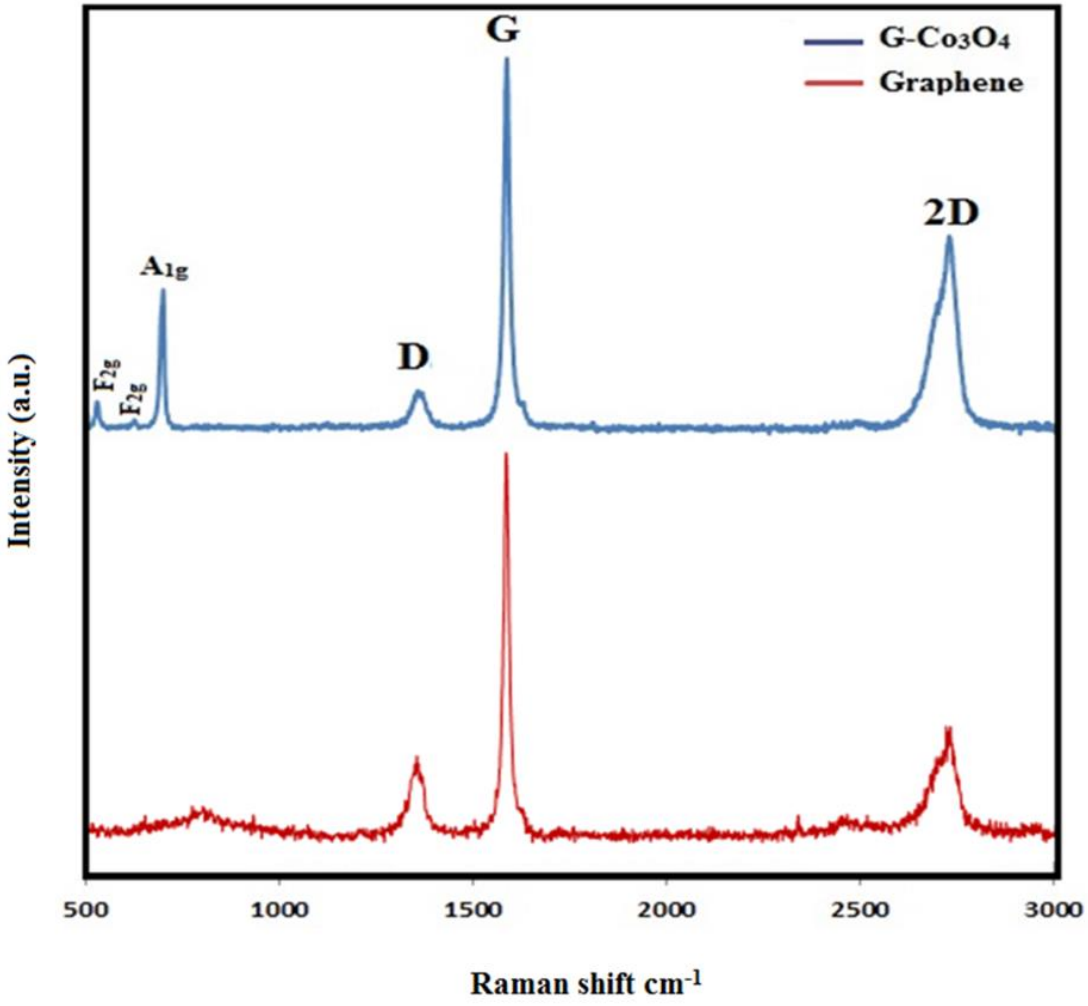

Figure 6.1: Raman spectra of graphene and graphene-Co_3O_4 composites.

The X-ray diffractogram of Co_3O_4, graphene and the graphene-Co_3O_4 composites are displayed in Figure 6.2. The two intense diffraction peaks observed in graphene and graphene-Co_3O_4 samples at around 2θ values of 26° and 55° respectively are attributed to

(002) and (004) reflections of graphite. These results clearly showed that the crystalline order of graphene is well-preserved, after the formation of the graphene-Co_3O_4 composites. The diffraction peaks at $2\theta = 19.04^o$, 31.34^o, 36.93^o, 38.64^o, 44.92^o, 55.79^o, 59.51^o and 65.40^o respectively are assigned to that of pure Co_3O_4 and can be indexed to (111), (220), (331), (222), (400), (422), (511) and (440) planes corresponding to a cubic crystal system (JCPDS 43-1003) (space group Fd-3m) with a lattice parameter of a = b = c = 8.08 Å. The absence of any other peaks indicates the phase-pure nature of the graphene-Co_3O_4 composites prepared in this work, without the presence of any residue precursors or impurities. The size of the graphene-Co_3O_4 composites were calculated from the (311) diffraction peak using the Debye-Scherrer equation [243]:

$$L = \frac{k\lambda}{\beta\cos\theta} \qquad (6.1)$$

where L is the mean dimension of the particle, θ is the diffraction angle, λ is the wavelength of the using Cu-Kα radiation, β is the full width of at half maximum (FWHM) of the diffraction peak and k is the diffraction constant (0.89). The calculated average sizes were about 0.24 nm, which is in good agreement with the TEM results.

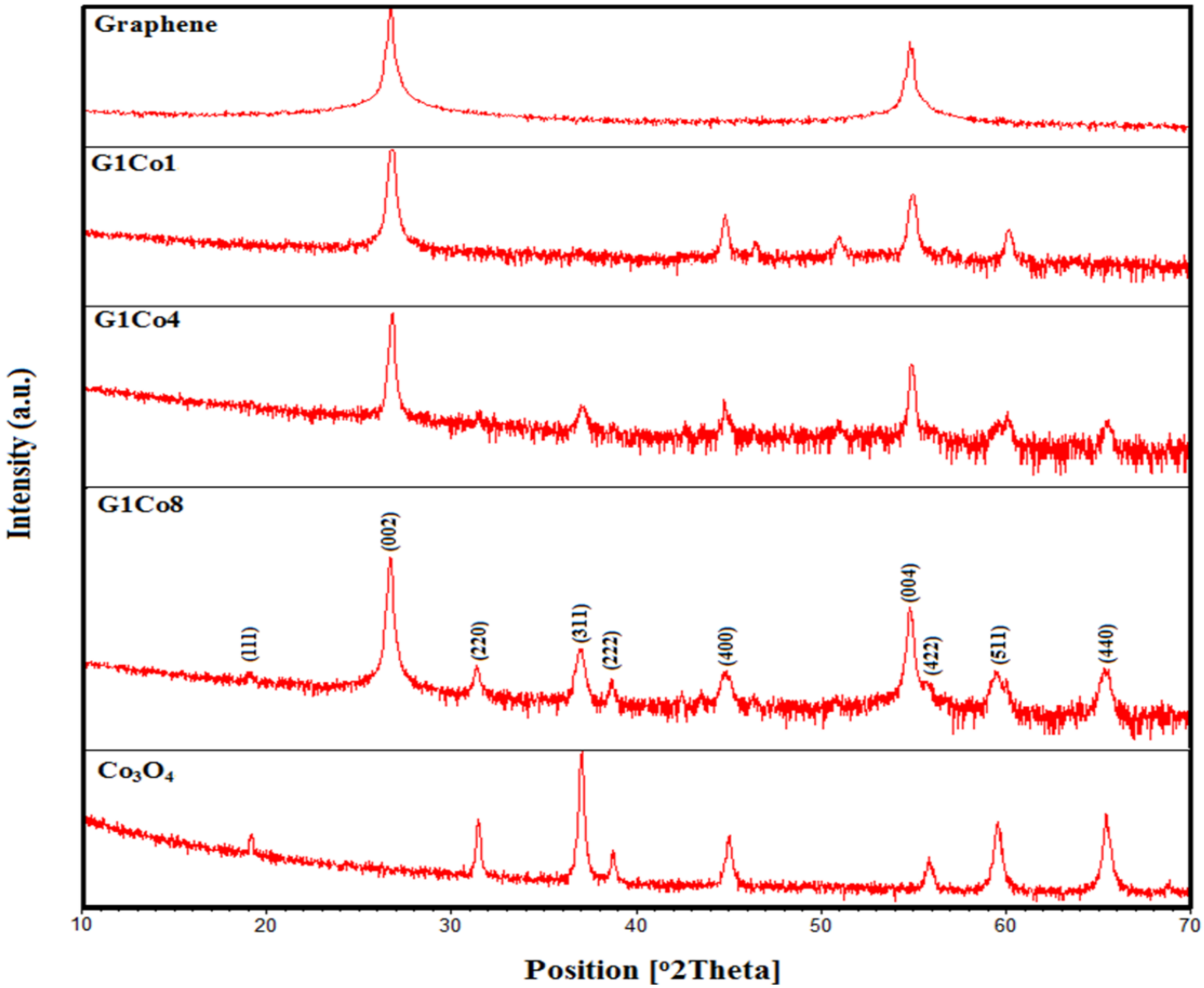

Figure 6.2: XRD pattern of graphene, Co_3O_4 and graphene-Co_3O_4 composites.

The FESEM images of graphene-Co_3O_4 composites from different precursor mass ratios are presented in Figure 6.3a-c. Figure 6.3a shows the FESEM image of G1Co1 composites, it can be seen that several porous agglomerates made by granular-shaped nanoparticles of Co_3O_4 were deposited on the edges and surface of the graphene sheets. An increase of the Co_3O_4 precursor (G1Co4) led to relatively more agglomerates and uneven spread of the granular-shaped nanoparticles on the surface and edges of the graphene sheets (Figure 6.3b). With further increase of Co_3O_4 precursor (G1Co8), the agglomerates formed by the granular-shaped nanoparticles took on a flower-like shape of diameter 6-7 μm and were deposited on the edges of the graphene sheets as shown in Figure 6.3c. It can be observed that as the amount of urea added to the synthesis route increases, the morphology of Co_3O_4 transforms from granular shaped nanoparticles to flower-like structures grown on the edges of the graphene sheets. The observed changes in morphology are due to the growth solution becoming more basic with increasing amount of urea. It is well-known that alkaline precursors can alter the pH of the reactant solution and subsequently affect the growth morphology change [180]. The chemical composition of the composites were analysed by an energy dispersive spectroscopy (EDS). The peaks of C, O and Co in the EDS spectrum (Figure 6.3d) depict the presence of carbon (graphene), oxygen and cobalt compounds. The peak corresponding to Si in the EDS spectrum is due to the silicon substrate used for the characterisation. The atomic ratio of Co to O is approximately 3:4, in agreement with the stoichiometric ratio of Co_3O_4. No other peak was observed confirming the purity of the as prepared graphene-Co_3O_4 composites.

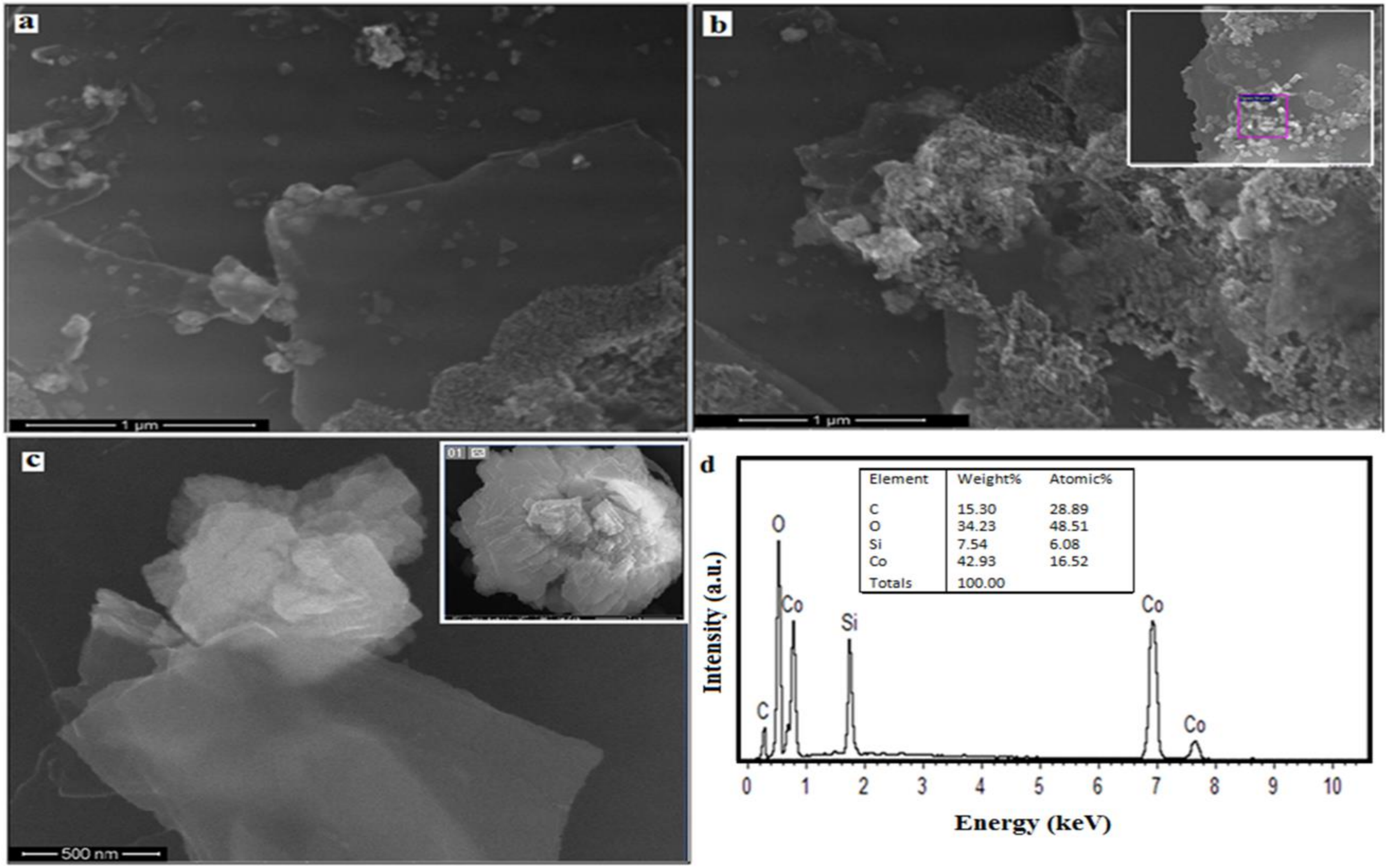

Element	Weight%	Atomic%
C	15.30	28.89
O	34.23	48.51
Si	7.54	6.08
Co	42.93	16.52
Totals	100.00	

Figure 6.3: FE-SEM images of (a) G1Co1 composite (b) G1Co4 composite (c) G1Co8 composite and (d) the EDS spectrum of graphene-Co_3O_4 composites. Inset in (b) and (c) show high magnification of G1Co4 and G1Co8 respectively.

TEM analysis as shown in Figure 6.4 provides further information on the morphology of the composites. It can be seen that the composite structures in Figure 6.4(a-c) comprises of Co_3O_4 nanoparticles superimposed on the transparent plate-like graphene. It was observed that the sizes of the nanoparticles increased with the concentration of the Co_3O_4 precursor, in well agreement with the FESEM results. The Co_3O_4 nanoparticles in G1Co1 were found to have an average size of ca. 70 nm. This value increased to 130 nm for G1Co4 and further to 160 nm for G1Co8 nanocomposite material. In high resolution TEM image, the well crystalline structures with lattice fringes of 0.24 nm are clearly observed (Figure 6.4d), corresponding to the (311) reflection of Co_3O_4 in the XRD analysis.

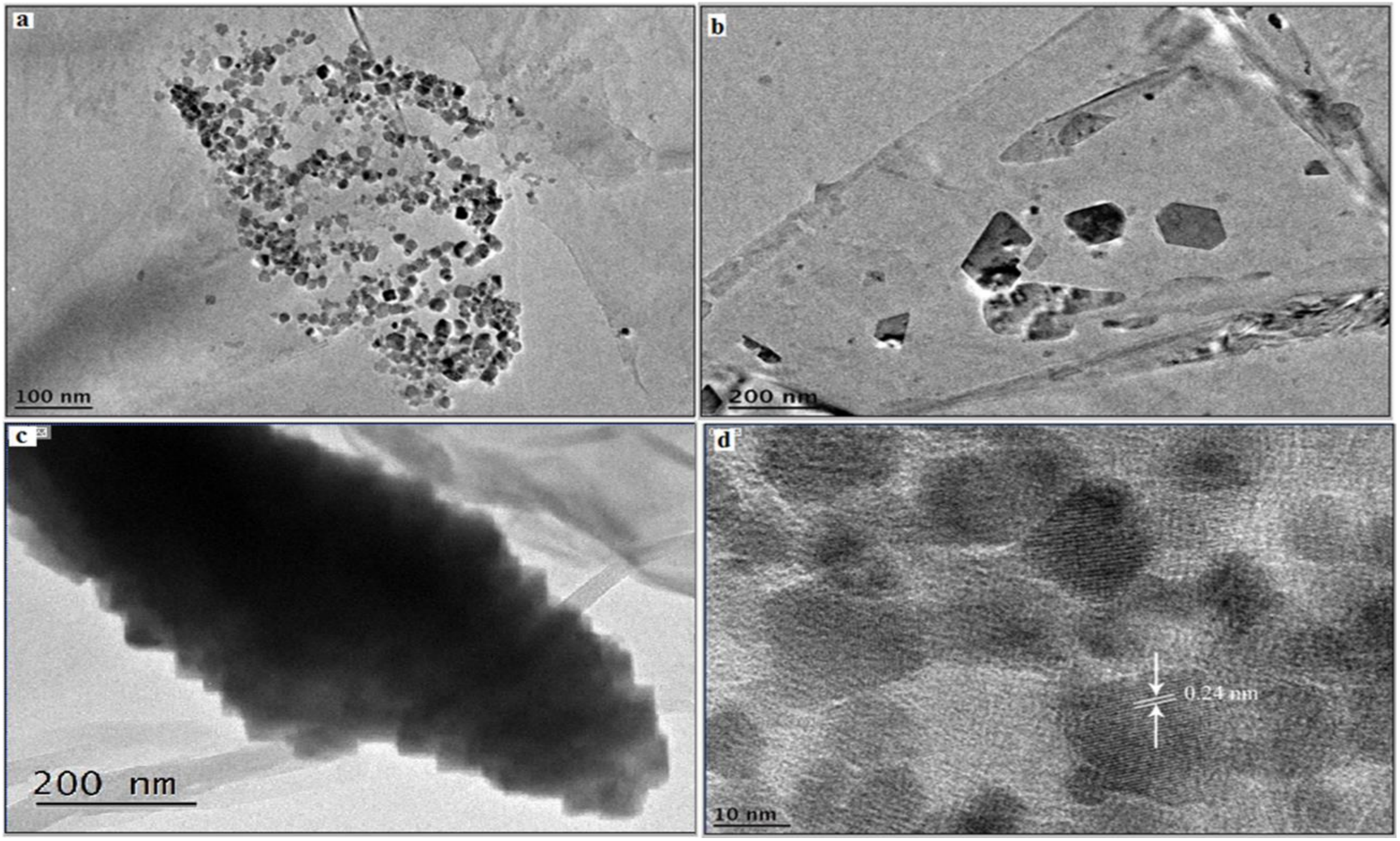

Figure 6.4: TEM images of (a) G1Co1 composite (b) G1Co4 composite (c) G1Co8 composite and HRTEM image of (d) graphene-Co_3O_4 composite.

6.3 Electrochemical performance

Cyclic voltammetry (CV) analysis was used to study the electrochemical behavior of the graphene-Co_3O_4 composite electrodes and the results are illustrated in Figure 6.5(a-e). The CV tests were measured within the potential range of -1 to 1 V at different scan rates varying from 5 to 20 mV/s. At a scan rate of 10 mV/s, it can be observed that the areas under the CV curves of the graphene-Co_3O_4 composite electrodes are seemingly larger than that of the $C0_3O_4$ electrode entailing the higher specific capacitance of the graphene-$C0_3O_4$ electrodes (Figure 6.5a). The presence of redox peaks during the anodic and cathodic sweeps of the graphene-$C0_3O_4$ composite electrodes are notably noticed and they become more distinct with increase of Co_3O_4 content. The anodic peaks at around (-0.08 V, 0.12 V and 0.38 V) and cathodic peaks at about (0.08 V, -0.17 V and -0.39 V) indicates the continuous and reversible faradaic redox reactions of Co_3O_4 involved during the charge and discharge processes, which is essential for pseudocapacitance contribution on charge storage capability. The electrochemical processes of these redox peaks could be expressed in two sequential reactions described as follows [28]:

$$Co_3O_4 + OH^- + H_2O \leftrightarrow CoOOH + e^- \tag{6.2}$$

$$CoOOH + OH^- \leftrightarrow CoO_2 + H_2O + e^- \tag{6.3}$$

Figure 6.5(b-e) shows the different graphene-Co_3O_4 composite electrodes at different scan rates, it can be seen that the integrated area of the CV curves on the current-potential axis increases as the scan rates are increased from 5 to 20 mV/s signifying good reversibility of fast charge-discharge response [28], [251], [258]. It can also be stated that the anodic and cathodic peaks become broader and shifted to higher and lower potentials respectively with an increase of scan rates as a result of possible polarization of the electrode which indicates the quasi-reversible characteristics of the redox couples [169], [259]. The galvanostatic charge/discharge behaviors of Co, G1Co1, G1Co4 and G1Co8 electrodes were measured by chronopotentiometry from 0 to 1 V at a constant current density of 0.3 A/g in 1 M KOH solution and the corresponding results are shown in Figure 6.6a. All the samples demonstrated nearly linear and triangular charge/discharge behaviors with time indicating good capacitive performance [214]. The discharge time of G1Co4 electrode is about 15 seconds which is the longest discharge time when compared to other electrodes G1Co8 (6.2 seconds), G1Co1 (7.6 seconds) and Co (5.9 seconds) respectively. This implies that the G1Co4 electrode exhibits the best capacitance. The capacitance (C) of the as-prepared electrodes were calculated from the slope of the discharge curves using the following equation 3.22 [150]. The specific capacitance of the samples evaluated at the current density of 0.3 A/g are Co (214 F/g), G1Co1 (300 F/g), G1Co4 (384 F/g) and G1Co8 (231 F/g) respectively. The resultant specific capacitance of graphene-Co_3O_4 composite electrodes are comparable with similar work reported on other graphene hybrid composites electrode in literatures [260]–[262].

Figure 6.6b shows the galvanostatic charge/discharge curves of the G1Co4 electrode at various current densities of 0.2, 0.3, 0.4 and 0.5 A/g in the potential range of 0 – 1 V. The curves remained almost symmetrical throughout the different current densities implying that the cell has excellent electrochemical reversibility. From these curves, the specific capacitance was calculated using equations 3 and 4 (Figure 6.6c). It can be observed that lower current density used in charging/discharging the electrode led to better specific capacitance. This is due to the fact that at lower current densities, there is adequate time for the inner active sites of the electrode to be fully utilised thereby contributing to a higher specific capacitance [258].

Figure 6.6d shows the cycling performance of the G1Co4 electrode subjected to galvanostatic charge/discharge cycling at a current density of 0.2 A/g in the potential range of 0 – 1V. During the cycling process, the electrode retained 80 % of its initial capacitance after 1000 cycles indicative of its good electrochemical cyclability upon repetitive charge-discharge process.

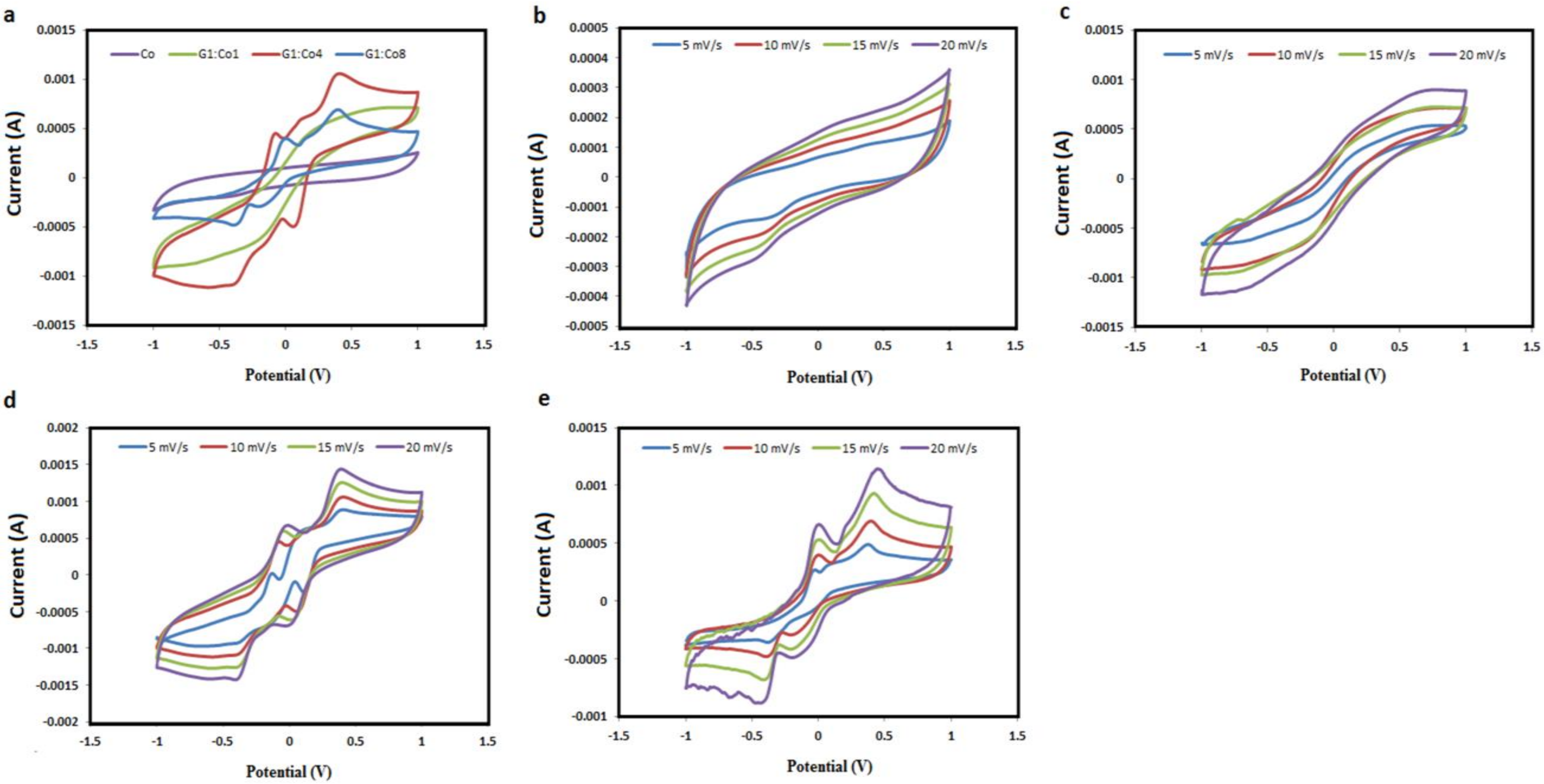

Figure 6.5: Cyclic voltammograms (CV) curves of (a) G1Co8, G1Co4, G1Co1 composites and cobalt at a scan rate of 10 mV/s, (b) Cobalt at different scan rates in the range of 5-20 mV/s, (c) G1Co1 at different scan rates in the range of 5-20 mV/s, (d) G1Co4 at different scan rates in the range of 5-20 mV/s and (e) G1Co8 at different scan rates in the range of 5-20 mV/s.

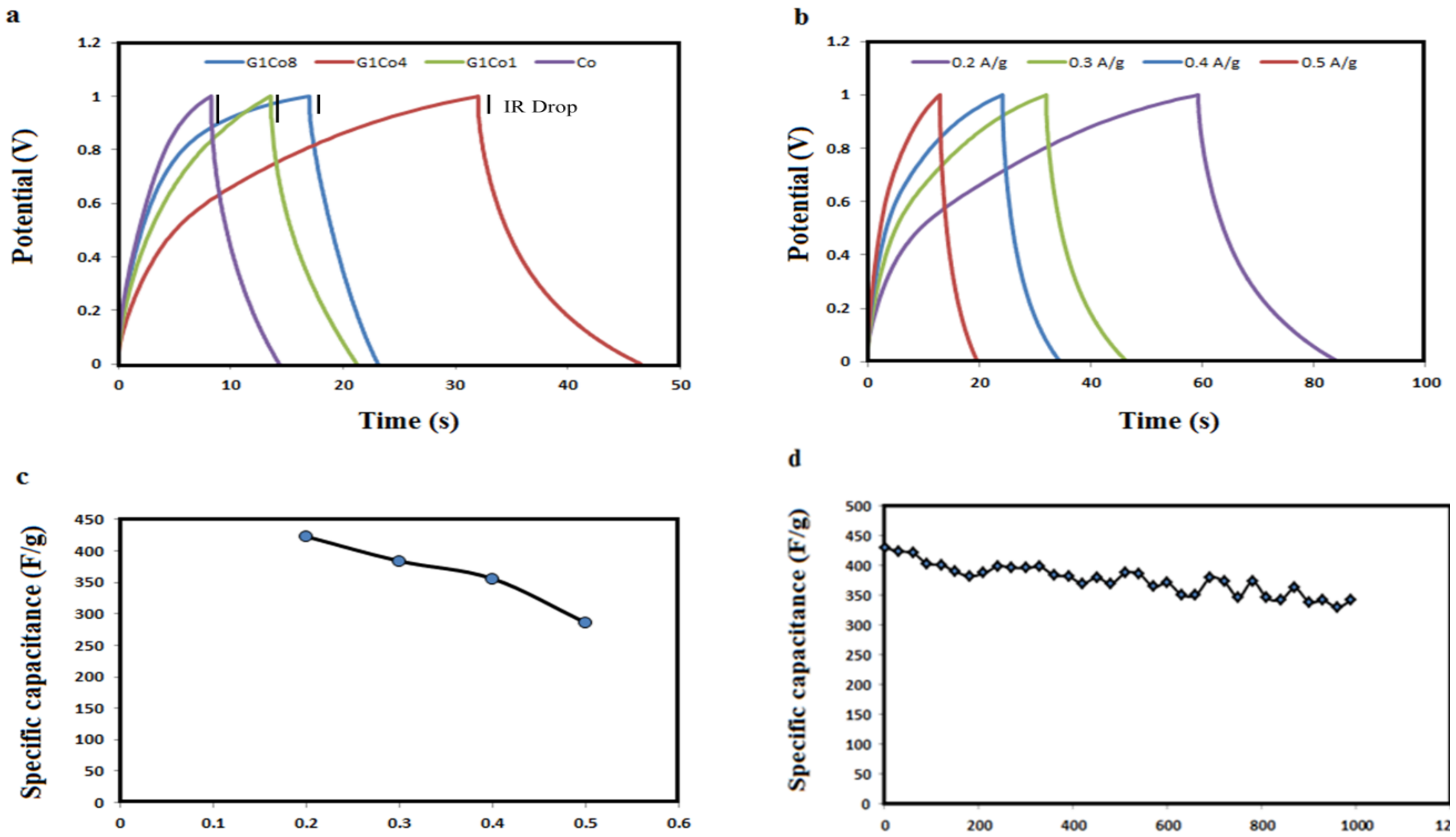

Figure 6.6: Charge-discharge curves of (a) G1Co8, G1Co4, G1Co1 composites and cobalt at a current density of 0.3 A/g (b) Charge-discharge curves of G1Co4 at different current densities (0.2, 0.3, 0.4 and 0.5 A/g) (c) variation of specific capacitance of G1Co4 against various current densities and (d) cycling test for G1Co4 at the current density of 0.2 A/g up to 1000 cycles.

The graphene-Co_3O_4 composite electrodes measured in a frequency range from 0.01 Hz to 100 kHz at an open circuit potential with alternating current (AC) amplitude of 10 mV were analysed as shown in Figure 6.7. All the impedance responses showed semi-circular loop at high frequency and a linear line at low frequency.

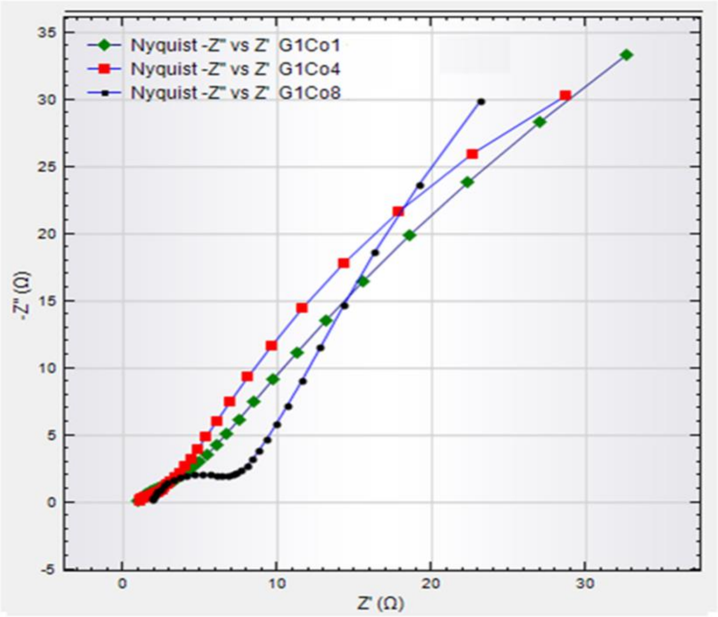

Figure 6.7: Nyquist plot of the G1Co8, G1Co4 and G1Co1 composites electrodes measured in a frequency range from 0.01 Hz to 100 kHz.

In comparison, the charge-transfer resistance (R_{ct}) values of the electrochemical capacitors decreases in the order of G1Co8 > G1Co1 > G1Co4, whereby the higher the charge-transfer resistance (R_{ct}) value of the electrode the lower its specific capacitance. This finding is in agreement with the measured specific capacitance presented earlier.

The energy storage (E) per mass and power density (P) of the graphene-Co_3O_4 composite electrochemical capacitors were calculated using the following equations 3.27 and 3.28 respectively [150]. The calculated energy storage and power density of the graphene-

Co_3O_4 composite electrochemical capacitors are presented in the Ragone plot (Figure 6.7), in which the reported data of other typical metal oxides and graphene-metal composites based electrochemical capacitor are also given [222], [225], [236], [263]–[267]. Among the graphene-Co_3O_4 composite electrochemical capacitors, G1Co4 electrode demonstrated superior energy density of 64 Wh/kg at a power density 103 kW/kg which is comparable with the reported literatures presented in the Ragone plot.

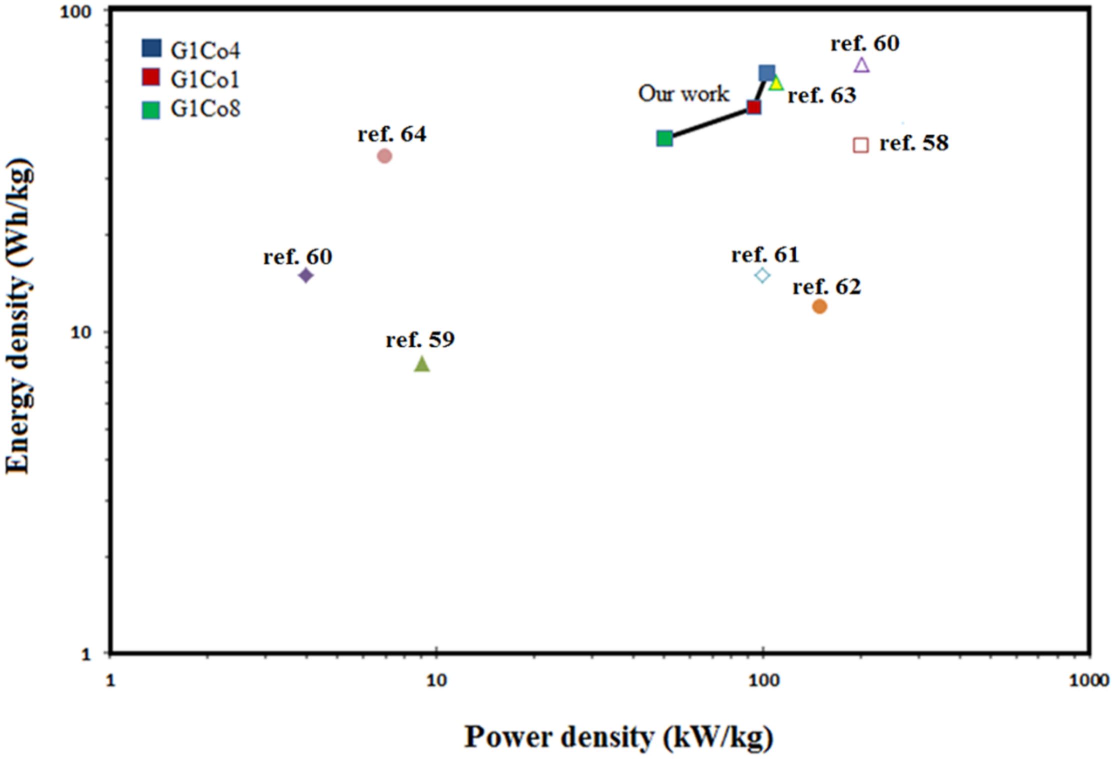

Figure 6.8: Ragone plot comparing the power and energy densities of G1Co8, G1Co4 and G1Co1 and other graphene/metal oxide composites electrodes.

6.4 Chapter Summary

In this chapter, we have successfully synthesised graphene-Co_3O_4 composites through a combined method of liquid phase exfoliation process and a solvothermal synthesis route. Experimental results confirmed that the addition of graphene significantly improved the electrochemical properties of the electrode. This improvement is high likely due to the pristine nature of the graphene as a good conductive support that enhanced the electronic structure of the as produced hybrid material. Different ratios of Co_3O_4 to graphene showed an obvious influence on the diffraction peaks, morphology and electrochemical properties of the composites. Electrochemical analysis indicated that G1Co4 composite electrode demonstrated a superior specific capacitance of 384 F/g at a current density of 0.3 A/g coupled with retention of 80% of its capacitance after 1000 cycles. This method of synthesis provides an effective, simple and practical route of preparing graphene-Co_3O_4 composites material for electrochemical capacitor applications.

Chapter 7

Solvothermal Synthesis of Graphene/$NiCo_2O_4$ Nanocomposite as an Electrode Material for Electrochemical Capacitors

7.1 Overview

The energy density of electrochemical capacitors is proportional to its capacitance and the square of the applied voltage. Hence, an increased performance in either or both factors is an effective way to improve the energy density [268], [269]. The capacitive performance of electrochemical capacitors depends mainly on the physiochemical properties of the electrode material. As the nanotechnology evolves, numerous compounds have been studied as feasible electrode materials, including eco-friendly transition metal oxides (TMOs) such as ZnO [20], Co_3O_4 [270], MnO_2 [271] and NiO [272], owing to their fast and reversible redox reactions to store charges, large natural abundance and low manufacturing cost [3], [103], [125], [268]. However, significant advances have distinguished mixed transition metal oxides (MTMOs) as promising and cost effective electrode materials, possessing unique oxidation states which enable multiple redox reactions, leading to superior capacitive properties when compared to TMOs [171], [269], [273].

Among different nanostructured of MTMOs, nickel cobaltite ($NiCo_2O_4$) with a general formula of $Co^{2+}_{1-x}C0^{3+}_{x}[Co^{3+}Ni^{2+}_{x}Ni^{3+}_{1-x}]O_4$ ($0<x<1$) where the Ni cations occupy the octahedral sites and the Co cations inhabit the octahedral and tetrahedral sites [5], [19] has drawn significant attention as electrode material due to its higher electrical conductivity (ranging from 0.05 to 10^{-6} S/cm) compared to single cobalt (333 S/cm) or nickel oxides (2×10^{-6} S/cm) component respectively [19]. This factor is advantageous for fast electrons transfer in an electrode thereby enhancing its electrochemical performance; especially its high rate capability [5], [19], [23]. Other attractive advantages of using nickel cobaltite as an electrode material are that it has low toxicity; low cost and its natural abundance [120], [264], [269].

It is well-known that the electrical conductivity of pseudocapacitive electrodes can be improved through the formation of an integrated structure with a conductive porous network and shortened ion transport paths by the integration of carbon materials (graphene, carbon nanotubes) [11], [51], [58], [120]. Graphene, an allotrope of carbon with superior electronic conductivity, mechanical, chemical stability and flexibility properties when compared to other carbon allotropes is an excellent candidate to serve as unique building block in composite materials [2], [11], [274]. Up to date, considerable works have been reported on the synthesis of graphene-$NiCo_2O_4$ nanocomposites for supercapacitor application. Guangyu et al. had reported the preparation of $NiCo_2O_4$ nanowires loaded on graphene via hydrothermal route. The experimental results demonstrated improved electrochemical performance of the composites electrode if compared to $NiCo_2O_4$ MTMO material [275]. Daniel Carriazo et al prepared superior $NiCo_2O_4$-graphene oxide nanocomposites using the microwave-assisted method [35]. Li Wang et al. successfully synthesized improved reduced graphene oxide-$NiCo_2O_4$ nanoflakes by combining the *in situ* assembling and thermal treatment methods [13]. A common concern among the mentioned literatures is the utilisation of the modified Hummers method followed by a chemical reduction process to produce reduced graphene oxide. These processes involved the use of highly reactive oxidising agents (potassium permanganate, sulphuric acid and sodium nitrate) and reducing agents (hydrazine) [46] which not only reduced the quality of the graphene [250], [276], but are generally harmful to the researchers and the environment.

Herein, we discuss the surface characteristics, structural and electrochemical properties of the graphene-$NiCo_2O_4$ nanocomposites obtained via a combination of facile solvent exfoliation and solvothermal processes (section 3.3.5). In using this synthesis route, highly pyrolytic graphite flakes are sonicated in an optimum ratio of ethanol and de-ionized water [45], [233], [277]–[280]. The use of ethanol as the exfoliation medium for this synthesis method presents a cheap, safe and bottom-up approach to produce high quality graphene. The graphene-$NiCo_2O_4$ nanocomposites with different weight ratios were prepared via solvothermal method, followed by proper thermal treatment to study the effect of the ratio of graphene- $NiCo_2O_4$ to its surface characteristics, structural and electrochemical properties.

7.2 Structural and Morphological characterisation

The physiochemical makeup of the various graphene-$NiCo_2O_4$ composites and $NiCo_2O_4$ were studied by XRD patterns illustrated in Figure 7.1. The diffraction peaks of the graphene-$NiCo_2O_4$ composites at 2 theta values of 18.9, 31.1, 36.7, 38.4, 44.6, 55.4 and 64.9^o were all well indexed to the crystal planes (111), (220), (331), (222), (400), (422), (511) and (440) of a face-centred cubic spinel $NiCo_2O_4$ (JCPDS card no 20-0781), space group Fd3m (227) with lattice constants of a = b = c = 8.1140 Å. The two diffraction peaks at 2 theta values of 26.8 and 54.9^o of the graphene-$NiCo_2O_4$ composites are in agreement to the (002) and (004) reflections of graphene, and no excrescent peaks were noticed on the as-prepared composites, implying that the graphene was homogenously surrounded by pure spinel $NiCo_2O_4$ structure. Furthermore, with the increased in mass loading of $NiCo_2O_4$ precursors, the intensification of the respective diffraction peaks were observed. The absence of any other peaks implies the phase-pure nature of the graphene-$NiCo_2O_4$ composites prepared in this work.

To further study the composition and structures of these samples, Raman analysis was performed with typical spectra range of 100 to 3200 cm^{-1} (Figure 7.2). For the graphene-$NiCo_2O_4$ composites, the distinct peaks associated with a graphene were observed at ~1579 cm^{-1} (G band) relating to the C-C bond stretching and the main Raman signature for all sp^2 carbons, at ~2725 cm^{-1} (2D band) and at ~1357 cm^{-1} (D band) which is the dominant sp^2 Raman signature of defects (disorder). The observed D band peak is most likely due to the presence of edges caused by the exfoliation process of graphite to graphene [45], [188], [209]. Further peaks observed at ~186, ~477, ~523 and ~671 cm^{-1} correspond to the F_{2g}, E_g, F_{2g} and A_{1g} models of $NiCo_2O_4$ respectively. Only the Co-O and Ni-O vibrations of $NiCo_2O_4$ composites were detected, while no peak corresponding to the OH group was observed, implying that pure $NiCo_2O_4$ composites were formed after calcination. This is in agreement with the observations reported in other literatures [118], [281], [282]. It can be observed from the respective spectra that the increase of $NiCo_2O_4$ precursors led to more dominate $NiCo_2O_4$ peaks. These results detailed the formation of graphene-$NiCo_2O_4$ composites in all samples which are in good agreement with the XRD results.

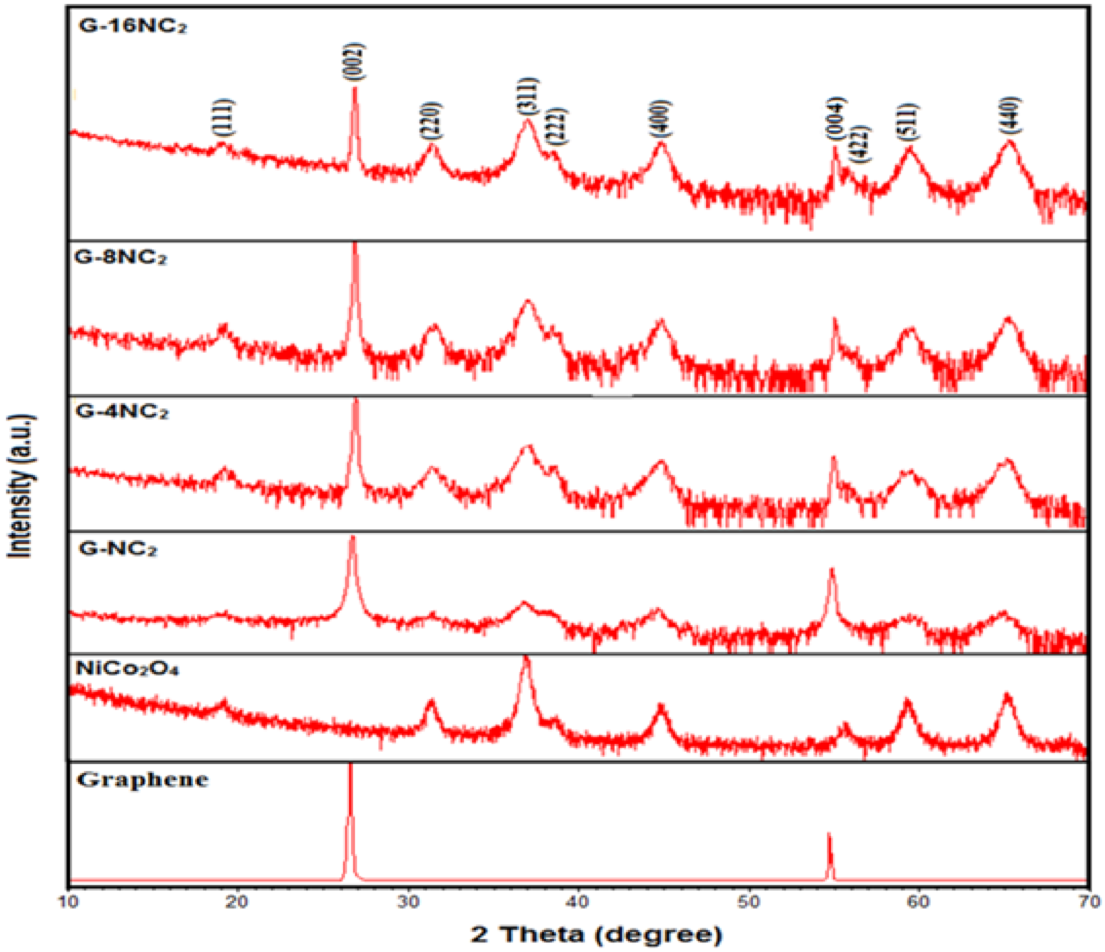

Figure 7.1: XRD pattern of $NiCo_2O_4$ and graphene-$NiCo_2O_4$ composites.

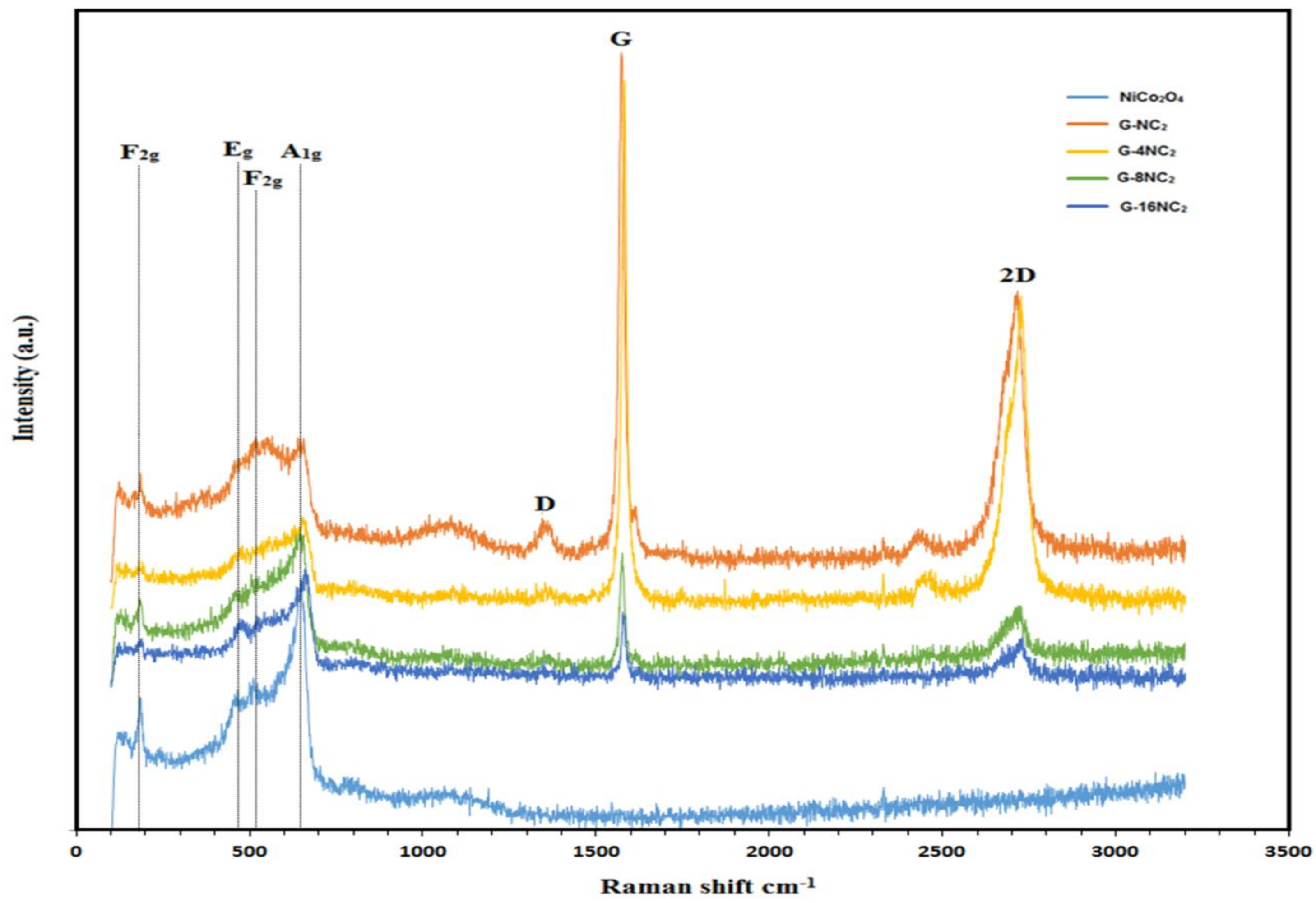

Figure 7.2: Raman spectra of $NiCo_2O4$ and graphene-$NiCo_2O_4$ composites.

Figure 7.3(a-d) depicts the surface morphology of the as-prepared graphene-$NiCo_2O_4$ composites GNC_2, G-4NC_2, G-8NC_2 and G-16NC_2 respectively. The FE-SEM images show the formation of $NiCo_2O_4$ nanoarrays with good and uniform distribution on the surface and edges of the graphene sheets. It can be seen that the vertical aligned graphene sheets intersecting with one another forming an intrinsic transportation network for the $NiCo_2O_4$ nanoarrays. Nonetheless, with an increase $NiCo_2O_4$ precursor, more heavy clusters (agglomeration) of the $NiCo_2O_4$ nanoarrays were formed on the graphene sheets (Figure 7.3 (c-d)).

For further understanding of the morpholgy and microstructure of the as-prepared graphene-$NiCo_2O_4$ composites, TEM, high resolution TEM (HRTEM) and energy-dispersive X-ray spectroscopy (EDS) analysis were also carried out. Figure 7.4a depicts a transparent plate-like graphene sheet which was very stable under the electron beam. $NiCo_2O_4$ composites were observed to be consisted of series of bead-chains of nanoarrays, as shown in the TEM image (Figure 7.4b). These nanoarrays of $NiCo_2O_4$ particles were highly dispersed and well anchored onto the graphene sheets (Figure 7.4c). No free $NiCo_2O_4$ nanoparticles were discerned outside the graphene sheets. The poly-crystalline nature of the prepared graphene-$NiCo_2O_4$ composites is evidenced by the random orientation of the lattice phase shown in Figure 7.4d.

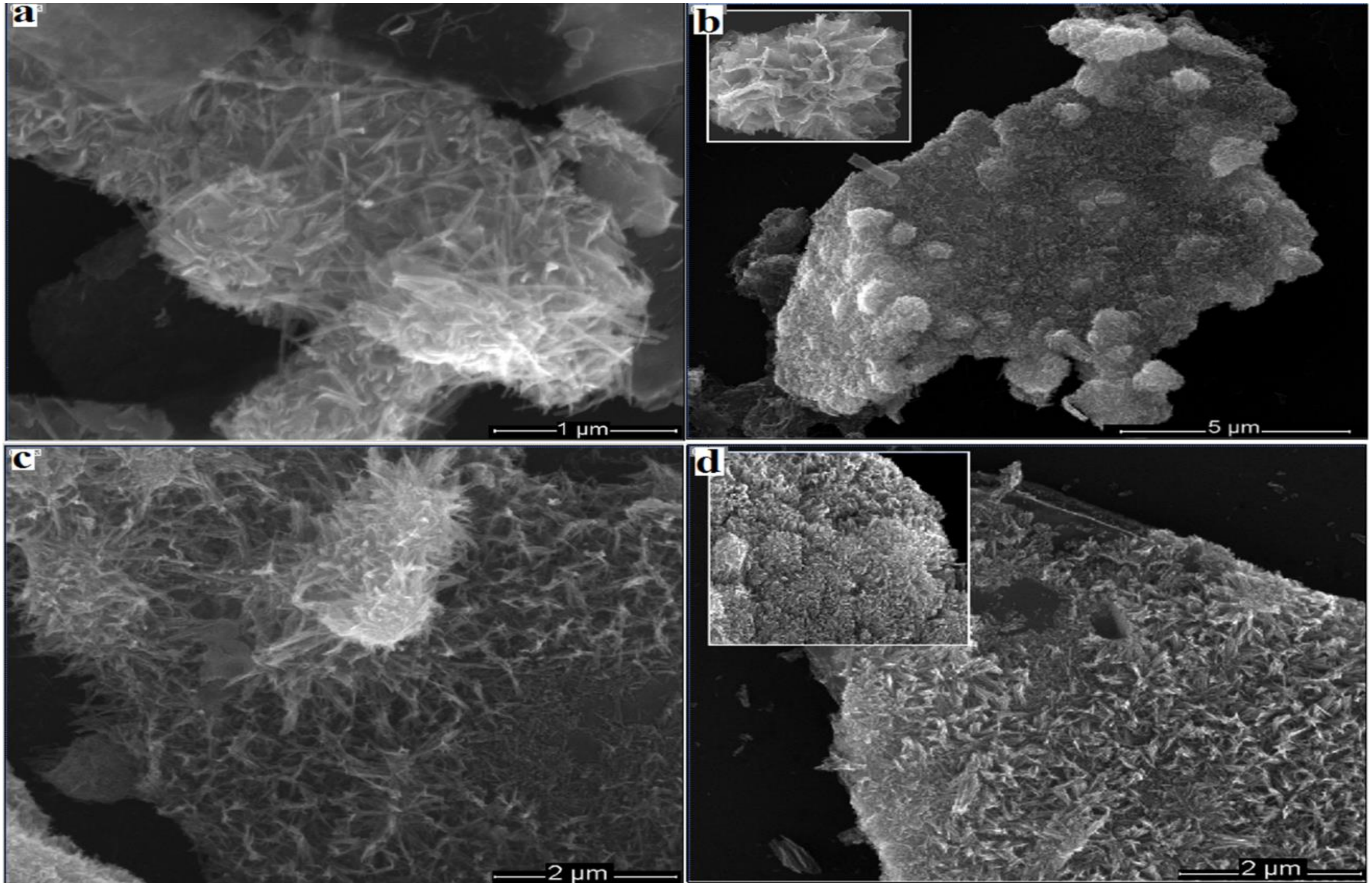

Figure 7.3: FE-SEM images of (a) GNC2, (b) G-4NC2, (C) G-8NC2 and (d) G-16NC2. Inset in (b) and (d) show high magnification of G-4NC2 and G-16NC2 respectively.

The lattice fringes with interplanar spacing of 0.28 and 0.47 nm corresponds to the (220) and (111) plane of the spinel phase $NiCo_2O_4$ respectively. This is in agreement with the XRD result as previously reported [23]. The EDS spectrum of the graphene-$NiCo_2O_4$ composites in Figure 7.5 showed that the composites consisted of C, O, Co and Ni peaks respectively. The Si peak is due to the silicon substrate used during characterisation. The atomic ratio of Ni to Co is approximately 1:2, which is in order with the stoichiometric ratio of $NiCo_2O_4$. No other peaks were observed, confirming the purity of the as prepared graphene-$NiCo_2O_4$ composites.

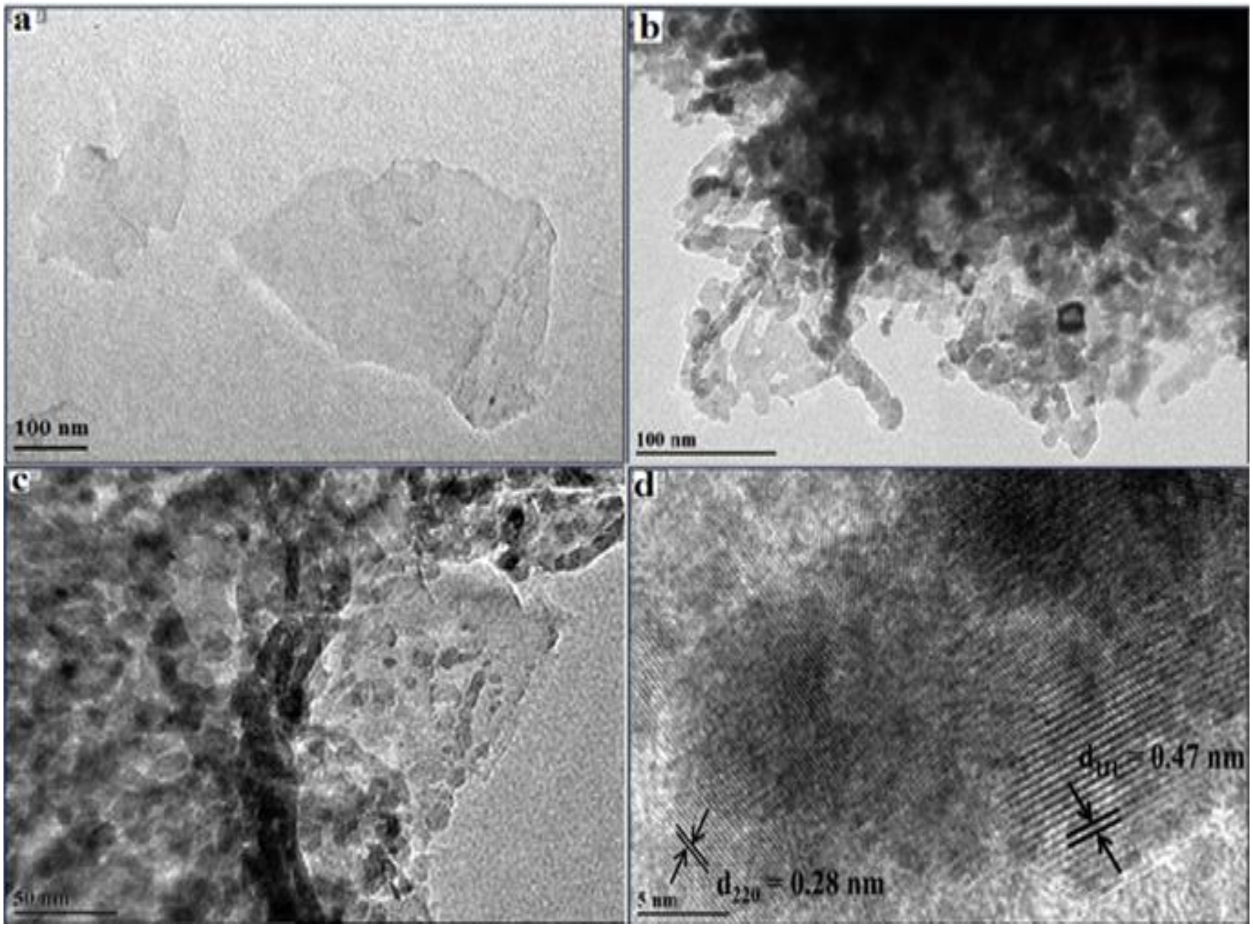

Figure 7.4: TEM images of (a) graphene (b) $NiCo_2O_4$ (c) graphene-$NiCo_2O_4$ composite and HRTEM image of (d) graphene-$NiCo_2O_4$ composite (e) the EDS spectrum and its corresponding SEM image of graphene-$NiCo_2O_4$ composite.

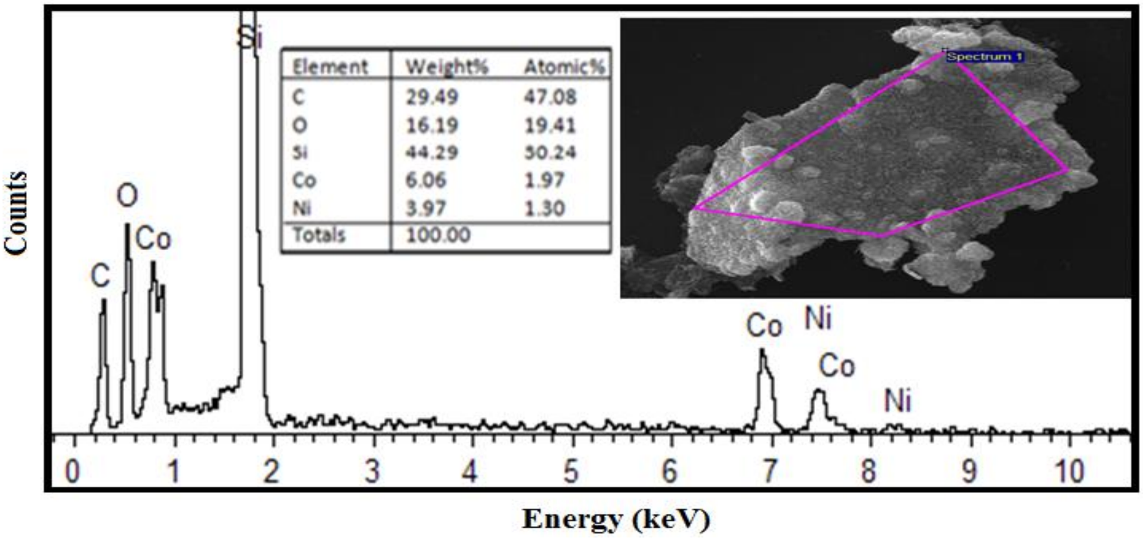

Element	Weight%	Atomic%
C	29.49	47.08
O	16.19	19.41
Si	44.29	30.24
Co	6.06	1.97
Ni	3.97	1.30
Totals	100.00	

Figure 7.5: The EDS spectrum and its corresponding SEM image of graphene-$NiCo_2O_4$ composite.

7.3 Electrochemical performance

Figure 7.6a depicts the results of cyclic voltammetry analysis used in studying the electrochemical behavior of the $NiCo_2O_4$ and graphene-$NiCo_2O_4$ composite electrodes using 2 M KOH aqueous solution. The analysis was performed in the potential range between -1 V to 1 V at a sweep rate of 50 mV/s. The main purpose for using both positive and negative bias modes is to reflect the symmetrical nature of the electrodes in the two electrode cell [283]. The coupled pairs of well-defined peaks are clearly observed in anodic and cathodic sweeps in all CV curves of the samples, mainly due to the reversible redox reactions of Co^{2+}/Co^{3+} and $^{+}$ transitions in $NiCo_2O_4$ material. The electrochemical reaction of $NiCo_2O_4$ in an alkaline electrolyte can be expressed as follows:

$$NiCo_2O_4 + OH^- + H_2O \leftrightarrow NiOOH + 2CoOOH + e^- \qquad (7.1)$$

$$MOOH + OH^- \leftrightarrow MO_2 + H_2O + e^- \qquad (7.2)$$

where M is indicative of Co or Ni ions. As observed, the integrated area of the as-prepared graphene-$NiCo_2O_4$ based electrodes are larger compared to $NiCo_2O_4$ based electrodes which clearly indicates the improvement in capacitance performance; likely due to the synergistic effect of the pseudocapacitance and double layer capacitance of the composite materials. Additionally, these CV results showed that the integrated area for each composite was significantly different; revealing that the amount of $NiCo_2O_4$ loaded on the graphene sheets greatly affects the electrochemical behavior of the respective electrode.

Further CV analysis was performed on G-16NC_2 at different scan rates; it can be seen from Figure 7.6b that there were no significant changes in the shape of the CV curves, demonstrating the high electrochemical reactivity of the composite electrode materials [23]. Furthermore, an increase in scan rate led to the anodic and cathodic peak potentials shifted towards more anodic and cathodic directions, respectively, these shifts occurred as a result of the electric polarisation strengthening at a higher scan rate [13] caused by the ion diffusion rate limited to satisfy the electronic neutralisation during redox reaction [284]. The galvanostatic charge/discharge analysis results of the as-prepared electrode materials measured by chronopotentiometry from 0 to 1 V at a constant current density of 0.5 A/g and the corresponding results are depicted in Figure 7.6c. The G-8NC_2 electrode demonstrated the longest discharge time implying that the electrode has the highest charge storage capability. The coulombic efficiency (η) of the as-prepared electrodes was calculated from the charge time and discharge time profiles shown in Figure 7.6c by the following equation [285]:

$$\eta = \frac{t_D}{t_C} \times 100\% \qquad (7.7)$$

where t_C and t_D are the time of charge and discharge in seconds respectively. The calculated coulombic efficiency (η) obtained are G-16NC_2 (61%), G-8NC_2 (74%), G-4NC_2 (73%), GNC_2 (63%) and $NiCo_2O_4$ (67%). The charge/discharge profile of an ideal capacitor is expected to be triangular in nature (i.e. η = unity), however the deviation observed is due to the pseudocapacitive nature of the electrode materials [286] which also supports the cyclic voltammetry results. In order to obtain more information on the charge storage ability of the electrode, the specific capacitances were calculated according to the equation 3.22 [195]:

The calculated specific capacitance of the as-prepared electrode materials at the current density of 0.5 A/g are G-16NC_2 (352 F/g), G-8NC_2 (698 F/g), G-4NC_2 (493 F/g), GNC_2 (281 F/g) and $NiCo_2O_4$ (247 F/g) respectively. The electrochemical performance of the electrode is comparable to those reported in [14], [263], [287]. Figure 7.6d shows the galvanostatic charge/discharge curves of the G-8NC_2 electrode within the potential window range of 0 to 1 V at various current densities (0.5, 0.6, 0.7, 0.9 and 1 A/g respectively). The excellent electrochemical reversibility of the electrode material was once again manifested, as the charge/discharge curves remained almost symmetrical throughout the analysis at different charge/discharge current densities.

From the discharge profiles, the specific capacitance was calculated using equation 3.22 and plotted against current density as illustrated in Figure 7.7a. The results show that the specific capacitance is higher at lower current density, generally due to lower Ohmic drop that allows the inner active sites of the electrode to be fully utilised. [258]. Figure 7.7b shows the cyclic stability of the G-8NC_2 electrode, which was analysed over 5000 cyclic galvanostatic charge-discharge test at a current density of 1 A/g within a potential range of 0-1 V. The results show that the electrode retained 75% of its initial capacitance at the end of analysis, which is a good indication of its superior electrochemical cyclability. The decay of capacitance observed can be attributed to the weak interfacial contact between the electrode material and the electrolyte during the continuous charge/discharge process [272], [288].

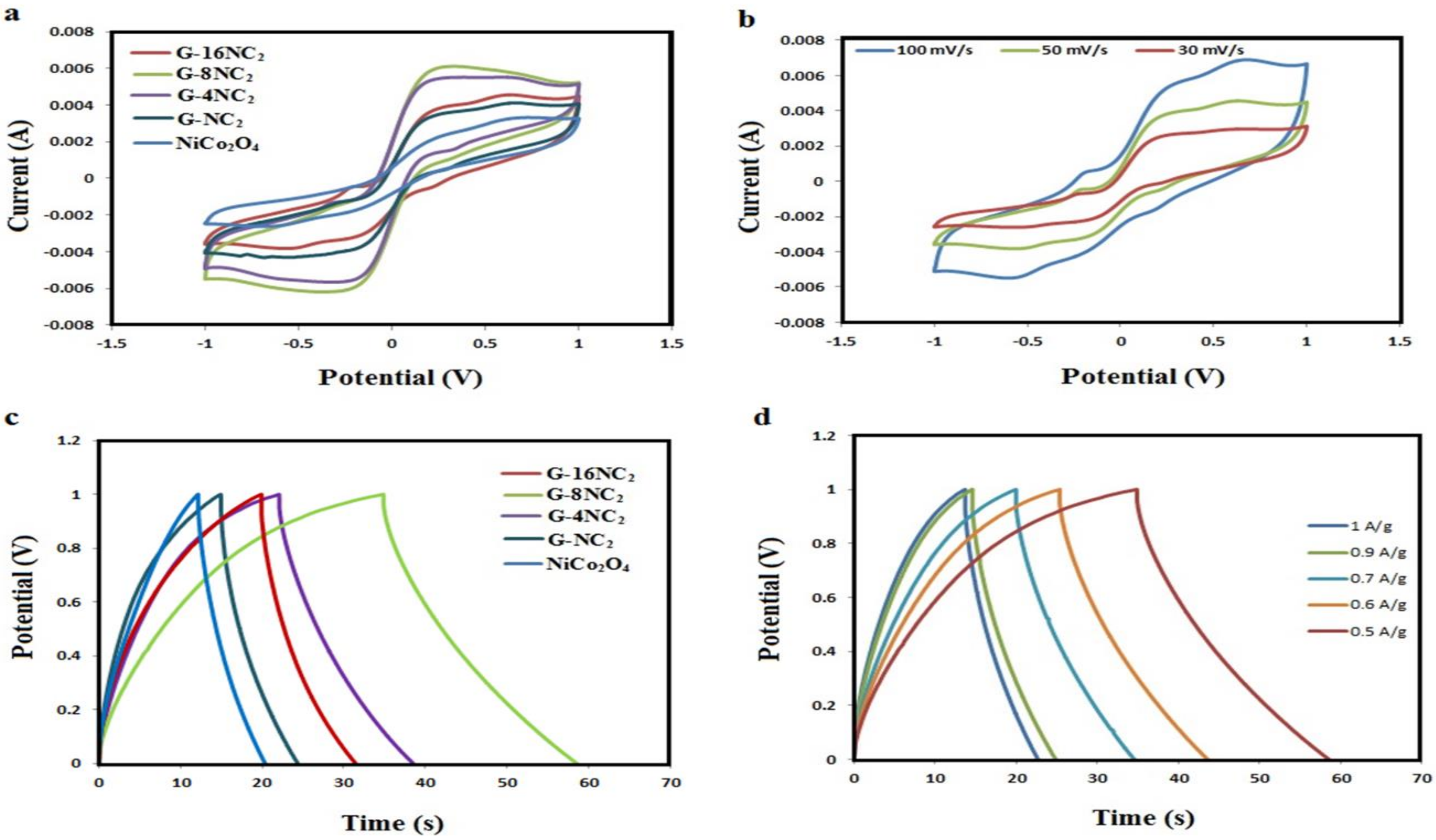

Figure 7.6: Cyclic voltammograms (CV) curves of (a) GNC2, G-4NC2, G-8NC2 and G-16NC2 composites and $NiCo_2O_4$ at a scan rate of 50 mV/s, (b) G-16NC2 at different scan rates in the range of 30-100 mV/s, (c) Charge-discharge curves of GNC2, G-4NC2, G-8NC2 and G-16NC2 composites and NiCo2O4 at a current density of 0.5 A/g (d) Charge-discharge curves of G1Co4 at different current densities (0.5, 0.6, 0.7, 0.9 and 1 A/g).

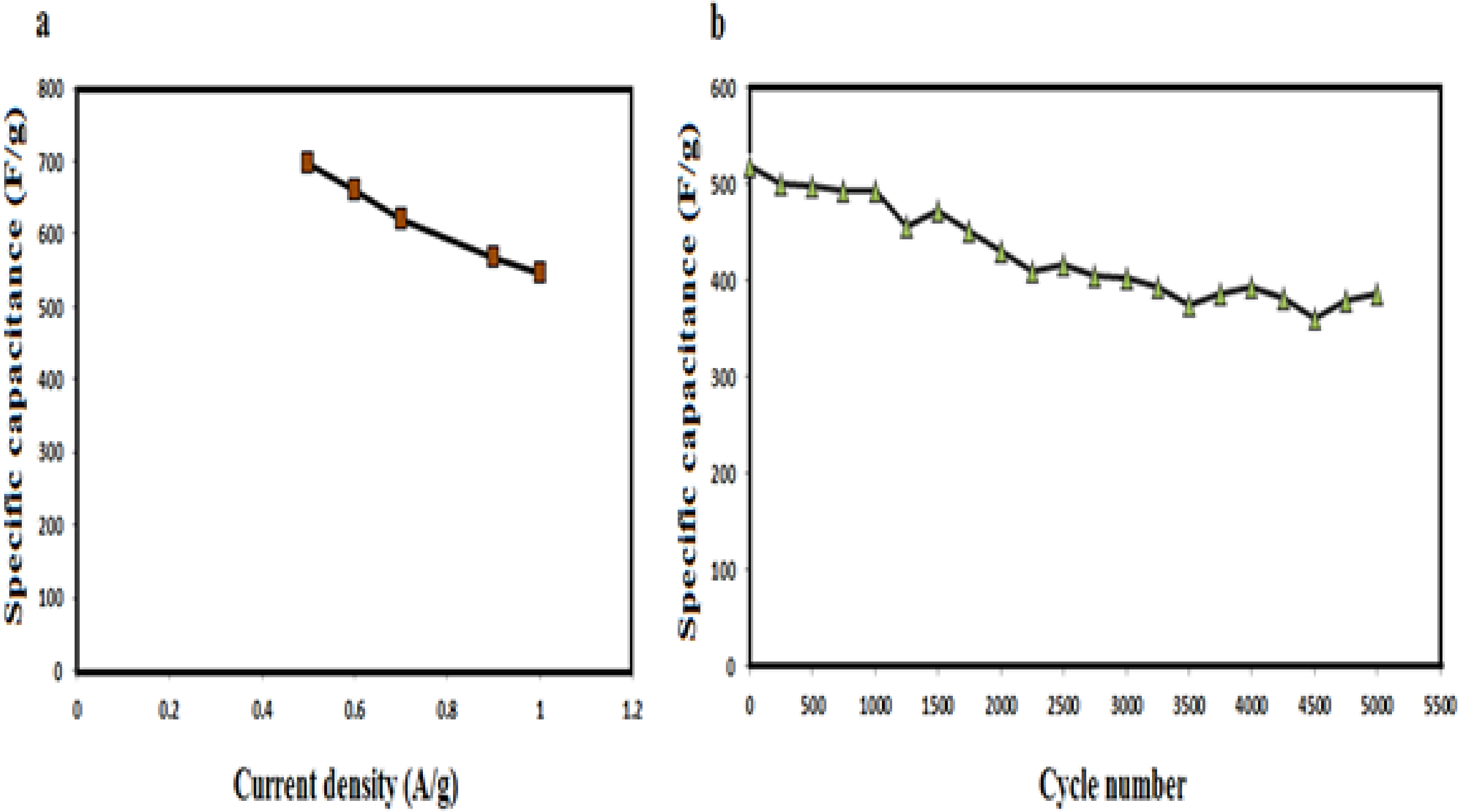

Figure 7.7: (a) Specific capacitance of G-8NC2 at different current densities and (b) cycling performance of G-8NC2 composite electrode for 5000 cycles at a current density of 1 A/g.

The Nyquist plots (Figure 7.8a) of the graphene-$NiCo_2O_4$ composites based electrode were semicircular over the high frequency range and a linear line at low frequency region. While the electrochemical capacitors have similar equivalent series resistance (ESR), they showed markedly different R_{ct} values, as observed from the radius difference of the semicircle on the respective Nyquist plot. In comparison, the charge-transfer resistance (R_{ct}) values of the graphene-$NiCo_2O_4$ composite electrochemical capacitors decreases in the order of GNC_2 > G-16NC_2 > G-4NC_2 > G-8NC_2. The lower R_{ct} value reflects improved capacitive behavior and these results are in agreement with the other electrochemical results presented earlier.

To further analyse the electrochemical performance of the graphene-$NiCo_2O_4$ composite electrochemical capacitor, their energy density (E) and power density (P) were estimated from equations 3.27 and 3.30 respectively [224]. The calculated results were presented in a Ragone plot (Figure 7.7b) and were compared to the reported data of other typical metal oxides and graphene-metal composites based electrochemical capacitors [120], [167], [236], [263], [264], [266], [267], [288]. The G-8NC_2 based electrode was measured with an energy density of 96.9 Wh/kg at power density of 13.9 kW/kg, which is relatively higher than other reported graphene-$NiCo_2O_4$ composite based electrochemical electrodes.

The improved electrochemical performance obtained from the experimental results can be attributed to the following factors: (i) the integration of graphene with $NiCo_2O_4$ which significantly improved the electrical conductivity of the hybrid structure by providing a fast electron transfer and large contact area for electrolyte ions penetration. (ii) the facile and green approach of producing graphene in this work preserved the pristine structure of graphene resulting in better electrical properties and (iii) the highly-dispersed $NiCo_2O_4$ composites on the graphene sheets possess multiple oxidation states hereby enabling rich redox reactions for pseudocapacitance [19].

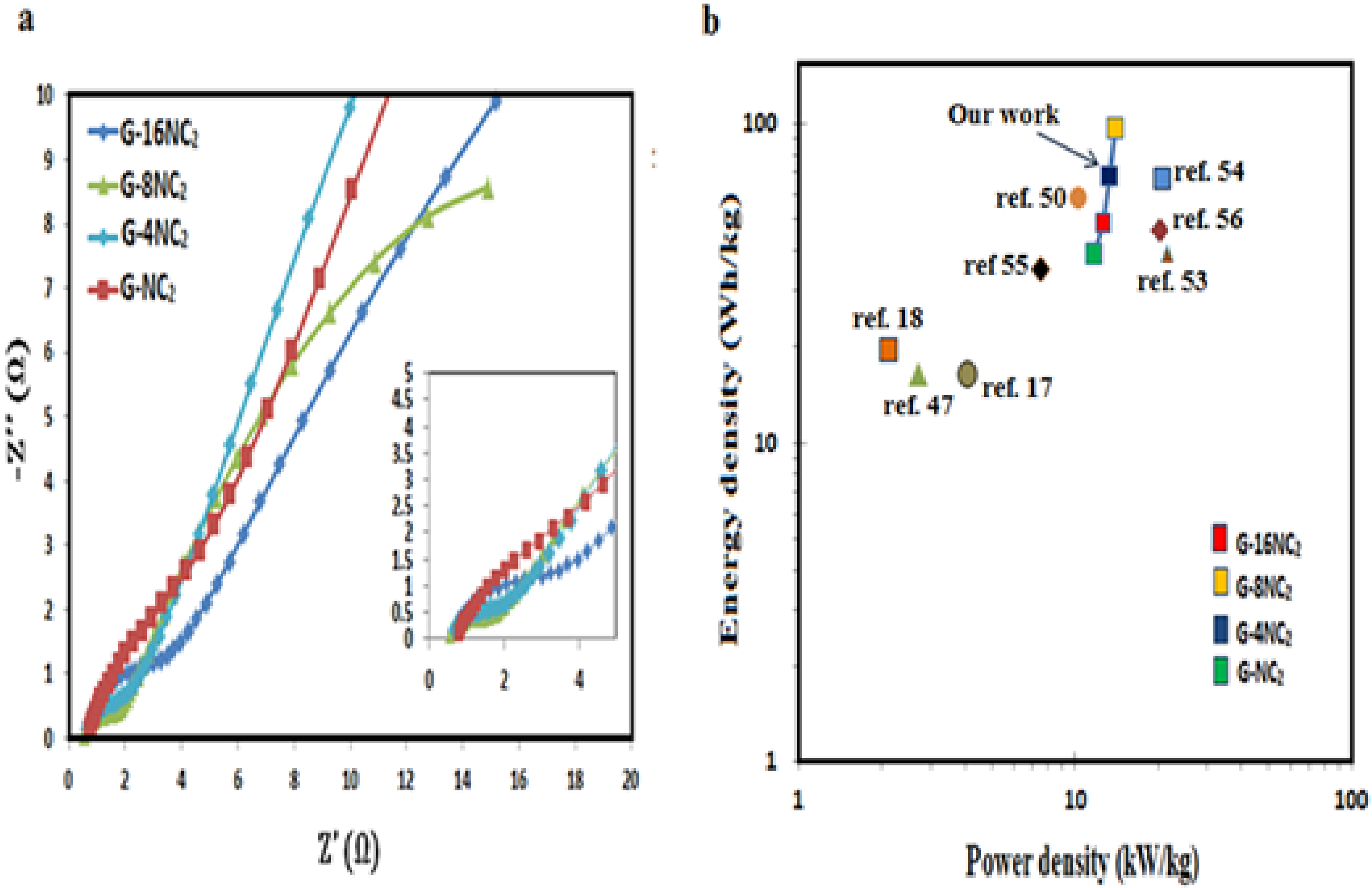

Figure 7.8: (a) Nyquist plot of the GNC2, G-4NC2, G-8NC2 and G-16NC2 composites electrodes and (b) Ragone plot comparing the power and energy densities of GNC2, G-4NC2, G-8NC2 and G-16NC2 and some selected composites electrodes.

The synergistic effects resulting from the combination of the graphene and $NiCo_2O_4$ composites prevents the restacking of graphene sheets and agglomeration of $NiCo_2O_4$, subsequently providing a larger electrochemically active surface area for exploiting the advantages of double-layer capacitance provided by graphene and pseudocapacitance from $NiCo_2O_4$ nanomaterials [275].

7.4 Chapter Summary

Graphene-$NiCo_2O_4$ composites were successfully prepared through a combined system of liquid phase exfoliation route and solvothermal synthesis process. The experimental results detailed that the addition of graphene enhanced the electrochemical properties of the electrodes. It was also obvious that the different ratios of $NiCo_2O_4$ to graphene significantly influenced the morphology, XRD diffraction peaks and electrochemical properties of the composites. G-8NC_2 composite electrode displayed a superior specific capacitance (698 F/g at a current density of 0.5 A/g) and good cycling stability (74% capacity retention after 5000 cycles at current density of 1 A/g). This method of synthesis provides a facile, effective and green synthesis process of preparing graphene which is vital for practical sustainability, as well as graphene-$NiCo_2O_4$ composites materials for electrochemical capacitor applications.

Chapter 8

Synthesis of $NiMoO_4$ Nanorods on Graphene and Superior Electrochemical Performance of the Resulting Ternary Based Composites

8.1 Overview

The electrode material is an integral part of the electrochemical capacitor that hugely determines its storage performance which sequentially affects the efficiency and versatility of energy to meet the demands of practical use [9], [10], [103]. To achieve these requirements, research and advances had focused on the development of electrode materials with tailored structures, low cost and high reactivity to deliver improved electrochemical performance over a prolonged period of time [22], [151], [269], [289]. The evolution on the studies of numerous feasible electrode materials have advanced from transition metal oxides to binary transition metals oxides owing to the better electrical conductivity and the ability to have multiple oxidation states which results in higher capacitance [22], [103], [290], [291].

Binary transition metals oxides (BTMOs) such as $NiCo_2O_4$ [287], $NiMoO_4$ [292], $CoMoO_4$ [291] and Zn_2SnO_4 [293] employ the synergistic effects of two pure oxides to enhance its electrochemical performance by a broaden potential window, enhanced conductivity, more interactive sites and an ameliorated stability [103]. Nickel molybdate ($NiMoO_4$), among various BTMOs belongs to the metal molybdate family, has drawn research interest due to its higher electrical conductivity (ca. 10^{-6} S/cm) compared to that of nickel oxide (NiO) and its high redox reactivity due to the presence of multiple oxidation states [290], [294]. Other advantages include environmental friendliness, relative abundance, and low cost [22], [121], [151], [295], [296]. Although $NiMoO_4$ is conceived as a promising, effective and scalable electrode material for electrochemical capacitors, advances have shown that BTMOs still suffer from poor electrical conductivity [22], [103], [297] and poor cycling stability [103], leading to a less satisfactory electrochemical performance. Research has indicated that integrating metal oxides with carbon-based materials improves their electrochemical performance. Carbonaceous compound normally can provide a rigid porous structure with more active sites that is beneficial for ion transport kinetics as well as the formation of capacitive double layer [22], [36], [56], [58], [103], [139].

Graphene, a two-dimensional allotrope of carbon with reported outstanding electrical conductivity, high experimental specific surface area, wide potential windows, good chemical and thermal stability if compared to other carbon allotropes is considered as an ideal conductive scaffolds for composite electrodes [2], [11], [70], [298]. Considerable efforts have been made to synthesise graphene-$NiMoO_4$ nanocomposites as electrode material for supercapacitors. T. Liu et al [36] demonstrated a microwave-solvothermal technique route for preparing reduced graphene-nickel molybdate composites and the experimental results exhibited an improved specific capacitance compared to that of pure nickel molybdate at the same current density. Li et al [299] synthesised $NiMoO_4$ nanosheets anchored on graphene sheets by hydrothermal approach, in which a superior capacitance value for the composite was reported. The reported works had used reduced graphene oxide prepared by modified Hummers method with subsequent chemical reduction process using strong oxidants and reductants. It has been known that the modified Hummers method utilised strong acids at high temperature resulting in structural defects and heteroatomic impurities incorporated into the graphitic structure

[46], [250], [300], [301]. This synthesis method is not only time consuming, laborious with multi-step process and unsafe to the researcher and environment at large; the presence of structural defects also results in inferior electrical properties compared to pristine graphene [276], [302].

Based on the above considerations, it is of paramount importance to overcome all the above-mentioned problems in order to achieve a scalable, safe and cost-effective route to produce graphene-$NiMoO_4$ nanocomposites with superior electrochemical performance.

In this chapter, a simple approach to synthesise graphene-$NiMoO_4$ nanocomposites using a combination of direct liquid-phase exfoliation of graphite and solvothermal route is employed (section 3.3.6). Graphene is synthesised via direct liquid-phase exfoliation of graphite in an apt ratio of water and ethanol, the as-synthesised graphene is then mixed with the $NiMoO_4$ precursors to produce graphene-$NiMoO_4$ nanocomposites via solvothermal method. To further study the synergistic effects of the nanocomposites, different weight ratios of graphene-$NiMoO_4$ nanocomposites were prepared and their surface and electrochemical properties were evaluated thoroughly

8.2 Structural and Morphological characterisation

The crystal structure and crystalline phase of $NiMoO_4$ and graphene-$NiMoO_4$ nanocomposites were investigated with XRD analysis and the results are depicted in Figure 8.1. The diffraction peaks of the graphene-$NiMoO_4$ nanocomposites show the diffraction patterns of α-phase $NiMoO_4$ with a monoclinic structure and the C2/m space group. The patterns of the graphene-$NiMoO_4$ can be indexed to the cell parameters of $a = 9.5660$ Å, $b = 8.7340$ Å, $c = 7.6490$ Å, $\alpha = \gamma = 90^o$ and $\beta = 114.22^o$.

The XRD peaks of $NiMoO_4$ and graphene-$NiMoO_4$ nanocomposites are in good agreement with the standard JCPDS card no 086-0361 and complement with those reported in literatures [22], [170], [297], [303] . This clearly indicates that pure $NiMoO_4$ nanocomposites were formed from the precursor with no individual phases of nickel or molybdate oxides detected. It is observed that the increase in mass load of the precursors lead to a corresponding increase in intensities of the respective diffraction peaks of the nanocomposites formed. The additional peaks at 2θ values of 26.6 and 54.7^o are attributed (002) and (004) reflections of graphene. Hence, the XRD analysis confirms the successful synthesis of graphene-$NiMoO_4$ nanocomposites.

The Energy dispersive X-ray (EDX) spectrum (Figure 8.2a) displays peaks corresponding to the C, Ni, Mo, and O elements, confirming the composition of the nanocomposites. The Si element is present due to the silicon substrate used during characterisation. No other peaks were detected signaling the purity of the nanocomposites. A typical graphene-$NiMoO_4$ nanocomposites Raman spectrum shown in Figure 8.2b shows the characteristic G (1573 cm^{-1}), D (1382 cm^{-1}) and 2D (2714 cm^{-1}) peaks belonging to the graphene skeleton which is not visible in the $NiMoO_4$ Raman spectrum. The intensive peak at 958 cm^{-1}, two strong maximum at 905 and 704 cm^{-1} and a group of weak peaks at 486, 384 and 256 cm^{-1} denoting the stoichiometric α-phase $NiMoO_4$.

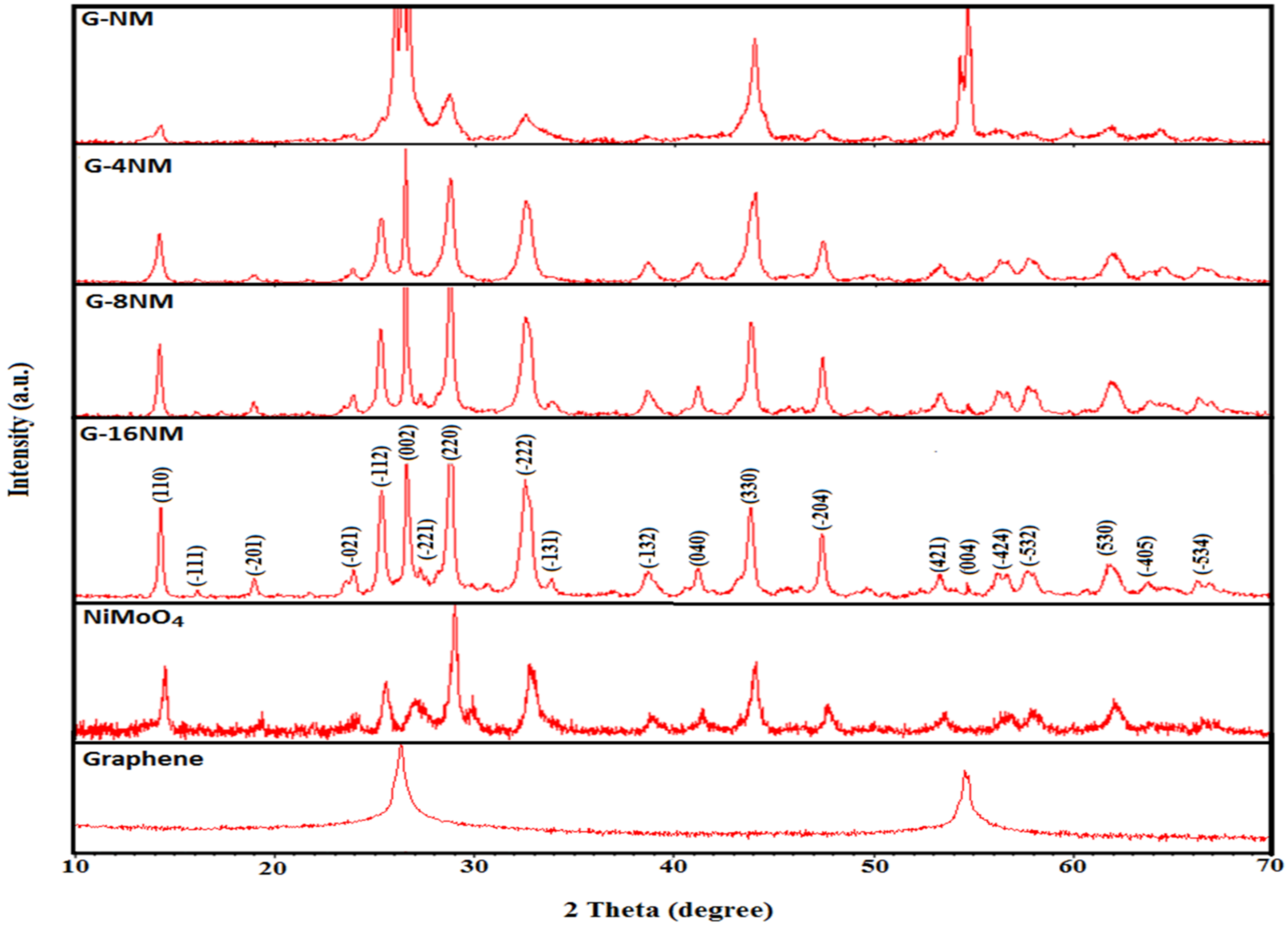

Figure 8.1: XRD pattern of graphene, $NiMoO_4$ and graphene- $NiMoO_4$ nanocomposites.

The peaks at 958 and 905 cm^{-1} are results of the symmetric and asymmetric stretching modes of the terminal Mo==O bond, while the Ni—O—Mo symmetric stretch is responsible for the peak at 704 cm^{-1}. The peaks at 486 and 384 cm^{-1} have been ascribed to the bending mode of Mo—O and the peak at 256 cm^{-1} is attributed to the deformation mode of Mo—O—Mo. This is consistent with reported literatures [297], [304] and is in agreement with the XRD results.

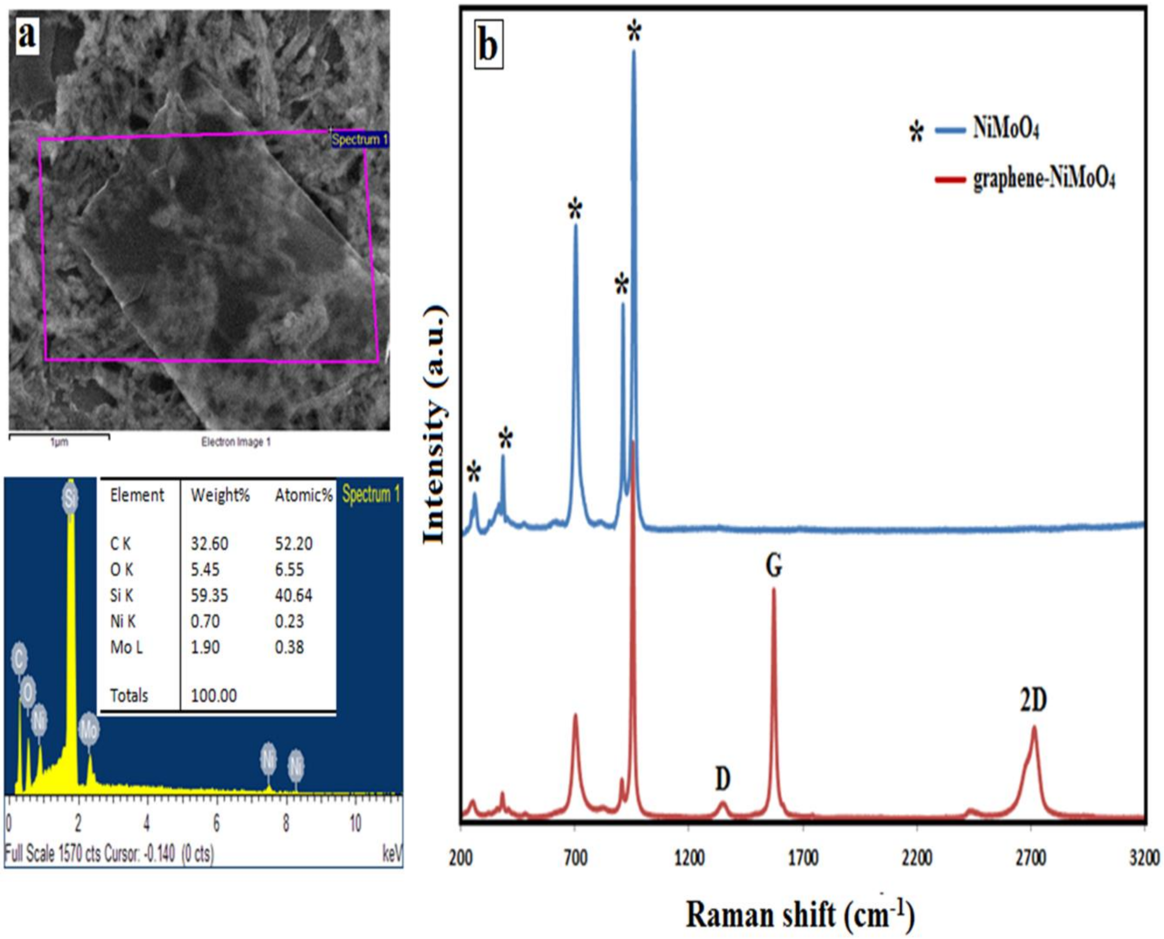

Element	Weight%	Atomic%
C K	32.60	52.20
O K	5.45	6.55
Si K	59.35	40.64
Ni K	0.70	0.23
Mo L	1.90	0.38
Totals	100.00	

Figure 8.2: Figure 8.2: Images of (a) EDX spectrum (scanning of SEM analysis) and (b) Raman spectra of $NiMoO_4$ and graphene-$NiMoO_4$ nanocomposite.

From the FE-SEM analysis, the as synthesised $NiMoO_4$ nanorods were approximately 4 to 6 μm in length (Figure 8.3a). These nanorods are observed to be anchored successfully on the surface and around the edges of the graphene sheets via solvothermal process (Figure 8.3(b-e)). Higher ratio of precursor used resulted in the formation of shorten $NiMoO_4$ nanorods, which tend to form agglomerations on the surface of the graphene sheet. Further insight into the morphology structure of the nanocomposites is demonstrated by transmission electron microscopy (TEM). The rod-like morphology observed in TEM images of $NiMoO_4$ (Figure 8.4a) is in accordance with the FESEM observations. From Figure 8.4b, the observed dark regions shows clusters of $NiMoO_4$ nanorods formed on the graphene sheet. The high resolution TEM image (HRTEM) of the graphene-$NiMoO_4$ nanocomposites (Figure 8.4c) reveals the interplanar spacing of ~ 0.27 nm corresponding to the (222) plane of $NiMoO_4$ [22], [297], [303] given in the XRD analysis.

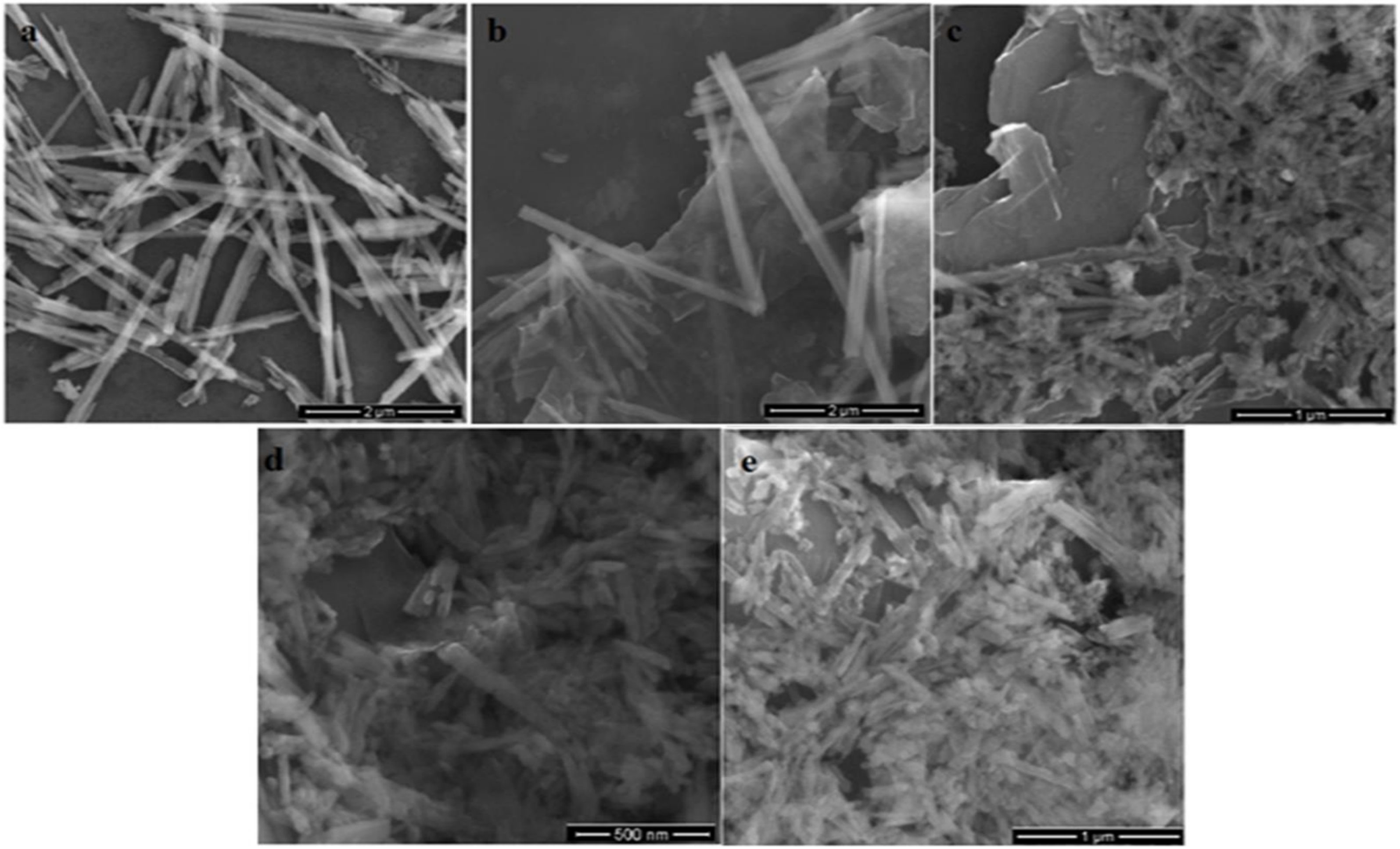

Figure 8.3: FE-SEM images of (a) $NiMoO_4$, (b) G-NM, (c) G-4NM, (d) G-8NM and (e) G-16NM.

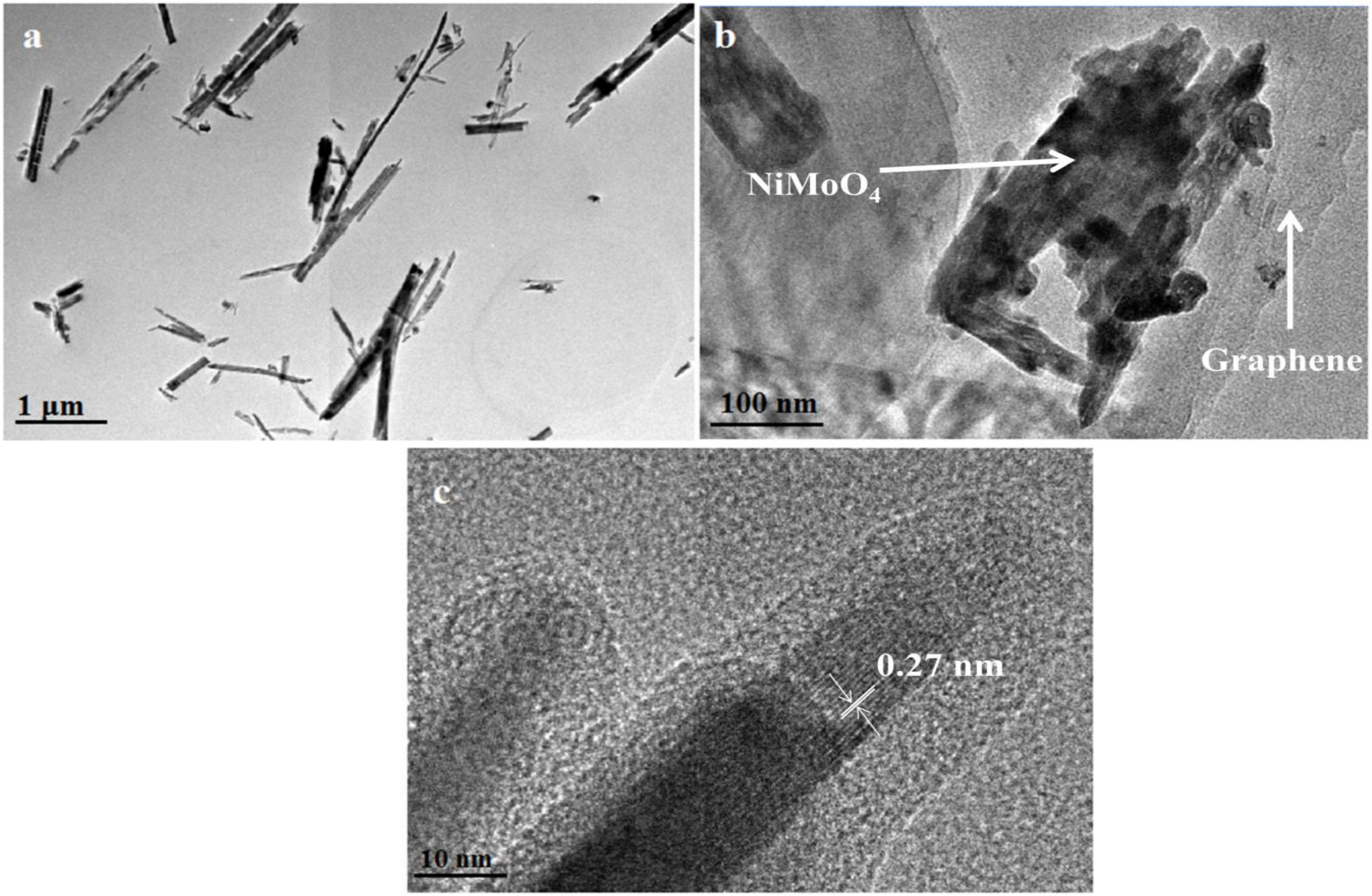

Figure 8.4: TEM images of (a) $NiMoO_4$, (b) graphene-$NiMoO_4$ nanocomposite and (c) HRTEM image of (b) graphene-$NiMoO_4$ nanocomposite.

8.3 Electrochemical performance

In order to evaluate the potential of graphene-$NiMoO_4$ composites as electrodes for electrochemical capacitors; cyclic voltammetry (CV) analysis was conducted within the potential range of -1V and 1V. Figure 8.5a shows the typical cyclic voltammograms of the $NiMoO_4$ and graphene-$NiMoO_4$ composite electrodes at a scan rate of 50 mV/s. The redox peaks seen in each cyclic voltammogram can be ascribed to the capacitive characteristics of the faradaic redox mechanism, mainly due to the reversible electron transfer process of the Ni^{2+}/Ni^{3+} redox couple [22], [295], [305]. It is observed from the various cyclic voltammograms that the current response and voltammetric charges of the graphene-$NiMoO_4$ composite electrodes are much higher than that of $NiMoO_4$ electrode, indicating better charge storage capability of the nanocomposite material [305] as a result of the combined contribution of the redox pseudocapacitance of $NiMoO_4$ and the double-layer capacitance of graphene in the composite. Furthermore, the obvious difference in the integrated area of the cyclic voltammograms of the graphene-$NiMoO_4$ composite electrodes (G-8NM > G-16NM > G-4NM > GNC_2) implies that the amount of $NiMoO_4$ loaded on the graphene sheets affects the capacitance of the respective electrode. Figure 8.5b depicts the cyclic voltammograms of the graphene-$NiMoO_4$ composite electrode (G-8NM) at various scan rates from 10 to 100 mV/s; with the 10-fold increment in scan rate. The shapes of the cyclic voltammograms were retained and not significantly altered, confirming the good ionic and electronic transportation, high rate capability and good reversibility of the graphene-$NiMoO_4$ composite electrode [22], [166], [305], [306]. The negligible shift of the redox peaks to the positive and negative directions as the scan rate increases (as observed in the cyclic voltammograms), is a good indication of the relatively low internal resistance of the composite electrode [305], [307], [308]. Figure 8.5c displays the galvanostatic charge/discharge curves of $NiMoO_4$ and graphene-$NiMoO_4$ composite electrodes measured by chronopotentiometry of 0 to 1 V at a constant current density of 3 A/g in 2 M KOH aqueous solution. The charging curve profiles of the as-prepared electrode materials are nearly symmetrical to the corresponding discharging curve profile demonstrating excellent electrochemical reversibility. Furthermore, the nearly linear relation of the charge/discharge potentials with time exhibited by the curves of the as-prepared electrode materials signifies a rapid I-V response and small equivalent series resistance [307] . Specific capacitance (C_s) of the as-prepared electrode materials were calculated from their respective discharge curve profiles using equation 3.22 [195].

The calculated C_s values of the electrodes at a current density of 0.3 A/g are G-16NM (642 F/g), G-8NM (670 F/g), G-4NM (629 F/g), GNC_2 (480 F/g) and $NiMoO_4$ (369 F/g) respectively. As shown in Figure 8.5d, the galvanostatic charge/discharge curves of the G-8NM electrode were analysed at different current densities within the potential window range of 0 to 1 V, in order to evaluate the rate capability of the electrode. The curves remained linear and symmetrical over the different current densities, designating the excellent electrochemical reversibility and low internal resistance of the electrode [307].

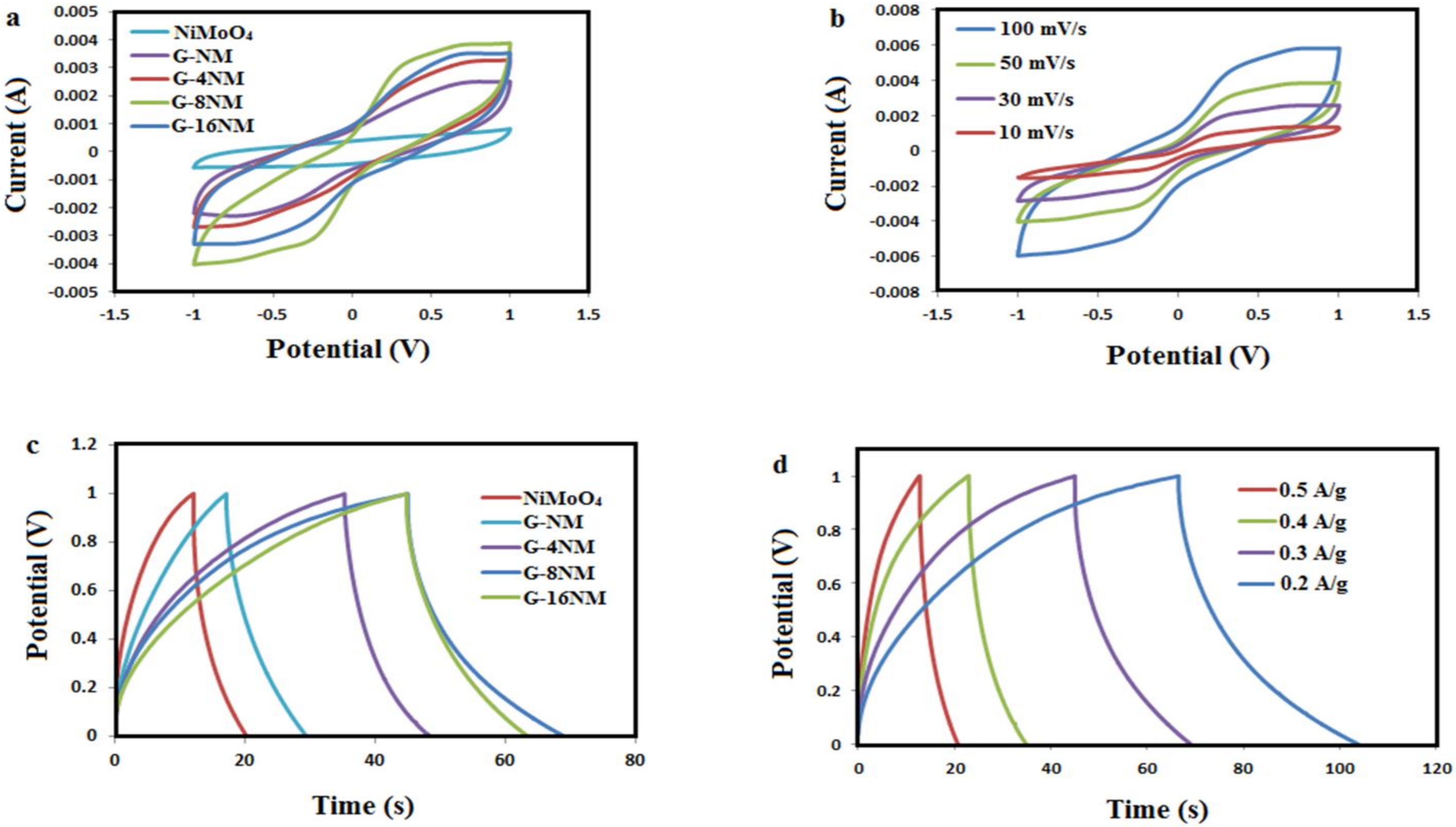

Figure 8.5: Cyclic voltammograms (CV) curves of (a) G-NM, G-4NM, G-8NM and G-16NM composites and $NiMoO_4$ at a scan rate of 50 mV/s, (b) G-8NM at different scan rates in the range of 10-100 mV/s, (c) Charge-discharge curves G-NM, G-4NM, G-8NM and G-16NM composites and $NiMoO_4$ at a current density of 0.3 A/g (d) Charge-discharge curves of G-8NM at different current densities (0.5, 0.4, 0.3 and 0.2).

Additionally, the specific capacitance were calculated from each discharge curve using equation 3.22 and plotted against current density as shown in Figure 8.6a. The improved specific capacitance observed at lower current density was expected since the inner active sites of the composite electrodes will not be fully utilised at higher current densities, resulting in slower redox reactions, and thus lower specific capacitance [258], [294]. Figure 8.6b shows the specific capacitance (C_s) and Coulombic efficiency (η) of the G-8NM electrode as a function of charge/discharge cycle numbers at 0.5 A/g. The electrode exhibited 88% capacitance retention after 3000 cycles indicating an excellent stability over the entire number of cycles. The Coulombic efficiency (η) was calculated from the galvanostatic charge/discharge curves as follows [285], [309]:

$$\eta = \frac{t_D}{t_C} \times 100 \tag{6}$$

where t_C and t_D are the times of charge and discharge in seconds with the same current, respectively. The initial coulombic efficiency is 73%; however it increases with cycle number and averages ca. 80% after 3000 cycles. This implies that the electrode achieved and sustained a good reversibility through the electrochemical reactions during the charge/discharge analysis [309]. In Figure 8.6c, the R_s values of the electrodes are identically to one another with negligible difference while significant differences were observed on their charge transfer resistance (R_{ct}) values. Comparing the R_{ct} values of the various Nyquist plots; the G-8NM electrode has the lowest R_{ct}, which is in good concordance with the calculated capacitance values from the charge/discharge curves. Figure 8.6d presents a Ragone plot of the energy densities and power densities of G-8NM electrode, as calculated from equations 3.27 and 3.30 respectively at various current densities, in comparison with various $NiMoO_4$ metal oxides reported for electrochemical capacitor applications [22], [121], [151], [153], [162], [296], [305], [310].

These results prove the improved specific capacitance, excellent rate capability and cycling performance of the graphene-$NiMoO_4$ composites electrodes for electrochemical capacitors. The enhanced electrochemical performance can be attributed to: (i) the addition of graphene prepared via exfoliation process in pristine manner, resulting better electrical characteristics. (ii) The strongly attached $NiMoO_4$ nanorods on graphene could synergistically improve the contact between electrolytes and shorten the ion diffusion path leading to an enhanced kinetics and higher conductivity (iii) the combined capacitance from the graphene (double layer capacitance) and $NiMoO_4$ (pseudocapacitance).

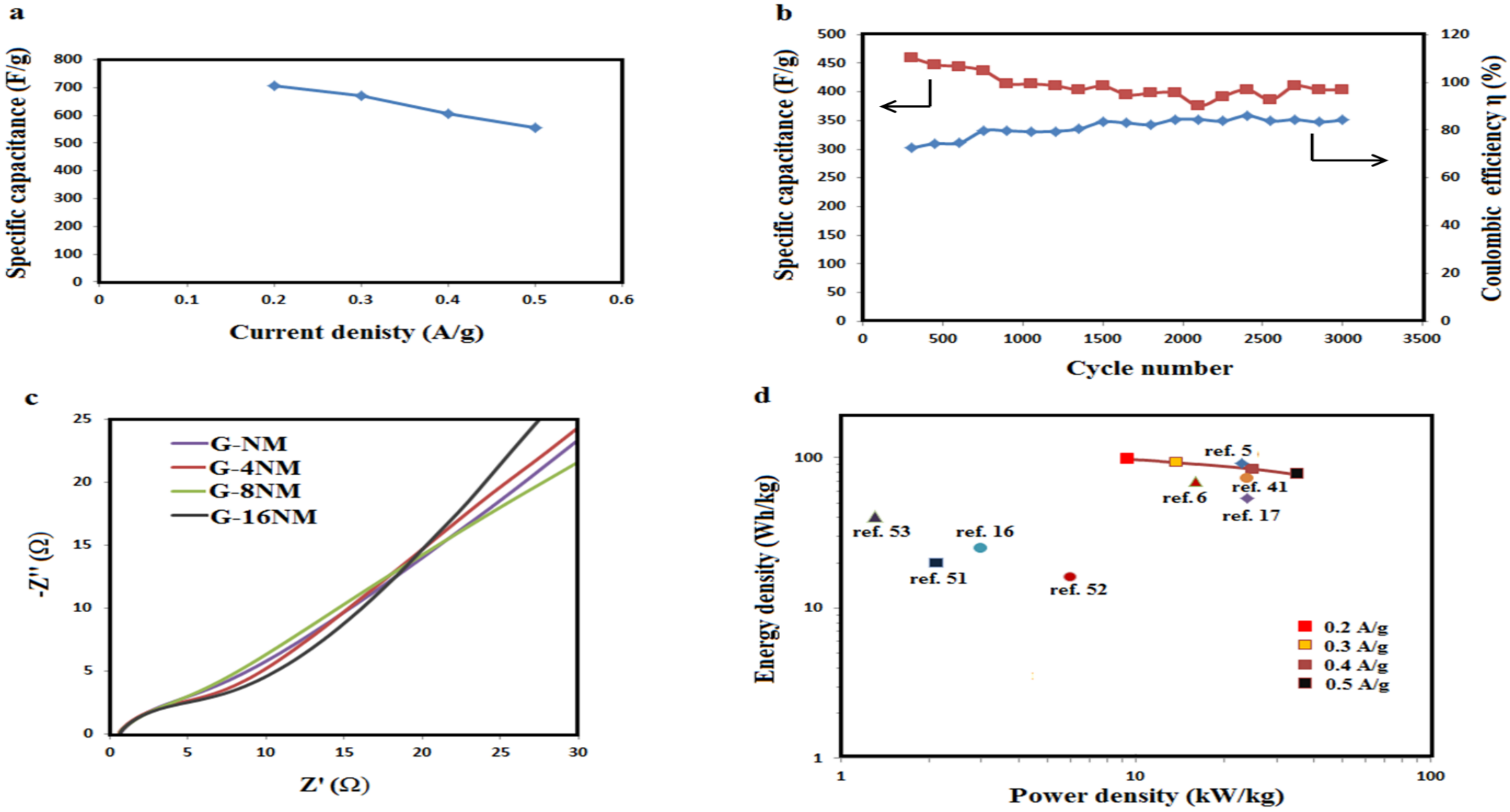

Figure 8.6: (a) Specific capacitance of G-8NM at different current densities (b) cycling performance and Coulombic efficiency of G-8NM composite electrode (c) Nyquist plot of the G-NM, G-4NM, G-8NM and G-16NM composites electrodes and (d) Ragone plot comparing the power and energy densities G-8NM at different current densities and some selected composites electrodes.

8.4 Chapter Summary

In conclusion, graphene-$NiMoO_4$ composites were successfully synthesised by a solvothermal method combined with subsequent calcination. It was observed that the morphology and electrochemical characteristics of the resultant composites greatly depends on the mass ratio of graphene to $NiMoO_4$. The 1:8 ratio exhibited well attached $NiMoO_4$ nanorods on the surface and edges of the graphene sheets with the highest specific capacitance of 670 F/g at 0.3 A/g, as compared to other tested composites. In addition, the capacitance retention was 88% with a Coulombic efficiency of ~ 80% obtained after 3000 cycles. The promising performance of the as-prepared graphene-$NiMoO_4$ composites electrodes, coupled with the simpler and safer synthesis route will open up interesting opportunity for mass production of graphene-$NiMoO_4$ based electrochemical capacitors.

Chapter 9

Conclusion and Recommendations

9.1 Conclusion

This study has detailed the synthesis, structural/morphological characterisation and electrochemical analysis on a series of binary and ternary composites comprising of graphene based TMOs and graphene based BTMOs, as electrode materials for supercapacitor application. The following conclusions drawn out from these studies are summarised and reviewed as follows:

1. A facile approach has been developed to synthesise graphene/metal oxide nanocomposites using highly pyrolytic graphite (HOPG) and transition metal oxides as precursors combined with ethanol and water as mixed solvent. This solvothermal route is simple, low-cost, green and scalable for industrial production.
2. The as-synthesised graphene-metal oxides were subjected to analytical characterisations such as X-ray Diffraction (XRD), Field Emission Scanning Electron Microscopy (FESEM), Transmission Electron Microscopy (TEM), Raman spectroscopy. The results obtained showed that the respective graphene/metal oxide nanocomposites were successfully synthesised void of impurities.
3. Electrodes were fabricated from the various graphene-metal oxides and assembled symmetrical in a two electrode configuration. Electrochemical test were conducted to ascertain their electrochemical performance. The

electrochemical results showed that the introduction of graphene to the metal oxides improved the electrical conductivity of the hybrid structure by providing a fast electron transfer and large contact area for electrolyte penetration.

4. The improved capacitances of the graphene/metal oxide composites were postulated to be the results of the following synergistic effects of the composites material: (i) the formation of metal oxides prevented the restacking of graphene sheets, thereby preserving their large specific surface area; (ii) graphene sheets act as a support to anchor metal oxides, thus preventing MOs to re-agglomerate during electrochemical charge-discharge process; (iii) Graphene sheets form conductive network which shortened ions transport pathway; (iv) the resultant composites combine the double layer capacitance from graphene and the pseudocapacitance from metal oxides.

5. Results demonstrated that the different ratios of graphene to metal oxides significantly affect the XRD diffraction peaks, morphologies and electrochemical properties of the composites. Consequently, the ratio of graphene to metal oxide play vital role in determining optimal electrochemical performance of the respective composites electrodes. It can be deduced that the introduction of higher loading of precursors resulted in agglomerations of MO, which forms less conductive layers onto the graphene sheets, thereby reducing the surface area accessible to the electrolyte ions.

6. The results of the ternary composites comprising of the graphene-based BTMOs showed improved electrochemical performance when compared to the

graphene-based TMOs. This is due to the multiple oxidation states present in the BTMOs which enable multiple redox reactions and higher electron conductivity owing to the relatively low activation energy for electron transfer.

A summary presented at Table 9 details the optimal ratios of the graphene/metal oxide with superior electrochemical properties.

Table 9.1: A table showing the electrochemical performance of the optimal ratio of graphene to metal oxide hybrid composites prepared in this study.

Electrode material	**Class of metal oxide**	**Ratio of Graphene/Metal oxide**	**Specific capacitance (F/g)**	**Current density (A/g)**	**Scan rate (mV/s)**	**Energy density (Wh/kg)**	**Cycle life**
Graphene/ZnO	TMO	1:8	246	-	5	11.80	83% after 1000th
Graphene/MnO_2	TMO	1:16	380	-	5	53	88.4% after 1000th
Graphene/ Co_3O_4	TMO	1:4	384	0.3	-	64	80% after 1000th
Graphene/ $NiCo_2O_4$	BTMO	1:8	698	0.3	-	96.9	75% after 5000th
Graphene/ $NiMoO_4$	BTMO	1:8	670	0.3	-	77.16	88% after 3000th

9.2 Recommendations

Electrochemical capacitors are emerging energy storage technology that would take a paramount role in the future of energy storage systems. In view of this, research and advancement have been recorded in recent years to developing new electrochemical capacitor materials in improving the performance and commercial viability of this technology. The continual progress of this development has narrowed two important material areas: the electrode and electrolyte material on achieving traction in mainstream application.

The work achieved in this study has provided a platform in addressing the perspectives and challenges of an electrode material. The results on the combination of graphene and metal oxides showed an improved energy storage capability and an excess addition of metal oxide to graphene hybrid composites was counterproductive. Therefore, further study is needed to optimise and correlate the amount of metal oxide in a hybrid composite with regards to performance which will give us an insight on the capacitive properties of metal oxides.

The exploration of graphene and mixed transition metal oxides could allow scientists to understand the complex chemical compositions of these metals coupled with the synergy between the double layer capacitance of graphene in providing unique morphologies, electrode architectures and possibly improved capacitive performances. Furthermore, a study to the different performances of these hybrid composite electrodes in aqueous, organic or ionic liquid electrolytes is vital progress expected for the electrochemical industry.

Graphene/metal oxide electrochemical capacitors as discussed in this thesis can act as a power source to portable electronic device with moderate energy demands; a typical example is to power a light-emitting diode (LED). Figure 9.1 shows how a series connected electrochemical capacitors provides power functions for a load. The boost converter ensures that the output voltage supplied to the device is constant and overvoltage of the electrochemical capacitors is prevented by the balancing resistors.

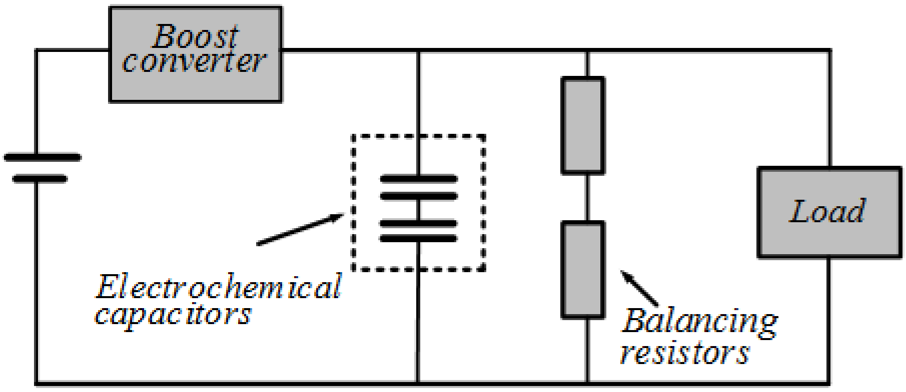

Figure 9.1: A circuit diagram of an electrochemical capacitor as a portable energy source

More work is required to achieve this application such as the development, fabrication and testing of a working graphene/metal oxide electrochemical capacitor prototype which would form part of my future research.

References

[1] X. Xia, Y. Zhang, D. Chao, C. Guan, Y. Zhang, L. Li, X. Ge, I. M. Bacho, J. Tu, and H. J. Fan, “Solution synthesis of metal oxides for electrochemical energy storage applications.,” *Nanoscale*, vol. 6, no. 10, pp. 5008–48, May 2014.

[2] H.-J. Choi, S.-M. Jung, J.-M. Seo, D. W. Chang, L. Dai, and J.-B. Baek, “Graphene for energy conversion and storage in fuel cells and supercapacitors,” *Nano Energy*, vol. 1, no. 4, pp. 534–551, Jul. 2012.

[3] G. Wang, L. Zhang, and J. Zhang, “A review of electrode materials for electrochemical supercapacitors.,” *Chem. Soc. Rev.*, vol. 41, no. 2, pp. 797–828, Jan. 2012.

[4] A. M. J Manyika, M Chui, J Bughin, R Dobbs, P Bisson, “Disruptive technologies : Advances that will transform life , business , and the global economy,” no. May, 2013.

[5] C. Yuan, H. Bin Wu, Y. Xie, and X. W. D. Lou, “Mixed Transition-Metal Oxides: Design, Synthesis, and Energy-Related Applications,” *Angew. Chemie Int. Ed.*, vol. 53, no. 6, pp. 1488–1504, 2014.

[6] J. Baker, “New technology and possible advances in energy storage,” *Energy Policy*, vol. 36, no. 12, pp. 4368–4373, Dec. 2008.

[7] T. Christen and M. W. Carlen, “Theory of Ragone plots,” *J. Power Sources*, vol. 91, no. 2, pp. 210–216, Dec. 2000.

[8] J. C. Ellenbogen, “Supercapacitors : A Brief Overview,” no. March, 2006.

[9] B. E. Conway, *Electrochemical Supercapacitors Scientific Fundamentals and Technological Applications*. Springer US, 1999.

[10] J. Z. Aiping Yu, Victor Chabot, *Electrochemical Supercapacitors for Energy Storage and Delivery*. CRC Press, 2013.

[11] Z.-S. Wu, G. Zhou, L.-C. Yin, W. Ren, F. Li, and H.-M. Cheng, “Graphene/metal oxide composite electrode materials for energy storage,” *Nano Energy*, vol. 1, no. 1, pp. 107–131, Jan. 2012.

[12] X. Li, H. Song, Y. Zhang, H. Wang, K. Du, H. Li, Y. Yuan, and J. Huang, “Enhanced Electrochemical Capacitance of Graphene Nanosheets Coating With Polyaniline for Supercapacitors,” vol. 7, pp. 5163–5171, 2012.

[13] L. Wang, X. Wang, X. Xiao, F. Xu, Y. Sun, and Z. Li, “Reduced graphene oxide/nickel cobaltite nanoflake composites for high specific capacitance supercapacitors,” *Electrochim. Acta*, vol. 111, no. 2013, pp. 937–945, 2013.

[14] L. Kang, J. Deng, T. Liu, M. Cui, X. Zhang, P. Li, Y. Li, X. Liu, and W. Liang, “One-step solution combustion synthesis of cobalt–nickel oxides/C/Ni/CNTs nanocomposites as electrochemical capacitors electrode materials,” *J. Power Sources*, vol. 275, pp. 126–135, Feb. 2015.

[15] L. Dong, Z. Chen, D. Yang, and H. Lu, “Hierarchically structured graphene-based supercapacitor electrodes,” *RSC Adv.*, vol. 3, no. 44, p. 21183, 2013.

[16] X. Dong, Y. Cao, J. Wang, M. B. Chan-Park, L. Wang, W. Huang, and P. Chen, “Hybrid structure of zinc oxide nanorods and three dimensional graphene foam for supercapacitor and electrochemical sensor applications,” *RSC Adv.*, vol. 2, no. 10, p. 4364, 2012.

[17] J. Zhang, J. Jiang, and X. S. Zhao, “Synthesis and Capacitive Properties of Manganese Oxide Nanosheets Dispersed on Functionalized Graphene Sheets,” *J. Phys. Chem. C*, vol. 115, no. 14, pp. 6448–6454, Apr. 2011.

[18] H. Wang, L.-F. Cui, Y. Yang, H. Sanchez Casalongue, J. T. Robinson, Y. Liang, Y. Cui, and H. Dai, “Mn_3O_4-graphene hybrid as a high-capacity anode material for lithium ion batteries.,” *J. Am. Chem. Soc.*, vol. 132, no. 40, pp. 13978–80, Oct. 2010.

[19] D. P. Dubal, P. Gomez-Romero, B. R. Sankapal, and R. Holze, “Nickel cobaltite as an emerging material for supercapacitors: An overview,” *Nano Energy*, vol. 11, no. 2015, pp. 377–399, 2015.

[20] X. Li, Z. Wang, Y. Qiu, Q. Pan, and P. Hu, “3D graphene/ZnO nanorods composite networks as supercapacitor electrodes,” *J. Alloys Compd.*, vol. 620, no. 2015, pp. 31–37, 2015.

[21] G. K. Veerasubramani, K. Krishnamoorthy, S. Radhakrishnan, N.-J. Kim, and S. J. Kim, “Synthesis, characterization, and electrochemical properties of $CoMoO_4$ nanostructures,” *Int. J. Hydrogen Energy*, vol. 39, no. 10, pp. 5186–5193, 2014.

[22] D. Guo, Y. Luo, X. Yu, Q. Li, and T. Wang, “High performance $NiMoO_4$ nanowires supported on carbon cloth as advanced electrodes for symmetric supercapacitors,” *Nano Energy*, vol. 8, pp. 174–182, 2014.

[23] L. Liu, H. Zhang, J. Yang, Y. Mu, and Y. Wang, “Self-assembled novel dandelion-like $NiCo_2O_4$ microspheres@nanomeshes with superior electrochemical performance for supercapacitors and lithium-ion batteries,” *J. Mater. Chem. A*, vol. 3, no. 44, pp. 22393–22403, 2015.

[24] Y. He, W. Chen, X. Li, Z. Zhang, J. Fu, C. Zhao, and E. Xie, “Freestanding Three-Dimensional Networks As Ultralight and Flexible Supercapacitor Electrodes,” pp. 174–182, 2013.

[25] X.-H. Xia, J.-P. Tu, X.-L. Wang, C.-D. Gu, and X.-B. Zhao, “Mesoporous Co_3O_4 monolayer hollow-sphere array as electrochemical pseudocapacitor material.,” *Chem. Commun. (Camb).*, vol. 47, no. 20, pp. 5786–5788, 2011.

[26] D. Zhou, Y. Cui, and B. Han, “Graphene-based hybrid materials and their applications in energy storage and conversion,” *Chinese Sci. Bull.*, vol. 57, no. 23, pp. 2983–2994, Aug. 2012.

[27] L. Li, K. H. Seng, H. Liu, I. P. Nevirkovets, and Z. Guo, “Synthesis of Mn_3O_4-anchored graphene sheet nanocomposites via a facile, fast microwave hydrothermal method and their supercapacitive behavior,” *Electrochim. Acta*, vol. 87, pp. 801–808, Jan. 2013.

[28] L.-J. Xie, J.-F. Wu, C.-M. Chen, C.-M. Zhang, L. Wan, J.-L. Wang, Q.-Q. Kong, C.-X. Lv, K.-X. Li, and G.-H. Sun, “A novel asymmetric supercapacitor with an activated carbon cathode and a reduced graphene oxide–cobalt oxide nanocomposite anode,” *J. Power Sources*, vol. 242, pp. 148–156, Nov. 2013.

[29] H. Wang, Y. Liang, T. Mirfakhrai, Z. Chen, H. S. Casalongue, and H. Dai, “Advanced asymmetrical supercapacitors based on graphene hybrid materials,” *Nano Res.*, vol. 4, no. 8, pp. 729–736, Apr. 2011.

[30] E. R. Ezeigwe, P. S. Khiew, C. W. Siong, and M. T. T. Tan, “Solvothermal synthesis of $NiCo_2O_4$ nanocomposites on liquid-phase exfoliated graphene as an electrode material for electrochemical capacitors,” *J. Alloys Compd.*, no. 2016, 2016.

[31] Y. Wu, S. Liu, H. Wang, X. Wang, X. Zhang, and G. Jin, “A novel solvothermal synthesis of Mn_3O_4/graphene composites for supercapacitors,” *Electrochim. Acta*, vol. 90, pp. 210–218, Feb. 2013.

[32] L. Zhu, S. Zhang, Y. Cui, H. Song, and X. Chen, “One step synthesis and capacitive performance of graphene nanosheets/Mn_3O_4 composite,” *Electrochim. Acta*, vol. 89, pp. 18–23, Feb. 2013.

[33] S. Deng, D. Sun, C. Wu, H. Wang, J. Liu, Y. Sun, and H. Yan, “Synthesis and electrochemical properties of MnO_2 nanorods/graphene composites for supercapacitor applications,” *Electrochim. Acta*, vol. 111, pp. 707–712, Nov. 2013.

[34] J. Yan, Z. Fan, T. Wei, W. Qian, M. Zhang, and F. Wei, “Fast and reversible surface redox reaction of graphene–MnO_2 composites as supercapacitor electrodes,” *Carbon N. Y.*, vol. 48, no. 13, pp. 3825–3833, Nov. 2010.

[35] D. Carriazo, J. Patiño, M. C. Gutiérrez, M. L. Ferrer, and F. del Monte, “Microwave-assisted synthesis of $NiCo_2O_4$–graphene oxide nanocomposites suitable as electrodes for supercapacitors,” *RSC Adv.*, vol. 3, no. 33, p. 13690, 2013.

[36] T. Liu, H. Chai, D. Jia, Y. Su, T. Wang, and W. Zhou, “Rapid microwave-assisted synthesis of mesoporous $NiMoO_4$ nanorod/reduced graphene oxide composites for high-performance supercapacitors,” *Electrochim. Acta*, vol. 180, no. 2015, pp. 998–1006, 2015.

[37] K.-H. Ye, Z.-Q. Liu, C.-W. Xu, N. Li, Y.-B. Chen, and Y.-Z. Su, “MnO_2/reduced graphene oxide composite as high-performance electrode for flexible supercapacitors,” *Inorg. Chem. Commun.*, vol. 30, pp. 1–4, Apr. 2013.

[38] Q. Cheng, J. Tang, J. Ma, H. Zhang, N. Shinya, and L.-C. Qin, “Graphene and nanostructured MnO_2 composite electrodes for supercapacitors,” *Carbon N. Y.*, vol. 49, no. 9, pp. 2917–2925, Aug. 2011.

[39] S.-M. Li, Y.-S. Wang, S.-Y. Yang, C.-H. Liu, K.-H. Chang, H.-W. Tien, N.-T. Wen, C.-C. M. Ma, and C.-C. Hu, “Electrochemical deposition of nanostructured manganese oxide on hierarchically porous graphene–carbon nanotube structure for ultrahigh-performance electrochemical capacitors,” *J. Power Sources*, vol. 225, pp. 347–355, Mar. 2013.

[40] R. Hu, J. Zhao, and J. Zheng, “Synthesis of SnO_2 /rGO hybrid materials by sol-gel/thermal reduction method and its application in electrochemical capacitors,” *Mater. Lett.*, vol. 197, pp. 59–62, 2017.

[41] J. Ding, M. Wang, J. Deng, W. Gao, Z. Yang, C. Ran, and X. Zhang, “A comparison study between ZnO nanorods coated with graphene oxide and reduced graphene oxide,” *J. Alloys Compd.*, vol. 582, pp. 29–32, Jan. 2014.

[42] X. Liu, X. Qi, Z. Zhang, L. Ren, Y. Liu, L. Meng, K. Huang, and J. Zhong, “One-step electrochemical deposition of nickel sulfide/graphene and its use for supercapacitors,” *Ceram. Int.*, vol. 40, no. 6, pp. 8189–8193, Jul. 2014.

[43] S.-M. Li, Y.-S. Wang, S.-Y. Yang, C.-H. Liu, K.-H. Chang, H.-W. Tien, N.-T. Wen, C.-C. M. Ma, and C.-C. Hu, “Electrochemical deposition of nanostructured manganese oxide on hierarchically porous graphene–carbon nanotube structure for ultrahigh-performance electrochemical capacitors,” *J. Power Sources*, vol. 225, pp. 347–355, Mar. 2013.

[44] T. Skaltsas, N. Karousis, H.-J. Yan, C.-R. Wang, S. Pispas, and N. Tagmatarchis, “Graphene exfoliation in organic solvents and switching solubility in aqueous media with the aid of amphiphilic block copolymers,” *J. Mater. Chem.*, vol. 22, no. 40, p. 21507, 2012.

[45] J. S. Y. Chia, M. T. T. Tan, P. S. Khiew, J. K. Chin, H. Lee, D. Bien, and W. S. Chiu, “A Novel One Step Synthesis of Graphene via Sonochemical-assisted Solvent Exfoliation Approach for Electrochemical Sensing Application,” *Chem. Eng. J.*, vol. 249, no. 1, pp. 270–278, Apr. 2014.

[46] S. Park and R. S. Ruoff, “Chemical methods for the production of graphenes.,” *Nat. Nanotechnol.*, vol. 4, no. 4, pp. 217–24, Apr. 2009.

[47] W. Riemenschneider and H. M. Bolt, “Ethanol,” *Ullmann’s Encycl. Ind. Chem.*, pp. 8676–8694, 2005.

[48] “BP Statistical Review of World Energy About this review,” British Petroleum Corp., June, p. 48, 2016.

[49] International Energy Agency, “World Energy Outlook 2016,” *Int. Energy Agency*, pp. 1–8, 2016.

[50] Iea, “World Energy Outlook 2012 Factsheet: How will global energy markets evolve to 2035?,” *Worldenergyoutlook.Org* , p. 6, 2012.

[51] J. Zhu, D. Yang, Z. Yin, Q. Yan, and H. Zhang, “Graphene and Graphene-Based Materials for Energy Storage Applications.,” *Small*, pp. 1–19, Jan. 2014.

[52] P. Yang and W. Mai, “Flexible solid-state electrochemical supercapacitors,” *Nano Energy*, vol. 8, pp. 274–290, Sep. 2014.

[53] P. Simon and Y. Gogotsi, “Materials for electrochemical capacitors.,” *Nat. Mater.*, vol. 7, no. 11, pp. 845–54, Nov. 2008.

[54] R. Ko and M. Carlen, “Principles and applications of electrochemical capacitors,” vol. 45, pp. 2483–2498, 2000.

[55] P. Sharma and T. S. Bhatti, “A review on electrochemical double-layer capacitors,” *Energy Convers. Manag.*, vol. 51, no. 12, pp. 2901–2912, Dec. 2010.

[56] L. L. Zhang and X. S. Zhao, “Carbon-based materials as supercapacitor electrodes.,” *Chem. Soc. Rev.*, vol. 38, no. 9, pp. 2520–31, Sep. 2009.

[57] A. Borenstein, O. Hanna, R. Attias, S. Luski, T. Brousse, and D. Aurbach, “Carbon-based composite materials for supercapacitor electrodes: a review,” *J. Mater. Chem. A*, vol. 5, no. 25, pp. 12653–12672, 2017.

[58] S. Bose, T. Kuila, A. K. Mishra, R. Rajasekar, N. H. Kim, and J. H. Lee, “Carbon-based nanostructured materials and their composites as supercapacitor electrodes,” *J. Mater. Chem.*, vol. 22, no. 3, p. 767, 2012.

[59] E. Frackowiak, “Storage of electrochemical energy in carbon materials,” vol. 48, pp. 1–4, 2002.

[60] E. Frackowiak and F. Béguin, “Carbon materials for the electrochemical storage of energy in capacitors,” *Carbon N. Y.*, vol. 39, no. 6, pp. 937–950, May 2001.

[61] J. Huang, B. G. Sumpter, and V. Meunier, “A universal model for nanoporous carbon supercapacitors applicable to diverse pore regimes, carbon materials, and electrolytes,” *Chem. - A Eur. J.*, vol. 14, no. 22, pp. 6614–6626, 2008.

[62] D. Qu, “Studies of the activated carbons used in double-layer supercapacitors,” *J. Power Sources*, vol. 109, no. 2, pp. 403–411, 2002.

[63] E. Frackowiak, G. Lota, J. Machnikowski, C. Vix-Guterl, and F. Béguin, “Optimisation of supercapacitors using carbons with controlled nanotexture and nitrogen content,” *Electrochim. Acta*, vol. 51, no. 11, pp. 2209–2214, 2006.

[64] C. Vix-Guterl, E. Frackowiak, K. Jurewicz, M. Friebe, J. Parmentier, and F. Béguin, “Electrochemical energy storage in ordered porous carbon materials,” *Carbon N. Y.*, vol. 43, no. 6, pp. 1293–1302, 2005.

[65] M. S. D. M. Endo, Y. J. Kim, T. Takeda, T. Maeda, T. Hayashi, K. Koshiba and H. Hara, “Poly(vinylidene chloride)-Based Carbon as an Electrode Material for High Power Capacitors with an Aqueous Electrolyte,” *J. Electrochem. Soc.*, vol. 148, no. 10, pp. A1135–A1140, 2001.

[66] P. Simon and A. Burke, “Nanostructured Carbons: Double-Layer Capacitance and More.”The Electrochemical Society Interface, 2008.

[67] K. H. B. Karl Heinz Büchel, Hans-Heinrich Moretto , Dietmar Werner , Peter Woditsch, *Industrial Inorganic Chemistry*, Second Edi. Wiley-VCH, 2000.

[68] E. Raymundo-Piñero, F. Leroux, and F. Béguin, “A High-Performance Carbon for Supercapacitors Obtained by Carbonization of a Seaweed Biopolymer,” *Adv. Mater.*, vol. 18, no. 14, pp. 1877–1882, Jul. 2006.

[69] E. Raymundo-Piñero, K. Kierzek, J. Machnikowski, and F. Béguin, “Relationship between the nanoporous texture of activated carbons and their capacitance properties in different electrolytes,” *Carbon N. Y.*, vol. 44, no. 12, pp. 2498–2507, Oct. 2006.

[70] R. Ramachandran, V. Mani, S. Chen, R. Saraswathi, and B. Lou, “Recent Trends in Graphene based Electrode Materials for Energy Storage Devices and Sensors Applications,” vol. 8, pp. 11680–11694, 2013.

[71] P. J. F. Harris, *Carbon Nanotubes and Related Structures: New materials for the Twenty-first Century*. Cambridge University Press, 1999.

[72] J. Li, X. Cheng, A. Shashurin, and M. Keidar, “Review of Electrochemical Capacitors Based on Carbon Nanotubes and Graphene,” vol. 2012, no. July, pp. 1–13, 2012.

[73] H. Pan, J. Li, and Y. Feng, “Carbon nanotubes for supercapacitor.,” *Nanoscale Res. Lett.*, vol. 5, no. 3, pp. 654–68, Jan. 2010.

[74] T. Chen and L. Dai, “Carbon nanomaterials for high-performance supercapacitors,” *Mater. Today*, vol. 16, no. 7–8, pp. 272–280, 2013.

[75] T. K. and M. I. Yuichi Hondaa, Tetsuhisa Haramotoa, Masayuki Takeshigea, Hideki Shiozakib, “Aligned MWCNT Sheet Electrodes Prepared by Transfer Methodology Providing High-Power Capacitor Performance,” *Electrochem. Solid-state Lett.*, vol. 10, no. 4, pp. A106–A110, 2007.

[76] E. Frackowiak, K. Metenier, V. Bertagna, and F. Beguin, “Supercapacitor electrodes from multiwalled carbon nanotubes,” *Appl. Phys. Lett.*, vol. 77, no. 15, pp. 2421–2423, 2000.

[77] W. L. and L. Dai, *Carbon Nanotubes*. InTech, 2010.

[78] B. Zhang, J. Liang, C. . Xu, B. . Wei, D. . Ruan, and D. . Wu, “Electric double-layer capacitors using carbon nanotube electrodes and organic electrolyte,” *Mater. Lett.*, vol. 51, no. 6, pp. 539–542, 2001.

[79] S. C. L. and Y. H. L. Kay Hyeok An, Won Seok Kim, Young Soo Park, Hee Jin Jeong, Young Chul Choi, Jeong-Mi Moo1, Dong Jae Bae, “Supercapacitors using singlewalled carbon nanotube electrodes,” in *AIP Conference Proceedings*, p. 241.

[80] J. C. F. and R. W. P. Tri D. Tran, “Carbon Aerogels and Their Applications in Supercapacitors and Electrosorption Processes,” PPG Industries, Inc., Monroeville, PA 15146, 2002.

[81] S.T. Mayer, R.W. Pekala and J.L. Kaschmitter, “The Aerocapacitor: An Electrochemical Double-Layer Energy-Storage Device,” *J. Electrochem. Soc.*, vol. 140, no. 2, pp. 446–451, 1993.

[82] U. Fischer, R. Saliger, V. Bock, R. Petricevic, and J. Fricke, “Carbon Aerogels as Electrode Material in Supercapacitors,” *J. Porous Mater.*, vol. 17, no. 1997, p. 281, 1997.

[83] E. J. Lee, Y. J. Lee, J. K. Kim, M. Lee, J. Yi, J. R. Yoon, J. C. Song, and I. K. Song, “Oxygen group-containing activated carbon aerogel as an electrode material for supercapacitor,” *Mater. Res. Bull.*, vol. 70, no. 2015, pp. 209–214, 2015.

[84] R. L. McCreery, K. K. Cline, C. A. McDermott, and M. T. McDermott, “Control of reactivity at carbon electrode surfaces,” *Colloids Surfaces A Physicochem. Eng. Asp.*, vol. 93, no. C, pp. 211–219, 1994.

[85] J. K. and A. Soffer, “Double Layer Capacitance and Charging Rate of Ultramicroporous Carbon Electrodes,” *J. Electrochem. Soc.*, vol. 124, no. 9, pp. 1379–1385, 1977.

[86] A. K. Geim, “Graphene: status and prospects.,” *Science*, vol. 324, no. 5934, pp. 1530–4, Jun. 2009.

[87] B. Garg, T. Bisht, and Y. C. Ling, “Graphene-based nanomaterials as heterogeneous acid catalysts: A comprehensive perspective,” *Molecules*, vol. 19, no. 9, pp. 14582–14614, 2014.

[88] Y. Zhu, S. Murali, W. Cai, X. Li, J. W. Suk, J. R. Potts, and R. S. Ruoff, “Graphene and graphene oxide: Synthesis, properties, and applications,” *Adv. Mater.*, vol. 22, no. 35, pp. 3906–3924, 2010.

[89] I. V. G. and a. a. F. K. S. Novoselov, A. K. Geim, S. V. Morozov, D. Jiang, Y. Zhang, S. V. Dubonos, “Electric Field Effect in Atomically Thin Carbon Films,” *Science (80-.).*, vol. 306, no. 5696, pp. 666–669, 2004.

[90] Y. Hernandez, V. Nicolosi, M. Lotya, F. M. Blighe, Z. Sun, S. De, I. T. McGovern, B. Holland, M. Byrne, Y. K. Gun’Ko, J. J. Boland, P. Niraj, G. Duesberg, S. Krishnamurthy, R. Goodhue, J. Hutchison, V. Scardaci, A. C. Ferrari, and J. N. Coleman, “High-yield production of graphene by liquid-phase exfoliation of graphite,” *Nat. Nanotechnol.*, vol. 3, no. 9, pp. 563–568, 2008.

[91] Y. Wu, B. Wang, Y. Ma, Y. Huang, N. Li, F. Zhang, and Y. Chen, “Efficient and large-scale synthesis of few-layered graphene using an arc-discharge method and conductivity studies of the resulting films,” *Nano Res.*, vol. 3, no. 9, pp. 661–669, 2010.

[92] M. Hirata, T. Gotou, S. Horiuchi, M. Fujiwara, and M. Ohba, “Thin-film particles of graphite oxide 1: High-yield synthesis and flexibility of the particles,” *Carbon N. Y.*, vol. 42, no. 14, pp. 2929–2937, 2004.

[93] Q. Ke and J. Wang, “Graphene-based materials for supercapacitor electrodes – A review,” *J. Mater.*, vol. 2, no. 1, pp. 37–54, 2016.

[94] M. D. Stoller, S. Park, Y. Zhu, J. An, and R. S. Ruoff, “Graphene-based ultracapacitors.,” *Nano Lett.*, vol. 8, no. 10, pp. 3498–502, Oct. 2008.

[95] S. R. C. Vivekchand, C. S. Rout, K. S. Subrahmanyam, a Govindaraj, and C. N. R. Rao, “Graphene-based electrochemical supercapacitors,” vol. 120, no. 1, pp. 9–13, 2008.

[96] D. A. and C. Z. Yu Aiping, Roes Isaac, “Ultrathin, transparent, and flexible graphene films for supercapacitor application,” *Appl. Phys. Lett.*, vol. 96, no. 25, p. 253105, 2010.

[97] D. W. Wang, F. Li, Z. S. Wu, W. Ren, and H. M. Cheng, “Electrochemical interfacial capacitance in multilayer graphene sheets: Dependence on number of stacking layers,” *Electrochem. commun.*, vol. 11, no. 9, pp. 1729–1732, 2009.

[98] C. Liu, Z. Yu, D. Neff, A. Zhamu, and B. Z. Jang, “Graphene-based supercapacitor with an ultrahigh energy density.,” *Nano Lett.*, vol. 10, no. 12, pp. 4863–8, Dec. 2010.

[99] Y. Wang, Z. Shi, Y. Huang, Y. Ma, C. Wang, M. Chen, and Y. Chen, “Supercapacitor Devices Based on Graphene Materials.pdf,” *J. Phys. Chem. C*, vol. 113, pp. 13103–13107, 2009.

[100] X. Yang, J. Zhu, L. Qiu, and D. Li, “Bioinspired effective prevention of restacking in multilayered graphene films: Towards the next generation of high-performance supercapacitors,” *Adv. Mater.*, vol. 23, no. 25, pp. 2833–2838, 2011.

[101] Y. Zhu, S. Murali, M. D. Stoller, K. J. Ganesh, W. Cai, P. J. Ferreira, A. Pirkle, R. M. Wallace, K. a Cychosz, M. Thommes, D. Su, E. a Stach, and R. S. Ruoff, “Carbon-Based Supercapacitors,” *Science (80-.).*, vol. 332, no. June, pp. 1537–1542, 2011.

[102] C. Zheng, X. F. Zhou, H. L. Cao, G. H. Wang, and Z. P. Liu, “Edge-enriched porous graphene nanoribbons for high energy density supercapacitors,” *J. Mater. Chem. A*, vol. 2, no. 20, p. 7484, 2014.

[103] Y. Zhang, L. Li, H. Su, W. Huang, and X. Dong, “Binary metal oxide: advanced energy storage materials in supercapacitors,” *J. Mater. Chem. A*, vol. 3, no. 1, pp. 43–59, 2015.

[104] a Rudge, I. Davey, I. Raistrick, S. Gottesfeld, and J. Ferraris, “Conducting polymers as active materials in electrochemical capacitors,” *J. Power Sources*, vol. 47, no. 1–2, pp. 89–107, 1994.

[105] E. Frackowiak, V. Khomenko, K. Jurewicz, K. Lota, and F. Béguin, "Supercapacitors based on conducting polymers/nanotubes composites," *J. Power Sources*, vol. 153, no. 2, pp. 413–418, Feb. 2006.

[106] G. a. Snook, P. Kao, and A. S. Best, "Conducting-polymer-based supercapacitor devices and electrodes," *J. Power Sources*, vol. 196, no. 1, pp. 1–12, 2011.

[107] L. Yuan, X. Xiao, T. Ding, J. Zhong, X. Zhang, Y. Shen, B. Hu, Y. Huang, J. Zhou, and Z. L. Wang, "Paper-based supercapacitors for self-powered nanosystems," *Angew. Chemie - Int. Ed.*, vol. 51, no. 20, pp. 4934–4938, 2012.

[108] H. Li, J. Wang, Q. Chu, Z. Wang, F. Zhang, and S. Wang, "Theoretical and experimental specific capacitance of polyaniline in sulfuric acid," *J. Power Sources*, vol. 190, no. 2, pp. 578–586, 2009.

[109] W. Li, J. Chen, J. Zhao, J. Zhang, and J. Zhu, "Application of ultrasonic irradiation in preparing conducting polymer as active materials for supercapacitor," *Mater. Lett.*, vol. 59, no. 7, pp. 800–803, 2005.

[110] K. Lota, V. Khomenko, and E. Frackowiak, "Capacitance properties of poly(3,4-ethylenedioxythiophene)/carbon nanotubes composites," *J. Phys. Chem. Solids*, vol. 65, no. 2–3, pp. 295–301, 2004.

[111] S. Lagoutte, P.-H. Aubert, F. Tran-Van, X. Sallenave, C. Laffaiteur, C. Sarrazin, and C. Chevrot, "Electrochemical and optical properties of poly (3, 4-dimethylthiophene) and its copolymers with 3-methylthiophenein ionic liquids media," *Electrochim. Acta*, vol. 106, pp. 13–22, 2013.

[112] D. Mo, W. Zhou, X. Ma, J. Xu, D. Zhu, and B. Lu, "Electrochemical synthesis and capacitance properties of a novel poly(3,4-ethylenedioxythiophene bis-substituted bithiophene) electrode material," *Electrochim. Acta*, vol. 132, no. 2014, pp. 67–74, 2014.

[113] E. Tamburri, S. Orlanducci, F. Toschi, M. L. Terranova, and D. Passeri, "Growth mechanisms, morphology, and electroactivity of PEDOT layers produced by electrochemical routes in aqueous medium," *Synth. Met.*, vol. 159, no. 5–6, pp. 406–414, 2009.

[114] F. Ç. Cebeci, E. Sezer, and a. S. Sarac, "A novel EDOT-nonylbithiazole-EDOT based comonomer as an active electrode material for supercapacitor applications," *Electrochim. Acta*, vol. 54, no. 26, pp. 6354–6360, 2009.

[115] Y. Huang, J. Tao, W. Meng, M. Zhu, Y. Huang, Y. Fu, Y. Gao, and C. Zhi, "Super-high rate stretchable polypyrrole-based supercapacitors with excellent cycling stability," *Nano Energy*, vol. 11, no. 2015, pp. 518–525, 2015.

[116] C. Zhao, C. Wang, Z. Yue, K. Shu, and G. G. Wallace, “Intrinsically stretchable supercapacitors composed of polypyrrole electrodes and highly stretchable gel electrolyte,” *ACS Appl. Mater. Interfaces*, vol. 5, no. 18, pp. 9008–9014, 2013.

[117] W. Deng, X. Ji, Q. Chen, and C. E. Banks, “Electrochemical capacitors utilising transition metal oxides: an update of recent developments,” *RSC Adv.*, vol. 1, no. 7, p. 1171, 2011.

[118] Z. Liu, K. Xiao, Q. Xu, N. Li, Y. Su, H. Wang, and S. Chen, “Fabrication of hierarchical flower-like super-structures consisting of porous $NiCo_2O_4$ nanosheets and their electrochemical and magnetic properties,” *RSC Adv.*, vol. 3, no. 13, p. 4372, 2013.

[119] Q. Wang, X. Wang, J. Xu, X. Ouyang, X. Hou, D. Chen, R. Wang, and G. Shen, “Flexible coaxial-type fiber supercapacitor based on $NiCo_2O_4$ nanosheets electrodes,” *Nano Energy*, vol. 8, pp. 44–51, 2014.

[120] J. Zhu, Z. Xu, and B. Lu, “Ultrafine Au nanoparticles decorated $NiCo_2O_4$ nanotubes as anode material for high-performance supercapacitor and lithium-ion battery applications,” *Nano Energy*, vol. 7, pp. 114–123, 2014.

[121] S. E. Moosavifard, J. Shamsi, and M. Ayazpour, “2D high-ordered nanoporous $NiMoO_4$ for high-performance supercapacitors,” *Ceram. Int.*, vol. 41, no. 1, pp. 1831–1837, 2015.

[122] H. Wan, J. Jiang, X. Ji, L. Miao, L. Zhang, K. Xu, H. Chen, and Y. Ruan, “Rapid microwave-assisted synthesis $NiMoO_4H_2O$ nanoclusters for supercapacitors,” *Mater. Lett.*, vol. 108, pp. 164–167, 2013.

[123] D. Cai, B. Liu, D. Wang, Y. Liu, L. Wang, H. Li, Y. Wang, C. Wang, Q. Li, and T. Wang, “Enhanced performance of supercapacitors with ultrathin mesoporous $NiMoO_4$ nanosheets,” *Electrochim. Acta*, vol. 125, no. 2014, pp. 294–301, 2014.

[124] V. Šepelák, S. M. Becker, I. Bergmann, S. Indris, M. Scheuermann, A. Feldhoff, C. Kübel, M. Bruns, N. Stürzl, A. S. Ulrich, M. Ghafari, H. Hahn, C. P. Grey, K. D. Becker, and P. Heitjans, “Nonequilibrium structure of Zn_2SnO_4 spinel nanoparticles,” *J. Mater. Chem.*, vol. 22, p. 3117, 2012.

[125] W. Fu, X. Li, C. Zhao, Y. Liu, P. Zhang, J. Zhou, X. Pan, and E. Xie, “Facile hydrothermal synthesis of flowerlike $ZnCo_2O_4$ microspheres as binder-free electrodes for supercapacitors,” *Mater. Lett.*, vol. 149, pp. 1–4, 2015.

[126] H. Chen, Q. Zhang, X. Han, J. Cai, M. Liu, Y. Yang, and K. Zhang, “3D hierarchically porous zinc-nickel-cobalt oxide nanosheets grown on Ni foam as binder-free electrodes for electrochemical energy storage,” *J. Mater. Chem. A*, vol. 3, no. 47, pp. 24022–24032, 2015.

[127] L. Li, Y. Zhang, F. Shi, Y. Zhang, J. Zhang, C. Gu, X. Wang, and J. Tu, “Spinel Manganese − Nickel − Cobalt Ternary Oxide Nanowire Array for High-Performance Electrochemical Capacitor Applications,” pp. 4–11, 2014.

[128] S. Chen, G. Yang, and H. Zheng, “Aligned Ni-Co-Mn oxide nanosheets grown on conductive substrates as binder-free electrodes for high capacity electrochemical energy storage devices,” *Electrochim. Acta*, vol. 220, no. 2016, pp. 296–303, 2016.

[129] T. C. and T. S. F. Guoping Xiong, Pingge He, Lei Liu, “Synthesis of porous Ni-Co-Mn oxide nanoneedles and the temperature dependence of their pseudocapacitive behavior Synthesis of porous Ni – Co – Mn oxide nanoneedles and the temperature dependence of their pseudocapacitive behavior,” *Front. Energy Res.*, vol. 3, no. August, pp. 1–9, 2015.

[130] C. Wu, J. Cai, Q. Zhang, X. Zhou, Y. Zhu, P. K. Shen, and K. Zhang, “Hierarchical mesoporous zinc-nickel-cobalt ternary oxide nanowire arrays on nickel foam as high-performance electrodes for supercapacitors,” *ACS Appl. Mater. Interfaces*, vol. 7, no. 48, pp. 26512–26521, 2015.

[131] W. Hu, H. Wei, Y. She, X. Tang, M. Zhou, Z. Zang, J. Du, C. Gao, Y. Guo, and D. Bao, “Flower-like nickel-zinc-cobalt mixed metal oxide nanowire arrays for electrochemical capacitor applications,” *J. Alloys Compd.*, vol. 708, no. 2017, pp. 146–153, 2017.

[132] A. Maitra, A. K. Das, R. Bera, S. K. Karan, S. Paria, S. K. Si, and B. B. Khatua, “An Approach To Fabricate PDMS Encapsulated All-Solid-State Advanced Asymmetric Supercapacitor Device with Vertically Aligned Hierarchical Zn–Fe–Co Ternary Oxide Nanowire and Nitrogen Doped Graphene Nanosheet for High Power Device Applications,” *ACS Appl. Mater. Interfaces*, p. acsami.6b13259, 2017.

[133] Q. Zhang, B. Zhao, J. Wang, C. Qu, H. Sun, K. Zhang, and M. Liu, “High-performance hybrid supercapacitors based on self-supported 3D ultrathin porous quaternary Zn-Ni-Al-Co oxide nanosheets,” *Nano Energy*, vol. 28, no. 2016, pp. 475–485, 2016.

[134] S. R. Sivakkumar and a. G. Pandolfo, “Evaluation of lithium-ion capacitors assembled with pre-lithiated graphite anode and activated carbon cathode,” *Electrochim. Acta*, vol. 65, pp. 280–287, Mar. 2012.

[135] H. Xia, Y. Wang, J. Lin, and L. Lu, “Hydrothermal synthesis of MnO_2/CNT nanocomposite with a CNT core/porous MnO_2 sheath hierarchy architecture for supercapacitors.,” *Nanoscale Res. Lett.*, vol. 7, no. 1, p. 33, Jan. 2012.

[136] K. R. Reddy, B. C. Sin, K. S. Ryu, J.-C. Kim, H. Chung, and Y. Lee, "Conducting polymer functionalized multi-walled carbon nanotubes with noble metal nanoparticles: Synthesis, morphological characteristics and electrical properties," *Synth. Met.*, vol. 159, no. 7–8, pp. 595–603, 2009.

[137] Y. Hou, Y. Cheng, T. Hobson, and J. Liu, "Design and synthesis of hierarchical MnO_2 nanospheres/carbon nanotubes/conducting polymer ternary composite for high performance electrochemical electrodes.," *Nano Lett.*, vol. 10, no. 7, pp. 2727–33, Jul. 2010.

[138] W. Jiang, K. Zhang, L. Wei, D. Yu, J. Wei, and Y. Chen, "Hybrid ternary rice paper-manganese oxide-carbon nanotube nanocomposites for flexible supercapacitors.," *Nanoscale*, vol. 5, no. 22, pp. 11108–17, Nov. 2013.

[139] S. L. Candelaria, Y. Shao, W. Zhou, X. Li, J. Xiao, J.-G. Zhang, Y. Wang, J. Liu, J. Li, and G. Cao, "Nanostructured carbon for energy storage and conversion," *Nano Energy*, vol. 1, no. 2, pp. 195–220, Mar. 2012.

[140] B. Gersten, "Solvothermal Synthesis of Nanoparticles," *Chemfiles*, vol. 5, no. 13, pp. 13–17.

[141] S.C. Singh, D.P. Singh, P.K. Dubey, R.S Tiwari, J. Singh and O.N Srivastava, "Metal Oxide Nanostructures; Synthesis, Characterizations and Applications."In book: Encyclopedia of Semiconductor Nanotechnology, First Edi.American Scientific Publishers, pp1000, 2010.

[142] Zhanfeng Zheng, "Synthesis and Modifications of Metal Oxide Nanostructures and Their Applications," PhD thesis, Quessland University of Technology, 2009.

[143] A. K. Jain and R. K. Singla, "An Overview of Microwave Assisted Technique: Green Synthesis," *Webmedcentral*, vol. 2, no. 9, pp. 1–15, 2011.

[144] A. J. Bard and L. R. Faulkner, *ELECTROCHEMICAL METHODS Fundamentals and Applications*, Second Edi. John Wiley & Sons, Inc., 2001.

[145] a. S. M. S. Rahman, M. a. Islam, and K. M. Shorowordi, "Electrodeposition and Characterization of Copper Oxide Thin Films for Solar cell Applications," *Procedia Eng.*, vol. 105, no. Icte 2014, pp. 679–685, 2015.

[146] M. Khalil, S. Wang, J. Yu, R. L. Lee, and N. Liu, "Electrodeposition of Iridium Oxide Nanoparticles for pH Sensing Electrodes," *J. Electrochem. Soc.*, vol. 163, no. 9, pp. B485–B490, 2016.

[147] C. Hu, T. Lu, F. Chen, and R. Zhang, "A brief review of graphene–metal oxide composites synthesis and applications in photocatalysis," *J. Chinese Adv. Mater. Soc.*, vol. 1, no. 1, pp. 21–39, Mar. 2013.

[148] H. S. Nalwa, *Handbook of Nanostructured Materials and Nanotechnology*. Academy Press, 1999.

[149] C. Wang, J. Xu, M.-F. Yuen, J. Zhang, Y. Li, X. Chen, and W. Zhang, "Hierarchical Composite Electrodes of Nickel Oxide Nanoflake 3D Graphene for High-Performance Pseudocapacitors," *Adv. Funct. Mater.*, vol. 24, p. 6372-6380, Aug. 2014.

[150] A. Bello, O. O. Fashedemi, J. N. Lekitima, M. Fabiane, D. Dodoo-Arhin, K. I. Ozoemena, Y. Gogotsi, A. T. Charlie Johnson, and N. Manyala, "High-performance symmetric electrochemical capacitor based on graphene foam and nanostructured manganese oxide," *AIP Adv.*, vol. 3, no. 8, p. 082118, 2013.

[151] A. Ajay, A. Paravannoor, J. Joseph, V. Amruthalakshmi, S. S. Anoop, S. V. Nair, and A. Balakrishnan, "2 D amorphous frameworks of $NiMoO_4$ for supercapacitors: Defining the role of surface and bulk controlled diffusion processes," *Appl. Surf. Sci.*, vol. 326, no. 2015, pp. 39–47, 2015.

[152] D. Cai, B. Liu, D. Wang, L. Wang, Y. Liu, H. Li, Y. Wang, Q. Li, and T. Wang, "Construction of unique $NiCo_2O_4$ nanowire@$CoMoO_4$ nanoplate core/shell arrays on Ni foam for high areal capacitance supercapacitors," *J. Mater. Chem. A*, vol. 2, p. 4954, 2014.

[153] D. Cai, D. Wang, B. Liu, Y. Wang, Y. Liu, L. Wang, H. Li, H. Huang, Q. Li, and T. Wang, "Comparison of the electrochemical performance of $NiMoO_4$ nanorods and hierarchical nanospheres for supercapacitor applications," *ACS Appl. Mater. Interfaces*, vol. 5, no. 24, pp. 12905–12910, 2013.

[154] J. Zhou, Y. Huang, X. Cao, B. Ouyang, W. Sun, C. Tan, Y. Zhang, Q. Ma, S. Liang, Q. Yan, and H. Zhang, "Two-dimensional $NiCo_2O_4$ nanosheet-coated three-dimensional graphene networks for high-rate, long-cycle-life supercapacitors," *Nanoscale*, vol. 7, no. 16, pp. 7035–7039, 2015.

[155] X. Zhao, L. Zhang, S. Murali, M. D. Stoller, Q. Zhang, Y. Zhu, and R. S. Ruoff, "Incorporation of manganese dioxide within ultraporous activated graphene for high-performance electrochemical capacitors.," *ACS Nano*, vol. 6, no. 6, pp. 5404–12, Jun. 2012.

[156] Z. Zhang, Y. Liu, Z. Huang, L. Ren, X. Qi, X. Wei, and J. Zhong, "Facile hydrothermal synthesis of $NiMoO_4$@$CoMoO_4$ hierarchical nanospheres for supercapacitor applications," *Phys. Chem. Chem. Phys.*, vol. 17, no. 32, pp. 20795–20804, 2015.

[157] X. Zhang, X. Sun, H. Zhang, C. Li, and Y. Ma, “Comparative performance of birnessite-type MnO_2 nanoplates and octahedral molecular sieve (OMS-5) nanobelts of manganese dioxide as electrode materials for supercapacitor application,” *Electrochim. Acta*, vol. 132, no. 2014, pp. 315–322, Jun. 2014.

[158] L. Zhang, G. Du, B. Zhou, and L. Wang, “Green synthesis of flower-like ZnO decorated reduced graphene oxide composites,” *Ceram. Int.*, vol. 40, no. 1, pp. 1241–1244, Jan. 2014.

[159] F. Zhang, T. Zhang, X. Yang, L. Zhang, K. Leng, Y. Huang, and Y. Chen, “A high-performance supercapacitor-battery hybrid energy storage device based on graphene-enhanced electrode materials with ultrahigh energy density,” *Energy Environ. Sci.*, vol. 6, no. 5, p. 1623, 2013.

[160] D. Zhang and W. Zou, “Decorating reduced graphene oxide with Co_3O_4 hollow spheres and their application in supercapacitor materials,” *Curr. Appl. Phys.*, vol. 13, no. 8, pp. 1796–1800, Oct. 2013.

[161] T. Zhai, F. Wang, M. Yu, S. Xie, C. Liang, C. Li, F. Xiao, R. Tang, Q. Wu, X. Lu, and Y. Tong, “3D MnO_2-graphene composites with large areal capacitance for high-performance asymmetric supercapacitors.,” *Nanoscale*, vol. 5, no. 15, pp. 6790–6, Aug. 2013.

[162] C. Z. and X. Z. Z. Yin, Y. Chen, Y. Zhao, C. Li, “Hierarchical nanosheet-based $CoMoO_4$ –$NiMoO_4$ nanotubes for applications in asymmetric supercapacitors and the oxygen evolution reaction,” *J. Mater. Chem. A*, vol. 3, no. 45, pp. 22750–22758, 2015.

[163] W. Yang, Z. Gao, J. Ma, J. Wang, B. Wang, and L. Liu, “Effects of solvent on the morphology of nanostructured Co_3O_4 and its application for high-performance supercapacitors,” *Electrochim. Acta*, vol. 112, pp. 378–385, Dec. 2013.

[164] M. Tamaddoni Saray and H. Hosseini, “Mesoporous $MnNiCoO_4$@MnO2 core-shell nanowire/nanosheet arrays on flexible carbon cloth for high-performance supercapacitors,” *Electrochim. Acta*, 2016.

[165] H. Jiang, Y. Dai, Y. Hu, W. Chen and C. Li “Nanostructured Ternary Nanocomposite of rGO/CNTs/MnO_2 for High-Rate Supercapacitors,”ACS *Sustaible Chem. Eng*, vol 2, no1, pp 70-4, 2014.

[166] B. Senthilkumar, K. V Sankar, L. Vasylechko, Y.-S. Lee, and R. K. Selvan, “Synthesis and electrochemical performances of maricite-$NaMPO_4$ (M = Ni, Co, Mn) electrodes for hybrid supercapacitors,” *RSC Adv.*, vol. 4, no. 95, pp. 53192–53200, 2014.

[167] M. Sarfraz, M. F. a. Aboud, and I. Shakir, "Molybdenum oxide nanowires based supercapacitors with enhanced capacitance and energy density in ethylammonium nitrate electrolyte," *J. Alloys Compd.*, vol. 650, pp. 123–126, 2015.

[168] K. Qiu, Y. Lu, D. Zhang, J. Cheng, H. Yan, J. Xu, X. Liu, J.-K. Kim, and Y. Luo, "Mesoporous, hierarchical core/shell structured $ZnCo_2O_4/MnO_2$ nanocone forests for high-performance supercapacitors," *Nano Energy*, vol. 11, no. 2015, pp. 687–696, 2015.

[169] X. Qing, S. Liu, K. Huang, K. Lv, Y. Yang, Z. Lu, D. Fang, and X. Liang, "Facile synthesis of Co_3O_4 nanoflowers grown on Ni foam with superior electrochemical performance," *Electrochim. Acta*, vol. 56, no.14, pp. 4985–4991, 2011.

[170] K. A. Owusu, L. Qu, J. Li, Z. Wang, K. Zhao, C. Yang, K. M. Hercule, C. Lin, C. Shi, Q. Wei, L. Zhou, and L. Mai, "Low-crystalline iron oxide hydroxide nanoparticle anode for high-performance supercapacitors," *Nat. Commun.*, vol. 8, p. 14264, 2017.

[171] A. K. Mondal, D. Su, S. Chen, K. Kretschmer, X. Xie, H.-J. Ahn, and G. Wang, "A microwave synthesis of mesoporous $NiCo_2O_4$ nanosheets as electrode materials for lithium-ion batteries and supercapacitors.," *Chemphyschem*, vol. 16, no. 1, pp. 169–75, 2015.

[172] B. Saravanakumar, K. K. Purushothaman, and G. Muralidharan, "Interconnected V_2O_5 nanoporous network for high-performance supercapacitors," *ACS Appl. Mater. Interfaces*, vol. 4, no. 9, pp. 4484–4490, 2012.

[173] G. P. Pandey, T. Liu, E. Brown, Y. Yang, Y. Li, X. S. Sun, Y. Fang, and J. Li, "Mesoporous Hybrids of Reduced Graphene Oxide and Vanadium Pentoxide for Enhanced Performance in Lithium-Ion Batteries and Electrochemical Capacitors," *ACS Appl. Mater. Interfaces*, vol. 8, no. 14, pp. 9200–9210, 2016.

[174] L. Gao, X. Wang, Z. Xie, W. Song, L. Wang, X. Wu, F. Qu, D. Chen, and G. Shen, "High-performance energy-storage devices based on WO3 nanowire arrays/carbon cloth integrated electrodes," *J. Mater. Chem. A*, vol. 1, no. 24, p. 7167, 2013.

[175] J.-H. Zhong, A.-L. Wang, G.-R. Li, J.-W. Wang, Y.-N. Ou, and Y.-X. Tong, "$Co_3O_4/Ni(OH)_2$ composite mesoporous nanosheet networks as a promising electrode for supercapacitor applications," *J. Mater. Chem.*, vol. 22, no. 12, p. 5656, 2012.

[176] J.-Y. Kim, K.-H. Kim, H.-K. Kim, S.-H. Park, K. C. Roh, and K.-B. Kim, "Template-Free Synthesis of Ruthenium Oxide Nanotubes for High-Performance Electrochemical Capacitors," *ACS Appl. Mater. Interfaces*, vol. 7, no. 30, pp. 16686–16693, 2015.

[177] P. Lorkit, M. Panapoy, and B. Ksapabutr, “Iron oxide-based supercapacitor from ferratrane precursor via sol-gel-hydrothermal process,” *Energy Procedia*, vol. 56, no. C, pp. 466–473, 2014.

[178] X. Feng, Z. Yan, N. Chen, Y. Zhang, Y. Ma, X. Liu, Q. Fan, L. Wang, and W. Huang, “The synthesis of shape-controlled MnO_2/graphene composites via a facile one-step hydrothermal method and their application in supercapacitors,” *J. Mater. Chem. A*, vol. 1, no. 41, p. 12818, 2013.

[179] Y. Liu, X. Wang, W. Ma, J. Mujtaba, G. Sun, J. Zhao, and H. Sun, “One-pot hydrothermal synthesis of hollow Fe_3O_4 microspheres assembled with nanoparticles for lithium-ion battery anodes,” *Mater. Lett.*, vol. 172, pp. 76–80, 2016.

[180] Z. H. Ibupoto, S. Elhag, M. S. AlSalhi, O. Nur, and M. Willander, “Effect of urea on the morphology of CO_3O_4 nanostructures and their application for potentiometric glucose biosensor,” *Electroanalysis*, vol. 26, no. 8, pp. 1773–1781, 2014.

[181] J. Zhang, Ed., *PEM Fuel Cell Electrocatalysts and Catalyst Layers: Fundamentals and Applications*. London: Springer, 2008.

[182] V. S. Ramachandran, And, and J. J. Beaudoin, Eds., *Handbook Of Analytical Techniques In Concrete Science And Technology - Principles, Techniques, and Applications*. New York: William Andrew Publishing, 2001.

[183] I. Chorendorff and J. W. Niemantsverdriet, Eds., *Concepts of Modern Catalysis and Kinetics*. Wiley-VCH Verlag GmbH & Co. KGaA, 2003.

[184] R. J. Beane, “Using the Scanning Electron Microscope for Discovery Based Learning in Undergraduate Courses,”*Journal of Geoscience Education*, vol. 52, pp. 250–253, 2004.

[185] D. J. Stokes, “Environmental scanning electron microscopy for biology and polymer science,” *Microsc. Microanalysis*, 25th anniversary issue, pp. 67–71, 2012.

[186] D. Stokes, *Principles and Practice of Variable Pressure : Environmental Scanning Electron Microscopy (VP – ESEM).* Chichester: Wiley, 2009.

[187] T. Lu, Y. Zhang, H. Li, L. Pan, Y. Li, and Z. Sun, “Electrochemical behaviors of graphene–ZnO and graphene–SnO_2 composite films for supercapacitors,” *Electrochim. Acta*, vol. 55, no. 13, pp. 4170–4173, May 2010.

[188] A. C. Ferrari and D. M. Basko, "Raman spectroscopy as a versatile tool for studying the properties of graphene.," *Nat. Nanotechnol.*, vol. 8, no. 4, pp. 235–46, Apr. 2013.

[189] E. Smith and G. Dent, *Modern Raman Spectrocopy: A Practical Approach*. West Sussex: Wiley, 2005.

[190] J. R. Ferraro, K. Nakamoto, and C. W. Brown, *Introductory Raman Spectroscopy: Second Edition*, Second edi. Elsevier, 2003.

[191] R. Baddour-hadjean and J.-P. Pereira-Ramos, "Raman Microspectrometry Applied to the Study of Electrode Materials for Lithium Batteries," *Chem. Rev.*, vol. 110, pp. 1278–1319, 2010.

[192] D. Ghosh, S. Giri, and C. K. Das, "Synthesis, characterization and electrochemical performance of graphene decorated with 1D $NiMoO_4.nH_2O$ nanorods.," *Nanoscale*, vol. 5, no. 21, pp. 10428–37, 2013.

[193] R. F. Egerton, *Physical Principles of Electron Microscopy- An Introduction to TEM, SEM and AEM*. Springer, 2005.

[194] Y. Qian, S. Lu, and F. Gao, "Synthesis of manganese dioxide/reduced graphene oxide composites with excellent electrocatalytic activity toward reduction of oxygen," *Mater. Lett.*, vol. 65, no. 1, pp. 56–58, Jan. 2011.

[195] M. D. Stoller and R. S. Ruoff, "Best practice methods for determining an electrode material's performance for ultracapacitors," *Energy Environ. Sci.*, vol. 3, no. 9, p. 1294, 2010.

[196] J. David K. Gosser, *Cyclic Voltammetry Simulation and Analysis of Reaction Mechanisms*. VCH Publishers, Inc., 1993.

[197] C. Lei and C. Lekakou, "Carbon-based nanocomposite EDLC supercapacitor s," pp. 0–4.

[198] L. S. Aravinda, K. K. Nagaraja, H. S. Nagaraja, K. U. Bhat, and B. R. Bhat, "ZnO/carbon nanotube nanocomposite for high energy density supercapacitors," *Electrochim. Acta*, vol. 95, pp. 119–124, Apr. 2013.

[199] M. D. Stoller, S. Park, Y. Zhu, J. An, and R. S. Ruoff, "Graphene-based ultracapacitors.," *Nano Lett.*, vol. 8, no. 10, pp. 3498–502, Oct. 2008.

[200] J. Wang, Z. Gao, Z. Li, B. Wang, Y. Yan, Q. Liu, T. Mann, M. Zhang, and Z. Jiang, "Green synthesis of graphene nanosheets/ZnO composites and electrochemical properties," *J. Solid State Chem.*, vol. 184, no. 6, pp. 1421–1427, Jun. 2011.

[201] M. Selvakumar, D. Krishna Bhat, a. Manish Aggarwal, S. Prahladh Iyer, and G. Sravani, "Nano ZnO-activated carbon composite electrodes for supercapacitors," *Phys. B Condens. Matter*, vol. 405, no. 9, pp. 2286–2289, May 2010.

[202] Z. Fan and J. G. Lu, "Zinc oxide nanostructures: synthesis and properties.," *J. Nanosci. Nanotechnol.*, vol. 5, no. 10, pp. 1561–73, Oct. 2005.

[203] Y. Zhu, H. I. Elim, Y.-L. Foo, T. Yu, Y. Liu, W. Ji, J.-Y. Lee, Z. Shen, a. T. S. Wee, J. T. L. Thong, and C. H. Sow, "Multiwalled Carbon Nanotubes Beaded with ZnO Nanoparticles for Ultrafast Nonlinear Optical Switching," *Adv. Mater.*, vol. 18, no. 5, pp. 587–592, Mar. 2006.

[204] M.-J. L. and W.-G. J. Fatima T Johra, "Solution- based fabrication of a graphene-ZnO nanocomposite," *J Sol-Gel Sci Technol*, vol. vol. 66, pp. 481–487, 2013.

[205] T. Lu, L. Pan, H. Li, G. Zhu, T. Lv, X. Liu, Z. Sun, T. Chen, and D. H. C. Chua, "Microwave-assisted synthesis of graphene–ZnO nanocomposite for electrochemical supercapacitors," *J. Alloys Compd.*, vol. 509, no. 18, pp. 5488–5492, May 2011.

[206] Z. Li, Z. Zhou, G. Yun, K. Shi, X. Lv, and B. Yang, "High- performance solid-state supercapacitors based on graphene-ZnO hybrid nanocomposites," pp. 1–9, 2013.

[207] Y. Zhang, H. Li, L. Pan, T. Lu, and Z. Sun, "Capacitive behavior of graphene–ZnO composite film for supercapacitors," *J. Electroanal. Chem.*, vol. 634, no. 1, pp. 68–71, Sep. 2009.

[208] W. Han, L. Ren, X. Qi, Y. Liu, X. Wei, Z. Huang, and J. Zhong, "Synthesis of CdS/ZnO/graphene composite with high-efficiency photoelectrochemical activities under solar radiation," *Appl. Surf. Sci.*, vol. 299, no. 2014, pp. 12–18, Apr. 2014.

[209] A. C. Ferrari, "Raman spectroscopy of graphene and graphite: Disorder, electron–phonon coupling, doping and nonadiabatic effects," *Solid State Commun.*, vol. 143, no. 1–2, pp. 47–57, Jul. 2007.

[210] H. Zeng, Y. Cao, S. Xie, J. Yang, Z. Tang, X. Wang, and L. Sun, "Synthesis, optical and electrochemical properties of ZnO nanowires/graphene oxide heterostructures.," *Nanoscale Res. Lett.*, vol. 8, no. 1, p. 133, Jan. 2013.

[211] C.-T. Hsieh, J.-S. Lin, Y.-F. Chen, C.-Y. Lin, and W.-Y. Li, "Graphene sheets anchored with ZnO nanocrystals as electrode materials for electrochemical capacitors," *Mater. Chem. Phys.*, vol. 143, no. 2, pp. 853–859, Jan. 2014.

[212] Y. Zhang, X. Sun, L. Pan, H. Li, Z. Sun, C. Sun, and B. K. Tay, “Carbon nanotube–ZnO nanocomposite electrodes for supercapacitors,” *Solid State Ionics*, vol. 180, no. 32–35, pp. 1525–1528, Nov. 2009.

[213] Z. Qin, Z. J. Li, G. Q. Yun, K. Shi, K. Li, and B. C. Yang, “ZnO nanorods inserted graphene sheets with improved supercapacitive performance,” *Appl. Surf. Sci.*, vol. 292, pp. 544–550, Feb. 2014.

[214] X. Liu, X. Qi, Z. Zhang, L. Ren, G. Hao, Y. Liu, Y. Wang, K. Huang, X. Wei, J. Li, Z. Huang, and J. Zhong, “Electrochemically reduced graphene oxide with porous structure as a binder-free electrode for high-rate supercapacitors,” *RSC Adv.*, vol. 4, no. 26, p. 13673, 2014.

[215] L. Deng, Z. Hao, J. Wang, G. Zhu, L. Kang, Z.-H. Liu, Z. Yang, and Z. Wang, “Preparation and capacitance of graphene/multiwall carbon nanotubes/MnO_2 hybrid material for high-performance asymmetrical electrochemical capacitor,” *Electrochim. Acta*, vol. 89, pp. 191–198, Feb. 2013.

[216] Z. Li, P. Liu, G. Yun, K. Shi, X. Lv, K. Li, J. Xing, and B. Yang, “3D (Three-dimensional) sandwich-structured of ZnO (zinc oxide)/rGO (reduced graphene oxide)/ZnO for high performance supercapacitors,” *Energy*, pp. 6–11, Apr. 2014.

[217] C. D. Lokhande, D. P. Dubal, and O.-S. Joo, “Metal oxide thin film based supercapacitors,” *Curr. Appl. Phys.*, vol. 11, no. 3, pp. 255–270, May 2011.

[218] C. Yang, M. Zhou, and Q. Xu, “Three-dimensional ordered macroporous MnO_2/carbon nanocomposites as high-performance electrodes for asymmetric supercapacitors.,” *Phys. Chem. Chem. Phys.*, vol. 15, no. 45, pp. 19730–40, Dec. 2013.

[219] Q. Cheng, J. Tang, J. Ma, H. Zhang, N. Shinya, and L.-C. Qin, “Graphene and nanostructured MnO_2 composite electrodes for supercapacitors,” *Carbon N. Y.*, vol. 49, no. 9, pp. 2917–2925, Aug. 2011.

[220] X. Dai, W. Shi, H. Cai, R. Li, and G. Yang, “Facile preparation of the novel structured α-MnO_2/Graphene nanocomposites and their electrochemical properties,” *Solid State Sci.*, vol. 27, no. 2014, pp. 17–23, Jan. 2014.

[221] Y. Liu, D. Yan, Y. Li, Z. Wu, R. Zhuo, S. Li, J. Feng, J. Wang, P. Yan, and Z. Geng, “Manganese dioxide nanosheet arrays grown on graphene oxide as an advanced electrode material for supercapacitors,” *Electrochim. Acta*, vol. 117, pp. 528–533, Jan. 2014.

[222] J. Cao, Y. Wang, Y. Zhou, J.-H. Ouyang, D. Jia, and L. Guo, “High voltage asymmetric supercapacitor based on MnO_2 and graphene electrodes,” *J. Electroanal. Chem.*, vol. 689, no. 2013, pp. 201–206, Jan. 2013.

[223] S. Chen, J. Zhu, X. Wu, Q. Han, and X. Wang, "Graphene Oxide−MnO_2 Nanocomposites for Supercapacitors." *ACS nano,* vol. 4, no. 5, pp2822-2830, 2010.

[224] M. Kim, M. Yoo, Y. Yoo, and J. Kim, "Microelectronics Reliability Capacitance behavior of composites for supercapacitor applications prepared with different durations of graphene /nanoneedle MnO_2 reduction," *Microelectron. Reliab.*, vol. 54, no. 3, pp. 587–594.

[225] G. Zhang, L. Ren, L. Deng, J. Wang, L. Kang, and Z.-H. Liu, "Graphene–MnO_2 nanocomposite for high-performance asymmetrical electrochemical capacitor," *Mater. Res. Bull.*, vol. 49, no. 2014, pp. 577–583, Jan. 2014.

[226] Y. Dong, K. Li, P. Jiang, G. Wang, H. Miao, J. Zhang, and C. Zhang, "Simple hydrothermal preparation of α-, β-, and γ-MnO_2 and phase sensitivity in catalytic ozonation," *RSC Adv.*, vol. 4, no. 74, p. 39167, Aug. 2014.

[227] Y. Wang, H. Liu, M. Bao, B. Li, H. Su, Y. Wen, and F. Wang, "Structural-controlled synthesis of manganese oxide nanostructures and their electrochemical properties," *J. Alloys Compd.*, vol. 509, no. 33, pp. 8306–8312, Aug. 2011.

[228] A. Jorio, "Raman Spectroscopy in Graphene-Based Systems: Prototypes for Nanoscience and Nanometrology," *ISRN Nanotechnol.*, vol. 2012, no. 2, pp. 1–16, 2012.

[229] W. Han, L. Ren, L. Gong, X. Qi, Y. Liu, L. Yang, X. Wei, and J. Zhong, "Self-Assembled Three-Dimensional Graphene-Based Aerogel with Embedded Multifarious Functional Nanoparticles and Its Excellent Photoelectrochemical Activities," *Am. Chem. Soc.*, p. 741−748, 2014.

[230] T. Gao, H. Fjellvåg, and P. Norby, "A comparison study on Raman scattering properties of alpha- and beta-MnO_2.," *Anal. Chim. Acta*, vol. 648, no. 2, pp. 235–9, Aug. 2009.

[231] S. Cheng, L. Yang, D. Chen, X. Ji, Z. Jiang, D. Ding, and M. Liu, "Phase evolution of an alpha MnO_2-based electrode for pseudo-capacitors probed by in operando Raman spectroscopy," *Nano Energy*, vol. 9, pp. 161–167, Oct. 2014.

[232] Y. Li, J. Wang, Y. Zhang, M. N. Banis, J. Liu, D. Geng, R. Li, and X. Sun, "Facile controlled synthesis and growth mechanisms of flower-like and tubular MnO_2 nanostructures by microwave-assisted hydrothermal method.," *J. Colloid Interface Sci.*, vol. 369, no. 1, pp. 123–8, Mar. 2012.

[233] E. R. Ezeigwe, M. T. T. Tan, P. S. Khiew, and C. W. Siong, "One-step green synthesis of graphene/ZnO nanocomposites for electrochemical capacitors," *Ceram. Int.*, vol. 41, no. 1, pp. 715–724, Jan. 2015.

[234] M. Kim, Y. Hwang, K. Min, and J. Kim, “Concentration dependence of graphene oxide-nanoneedle manganese oxide composites reduced by hydrazine hydrate for an electrochemical supercapacitor.,” *Phys. Chem. Chem. Phys.*, vol. 15, no. 37, pp. 15602–11, Oct. 2013.

[235] Z. Zhang, X. Liu, X. Qi, Z. Huang, L. Ren, and J. Zhong, “Hydrothermal synthesis of Ni_3S_2 /graphene electrode and its application in a supercapacitor,” *RSC Adv.*, vol. 4, no. 70, p. 37278, Jul. 2014.

[236] H. Song, X. Li, Y. Zhang, H. Wang, H. Li, and J. Huang, “A nanocomposite of needle-like MnO_2 nanowires arrays sandwiched between graphene nanosheets for supercapacitors,” *Ceram. Int.*, vol. 40, no. 1, pp. 1251–1255, Jan. 2014.

[237] H. Cheng, Z. G. Lu, J. Q. Deng, C. Y. Chung, K. Zhang, and Y. Y. Li, “A facile method to improve the high rate capability of Co_3O_4 nanowire array electrodes,” *Nano Res.*, vol. 3, no. 12, pp. 895–901, 2010.

[238] Y. Sun, X. Y. Feng, and C. H. Chen, “Hollow Co_3O_4 thin films as high performance anodes for lithium-ion batteries,” *J. Power Sources*, vol. 196, no. 2, pp. 784–787, 2011.

[239] E. Jokar, A. Iraji zad, and S. Shahrokhian, “Growth control of cobalt oxide nanoparticles on reduced graphene oxide for enhancement of electrochemical capacitance,” *Int. J. Hydrogen Energy*, vol. 39, no. 36, pp. 21068–21075, Dec. 2014.

[240] A. R. Puigdollers, G. Alonso, and P. Gamallo, “First-principles study of structural, elastic and electronic properties of α-, β- and γ-graphyne,” *Carbon N. Y.*, vol. 96, no. 2016, pp. 879–887, 2016.

[241] K. R. Reddy, B. C. Sin, C. H. Yoo, W. Park, K. S. Ryu, J. S. Lee, D. Sohn, and Y. Lee, “A new one-step synthesis method for coating multi-walled carbon nanotubes with cuprous oxide nanoparticles,” *Scr. Mater.*, vol. 58, no. 11, pp. 1010–1013, 2008.

[242] K. R. Reddy, B. C. Sin, C. H. Yoo, D. Sohn, and Y. Lee, “Coating of multiwalled carbon nanotubes with polymer nanospheres through microemulsion polymerization,” *J. Colloid Interface Sci.*, vol. 340, no. 2, pp. 160–165, 2009.

[243] K. R. Reddy, V. G. Gomes, and M. Hassan, “Carbon functionalized TiO_2 nanofibers for high efficiency photocatalysis,” *Mater. Res. Express*, vol. 1, no. 1, p. 015012, 2014.

[244] Y. R. Lee, S. C. Kim, H. Il Lee, H. M. Jeong, A. V. Raghu, K. R. Reddy, and B. K. Kim, “Graphite oxides as effective fire retardants of epoxy resin,” *Macromol. Res.*, vol. 19, no. 1, pp. 66–71, 2011.

[245] K. R. Reddy, M. Hassan, and V. G. Gomes, “Hybrid nanostructures based on titanium dioxide for enhanced photocatalysis,” *Appl. Catal. A Gen.*, vol. 489, no. 2015, pp. 1–16, 2015.

[246] S. J. Han, H.-I. Lee, H. M. Jeong, B. K. Kim, A. V. Raghu, and K. R. Reddy, “Graphene Modified Lipophilically by Stearic Acid and its Composite With Low Density Polyethylene,” *J. Macromol. Sci. Part B*, vol. 53, no. 7, pp. 1193–1204, 2014.

[247] S. H. Choi, D. H. Kim, A. V. Raghu, K. R. Reddy, H.-I. Lee, K. S. Yoon, H. M. Jeong, and B. K. Kim, “Properties of Graphene/Waterborne Polyurethane Nanocomposites Cast from Colloidal Dispersion Mixtures,” *J. Macromol. Sci. Part B*, vol. 51, no. 1, pp. 197–207, 2012.

[248] M. Hassan, K. R. Reddy, E. Haque, A. I. Minett, and V. G. Gomes, “High-yield aqueous phase exfoliation of graphene for facile nanocomposite synthesis via emulsion polymerization,” *J. Colloid Interface Sci.*, vol. 410, pp. 43–51, 2013.

[249] M. Pumera, “Graphene-based nanomaterials and their electrochemistry.,” *Chem. Soc. Rev.*, vol. 39, no. 11, pp. 4146–57, Nov. 2010.

[250] A. Martín and A. Escarpa, “Graphene: The cutting–edge interaction between chemistry and electrochemistry,” *TrAC Trends Anal. Chem.*, vol. 56, pp. 13–26, Apr. 2014.

[251] J. Yan, T. Wei, W. Qiao, B. Shao, Q. Zhao, L. Zhang, and Z. Fan, “Rapid microwave-assisted synthesis of graphene nanosheet/Co_3O_4 composite for supercapacitors,” *Electrochim. Acta*, vol. 55, no. 23, pp. 6973–6978, Sep. 2010.

[252] S. Park and S. Kim, “Effect of carbon blacks filler addition on electrochemical behaviors of Co_3O_4/graphene nanosheets as a supercapacitor electrodes,” *Electrochim. Acta*, vol. 89, pp. 516–522, Feb. 2013.

[253] M. Wall, “Raman spectroscopy optimizes graphene characterization,” *Adv. Mater. Process.*, vol. 170, no. 4, pp. 35–38, 2012.

[254] J. S. Park, a. Reina, R. Saito, J. Kong, G. Dresselhaus, and M. S. Dresselhaus, “G′ band Raman spectra of single, double and triple layer graphene,” *Carbon N. Y.*, vol. 47, no. 5, pp. 1303–1310, 2009.

[255] I. Calizo, D. Teweldebrhan, W. Bao, F. Miao, C. N. Lau, and a a Balandin, "Spectroscopic raman nanometrology of graphene and graphene multilayers on arbitrary substrates," *J. Phys. Conf. Ser.*, vol. 109, p. 012008, 2008.

[256] M. Kumar, a. Subramania, and K. Balakrishnan, "Preparation of electrospun Co_3O_4 nanofibers as electrode material for high performance asymmetric supercapacitors," *Electrochim. Acta*, vol. 149, pp. 152–158, Dec. 2014.

[257] X. Dong, D. Fu, W. Fang, Y. Shi, P. Chen, and L. J. Li, "Doping single-layer graphene with aromatic molecules," *Small*, vol. 5, no. 12, pp. 1422–1426, 2009.

[258] J. Xu, L. Gao, J. Cao, W. Wang, and Z. Chen, "Preparation and electrochemical capacitance of cobalt oxide (Co_3O_4) nanotubes as supercapacitor material," *Electrochim. Acta*, vol. 56, no. 2, pp. 732–736, Dec. 2010.

[259] J. Deng, L. Kang, G. Bai, Y. Li, P. Li, X. Liu, Y. Yang, F. Gao, and W. Liang, "Solution combustion synthesis of cobalt oxides (Co_3O_4 and Co_3O_4/CoO) nanoparticles as supercapacitor electrode materials," *Electrochim. Acta*, vol. 132, pp. 127–135, Jun. 2014.

[260] M. Hassan, E. Haque, K. R. Reddy, A. I. Minett, J. Chen, and V. G. Gomes, "Edge-enriched graphene quantum dots for enhanced photo-luminescence and supercapacitance," *Nanoscale*, vol. 6, no. 20, pp. 11988–11994, 2014.

[261] M. Hassan, K. R. Reddy, E. Haque, S. N. Faisal, S. Ghasemi, A. I. Minett, and V. G. Gomes, "Hierarchical assembly of graphene/polyaniline nanostructures to synthesize free-standing supercapacitor electrode," *Compos. Sci. Technol.*, vol. 98, pp. 1–8, 2014.

[262] B. Brown, I. a. Cordova, C. B. Parker, B. R. Stoner, and J. T. Glass, "Optimization of active manganese oxide electrodeposits using graphenated carbon nanotube electrodes for supercapacitors," *Chem. Mater.*, vol. 27, no. 7, pp. 2430–2438, 2015.

[263] M. He, L. Kang, C. Liu, Z. Lei, and Z.-H. Liu, "Layer-by-layer assembly of manganese–cobalt–nickel oxide nanosheets/graphene composite films," *Mater. Res. Bull.*, vol. 68, pp. 194–202, Aug. 2015.

[264] W. Liu, C. Lu, K. Liang, and B. K. Tay, "A three dimensional vertically aligned multiwall carbon nanotube/$NiCo_2O_4$ core/shell structure for novel high-performance supercapacitors," *J. Mater. Chem. A*, vol. 2, no. 14, pp. 5100–5107, 2014.

[265] Z. Fan, J. Yan, T. Wei, L. Zhi, G. Ning, T. Li, and F. Wei, "Asymmetric Supercapacitors Based on Graphene/MnO_2 and Activated Carbon Nanofiber

Electrodes with High Power and Energy Density," *Adv. Funct. Mater.*, vol. 21, no. 12, pp. 2366–2375, Jun. 2011.

[266] C. J. Jafta, F. Nkosi, L. le Roux, M. K. Mathe, M. Kebede, K. Makgopa, Y. Song, D. Tong, M. Oyama, N. Manyala, S. Chen, and K. I. Ozoemena, "Manganese oxide/graphene oxide composites for high-energy aqueous asymmetric electrochemical capacitors," *Electrochim. Acta*, vol. 110, pp. 228–233, Nov. 2013.

[267] X. Zhang, D. Zhao, Y. Zhao, P. Tang, Y. Shen, C. Xu, H. Li, and Y. Xiao, "High performance asymmetric supercapacitor based on MnO_2 electrode in ionic liquid electrolyte," *J. Mater. Chem. A*, vol. 1, no. 11, p. 3706, 2013.

[268] C. Zhong, Y. Deng, W. Hu, J. Qiao, L. Zhang, and J. Zhang, "A review of electrolyte materials and compositions for electrochemical supercapacitors," *Chem. Soc. Rev.*, vol. 44, no. November, pp. 7484–7539, 2015.

[269] D. Chen, Q. Wang, R. Wang, and G. Shen, "Ternary oxide nanostructured materials for supercapacitors: a review," *J. Mater. Chem. A*, vol. 3, no. 19, pp. 10158–10173, 2015.

[270] J. P. Cheng, X. Chen, J.-S. Wu, F. Liu, X. B. Zhang, and V. P. Dravid, "Porous cobalt oxides with tunable hierarchical morphologies for supercapacitor electrodes," *CrystEngComm*, vol. 14, no. 20, p. 6702, 2012.

[271] E. R. Ezeigwe, M. T. T. Tan, P. S. Khiew, and C. W. Siong, "Solvothermal synthesis of graphene–MnO_2 nanocomposites and their electrochemical behavior," *Ceram. Int.*, vol. 41, no. 9, pp. 11418–11427, 2015.

[272] J. M. Xu, K. Y. Ma, and J. P. Cheng, "Controllable in situ synthesis of $Ni(OH)_2$ and NiO films on nickel foam as additive-free electrodes for electrochemical capacitors," *J. Alloys Compd.*, vol. 653, pp. 88–94, 2015.

[273] Y. Chen, B. Liu, W. Jiang, Q. Liu, J. Liu, J. Wang, H. Zhang, and X. Jing, "Coaxial three-dimensional $CoMoO_4$ nanowire arrays with conductive coating on carbon cloth for high-performance lithium ion battery anode," *J. Power Sources*, vol. 300, pp. 132–138, 2015.

[274] W. Sun and Y. Wang, "Graphene-based nanocomposite anodes for lithium-ion batteries.," *Nanoscale*, vol. 6, pp. 11528-11552, 2014.

[275] G. He, L. Wang, H. Chen, X. Sun, and X. Wang, "Preparation and performance of $NiCo_2O_4$ nanowires-loaded graphene as supercapacitor material," *Mater. Lett.*, vol. 98, pp. 164–167, 2013.

[276] W. Du, X. Jiang, and L. Zhu, “From graphite to graphene: direct liquid-phase exfoliation of graphite to produce single- and few-layered pristine graphene,” *J. Mater. Chem. A*, vol. 1, no. 36, p. 10592, 2013.

[277] S. S. Low, M. T. T. Tan, H. S. Loh, P. S. Khiew, and W. S. Chiu, “Facile hydrothermal growth graphene/ZnO nanocomposite for development of enhanced biosensor,” *Anal. Chim. Acta*, vol. 903, no. 2016, pp. 131–141, 2016.

[278] S. S. Low, M. T. T. Tan, P. S. Khiew, H.-S. Loh, and W. S. Chiu, “One Step Green Preparation of Graphene/ZnO Nanocomposite for Electrochemical Sensing,” *J. Nanosci. Nanotechnol.*, vol. 16, no. 7, pp. 7420–7426, 2016.

[279] E. R. Ezeigwe, C. J. Sin, P. S. Khiew, C. W. Siong, and M. T. T. Tan, “Cobalt oxide nanoparticles grown on exfoliated graphene for enhanced electrochemical performance,” *Mater. Chem. Phys.*, pp. 1–9, 2016.

[280] S. S. Low, J. S. Y. Chia, M. T. T. Tan, H.-S. Loh, P. S. Khiew, A. Singh, and W. S. Chiu, “A Proof of Concept: Detection of Avian Influenza H5 Gene by a Graphene-Enhanced Electrochemical Genosensor,” *J. Nanosci. Nanotechnol.*, vol. 16, no. 3, pp. 2438–2446, 2016.

[281] J. Cheng, Y. Lu, K. Qiu, H. Yan, J. Xu, L. Han, X. Liu, J. Luo, J.-K. Kim, and Y. Luo, “Hierarchical Core/Shell $NiCo_2O_4$@$NiCo_2O_4$ Nanocactus Arrays with Dual-functionalities for High Performance Supercapacitors and Li-ion Batteries,” *Sci. Rep.*, vol. 5, no. February, p. 12099, 2015.

[282] A. K. Das, R. K. Layek, N. H. Kim, D. Jung, and J. H. Lee, “Reduced graphene oxide (RGO)-supported $NiCo_2O_4$ nanoparticles: an electrocatalyst for methanol oxidation.,” *Nanoscale*, vol. 6, no. 18, pp. 10657–65, 2014.

[283] Z. Dai, C. Peng, J. H. Chae, K. C. Ng, and G. Z. Chen, “Cell voltage versus electrode potential range in aqueous supercapacitors,” *Sci. Rep.*, vol. 5, p. 9854, 2015.

[284] S. Yang, X. Wu, C. Chen, H. Dong, W. Hu, and X. Wang, “Spherical α-$Ni(OH)_2$ nanoarchitecture grown on graphene as advanced electrochemical pseudocapacitor materials.,” *Chem. Commun. (Camb).*, vol. 48, no. 22, pp. 2773–5, 2012.

[285] M. Rajkumar, C. T. Hsu, T. H. Wu, M. G. Chen, and C. C. Hu, “Advanced materials for aqueous supercapacitors in the asymmetric design,” *Prog. Nat. Sci. Mater. Int.*, vol. 25, no. 6, pp. 527–544, 2015.

[286] X. Xu, J. Shen, N. Li, and M. Ye, “Microwave-assisted synthesis of graphene/$CoMoO_4$ nanocomposites with enhanced supercapacitor performance,” *J. Alloys Compd.*, vol. 616, no. 2014, pp. 58–65, 2014.

[287] C.-C. Tseng, J.-L. Lee, Y.-M. Liu, M.-D. Ger, and Y.-Y. Shu, “Microwave-assisted hydrothermal synthesis of spinel nickel cobaltite and application for supercapacitors,” *J. Taiwan Inst. Chem. Eng.*, vol. 44, no. 3, pp. 415–419, 2013.

[288] D. Kong, W. Ren, C. Cheng, Y. Wang, Z. Huang, and H. Y. Yang, “Three-Dimensional $NiCo_2O_4$@Polypyrrole Coaxial Nanowire Arrays on Carbon Textiles for High-Performance Flexible Asymmetric Solid-State Supercapacitor,” *ACS Appl. Mater. Interfaces*, vol. 7, no. 38, pp. 21334–21346, 2015.

[289] Q. Yang and S.-Y. Lin, “Rationally designed nanosheet-based $CoMoO_4$ –$NiMoO_4$ nanotubes for high-performance electrochemical electrodes,” *RSC Adv.*, vol. 6, no. 13, pp. 10520–10526, 2016.

[290] K. Xiao, L. Xia, G. Liu, S. Wang, L.-X. Ding, and H. Wang, “Honeycomb-like $NiMoO_4$ ultrathin nanosheet arrays for high-performance electrochemical energy storage,” *J. Mater. Chem. A*, vol. 3, no. 11, pp. 6128–6135, 2015.

[291] M.-C. Liu, L.-B. Kong, C. Lu, X.-M. Li, Y.-C. Luo, and L. Kang, “Facile fabrication of $CoMoO_4$ nanorods as electrode material for electrochemical capacitors,” *Mater. Lett.*, vol. 94, no. 2013, pp. 197–200, 2013.

[292] L. Lin, T. Liu, J. Liu, R. Sun, J. Hao, K. Ji, and Z. Wang, “Facile synthesis of groove-like $NiMoO_4$ hollow nanorods for high-performance supercapacitors,” *Appl. Surf. Sci.*, vol. 360, no. 2016, pp. 234–239, 2016.

[293] H. Wu, Z. Lou, H. Yang, and G. Shen, “A flexible spiral-type supercapacitor based on $ZnCo_2O_4$ nanorod electrodes,” *Nanoscale*, vol. 7, no. 5, pp. 1921–1926, 2015.

[294] P. R. Jothi, K. Shanthi, R. R. Salunkhe, M. Pramanik, V. Malgras, S. M. Alshehri, and Y. Yamauchi, “Synthesis and Characterization of α-$NiMoO_4$ Nanorods for Supercapacitor Application,” *Eur. J. Inorg. Chem.*, vol. 2015, no. 22, pp. 3694–3699, 2015.

[295] D. Cai, B. Liu, D. Wang, Y. Liu, L. Wang, H. Li, Y. Wang, C. Wang, Q. Li, and T. Wang, “Facile hydrothermal synthesis of hierarchical ultrathin mesoporous $NiMoO_4$ nanosheets for high performance supercapacitors,” *Electrochim. Acta*, vol. 115, no. 2014, pp. 358–363, 2014.

[296] B. Senthilkumar, K. Vijaya Sankar, R. Kalai Selvan, M. Danielle, and M. Manickam, “Nano α-$NiMoO_4$ as a new electrode for electrochemical supercapacitors,” *RSC Adv.*, vol. 3, pp. 352–357, 2013.

[297] P. R. Jothi, S. Kannan, and G. Velayutham, “Enhanced methanol electro-oxidation over in-situ carbon and graphene supported one dimensional $NiMoO_4$ nanorods,” *J. Power Sources*, vol. 277, no. 2015, pp. 350–359, 2015.

[298] M. Pumera, “Graphene-based nanomaterials for energy storage,” *Energy Environ. Sci.*, vol. 4, no. 3, p. 668, 2011.

[299] Y. Li, J. Jian, L. Xiao, H. Wang, L. Yu, G. Cheng, J. Zhou, and M. Sun, “Synthesis of $NiMoO_4$ nanosheets on graphene sheets as advanced supercapacitor electrode materials,” *Mater. Lett.*, vol. 184, pp. 21–24, 2016.

[300] W. Gao, “The chemistry of graphene oxide,” *Graphene Oxide Reduct. Recipes, Spectrosc. Appl.*, pp. 61–95, 2015.

[301] L. Tang, X. Li, R. Ji, K. S. Teng, G. Tai, J. Ye, C. Wei, and S. P. Lau, “Bottom-up synthesis of large-scale graphene oxide nanosheets,” *J. Mater. Chem.*, vol. 22, no. 12, p. 5676, 2012.

[302] T. Kuila, S. Bose, A. K. Mishra, P. Khanra, N. H. Kim, and J. H. Lee, “Chemical functionalization of graphene and its applications,” *Prog. Mater. Sci.*, vol. 57, no. 7, pp. 1061–1105, Sep. 2012.

[303] B. Wang, S. Li, X. Wu, J. Liu, and W. Tian, “Hierarchical $NiMoO_4$ nanowire arrays supported on macroporous graphene foam as binder-free 3D anodes for high-performance lithium storage,” *Phys. Chem. Chem. Phys.*, vol. 18, no. 2, pp. 908–915, 2016.

[304] H. M. Abdel-Dayem, “Dynamic phenomena during reduction of α -$NiMoO_4$ in different atmospheres: In-situ thermo-raman spectroscopy study,” *Ind. Eng. Chem. Res.*, vol. 46, no. 8, pp. 2466–2472, 2007.

[305] S. E. Moosavifard, J. Shamsi, S. Fani, and S. Kadkhodazade, “3D ordered nanoporous $NiMoO_4$ for high-performance supercapacitor electrode materials,” *RSC Adv.*, vol. 4, no. 94, pp. 52555–52561, 2014.

[306] M. C. Liu, L. B. Kong, C. Lu, X. J. Ma, X. M. Li, Y. C. Luo, and L. Kang, “Design and synthesis of $CoMoO_4$-$NiMoO_4xH_2O$ bundles with improved electrochemical properties for supercapacitors,” *J. Mater. Chem. A*, vol. 1, no. 4, pp. 1380–1387, 2013.

[307] J. Yan, Z. Fan, W. Sun, G. Ning, T. Wei, Q. Zhang, R. Zhang, L. Zhi, and F. Wei, “Advanced Asymmetric Supercapacitors Based on $Ni(OH)_2$/Graphene and Porous Graphene Electrodes with High Energy Density,” *Adv. Funct. Mater.*, vol. 22, no. 12, pp. 2632–2641, Jun. 2012.

[308] G. Zhang and X. W. Lou, “General solution growth of mesoporous $NiCo_2O_4$ nanosheets on various conductive substrates as high-performance electrodes for supercapacitors,” *Adv. Mater.*, vol. 25, no. 7, pp. 976–979, 2013.

[309] Y.-L. Chen, Z.-A. Hu, Y.-Q. Chang, H.-W. Wang, Z.-Y. Zhang, Y.-Y. Yang, and H.-Y. Wu, “Zinc Oxide/Reduced Graphene Oxide Composites and Electrochemical Capacitance Enhanced by Homogeneous Incorporation of Reduced Graphene Oxide Sheets in Zinc Oxide Matrix,” *J. Phys. Chem. C*, vol. 115, no. 5, pp. 2563–2571, Feb. 2011.

[310] X. Liu, K. Zhang, B. Yang, W. Song, Q. Liu, F. Jia, S. Qin, W. Chen, J. Li, and Z. Zhang, “Three-dimensional graphene supported nickel molybdate nanowires as novel ultralight and flexible electrode for supercapacitors.,” *Mater. Lett.*, vol. 164, no. 2016, pp. 1–16, 2015.

Appendices

List of Publication

Publications (Published)

1. Ejikeme Raphael Ezeigwe, Poi Sim Khiew, Chiu Wee Siong, Ing Kong, and Michelle T.T. Tan, 2017. *Synthesis of $NiMoO_4$ nanorods on graphene and superior electrochemical performance of the resulting ternary based composites*. Ceramics International. 43, p 13772-13780.
2. Ejikeme Raphael Ezeigwe, Poi Sim Khiew, Chiu Wee Siong, and Michelle T.T. Tan, 2017. *Solvothermal synthesis of $NiCo_2O_4$ nanocomposites on liquid-phase exfoliated graphene as an electrode material for electrochemical capacitors.* Journal of Alloys and Compounds. 693, p 1133-1142.
3. Ejikeme Raphael Ezeigwe, Chu Joon Sin, Poi Sim Khiew, Chiu Wee Siong, and Michelle T.T. Tan, 2016. *Cobalt oxide nanoparticles grown on exfoliated graphene for enhanced electrochemical performance. Materials Chemistry and Physics.* 183, p 56-64.
4. Ejikeme Raphael Ezeigwe, Michelle T.T. Tan, Poi Sim Khiew and Chiu Wee Siong, 2015. *Solvothermal synthesis of graphene–MnO_2 nanocomposites and their electrochemical behavior. Ceramics International.* 41 p 11418-11427.
5. Ejikeme Raphael Ezeigwe, Michelle T.T. Tan, Poi Sim Khiew, Chiu Wee Siong, 2015. *One-step Green Synthesis of Graphene/ZnO Nanocomposites for Electrochemical Capacitors*. Ceramics International. 41, p 715-724

Conference participation:-

✓ International Conference on Advanced Materials and Nanotechnology, Kuala Lumpur, Malaysia. (ICAMN 2016) – **Best Oral Presenter Award**